

**INVESTIGATION OF FLOW DYNAMICS OF CONICAL
FLUIDIZED BED**

A thesis

submitted in partial fulfillment of the

requirements for the degree of

DOCTOR OF PHILOSOPHY

by

LIPIKA KALO

(126107002)



DEPARTMENT OF CHEMICAL ENGINEERING

INDIAN INSTITUTE OF TECHNOLOGY GUWAHATI

GUWAHATI-781039

DECEMBER 2018

CERTIFICATE

It is certified that the work contained in the thesis entitled **Investigation of Flow Dynamics of Conical Fluidized Bed** by **Lipika Kalo**, a student in the Department of Chemical Engineering, Indian Institute of Technology Guwahati, Guwahati, India, for the award of the degree of **Doctor of Philosophy** has been carried out under my supervision and this work has not been submitted elsewhere for the degree.

Dr. Rajesh Kumar Upadhyay

Associate Professor

Department of Chemical Engineering

Indian Institute of Technology Guwahati

Guwahati – 781039, Assam, India.



ACKNOWLEDGEMENTS

I wish to express my gratitude to my supervisor, Dr. Rajesh Kumar Upadhyay, Department of Chemical Engineering, Indian Institute of Technology Guwahati, India who taught me every aspect of research. His patience, motivation, and guidance has always helped me to grow continuously. I have learnt many things from his valuable comments and insightful discussions throughout the work.

I wish to express my sincere thanks to my Doctoral committee members Dr. T. K. Mandal, Prof. S. K. Majumder, Dr. Amaresh Dalal for their valuable comments and suggestions throughout my work.

I am profoundly thankful to the present and previous Head of Department of Chemical Engineering, Prof. Bishnupada Mandal and Prof. V. S. Moholkar for providing me the necessary facilities in the department during my research work.

I express my sincere thanks to Dr. H. J. Pant, Isotope and Radiation Application Division, Bhabha Atomic Research Centre (BARC), Mumbai for his support in providing radioactive tracer particles for my experiments and for helping me on radioactive tracer particle handling.

I am also grateful to Prof. M. C. Cassanello, Departamento de Industrias, Universidad de Buenos Aires, Buenos Aires, Argentina, for helping me with the time series analysis of RPT and for giving me valuable suggestions.

I would like to express my gratitude to Premkumar K for his continuous encouragement, insightful discussion and suggestion, and constant help throughout my work who always put extra effort for me. I am greatly indebted to Deepak Kumar for always being there to help me for

my experiments. I am indebted to Richa Sharma who has always been there for me and has provided her support whenever I needed. I am greatly indebted to all my colleagues and friends, the list is indefinite but to name a few: Trilokpati Tribedi, Rajani kant Boro, Biswajeet, Jitendra, Roopesh, Karan, Sonit, Soorya, Dr. Shilpi Verma, Premsagar, Roushni, Keshav, Punam, Sandeep, Tarang, Angela, Rukhsar, Sanjukta, Shreedevi. They have been always there for me with their suggestions, moral support and hand of help for everything I needed.

Last but not the least, I would like to acknowledge the continuous love and support from my family. Their encouragement and trust in me has helped me go one step further. Thanks to Titu, Lisa and Bapi bhai for being a constant source of inspiration and support every time I needed.

I would like to thank MHRD (Ministry of Human Resource and Development) for providing the assistantship during Ph.D.

Finally, I would like to thank all those who have helped me during the research work.

Lipika Kalo

IIT Guwahati

Abstract

Conical fluidized beds are used for various applications in many industries. Despite their wide applications, the detailed understanding of conical fluidized bed is still missing. A detailed data on the local hydrodynamic of these systems can be useful for their design, operation, and scale-up. Most of the literature on conical fluidized beds only reveal about their overall performance in terms of overall pressure drop, minimum fluidization velocity prediction, global mixing and segregation characteristics. However, the local interaction between the fluid-solid and solid-solid are more critical. Further, the effect of particle size, particle size distribution and column dimensions on mixing and segregation of the conical bed are not well understood. To the best no scale-up studies are reported in literature on conical fluidized bed. Such studies are largely missing due to lack of experimental data as most of the technique work in optical range and is not applicable in dense conical fluidized bed. Further, very few measurement techniques are available which can provide the data with the same accuracy at both scales.

In current thesis, radioactive particle tracking (RPT) technique was used to study the flow behavior in conical fluidized bed. Experiments were performed for both gas-solid and liquid-solid conical fluidized beds for different fluid inlet velocities and particle sizes. Binary bed of same density and different particle size was used to study the effect of bed composition and fluid inlet velocity on performance of gas-solid and liquid-solid conical fluidized beds. Effect of operating conditions on axial and radial mean velocities, axial and radial RMS velocities, and granular temperature were studied. Further, time series analysis was performed to quantify Hurst's exponent, axial and radial autocorrelation functions. Chaos analysis was performed to estimate Kolmogorov entropy and correlation dimensions. Further, segregation index was

calculated to quantify the mixing and segregation behavior of the gas-solid and liquid-solid conical fluidized beds for different fluid inlet velocities and bed compositions. It was found that both gas-solid and liquid-solid fluidized beds provide better mixing compared to their cylindrical fluidized bed. Particle-particle interactions were found to be critical in determining the flow physics at the top section of the mono and binary dispersed conical fluidized beds. While, fluid-particle interactions were more critical at the bottom of the conical bed, which was relatively dilute compared to top section. Regime transition was observed for both gas-solid and liquid-solid conical fluidized beds at higher velocity. It was observed that regime transition only depends on fluid velocity and not on bed composition. Liquid-solid conical bed was found to be calm and homogeneously distributed compared to gas-solid conical bed.

Finally, scale-up studies are performed for gas-solid mono and binary dispersed conical fluidized beds using the inertia set of Glicksman law. Effect of fluid velocity on performance of scaled-up setup is also investigated. It was found that the behavior of the bed changes significantly with changing the column dimensions. Inertia set of Glickman law was able to predict the mean velocities of solids in mono dispersed bed. However, predictions were not good for local/fluctuation quantities like RMS velocity, granular temperature and autocorrelation function. For binary bed inertia set of Glickman law was not able to predict even mean velocities. Hence, used set of scale-up rule was not applicable for conical bed and a dedicated scale-up rule for conical fluidized bed is required. Further, a dedicated scale-up rule for binary bed will also be required which will be different from the mono dispersed bed.

TABLE OF CONTENTS

ABSTRACT	v
TABLE OF CONTENTS	vii
LIST OF FIGURES	xv
LIST OF TABLES	xxxii
1. INTRODUCTION	1
1.1 Fluidization	1
1.1.1 Classification of particles	3
1.2 Conical fluidized bed	5
1.2.1 Advantages	11
1.2.2 Disadvantages	15
1.2.3 Applications	16
1.3 Hydrodynamics of conical gas-solid fluidized bed	16
1.4 Motivation	18
1.5 Objectives of the thesis	20
1.6 Structure of the thesis	21
Notations	22
References	23
2. RADIOACTIVE PARTICLE TRACKING (RPT)	31
2.1 Introduction	31
2.2 Radioactive particle tracking technique	39
2.2.1 Methodology	39

2.2.2	Implementation of RPT	43
2.2.3	Calibration	48
2.2.4	Reconstruction algorithm	51
2.3	Advanced post processing techniques (time series analysis)	52
	Notations	57
	References	60
3.	EXPERIMENTAL INVESTIGATION OF GAS-SOLID	67
	CONICAL FLUIDIZED BED	
3.1	Introduction	67
3.2	Literature on G-S conical fluidized bed	69
3.3	Experimental setup	74
3.4	Results and discussions	77
3.4.1	Lagrangian track of particle position	77
3.4.2	Lagrangian velocity of the solids	79
3.5	Effect of gas velocity on monodispersed bed	83
3.5.1	Velocity vector plots	83
3.5.2	Number of occurrences	85
3.5.3	Ensemble averaged velocity	86
3.5.4	Solid velocity fluctuations	90
3.5.5	Granular temperature	93
3.5.6	Hurst exponent	95
3.5.7	Autocorrelation	97

3.5.8	Kolmogorov entropy	100
3.5.9	Correlation dimension	100
3.6	Effect of gas velocity on mono and binary dispersed beds	101
3.6.1	Ensemble averaged velocity	101
3.6.2	Solid velocity fluctuations	106
3.6.3	Granular temperature	107
3.6.4	Hurst exponent	111
3.6.5	Autocorrelation	112
3.6.6	Segregation index	116
3.6.7	Kolmogorov entropy	117
3.6.8	Correlation dimension	118
3.7	Effect of bed composition	119
3.7.1	Ensemble averaged velocity	120
3.7.2	Solid velocity fluctuations	122
3.7.3	Granular temperature	125
3.7.4	Hurst exponent	126
3.7.5	Autocorrelation	126
3.7.6	Segregation index	127
3.8	Summary	129
	Notations	131
	References	131
4.	EXPERIMENTAL INVESTIGATION OF LIQUID-SOLID	139

CONICAL FLUIDIZED BED

4.1	Introduction	139
4.2	Literature on L-S conical fluidized bed	140
4.3	Experimental setup	143
4.4	Results and discussions	146
4.4.1	Lagrangian velocity of the solids	146
4.5	Effect of liquid velocity on monodispersed bed	149
4.5.1	Velocity vector plots	149
4.5.2	Number of occurrences	151
4.5.3	Ensemble averaged velocity	151
4.5.4	Solid velocity fluctuations	154
4.5.5	Granular temperature	157
4.5.6	Hurst exponent	158
4.5.7	Autocorrelation	159
4.5.8	Kolmogorov entropy	163
4.5.9	Correlation dimension	163
4.6	Effect of liquid velocity on mono and binary dispersed beds	164
4.6.1	Ensemble averaged velocity	165
4.6.2	Solid velocity fluctuations	169
4.6.3	Granular temperature	170
4.6.4	Hurst exponent	175
4.6.5	Autocorrelation	176

4.6.6	Segregation index	180
4.6.7	Kolmogorov entropy	181
4.6.8	Correlation dimension	181
4.7	Effect of bed composition	182
4.7.1	Ensemble averaged velocity	182
4.7.2	Solid velocity fluctuations	184
4.7.3	Granular temperature	186
4.7.4	Hurst exponent	187
4.7.5	Autocorrelation	188
4.7.6	Segregation index	190
4.8	Summary	190
	Notations	192
	References	192
5.	SCALE UP OF CONICAL GAS-SOLID FLUIDIZED BED	197
5.1	Introduction	197
5.2	Present state of the art of scale-up studies	199
5.3	Experimental setup	202
5.4	Results and discussions	206
5.4.1	Lagrangian track of particle position	206
5.5	Effect of scale on monodispersed bed	207
5.5.1	Ensemble averaged velocity	208
5.5.2	Solid velocity fluctuations	211

5.5.3	Granular temperature	213
5.5.4	Hurst exponent	214
5.5.5	Autocorrelation	215
5.5.6	Kolmogorov entropy	217
5.5.7	Correlation dimension	218
5.6	Effect of scale on binary dispersed bed	219
5.6.1	Ensemble averaged velocity	219
5.6.2	Solid velocity fluctuations	221
5.6.3	Granular temperature	222
5.6.4	Hurst exponent	223
5.6.5	Autocorrelation	224
5.6.6	Kolmogorov entropy	228
5.6.7	Correlation dimension	229
5.7	Summary	230
	Notations	231
	References	232
6.	SUMMARY AND RECOMMENDATIONS	235
6.1	Summary	235
6.2	Recommendations and future directions	240
	APPENDIX A	241
A.1	Introduction	241
A.2	Euler – Euler modeling approach	242

A.3	Base case formulation (Gas-solid fluidized bed)	248
A.4	Effect of gas inlet velocity	255
A.5	Summary	257
	Notations	258
	References	260
	APPENDIX B	263





List of Figures

Figure No.	Figure Title	Page No.
1.1	Diagrams of fluidization regimes (Kunii and Levenspiel, 1991)	3
1.2	Geldart's classification of particles (Geldart, 1973)	5
1.3	Diagram of conical fluidization regimes (Peng and Fan, 1997)	8
1.4	Pressure drop-velocity curve (curve 1: conical fluidized bed, curve 2: cylindrical fluidized bed)	9
2.1	Schematic of optical fiber probe technique (Werther and Molerus, 1973)	32
2.2	Schematic of LDA technique (Durst et al., 1981)	34
2.3	Schematic of the PIV technique (Prasad, 2000)	35
2.4	Schematic of PEPT technique (Parker et al., 1997)	36
2.5	Schematic of RPT technique	37
2.6	Flow chart of measurement principle (Limtrakul et al., 2005)	41
2.7	Photograph of MIDAS [®]	44
2.8	Schematic diagram of pulse processing system	45
2.9	Photograph of MCA	46
2.10	Schematic diagram of NaI(Tl) scintillation detector	47
2.11	Photograph of NaI(Tl) scintillation detector	47
2.12	Schematic diagram of positioning of source and detector when the source is outside detector flat face and within the detector flat face	50

	(Beam et al., 1978)	
2.13	Schematic diagram of possibilities of photon travelling path through the detector (Beam et al., 1978)	51
3.1	Regimes in binary conical fluidized bed (Kwant et al., 1995)	74
3.2	Experimental setup of gas-solid conical fluidized bed for RPT	75
3.3	Schematic diagram of experimental setup	77
3.4	Trajectory of 1 mm tracer at 7.6 m/s with time in r-z plane (a) at 1 sec (b) at 2 sec (c) at 5 sec (d) at 10 sec (e) at 20 sec	78
3.5	Trajectory of 1 mm tracer at 7.6 m/s with time in x-y plane at:(a) 1 sec, (b) 2 sec, (c) 5 sec, (d) 10 sec, and (e) 20 sec	79
3.6	Axial Lagrangian velocity of 1 mm solid at 7.6 m/s	80
3.7	Radial Lagrangian velocity of 1 mm solid at 7.6 m/s	80
3.8	Effect of grid on mean axial velocity at $h/H=0.25$ and 7.6 m/s (1 mm solid)	81
3.9	Validation of stationarity of 1 mm solid at $h/H = 0.75$ at 7.6 m/s (a) V_{zmean} (b) V_{zrms}	83
3.10	Mean axial velocity vectors of 1 mm solids at (a) 3.8, (b) 5.7, and (c) 7.6 m/s	84
3.11	Mean axial velocity vectors of 0.6 mm solids at (a) 3.8, (b) 5.7, and (c) 7.6 m/s	85
3.12	Contour map of occurrence of 1 mm and 0.6 mm solid at 7.6 m/s velocity	86

- 3.13 Variation of mean axial velocity of solid at different velocities: (a) 89
1 mm particle on top section, (b) 0.6 mm particle on top section,
(c) 1 mm particle at bottom section, and (d) 0.6 mm particle at
bottom section
- 3.14 Variation of mean radial velocity of solid at different velocities: 90
(a) 1 mm particle on top section, (b) 0.6 mm particle on top
section, (c) 1 mm particle at bottom section, and (d) 0.6 mm
particle at bottom section
- 3.15 Variation of V_{zrms} of solid at different velocities: (a) 1 mm 92
particle on top section, (b) 0.6 mm particle on top section, (c) 1
mm particle at bottom section, and (d) 0.6 mm particle at bottom
section
- 3.16 Variation of V_{rrms} of solid at different velocities: (a) 1 mm 93
particle on top section, (b) 0.6 mm particle on top section, (c) 1
mm particle at bottom section, and (d) 0.6 mm particle at bottom
section
- 3.17 Variation of granular temperature of solid at different velocities: 95
(a) 1 mm particle on top section, (b) 0.6 mm particle on top
section, (c) 1 mm particle at bottom section, and (d) 0.6 mm
particle at bottom section
- 3.18 Hurst exponent at 7.6 m/s gas velocity for (a) 1 mm solid, and (b) 96
0.6 mm solid

3.19	Variation of axial autocorrelation of solid at different velocities: (a) 1 mm particle at 3.8 m/s, (b) 1 mm particle at 5.7 m/s, (c) 1 mm particle at 7.6 m/s, (d) 0.6 mm particle at 3.8 m/s, (e) 0.6 mm particle at 5.7 m/s, and (f) 0.6 mm particle at 7.6 m/s	98
3.20	Variation of radial autocorrelation of solid at different velocities: (a) 1 mm particle at 3.8 m/s, (b) 1 mm particle at 5.7 m/s, (c) 1 mm particle at 7.6 m/s, (d) 0.6 mm particle at 3.8 m/s, (e) 0.6 mm particle at 5.7 m/s, and (f) 0.6 mm particle at 7.6	99
3.21	Kolmogorov entropy of 1 mm and 0.6 mm particle with gas inlet velocity	100
3.22	Correlation dimension of 1 mm and 0.6 mm particle with gas inlet velocity	101
3.23	Variation of mean axial velocity of solid at different velocities with composition: (a) top section at 3.8 m/s, (b) top section at 5.7 m/s, (c) top section at 7.6 m/s, (d) bottom section at 3.8 m/s, (e) bottom section at 5.7 m/s, and (f) bottom section at 7.6 m/s	104
3.24	Variation of mean radial velocity of solid at different velocities with composition: (a) top section at 3.8 m/s, (b) top section at 5.7 m/s, (c) top section at 7.6 m/s, (d) bottom section at 3.8 m/s, (e) bottom section at 5.7 m/s, and (f) bottom section at 7.6 m/s	105
3.25	Variation of V_{zrms} of solid at different velocities with composition: (a) top section at 3.8 m/s, (b) top section at 5.7 m/s,	108

	(c) top section at 7.6 m/s, (d) bottom section at 3.8 m/s, (e) bottom section at 5.7 m/s, and (f) bottom section at 7.6 m/s	
3.26	Variation of V_{rms} of solid at different velocities with composition: (a) top section at 3.8 m/s, (b) top section at 5.7 m/s, (c) top section at 7.6 m/s, (d) bottom section at 3.8 m/s, (e) bottom section at 5.7 m/s, and (f) bottom section at 7.6 m/s	109
3.27	Variation of granular temperature of solid at different velocities with composition: (a) top section at 3.8 m/s, (b) bottom section at 3.8 m/s, (c) top section at 5.7 m/s, (d) bottom section at 5.7 m/s, (e) top section at 7.6 m/s, and (f) bottom section at 7.6 m/s	110
3.28	Hurst exponent versus gas inlet velocity	111
3.29	Variation of axial autocorrelation of solid at different velocities in binary bed (a) 1 mm particle at 3.8 m/s, (b) 1 mm particle at 5.7 m/s, (c) 1 mm particle at 7.6 m/s, (d) 0.6 mm particle at 3.8 m/s, (e) 0.6 mm particle at 5.7 m/s, and (f) 0.6 mm particle at 7.6 m/s	114
3.30	Variation of radial autocorrelation of solid at different velocities in binary bed (a) 1 mm particle at 3.8 m/s, (b) 1 mm particle at 5.7 m/s, (c) 1 mm particle at 7.6 m/s, (d) 0.6 mm particle at 3.8 m/s, (e) 0.6 mm particle at 5.7 m/s, and (f) 0.6 mm particle at 7.6 m/s	115
3.31	Variation of Segregation index of solid with gas inlet velocity for binary dispersed bed	117
3.32	Kolmogorov entropy of 1 mm and 0.6 mm particle with gas inlet	118

	velocity	
3.33	Correlation dimension of 1 mm and 0.6 mm particle with gas inlet velocity	119
3.34	Variation of mean axial velocity of solid with different composition: (a) 1 mm particle on top section, (b) 0.6 mm particle on top section, (c) 1 mm particle at bottom section, and (d) 0.6 mm particle at bottom section	121
3.35	Variation of mean radial velocity of solid with different composition: (a) 1 mm particle on top section, (b) 0.6 mm particle on top section, (c) 1 mm particle at bottom section, and (d) 0.6 mm particle at bottom section	122
3.36	Variation of V_{zrms} of solid with different composition: (a) 1 mm particle on top section, (b) 0.6 mm particle on top section, (c) 1 mm particle at bottom section, and (d) 0.6 mm particle at bottom section	123
3.37	Variation of V_{rrms} of solid with different composition: (a) 1 mm particle on top section, (b) 0.6 mm particle on top section, (c) 1 mm particle at bottom section, and (d) 0.6 mm particle at bottom section	124
3.38	Variation of granular temperature of solid with different composition: (a) 1 mm particle on top section, (b) 0.6 mm particle on top section, (c) 1 mm particle at bottom section, and (d) 0.6	125

	mm particle at bottom section	
3.39	Variation of axial autocorrelation of solid with different compositions in binary bed (a) 1 mm particle in mono bed, (b) 1 mm particle in 75b-25s bed, (c) 1 mm particle in 50b-50s bed, (d) 1 mm particle in 25b-75s bed, (e) 0.6 mm particle in mono bed, (f) 0.6 mm particle in 25b-75s bed, (g) 1 mm particle in 50b-50s bed, and (h) 1 mm particle in 75b-25s bed	128
3.40	Variation of segregation index with different compositions in binary bed	129
4.1	Regimes in binary conical fluidized bed (Kwant et al., 1995)	143
4.2	Experimental setup of liquid-solid conical fluidized bed for RPT	145
4.3	Schematic diagram of experimental setup	145
4.4	Axial Lagrangian velocity of 1 mm solid at 0.14 m/s	146
4.5	Radial Lagrangian velocity of 1 mm solid at 0.14 m/s	147
4.6	Effect of grid on mean axial velocity at $h/H = 0.75$ and 0.14 m/s (1 mm solid)	147
4.7	Validation of stationarity at $h/H = 0.75$ and 0.14 m/s (1 mm solid) (a) V_{zmean} (b) V_{zrms}	148
4.8	Velocity vector plots of mono bed (a) 1 mm solids at 0.07 m/s, (b) 1 mm solids at 0.1 m/s, (c) 1 mm solids at 0.14 m/s, (d) 0.6 mm solids at 0.07 m/s, (e) 0.6 mm solids at 0.1 m/s, and (f) 0.6 mm solids at 0.14 m/s	150

4.9	Contour map of occurrence of 1 mm and 0.6 mm solid of at 0.14 m/s velocity	151
4.10	Variation of mean axial velocity of solid at different velocities: (a) 1 mm particle on top section, (b) 0.6 mm particle on top section, (c) 1 mm particle at bottom section, and (d) 0.6 mm particle at bottom section	153
4.11	Variation of mean radial velocity of solid at different velocities: (a) 1 mm particle on top section, (b) 0.6 mm particle on top section, (c) 1 mm particle at bottom section, and (d) 0.6 mm particle at bottom section	154
4.12	Variation of V_{zrms} of solid at different velocities: (a) 1 mm particle on top section, (b) 0.6 mm particle on top section, (c) 1 mm particle at bottom section, and (d) 0.6 mm particle at bottom section	155
4.13	Variation of V_{rrms} of solid at different velocities: (a) 1 mm particle on top section, (b) 0.6 mm particle on top section, (c) 1 mm particle at bottom section, and (d) 0.6 mm particle at bottom section	156
4.14	Variation of granular temperature of solid at different velocities: (a) 1 mm particle on top section, (b) 0.6 mm particle on top section, (c) 1 mm particle at bottom section, and (d) 0.6 mm particle at bottom section	157

4.15	Hurst exponent at 0.14 m/s liquid velocity for (a) 1 mm solid, and (b) 0.6 mm solid	158
4.16	Variation of axial autocorrelation of solid at different velocities: (a) 1 mm particle at 0.07 m/s, (b) 1 mm particle at 0.1 m/s, (c) 1 mm particle at 0.14 m/s, (d) 0.6 mm particle at 0.07 m/s, (e) 0.6 mm particle at 0.1 m/s, and (f) 0.6 mm particle at 0.14 m/s	161
4.17	Variation of radial autocorrelation of solid at different velocities: (a) 1 mm particle at 0.07 m/s, (b) 1 mm particle at 0.1 m/s, (c) 1 mm particle at 0.14 m/s, (d) 0.6 mm particle at 0.07 m/s, (e) 0.6 mm particle at 0.1 m/s, and (f) 0.6 mm particle at 0.14 m/s	162
4.18	Kolmogorov entropy of 1 mm and 0.6 mm particle with liquid inlet velocity	163
4.19	Correlation dimension of 1 mm and 0.6 mm particle with liquid inlet velocity	164
4.20	Variation of mean axial velocity of solid at different velocities with composition: (a) top section at 0.07 m/s, (b) top section at 0.1 m/s, (c) top section at 0.14 m/s, (d) bottom section at 0.07 m/s, (e) bottom section at 0.1 m/s, and (f) bottom section at 0.14 m/s	167
4.21	Variation of radial velocity of solid at different velocities with composition: (a) top section at 0.07 m/s, (b) top section at 0.1 m/s, (c) top section at 0.14 m/s, (d) bottom section at 0.07 m/s, (e) bottom section at 0.1 m/s, and (f) bottom section at 0.14 m/s	168

- 4.22 Variation of V_{zrms} of solid at different velocities with 172
composition: (a) top section at 0.07 m/s, (b) top section at 0.1 m/s,
(c) top section at 0.14 m/s, (d) bottom section at 0.07 m/s, (e)
bottom section at 0.1 m/s, and (f) bottom section at 0.14 m/s
- 4.23 Variation of V_{rrms} of solid at different velocities with 173
composition: (a) top section at 0.07 m/s, (b) top section at 0.1 m/s,
(c) top section at 0.14 m/s, (d) bottom section at 0.07 m/s, (e)
bottom section at 0.1 m/s, and (f) bottom section at 0.14 m/s
- 4.24 Variation of granular temperature of solid at different velocities 174
with composition: (a) top section at 0.07 m/s, (b) top section at 0.1
m/s, (c) top section at 0.14 m/s, (d) bottom section at 0.07 m/s, (e)
bottom section at 0.1 m/s, and (f) bottom section at 0.14 m/s
- 4.25 Hurst exponent with liquid inlet velocity 175
- 4.26 Variation of axial autocorrelation of solid at different velocities in 178
binary bed (a) 1 mm particle at 0.07 m/s, (b) 1 mm particle at 0.1
m/s, (c) 1 mm particle at 0.14 m/s, (d) 0.6 mm particle at 0.07
m/s, (e) 0.6 mm particle at 0.1 m/s, and (f) 0.6 mm particle at 0.14
m/s
- 4.27 Variation of radial autocorrelation of solid at different velocities 179
in binary bed (a) 1 mm particle at 0.07 m/s, (b) 1 mm particle at
0.1 m/s, (c) 1 mm particle at 0.14 m/s, (d) 0.6 mm particle at 0.07
m/s, (e) 0.6 mm particle at 0.1 m/s, and (f) 0.6 mm particle at 0.14

	m/s	
4.28	Variation of segregation index of solid with liquid inlet velocity for binary dispersed bed	180
4.29	Kolmogorov entropy of 1 mm and 0.6 mm particle with liquid inlet velocity	181
4.30	Correlation dimension of 1 mm and 0.6 mm particle with liquid inlet velocity	182
4.31	Variation of mean axial velocity of solid with different composition: (a) 1 mm particle on top section, (b) 0.6 mm particle on top section, (c) 1 mm particle at bottom section, and (d) 0.6 mm particle at bottom section	183
4.32	Variation of mean radial velocity of solid with different composition: (a) 1 mm particle on top section, (b) 1 mm particle at bottom section, (c) 0.6 mm particle on top section, and (d) 0.6 mm particle at bottom section	184
4.33	Variation of V_{zrms} of solid at different composition: (a) 1 mm particle on top section, (b) 0.6 mm particle on top section, (c) 1 mm particle at bottom section, and (d) 0.6 mm particle at bottom section	185
4.34	Variation of V_{rrms} of solid at different composition: (a) 1 mm particle on top section, (b) 0.6 mm particle on top section, (c) 1 mm particle at bottom section, and (d) 0.6 mm particle at bottom	186

	section	
4.35	Variation of granular temperature of solid at different composition: (a) 1 mm particle on top section, (b) 0.6 mm particle on top section, (c) 1 mm particle at bottom section, and (d) 0.6 mm particle at bottom section	187
4.36	Variation of axial autocorrelation of solid with different compositions in binary bed (a) 1 mm particle in mono bed, (b) 1 mm particle in 75b-25s bed, (c) 1 mm particle in 50b-50s bed, (d) 1 mm particle in 25b-75s bed, (e) 0.6 mm particle in mono bed, (f) 0.6 mm particle in 25b-75s bed, (g) 1 mm particle in 50b-50s bed, and (h) 1 mm particle in 75b-25s bed	189
4.37	Variation of segregation index with different composition in binary bed	190
5.1	Photograph and schematic of scaled experimental setup	204
5.2	Trajectory of 2 mm tracer at 8.1 m/s with time in r-z plane at (a) 1 sec, (b) 2 sec, (c) 5 sec, (d) 10 sec, and (e) 20 sec	206
5.3	Trajectory of 2 mm tracer at 8.1 m/s with time in x-y plane at (a) 1 sec, (b) at 2 sec, (c) 5sec, (d) 10 sec, and (e) 20 sec	207
5.4	Variation of mean axial velocity of solid in mono bed (a) top section bigger solid, (b) top section smaller solid, (c) bottom section bigger solid, and (d) bottom section smaller solid	209
5.5	Variation of dimensionless mean axial velocity of solid in mono	210

	bed (a) top section bigger solid, (b) top section smaller solid, (c) bottom section bigger solid, and (d) bottom section smaller solid	
5.6	Variation of non-dimensional mean radial velocity of solid in mono bed (a) top section bigger solid, (b) top section smaller solid, (c) bottom section bigger solid, and (d) bottom section smaller solid	211
5.7	Variation of dimensionless V_{zrms} of solid in mono bed (a) top section bigger solid, (b) top section smaller solid, (c) bottom section bigger solid, and (d) bottom section smaller solid	213
5.8	Variation of non-dimensionalized granular temperature of solid in mono bed (a) top section bigger solid, (b) top section smaller solid, (c) bottom section bigger solid, and (d) bottom section smaller solid	214
5.9	Variation of axial autocorrelation of solid in mono bed (a) 2 mm particle at 5.4 m/s in large column, (b) 2 mm particle at 8.1 m/s in large column, (c) 1 mm particle at 3.8 m/s in small column, and (d) 1 mm particle at 5.7 m/s in small column	216
5.10	Variation of axial autocorrelation of solid in mono bed (a) 1 mm particle at 5.4 m/s in large column, (b) 1 mm particle at 8.1 m/s in large column, (c) 0.6 mm particle at 3.8 m/s in small column, and (d) 0.6 mm particle at 5.7 m/s in small column	217
5.11	Variation of dimensionless mean axial velocity of solid in 50b-50s	221

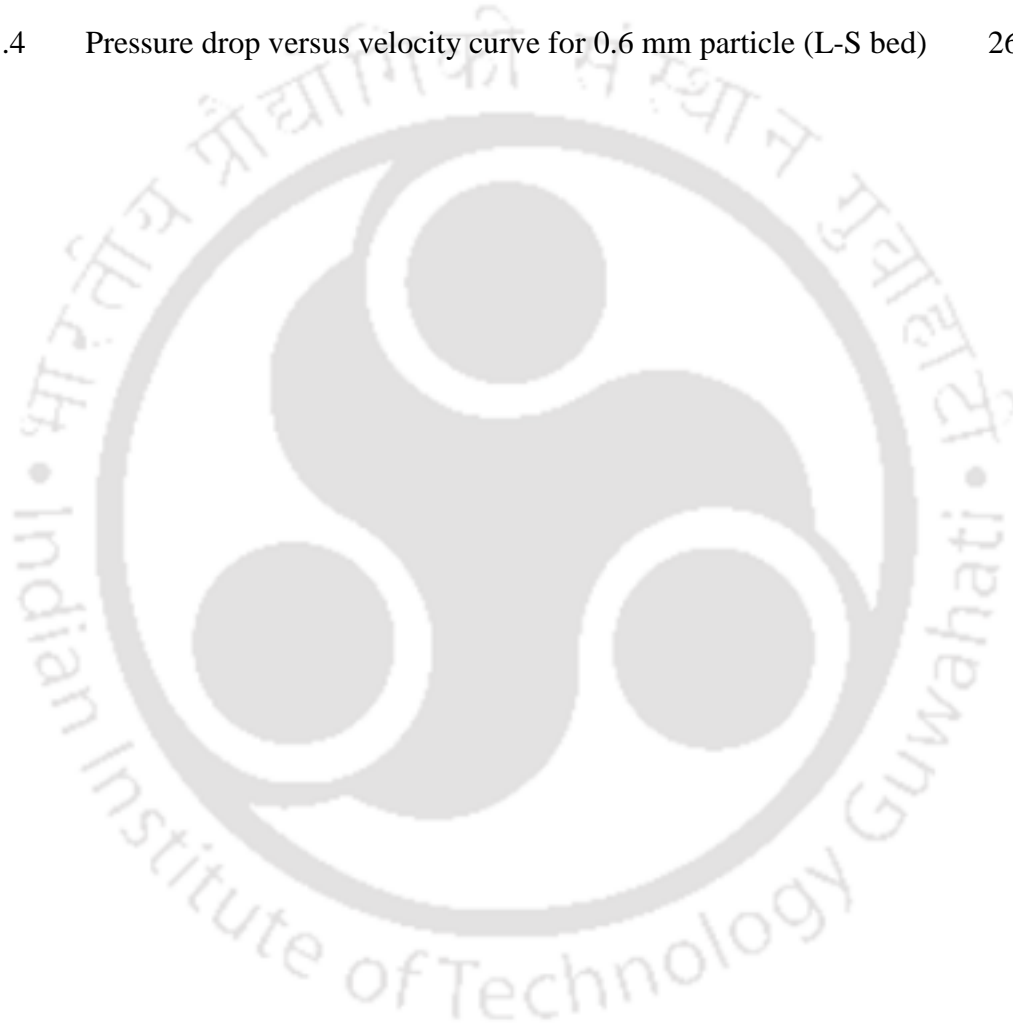
- bed (a) top section bigger solid, (b) top section smaller solid, (c) bottom section bigger solid, and (d) bottom section smaller solid
- 5.12 Variation of dimensionless V_{zrms} of solid in 50b-50s bed (a) top section bigger solid, (b) top section smaller solid, (c) bottom section bigger solid, and (d) bottom section smaller solid 222
- 5.13 Variation of non-dimensionalized granular temperature of solid in 50b-50s bed (a) top section bigger solid, (b) top section smaller solid, (c) bottom section bigger solid, and (d) bottom section smaller solid 223
- 5.14 Variation of axial autocorrelation of solid in 50b-50s bed (a) 2 mm particle at 5.4 m/s in large column, (b) 2 mm particle at 8.1 m/s in large column, (c) 1 mm particle at 3.8 m/s in small column, and (d) 1 mm particle at 5.7 m/s in small column 225
- 5.15 Variation of axial autocorrelation of solid in 50b-50s bed (a) 1 mm particle at 5.4 m/s in large column, (b) 1 mm particle at 8.1 m/s in large column, (c) 0.6 mm particle at 3.8 m/s in small column, and (d) 0.6 mm particle at 5.7 m/s in small column 226
- 5.16 Variation of radial autocorrelation of solid in 50b-50s bed (a) 2 mm particle at 5.4 m/s in large column, (b) 2 mm particle at 8.1 m/s in large column, (c) 1 mm particle at 3.8 m/s in small column, and (d) 1 mm particle at 5.7 m/s in small column 227
- 5.17 Variation of radial autocorrelation of solid in 50b-50s bed (a) 1 mm particle at 5.4 m/s in large column, (b) 1 mm particle at 8.1 m/s in large column, (c) 0.6 mm particle at 3.8 m/s in small column, and (d) 0.6 mm particle at 5.7 m/s in small column 228

mm particle at 5.4 m/s in large column, (b) 1 mm particle at 8.1 m/s in large column, (c) 0.6 mm particle at 3.8 m/s in small column, and (d) 0.6 mm particle at 5.7 m/s in small column

A.1	Schematic of computational domain of conical fluidized bed	249
A.2	Axial profiles of mean axial velocity and volume fraction for different grids in G-S conical fluidized bed ($U_g = 7.6$ m/s and 1 mm solid)	251
A.3	Axial profile of mean axial velocity and volume fraction for different drag model in G-S conical fluidized bed ($U_g = 7.6$ m/s and 1 mm solid)	253
A.4	Axial profiles of mean axial velocity and granular temperature for different specular coefficient in G-S conical fluidized bed ($U_g = 7.6$ m/s and 1 mm solid)	254
A.5	Axial profiles of mean axial velocity and volume fraction for different restitution coefficient in G-S conical fluidized bed ($U_g = 7.6$ m/s and 1 mm solid)	255
A.6	Radial profile of mean axial velocity of solid at different velocities: (a) 1 mm particle on top section, (b) 0.6 mm particle on top section, (c) 1 mm particle at bottom section, and (d) 0.6 mm particle at bottom section	256
A.7	Radial profile of mean granular temperature of solid at different velocities: (a) 1 mm particle on top section, (b) 0.6 mm particle on	257

top section, (c) 1 mm particle at bottom section, and (d) 0.6 mm particle at bottom section

B.1	Pressure drop versus velocity curve for 1 mm particle (G-S bed)	263
B.2	Pressure drop versus velocity curve for 0.6 mm particle (G-S bed)	264
B.3	Pressure drop versus velocity curve for 1 mm particle (L-S bed)	265
B.4	Pressure drop versus velocity curve for 0.6 mm particle (L-S bed)	266



List of Tables

Table No.	Title	Page No.
2.1	Look up table of calibration data	52
3.1	Operating conditions in conical gas-solid bed	76
3.2	Different bed compositions and operating velocities in gas-solid conical bed	76
3.3	Hurst exponents at different operating conditions for 1 mm and 0.6 mm particle in mono bed	96
3.4	Hurst exponents at different operating conditions for 1 mm and 0.6 mm particle in 50b-50s bed	112
3.5	Hurst exponents at different operating conditions for 1 mm and 0.6 mm particle in both mono and binary bed	126
4.1	Operating conditions in conical liquid-solid bed	144
4.2	Different bed compositions and operating velocities in conical liquid-solid bed	144
4.3	Hurst exponents at different operating conditions for 1 mm and 0.6 mm particle in mono bed	159
4.4	Hurst exponents at different operating conditions for 1 mm and 0.6 mm particle 50b-50s bed	176
4.5	Hurst exponents at different operating conditions for 1 mm and 0.6 mm particle in both mono and binary bed	188

5.1	Experimental conditions	204
5.2	Hurst exponents at different operating conditions for both the columns	215
5.3	Kolmogorov entropy at different operating conditions for both the columns	218
5.4	Correlation dimension at different operating conditions for both the columns	219
5.5	Hurst exponents at different operating conditions for both the columns	224
5.6	Kolmogorov entropy at different operating conditions for both the columns	229
5.7	Correlation dimension at different operating conditions for both the columns	230
A.1	Drag models	246
A.2	Simulation conditions and parameters in gas-solid (G-S) fluidized bed	250
B.1	Minimum fluidization velocity in gas-solid conical bed	264
B.2	Minimum fluidization velocity in liquid-solid conical bed	266

Chapter 1

Introduction

Scope

This chapter presents the introduction of fluidization and conical fluidized bed. The pros and cons of the conical fluidized bed application have been explained. The hydrodynamic change observed in conical geometry is briefed. This chapter also includes the motivation for the present work and objectives of the study. The structure of the complete thesis has been presented in the last section of this chapter.

1.1 Fluidization

Fluidization is an inherent process for any fluid-solid contact in the chemical, petrochemical and metallurgical industries, and encountered as well in energy production and food processing industries. Fluidized bed systems are widely applied because of their favorable characteristics such as isothermal conditions throughout the bed, excellent heat and mass transfer rates and the possibility of a continuous operation. The behavior of any fluid-solid bed largely depends on the fluid-solid and solid-solid interactions. These interactions change significantly with the change in fluid velocity, column dimensions and geometry, and solid type. This makes the overall fluid-solid system very complex and challenging.

In a fluid-solid bed at a low fluid flow rate, the fluid passes through the void spaces between the solids without disturbing the solids as the drag force exerted by the fluid on solids is very low, compared to the gravity force. Hence solids remain in static bed condition. This is known as the fixed or packed bed. As the flow rate of fluid increases, particles start vibrating; this stage is known as the expanded bed. The drag force, as well

as the pressure drop, increases with an increase in velocity throughout this stage. With further increase in velocity at a certain point, the drag force is balanced by the weight of the particles. At this point, the bed starts fluidizing. The velocity at this point is called minimum fluidization velocity. The minimum fluidization velocity mainly depends on the physical properties of the particles and the fluid being used. At an even higher flow rate, different fluidization behaviors are found depending upon the particle type and fluid (liquid/gas). In the case of liquid, when the column is operated beyond minimum fluidization velocity, a smooth homogeneous fluidization is observed and the bed expands uniformly, known as the smooth or particulate fluidization. In the case of gas, beyond minimum fluidization velocity, a heterogeneous bubbly fluidization is observed, known as the bubbling fluidization. At this stage, the bubble size is usually small. As the velocity further increases, the bubbles grow larger, which covers the whole cross-section of the bed, known as the slug. This stage is called slugging fluidization. Slugging regime appears in deep/narrow beds or bed fluidizing coarse particles. As the velocity increases beyond the slugging stage, the bed surface disappears and the particles are carried out of the bed known as the turbulent fluidized bed. To capture the solids internal or external cyclones are used and the captured solids are again introduced at the bottom of the bed. This arrangement of the bed with recirculation of solids is termed as circulating fluidized bed. With further increase in velocity the entrainment rate increases and big cyclones are needed to capture the solids. This regime is called fast fluidization. At a high flow rate, the fluidized bed becomes dilute or lean phase fluidized bed, which is called pneumatic transport of solids. Figure 1.1 shows the various regimes of fluidization with increasing fluid velocity.

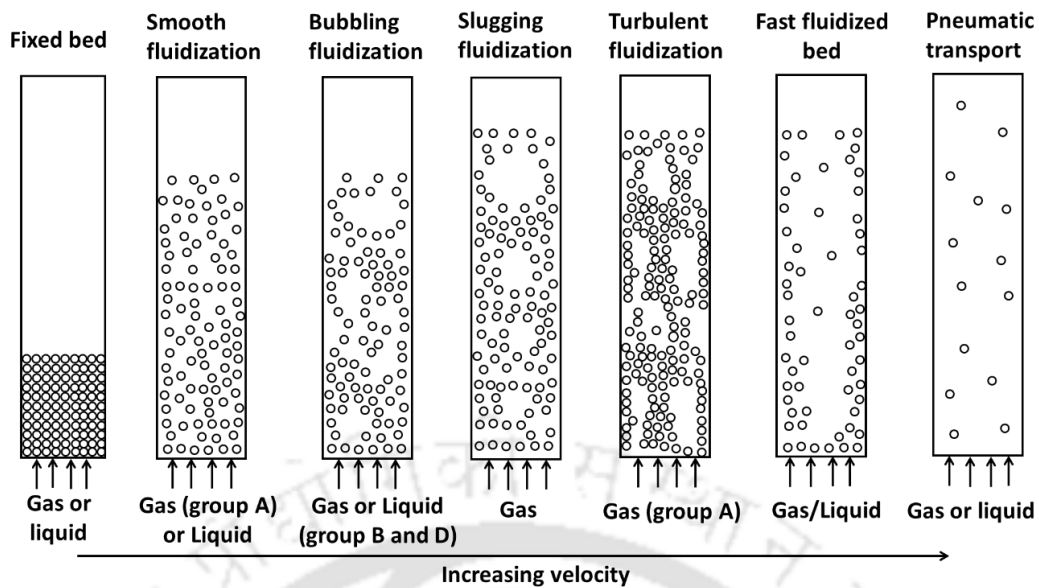


Figure 1.1 Diagrams of fluidization regimes (Kunii and Levenspiel, 1991)

1.1.1 Classification of particles

The solid particles which are used in fluidization are classified by Professor D. Geldart in 1973 into four groups depending on their size and density. These are as follows:

Group-A particles are also named as aeratable particles. The particles come into this category usually possess small diameter range, i.e. from 30 to 100 μm , and low particle density ($< \sim 1.4 \text{ g/cm}^3$). While fluidizing at minimum fluidization velocity, these particles fluidize easily and smoothly without forming bubbles. But when the velocity is increased to minimum bubbling velocity, bubble starts to form with the expansion of bed. These particles give controlled bubbling with small bubbles and bubbles coalesce and split as they progress towards the top. The bubble size is always less than 10 cm. Only axial slug formation occurs in these types of particles. Cloud to bubble volume ratio is negligible in this case. Rise velocity of the bubble is greater than the interstitial gas velocity. For these particles, minimum bubbling velocity is always greater than the minimum fluidization velocity. The particles like the fluid cracking catalyst and milk powder come under this category.

Group-B particles are known as bubbly particles. The particle size range is from 100 to 1000 μm and density range is from 1.4 to 4 g/cm^3 . While fluidizing these particles at minimum fluidization velocity, the bubble starts to form which grows large with increasing velocity. Cloud to bubble volume ratio is not negligible in this case. Examples of group B particles are glass bead and sand. For these particles, minimum bubbling velocity and minimum fluidization velocity are same.

Group-C particles are cohesive and very fine particles. Their particle size is less than 30 μm . For particle size less than 60 μm , relative density is less than 500 kg/m^3 and for particle size less than 20 μm , relative density is greater than 1000 kg/m^3 . These particles do not fluidize easily as their interparticle force is larger than the force exerted by the gas. Channeling occurs in small diameter bed. They rise as a plug of solids when fluidized and even they need an external force like mechanical agitation to fluidize. Particle mixing and heat transfer are poorer in comparison to other particles. Examples of these particles are flour, cement, face powder, fly ash and starch.

Group-D particles are also termed as spoutable particles. They are very large and dense. Their particle size is greater than 1000 μm . They need a high fluid flow rate and fluidizing those leads to abrasion. They show spouting behavior and channeling. They form a flat slug. Solid mixing, in this case, is relatively poor and back mixing in the dense region cannot take place due to the high gas velocity. Rise velocity of the bubble is less than interstitial gas velocity; therefore gas enters at the bottom of the bubble and comes out at the top. Examples of these particles are coffee beans, peas and dry grains. The Geldart classification of the particles is shown in Figure 1.2.

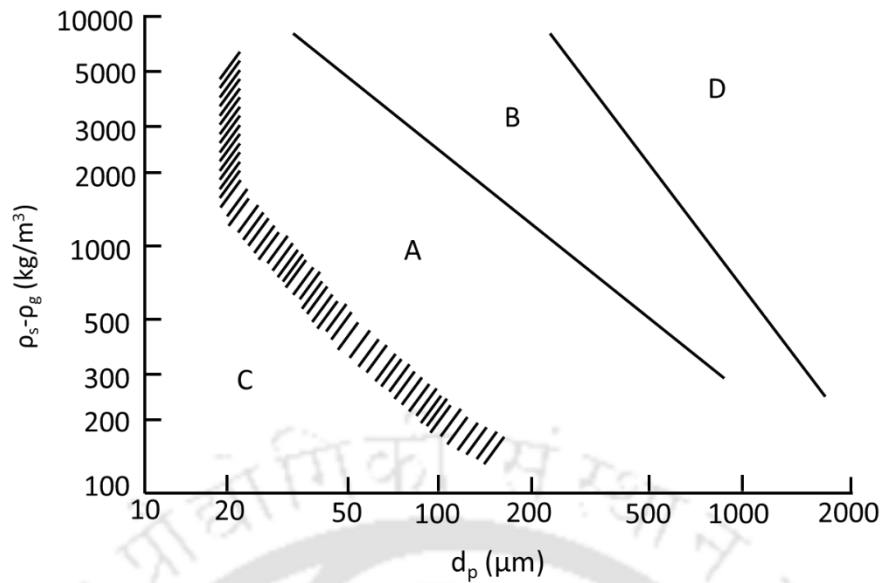


Figure 1.2 Geldart's classification of particles (Geldart, 1973)

1.2 Conical fluidized bed

Conical fluidized bed has become an area of research interest after 80s' due to their unique advantages over the cylindrical fluidized bed. The operational difficulties associated with cylindrical fluidized beds particularly while dealing with the particles of different size and densities such as entrainment, slugging, non-uniform fluidization, poor mixing, and operating velocity limitation can be avoided by using conical fluidized bed (Kim et al., 2000). In conical fluidized bed the diameter of the column changes with the height. Therefore, the axial velocity of solids decreases with the height in the column which significantly minimizes entrainment at the same instant, allowing fluidization of the bigger particle. This behavior of conical bed is very important in case of granulation, where particle size distribution is very wide (Venkatesh et al., 1996; Kim et al., 2000; Wiens and Pugsley, 2006). It also allows smooth fluidization of broad size distribution of solids, which is not possible in case of the deep cylindrical bed where the existence of large pressure difference between the top and bottom, causes expansion of bed and agitation of particles at the top as gas rises (Kim et al., 2000). Moreover, the modified

geometry provides better mixing characteristics than the cylindrical fluidized bed at lower velocity, which reduces gas consumption and prevents elutriation of fine particles (Venkatesh et al., 1996; Kim et al., 2000). Many researchers have tried to study the behavior of conical fluidized bed by using experimental and numerical approach.

The techniques like ECT and fiber optic probe (Pugsley, 2003) were also used to determine the mean radial volume fraction profiles inside the gas-solid conical fluidized bed. Pressure transducers are also used by Wormsbecker et al. (2009a) for hydrodynamic study. Wiens et al. (2006) have used two types of the particle for ECT study. Non-invasive radioactive particle tracking (RPT) technique has been employed for understanding particle flow pattern (Khanna, 2008) in the gas-solid conical fluidized bed. Depypere et al. (2005) used positron emission particle tracking technique to understand the particle motion. However, they have only presented particle tracks. Most of the studies reported in the literature are limited to the overall or mean quantity measurement. For detailed understating of conical fluidized bed measurement of the mean and local quantities are critical. Detail understanding of local parameter such as solid hold up, Lagrangian velocity, circulation pattern and mixing characteristics can be useful in estimation of heat and mass transfer of the fluidized bed. In addition, these data will be helpful in the design and scale-up of the conical fluidized bed. The data can further provide a base case for validation of computational fluid dynamic models.

In the conical fluidized bed, the wall is inclined from top to bottom. Due to this geometry, they show some characteristics of the spouted bed along with some characteristics of the cylindrical bed. Conical fluidized bed shows the gross circulation of solids like the spouted bed and intimate gas-solid contacting like the cylindrical bed (Wormsbecker et al., 2009a). However, there are some differences between conical and spouted bed like conical bed uses the distributor to introduce fluid whereas spouted bed uses an orifice to

introduce fluid into the bed. The conical fluidized bed uses Geldart A and B particles for fluidization but spouted bed uses Geldart D particles (Schaafsma et al., 2006). The velocity of the fluid through the column decreases as it moves upwards due to the change in bed cross-sectional area. Schaafsma et al. (2006) have used positron emission particle tracking (PEPT) to describe this circulation pattern of particles in a shallow bed of Geldart B powders. Pugsley et al. (2007) have used electrical capacitance tomography to understand the circulation pattern of the dry pharmaceutical granule. The cross-sectional area of the fluidized core region of the bed increases with increasing the gas velocity (Gernon et al., 2007). The use of a conical fluidized bed improves the quality of fluidization in case of cohesive particles as compared to the cylindrical fluidized bed where it does not fluidize well (Venkatesh et al., 1996). In the conical fluidized bed, with an increase in cone angle and static bed height the hydrodynamic characteristics like pressure drop and minimum fluidization velocity increases. Five flow regimes have been observed in the conical fluidized bed, with a change in velocity (Peng et al., 1997; Jing et al., 2000). They are termed as the fixed bed, partially fluidized bed, fully fluidized bed, transition regime, and turbulently fluidized bed. At the low flow rate, fixed bed regime exists, in conical fluidized bed like the cylindrical bed. In this regime, the fluid passes through the voids in between the particles without shifting the particles and bed height. The pressure drop increases with an increase in flow rate in the fixed bed and reaches its maximum value. As the fluid velocity further increases, the particle near the distributor forms a cavity. The cavity collapses with the increase in velocity and the bottom zone particles get fluidized. The particles on the top of the bed still remain stable. The velocity at this zone is known as the minimum velocity of partial fluidization. The pressure drop in this zone decreases with an increase in fluid velocity from its maximum value. With further increase in velocity, the voidage in the central core region increases with the

upward flow of particles, and in the annular region, voidage decreases with the downward flow of particles. This stage is known as the fully fluidized bed. At a higher flow rate in the transition regime, the central voidage increases but the particle flow direction remains the same. The variation in pressure drop is not observed in this zone. The bed becomes turbulent with further increase in velocity. The core region disappears, in this stage named as the turbulent fluidized bed. Figure 1.3 represents different regimes of the conical fluidized bed.

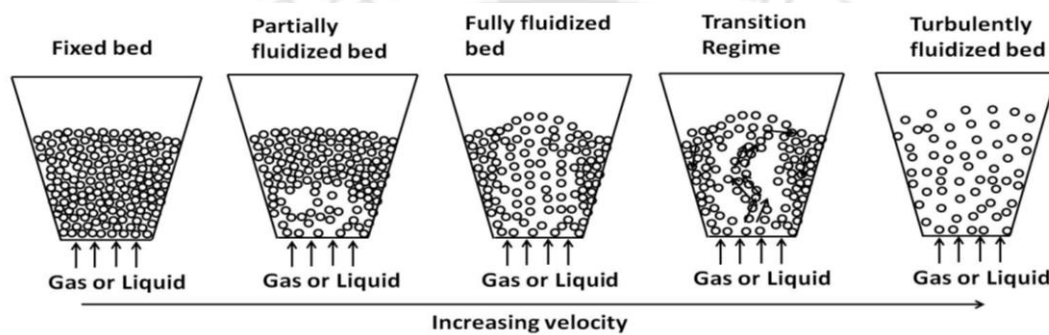


Figure 1.3 Diagram of conical fluidization regimes (Peng and Fan, 1997)

The hydrodynamic behavior of the conical fluidized bed is completely different from the cylindrical fluidized bed. This can be shown from the pressure drop-velocity relation of conical (curve 1) and cylindrical (curve 2) fluidized beds in Figure 1.4. The fluidization velocity of the conical fluidized bed is based on the cross-sectional area of the bottom of the bed. Both beds are operated at similar operating conditions with the same static bed height. The minimum fluidization velocity (u_{mpf}) in conical, at which the bottom of the column begins to fluidize, is greater than minimum fluidization velocity (u_{mf}) of the cylindrical column. The maximum pressure drop in conical at u_{mpf} is higher than the maximum pressure drop in cylindrical at u_{mf} . Hence the correlations developed for cylindrical set up cannot be used for the conical column.

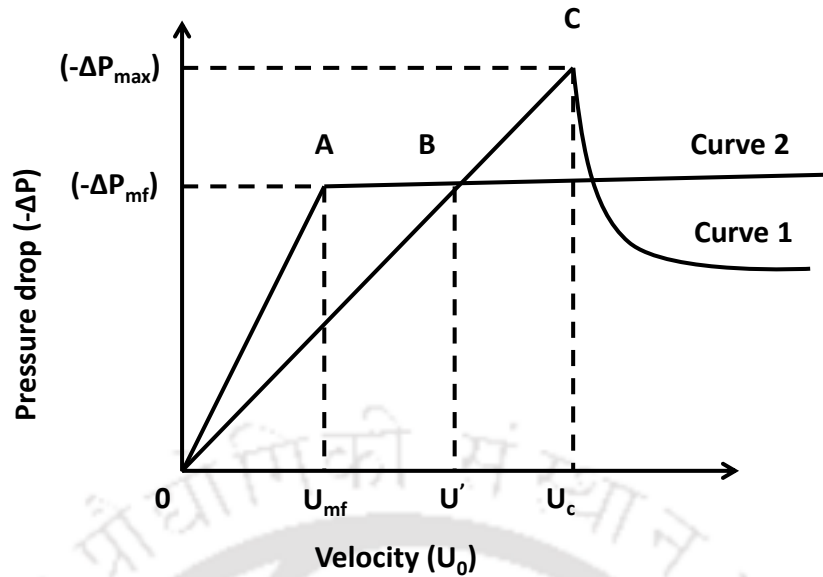


Figure 1.4 Pressure drop-velocity curve (curve 1: conical fluidized bed, curve 2: cylindrical fluidized bed)

The minimum fluidization velocity in case of conical fluidized bed varies from cylindrical bed due to the change in geometry. Different researchers have expressed various views regarding the calculation of minimum fluidization velocity in the conical fluidized bed. Gelperin et al. (1960) have stated that the superficial velocity at which the upper surface of the fluidized bed start fluidizing should be called as minimum fluidization velocity. However, their minimum fluidization velocity and maximum bed pressure drop calculated from their model at which the bottom of the bed start to fluidize is greater than the experimental data. According to Nishi (1979), the superficial velocity is considered as minimum fluidization velocity when the pressure drop of the bed was equal to the effective weight of the solids on the unit cross-sectional area of the bottom. However, while performing the experiment it was found that the bed top is not fluidizing at this superficial velocity. It indicates that the fluidizing velocity needed to fluidizing the top of the bed is higher than this superficial velocity.

Peng et al. (1997) developed a correlation for minimum fluidization velocity. It has been developed from the Ergun equation. The pressure drop through a packed bed with a differential height of dh has been given by Ergun equation

$$-dp = (C_1u + C_2u^2)dh \quad (1.1)$$

The overall pressure drop across the entire bed height, H , is obtained by integrating the following equation

$$(-dp) = \int_{P_0}^{P_{H+h_0}} (-dp) = \int_{h_0}^{H+h_0} (C_1u + C_2u^2)dh \quad (1.2)$$

For a two-dimensional tapered bed with a thickness of w_0 and an apex angle of θ , we have

$$u = u_0 \frac{L_0}{L} = u_0 \frac{h_0}{h} \quad (1.3)$$

$$L_1 = L_0 + 2H \tan \frac{\theta}{2} \quad (1.4)$$

In conical bed, as the cross-sectional area increases continuously from bottom to top, the force exerted by the fluidizing fluid on the particles is not directly proportional to the pressure drop. This force in a differential bed height of dh is equal to the product of the pressure drop through it, $(-dp)$ and cross-sectional area of the bed lw_0 . According to the proposed model, the particles on the bottom begin to fluidize when $F = G$. Thus, the overall force exerted by the fluidizing fluid on the particles in the entire bed with a height of H is

$$F = \int_0^F dF = \int_{h_0}^{H+h_0} Lw_0 (-dp) = \int_{h_0}^{H+h_0} Lw_0 (C_1u + C_2u^2)dh \quad (1.5)$$

The overall effective weight of the particles in the bed is

$$G = \int_{h_0}^{H+h_0} g(1 - \varepsilon_0)(\rho_s - \rho_f)Lw_0 dh \quad (1.6)$$

By equating these two equations following two equations (1.7) and (1.8) have been obtained. Equation (1.7) is for two-dimensional bed and equation (1.8) is for three-dimensional bed.

$$C_1 L_0 u_{mf} + C_2 \left(\frac{L_0^2}{L_1 - L_0} \right) \left(\ln \frac{L_1}{L_0} \right) u_{mf}^2 - (1 - \varepsilon_0) (\rho_s - \rho_f) g \left(\frac{L_0 + L_1}{2} \right) = 0 \quad (1.7)$$

$$C_1 u_{mf} + C_2 \left(\frac{D_0}{D_1} \right) u_{mf}^2 - (1 - \varepsilon_0) (\rho_s - \rho_f) \times g \left(\frac{D_0^2 + D_0 D_1 + D_1^2}{3 D_0^2} \right) = 0 \quad (1.8)$$

Where

$$C_1 = 150 \frac{(1 - \varepsilon_0)^2}{\varepsilon_0^3} \frac{\mu}{(\phi_s d_p)^2} \quad (1.9)$$

$$C_2 = 1.75 \frac{(1 - \varepsilon_0)}{\varepsilon_0^3} \frac{\rho_f}{\phi_s d_p} \quad (1.10)$$

1.2.1 Advantages

The advantages of the conical fluidized bed over the cylindrical fluidized bed are discussed below:

- The size distribution of the solid in a cylindrical fluidized bed is always restricted due to their constant axial velocity distribution inside the column. If the size distribution of the solid is broadened, the smaller solid may get entrained and bigger solid may get defluidized and settle near the bottom. The changing cross-sectional area of the conical fluidized bed along height makes it suitable for fluidizing a broad range of particles, unlike cylindrical fluidized bed. The small cross-section at the bottom of conical bed helps in maintaining a higher velocity than the top, which results in fluidization of coarse particles at the bottom and the

ascending area with the height, which results in a decrement of velocity, prevents entrainment of small particles. Therefore, the conical fluidized bed can deal with a bed of particles whose size distribution is wide. This feature of the conical column is important for applications in which the particle size changes with time (coal combustion, crystallization, granulation, microbial growth, etc.).

- In the cylindrical fluidized bed, in case of exothermic reaction taking place, an ample amount of heat is released near distributor that can destroy the distributor and the particles within. However, in the conical fluidized bed, the velocity near the bottom is comparatively higher, thus reducing solid concentration near the distributor. Hence, if an exothermic reaction is taking place in conical fluidized bed, due to lower accumulation of particles near the bottom, it decreases the reaction rate and the rate of heat release. Therefore, the harm to the column distributor and solid can be prevented (Shi et al., 1984).
- If the velocity of particles near distributor in a conical fluidized bed is higher than the terminal settling velocity of particles within, the bed can be operated without a distributor (Golubkovich, 1975).
- In the deep cylindrical fluidized bed, a large pressure difference between the bottom and top sections exist. This leads to expansion of gas continuously as it moves up and becomes highest on the top. Thus, the bed agitates violently on top that leads to instability of the bed on top and elutriation of particles from the column. However, in the case of the conical fluidized bed, as the cross-sectional area increases towards the top, it accommodates the expanded gas volume and let the bed fluidize smoothly without any agitation (Ridgway, 1965).
- The increase in the cross-sectional area also provides good mixing by allowing the particles to move freely. The increasing cross-sectional area results in the

formation of larger bubbles providing a higher degree of mixing in the upper part of the bed. It reduces back mixing in the axial direction. The conical fluidized bed provides better mixing characteristics than the cylindrical fluidized bed at lower velocity, which reduces the gas consumption and prevents the elutriation of fine particles (Kim et al., 2000; Wormsbecker et al., 2009a; Venkatesh et al., 1996). This behavior of conical bed is very important in case of granulation where particle size distribution is wide.

- In the cylindrical fluidized bed, there is a variation in the axial size distribution of particles with a larger number of coarse particle present near the bottom. The axial size distribution becomes homogeneous in conical bed due to the inclined wall (Kim et al., 2000). But an optimum angle is needed to reduce the resistance (height) of the bed, so that the coarser particles can travel up to a high level and this will reduce segregation, in case of conical bed. In case of the cylindrical fluidized bed, the increase in gas velocity does not affect much the stirring of particles, but in conical bed increasing gas velocity results in better stirring and provides a homogeneous axial size distribution of particles.
- In the cylindrical fluidized bed, the fluid velocity is the same throughout the column. Therefore, maintaining the smooth fluidization for a wide range of particle size distribution is difficult. To obtain smooth fluidization the fluid velocity should be 2-4 times of minimum fluidization velocity. This will cause fluidization of coarse particles but at the same time, it will cause elutriation of fine particles because the velocity will be more than the terminal velocity of the fine particles and it will also cause high mechanical degradation. This problem can be overcome by using conical fluidized bed, as its cross-sectional area increases with column height and the fluid velocity decreases with height.

Therefore, the fluid velocity at the bottom is high to fluidized coarse particles and the surface velocity can be adjusted by changing the cone angle to prevent elutriation of fines. However, in the cylindrical fluidized bed, the increase in fluid velocity does not improve the distribution of particles throughout the bed. In case of operation of cylindrical bed with a large number of fines will results in elutriation of fines and will cause accumulation of coarse particles near the bottom of the bed and will cause defluidization (Kim et al., 2000).

- In the cylindrical bed, the entrainment rate of a fine particle is 5 to 12 times greater than the conical fluidized bed for a given powder content and volumetric gas flow rate. In conical bed, the fines moving with a terminal velocity greater than the superficial gas velocity comes back from top to the upper surface of bed due to the decrease in axial velocity with the height. In case of the cylindrical fluidized bed, the superficial gas velocity is constant throughout the column, which prevents the reflux of particles and causes entrainment of fines (Shin et al., 2007).
- In case of granulation conical fluidized bed gives spout like the circulation of the particles with bubbling in the center region of the bed whereas cylindrical fluidized bed gives defluidization at the periphery of inlet due to the cohesive nature of granule. The cylindrical bed gives the same result and suitable hydrodynamics but slugging, channeling and defluidization like undesirable fluidization is observed when the granule is wet (Wormsbecker et al., 2009a).

Due to these advantages of conical fluidized bed over the cylindrical fluidized bed, the use of the conical fluidized bed is recently increasing.

1.2.2 Disadvantages

Though, conical fluidized bed provides some advantages over the cylindrical fluidized bed for certain applications it has some drawbacks too. It gives advantages only for an optimum cone angle. The cone angle highly depends on the type of application. An optimum cone angle is needed for the homogeneous axial size distribution of particles and the cone angle increases with the increasing particle size (Kim et al., 2000). The cone angle is the most important parameter to be determined for minimizing particle segregation (that mainly depends on the size distribution, density and cohesive force of the fine particles). In continuous operation of conical fluidized bed with wide particle size distribution, cone angle larger than optimum value causes a large number of coarse particles on the higher level of the bed and reverse in smaller cone angle bed. In the conical fluidized bed, most of the fines flow downward along the wall whereas most of the coarse particle present in the central region. This gives a non-uniform distribution of fines in the radial direction having more fine near wall than the center and in the annulus. The hydrodynamic characteristics of the conical fluidized bed such as minimum fluidization velocity and maximum bed pressure drop also depend on the cone angle of the bed. The range of partially fluidized bed is enlarged by increasing the cone angle (Khani, 2011). In conical fluidized bed abrasion and erosion of connected pipes and vessels occurs due to collision and attrition between particles and between particles and column wall. Careful attention is needed for maintaining good gas distribution in this bed. For industrial use, the conical fluidized bed needs more mechanical support than the cylindrical bed. The flow rate should not be too less or high in order to provide better results.

1.2.3 Applications

Conical fluidized beds have been used for various applications in industrial processes recently. The variety of applications of gas-solid fluidized beds are fluid catalytic cracking (Chen, 2006; Shan et al., 2001), fermentation, combustion and gasification of coal (Uemaki and Tsuji, 1986; Reh et al., 2003), Fischer-Tropsch synthesis (Fox, 1991), coking, drying (Wormsbecker et al., 2009b; Pugsley et al., 2007), granulation (Schaafsma et al., 2006; Ranjbarian and Farhadi, 2013), coating (Depypere et al., 2009; Atares et al., 2012; Hampel et al., 2013; Sibanc et al., 2013), crystallization (Levey et al., 1960; Ishii, 1973; Golubkovich, 1975; Dighe et al., 1981), removal of SO₂ from flue gas (Ma et al., 2000), sulfide ore roasting, methanol to olefins (MTO) process (Peng and Fan, 1997; Chen et al., 2005; Soundararajan et al., 2001), fluidized contactor for sawdust and mixtures of wood residues (Olazar et al., 1994) and food processes (Depypere et al., 2005) etc.

1.3 Hydrodynamics of conical gas-solid fluidized bed

In the conical fluidized bed, the local and global bed dynamic is expected to be different from the cylindrical one. Therefore, for their design and scale up the flow pattern, phase distribution and other dynamic property need to be explored. Further, it is also important to determine the effect of velocity, particle size and bed composition on the mixing pattern.

In the conical fluidized bed, the solid particle moves upward in the center and downward near the wall (Schaafsma et al., 2006; Khanna et al., 2008; Depypere et al., 2009). Though the solid circulation pattern in conical is similar to the cylindrical fluidized bed, their overall bed behavior is quite different. Two types of circulation pattern of solid have been observed in the cylindrical fluidized bed. At high velocity, the particle moves

upward in the center and down ward near the wall (Leva, 1962; Marsheck and Gomezplata, 1965; Lin et al., 1985; Baeyens and Geldart, 1986). At low velocity, the pattern gets reversed, i.e. particle moving upward from near the wall to the center and moving downward in the center (Ohki and Shirai, 1975; Whitehead et al., 1976, Kunii and Levenspiel, 1991). However both the flow pattern can also co-exist based on fluid velocity and aspect ratio (Werther and Molerus, 1973). However, in conical fluidized bed a single vertex of solid with upward motion in the center and downward motion along the wall is observed (Toyohara and Kawamura 1992; Kim et al., 2000; Tanfara et al., 2002; Schaafsma et al., 2006; Fan et al., 2008; Khanna et al., 2008; Depypere et al., 2009; Wormsbecker et al., 2009a; Liyan et al., 2012). A high bubble activity is observed in conical fluidized with a dominant flow of solid in the center (Schaafsma et al., 2006). The radial particle movement is relatively strong in conical fluidized compared to cylindrical bed (Stein et al., 2000; Fan et al., 2008; Depypere et al., 2009).

In addition, in the conical fluidized bed, the cone angle plays a major role. Tanfara et al. (2002) reported the better distribution of solid at a higher taper angle of 20° compared to smaller taper angle 8.1° (Depypere et al., 2009). The voidage profile of conical fluidized bed at low velocity and static bed height shows wave-like radial voidage (Pugsley, 2003) by the optical fiber probe. Visual observation shows smaller bubbles moving slowly upward through the bed at this operating condition. However, this voidage profile changes with the increase in velocity. Liyan et al. (2012) observed that the concentration of particles is low in the center and high near the wall while the axial velocity of the particle is high in the center and low near the wall. This indicates that particles are moving upward in the center and downward near the wall. Further, with the increase in cone angle, the fluidization velocity was observed to be decreasing axially. Therefore, the increase in cone angle may lead to more pronounced gulf streaming.

The changing solid particle induces various mixing and segregation pattern in the column. At low-velocity segregation occurs axially as the bed crosses the minimum fluidization velocity of the mixture (Gernon and Gilbertson, 2012). The segregation condition is dominated by the larger particles at the bottom and smaller particles on top (horizontal segregation). With the increase in velocity, the segregation gets dominated by mixing with a uniform distribution of solid. The radial segregation shows the larger particle getting accumulated at the center bottom and getting uniformly mixed as the velocity increases (Wormsbecker et al., 2005). Both axial and radial segregation does not show any change with changing static bed height.

1.4 Motivation

Conical fluidized beds have various applications in industrial processes such as drying, granulation, coking, biological treatment of wastewater, immobilized bio-film reaction, incineration of waste materials, nuclear fuel particle coating, crystallization, gasification and liquefaction of coal, sulfide ore roasting, catalytic polymerization and fluidization of cohesive powder, etc. Despite their wide application, the studies on conical fluidized beds are limited to visual observations, pressure drop measurement and measurement of global/average quantities. Most of the work available in the open literature is focused on developing the correlation for critical fluidization velocity and pressure drop. Very few works on flow pattern and volume fraction measurement are available. The parameters such as phase hold up, mean velocity, solid circulation, and fluctuation play a major role in determining the nature of the fluidized bed and their mixing characteristics. Detail hydrodynamic study including the mentioned parameter is not available till date.

In most of the industrial applications, wide distributions of solids in terms of size and/or density are used. The particle size distribution, as well as bed density distribution, plays a

significant role. When a mixture of solids having different size and/or density is fluidized, the behavior of fluidized bed is markedly different from the behavior of mono-disperse bed. In such case, a particular mixing/segregation pattern is reached which in turn gives rise to a steady distribution of mixture components along the bed height which depends both on constitutive solids properties and on the operating conditions of the process. The fluidized bed behavior such as bed expansion, particle segregation and mixing completely depends upon the size distribution. Thus, it is necessary to understand the behavior of particle size distribution in the binary conical fluidized bed. The flow pattern of solid and fluid phase is determined by the distribution of solid phase hold up, which affects the extent of mixing and rates of heat and mass transfer directly, which in turn will affect the overall performance of the reactor. In literature, many researchers have attempted to find the effect of different size and density of particles on the behavior of conical fluidized bed using binary mixtures. A large number of studies (Kwant et al., 1995; Sau et al., 2008; Sutar and Das, 2012) have been carried out to find the effect of bed composition on minimum fluidization velocity and pressure drop. Some studies have also been reported on the mixing of solids in the binary mixture fluidized bed. Though a lot of studies have been conducted on the binary bed, the effect of individual phase fraction and fluid velocity on mixing and segregation characteristics, are still missing. Thus, it is very important to understand the effect of particle size distribution on the performance of conical fluidized bed. Further, no studies are available on the effect of different fluid (gas and liquid) on the behavior of the conical fluidized bed in mono and binary dispersed bed.

The scale-up of any fluidized bed is an inherent part as it gives an idea about the effect of dimension. Even though various scaling laws have been developed for cylindrical fluidized bed, successful adaptations of these laws are rare. The scale-up can affect the particle-particle, particle – wall, and particle-fluid interactions, which need to be taken

into account. The detailed understanding of conical fluidized bed at the laboratory as well as pilot plant level has acted as a driving force for further investigations.

1.5 Objectives of the thesis

The main aim of the present study is to acquire detail knowledge of mono and binary dispersed conical fluidized bed by using state-of-the-art measurement technique. The main goal of these experiments was to find the effect of different operating parameters on hydrodynamics and mixing behavior of mono and binary dispersed beds. The specific objectives of the work are as follows,

- Experimental investigation of gas-solid conical fluidized bed through radiotracer based techniques
 - Effect of particle size for the monodispersed bed
 - Effect of fluid velocities for monodispersed and binary beds
 - Effect of bed composition for binary bed (mixing and segregation studies)
- Experimental investigation of liquid-solid conical fluidized bed through radiotracer based techniques
 - Effect of particle size for the monodispersed bed
 - Effect of fluid velocities for monodispersed and binary beds
 - Effect of bed composition for binary bed (mixing and segregation studies)
- Scale up studies on gas-solid conical fluidized bed
 - Monodispersed bed
 - Binary bed

1.6 Structure of the thesis

The first chapter of this report contains a brief review of the cylindrical and conical fluidized beds. In this chapter different flow regimes occurring in both beds have been described. The second chapter discusses various invasive and non-invasive techniques used for multiphase flow investigation. The measurement principle with the procedure used for RPT has been described in this chapter. Further, the time series analysis has been described in the second chapter.

In the third chapter, the implementation of RPT in the gas-solid conical fluidized bed is discussed. The effect of gas velocity and particle size on solid mean velocity, RMS velocity, and granular temperature are studied. Further to understand the mixing characteristic of the bed, time series analysis is performed and autocorrelation function, Hurst exponent, segregation index, Kolmogorov entropy and correlation dimension of the trajectory attractors are calculated for each case.

In chapter four experiments on the liquid-solid conical fluidized bed are discussed. The bed has been investigated for both mono and binary conditions to characterize the bed.

In the fifth chapter, the scale-up study on the gas-solid conical fluidized bed is discussed. Both mono and binary beds are investigated for mean velocity and fluctuation. Then the obtained results of the scaled-up column are compared with the smaller column.

Chapter six is all about the overall conclusion obtained from the current work and future recommendations. Appendix A shows the Euler-Euler simulation of the gas-solid conical fluidized bed. Appendix B shows the plots of pressure drop versus velocity in gas-solid and liquid-solid conical fluidized bed.

Notations

C_1, C_2	Constants in the Ergun equation, -
D_0	Bottom diameter of conical bed, m
D_1	Top diameter of conical bed, m
d_p	Solid diameter, μm
F	Force exerted by the fluidizing fluid on the particles, N
G	Effective weight of the particles in the bed, N
g	Gravity, m/s^2
h	Axial position, m
h_0	Distance between the apex and the inlet of the bed, m
H	Total height of the bed, m
L	Width of the wedge bed, m
L_0	Bottom width of the bed in wedge, m
L_1	Top width of the bed in wedge, m
P	Pressure, N/m^2
$(-\Delta P)$	Pressure drop, N/m^2
u	Superficial velocity of the fluidizing fluid, m/s
u_0	Superficial velocity of the fluidizing fluid at the inlet of the bed, m/s

u_1	Superficial velocity of the fluidizing fluid the top surface of the bed, m/s
u_{mf}	Minimum fluidization velocity, m/s
u_{mpf}	Minimum fluidization velocity at partially fluidized bed, m/s
w_0	Thickness of the wedge bed, m
ε_0	Voidage of the fixed bed, -
ρ_f	Fluid density, kg/m ³
ρ_s	Solid density, kg/m ³
θ	Tapered bed angle, -
ϕ_s	Sphericity of the solid particle, -

References

- Atarés, L., Depypere, F., Pieters, J.G., Dewettinck, K., 2012. Coating quality as affected by core particle segregation in fluidized bed processing. *J Food Eng.* 113, 415–421.
- Baeyens, J., Geldart, D., 1986. *Gas Fluidization Technology*. JohnWiley & Sons Ltd, 95–103.
- Chen, J.Q., Bozzano, A., Glover, B., Fuglerud, T., Kvisle, S., 2005. Recent advancements in ethylene and propylene production using the UOP/hydro MTO process, *Catal. Today.* 106, 103–107.
- Chen, Y. M., 2006. Recent advances in FCC technology. *Powder Technol.* 163, 2–8.

- Depypere, F., Pieters, J. G., Dewettinck, K., 2005. Expanded Bed Height Determination in a Tapered Fluidized Bed Reactor. *J Food Eng.* 67, 353-359.
- Depypere, F., Pieters, J. G., Dewettinck, K., 2009. PEPT Visualisation of Particle Motion in a Tapered Fluidized Bed Coater. *J Food Eng.* 93, 324-336.
- Dighe, S.V., Blinn, M.B., Buggy, J.J., Krasicki, B.R., Pierce, B.L., 1981. Proceedings of the 16th Intersociety Energy Conversion Engineering Conference. ASME, New York, 1059-1067.
- Fan, X., Parker, D.J., Yang, Z., Seville, J.P.K., Baeyens, J., 2008. The effect of bed materials on the solid/bubble motion in a fluidised bed. *Chem. Eng. Sci.* 63, 943–950.
- Fox, J.M., 1991. Fischer-Tropsch reactor selection. *Catal. Lett.* 7, 281–292.
- Geldart, D., 1973. Types of Gas Fluidization. *Powder Technol.* 7, 285-292.
- Gelperin, N.I., Aynshteyn, V.G., Gelperin, E.N., Lvova, S.D., 1960. Hydrodynamic characteristics of pseudo-liquefaction of granular materials in conical and conico-cylindrical equipment., *Khim. Tekhnol. Topliv Masel (USSR)*. 5, 51–57.
- Gernon, T. M., Gilbertson, M. A., 2012. Segregation of Particles in a Tapered Fluidized Bed. *Powder Technol.* 231, 88-101.
- Gernon, T. M., Gilbertson, M. A., Sparks, R. S. J., Field, M., 2007. Tapered Fluidized Beds and the Role of Fluidization in Mineral Emplacement. The 12th International Conference on Fluidization-New Horizons in Fluidization Engineering.
- Golubkovich, A.V., 1975. Investigation of Fluidized Bed Regimes in Conical Reactors. *Khim. I Neft. Mash.* 3, 21-22.

- Hampel, N., Bück, A., Peglow, M., Tsotsas, E., 2013. Continuous pellet coating in a Wurster fluidized bed process. *Chem. Eng. Sci.* 86, 87–98.
- Ishii, T., 1973. Multi Particle Crystal Growth Rates in Vertical Cones. *Chem. Eng. Sci.* 28, 1121–1128.
- Jing, S., Hu, Q., Wang, J., Jin, Y., 2000. Fluidization of Coarse Particles in Gas-Solid Conical Beds. *Chem. Eng. Process.* 39, 379-387.
- Khani, M.H., 2011. Models for Prediction of Hydrodynamic Characteristics of Gas-Solid Tapered and Mini-tapered Fluidized Beds. *Powder Technol.* 205, 224-230.
- Khanna, P., 2008. Particle Tracking in a Lab-Scale Conical Fluidized Bed Dryer, M. Sc. Thesis, University of Saskatchewan, Saskatoon, Saskatchewan.
- Kim, H. G., Lee, I. O., Chung, U. C., Kim, Y. H., 2000. Fluidization Characteristics of Iron Ore Fines of Wide Size Distribution in a Cold Tapered Gas-Solid Fluidized bed. *ISIJ International.* 40(1), 16-22.
- Kunii, D., Levenspiel, O., 1991. *Fluidization Engineering.* Butterworth-Heinemann, Boston, MA.
- Leva, M., 1962. Proc. Symp. on Interaction between Fluids and Particles. *Inst. Chem. Engineers.* London, 143.
- Levey, R.P. J r.; De La Garza, A.; Jacobs, S. C., Heidt, H. M.; Trent, P. E., *Chem. Eng. Progr.*, 1960, 56, 43.
- Lin, J., Chen, M., Chao, B., 1985. A novel radioactive particle tracking facility for measurement of solids motion in gas fluidized beds. *AIChE J.* 465–473.

- Liyan, S., Weiguo, X., Guodong, L., Dan, S., Huilin, L., Yanjia, T., Dan, L., 2012. Prediction of flow behavior of particles in a tapered bubbling fluidized bed using a second-order moment-frictional stresses model. *Chem. Eng. Sci.* 84, 170–181.
- Ma, X., Kaneko, T., Tashimo, T., Yoshida, T., Kato, K., 2000. Use of Limestone for SO₂ Removal from Flue Gas in the Semi-Dry FGD Process with a Powder-Particle Spouted Bed. *Chem. Eng. Sci.* 55, 4643–4652.
- Marsheck, R.M., Gomezplata, A., 1965. Particle flow patterns in a fluidized bed, *AICHE J.* 11, 167–173.
- Nishi, Y., 1979. Some considerations on pressure drop and minimum fluidizing velocity of tapered fluidized bed. *Kagaku Kogaku Ronbunshu* 5, 202-204.
- Ohki, K., Shirai, T., 1975. Particle velocity in Fluidised bed. In: D. Keairns, *Fluidisation Technology*, vol. 1. Washington: Hemi- sphere.
- Olazar, M., San Jose, M.J., Llamosas, R., Bilbao, J., 1994. Hydrodynamics of sawdust and mixtures of wood residues in conical spouted beds. *Ind. Eng. Chem. Res.* 33, 993-1000,
- Peng, Y., Fan, L. T., 1997. Hydrodynamic Characteristics of Fluidization in Liquid-Solid Tapered Beds. *Chem. Eng. Sci.* 52(14), 2277-2290.
- Pugsley, T., Tanfara, H., Malcus, S., Cui, H., Chaouki, J., Winters, C., 2003. Verification of fluidized bed electrical capacitance tomography measurements with a fibre optic probe. *Chem. Eng. Sci.* 58, 3923–3934.
- Pugsley, T., Chaplin, G., Khanna, P., 2007. Application of advanced measurement techniques to conical lab-scale fluidized bed dryers containing pharmaceutical granule. *Food Bioprod Process.* 85, 273–283.

- Ranjbarian, S., Farhadi, F., 2013. Evaluation of the effects of process parameters on granule mean size in a conical high shear granulator using response surface methodology. *Powder Technol.* 237, 186–190.
- Reh, L., 2003. Development potentials and research needs in circulating fluidized bed combustion. *China Particuology.* 1, 185–200.
- Ridgway, K., 1965. The tapered fluidized bed – a new processing tool. *Chem. Process Eng.* 6, 317 – 321.
- Schaafsma, S.H., Marx, T., Hoffmann, A.C., 2006. Investigation of the particle flowpattern and segregation in tapered fluidized bed granulators. *Chem. Eng. Sci.* 61, 4467–4475.
- Shan, J., Guobin, C., Fan, M., Yu, B., Jinfu, W., Yong, J., 2001. Fluidization of fine particles in conical beds. *Powder Technol.* 118, 271–274.
- Shin, M.K., Kim, E.M., Koo, B.S., Han, G.Y., Yoon, K.J., Lee, D.H., Kim, S.D., 2007. Entrainment characteristics of fine particles in cylindrical and conical inert-medium fluidized beds. *Ind. Eng. Chem. Res.* 46, 1408–1414.
- Sibanc, R., Srcic, S., Dreu, R., 2013. Numerical simulation of two-phase flow in a Wurster coating chamber and comparison with experimental results. *Chem. Eng. Sci.* 99, 225–237.
- Soundararajan, S., Dalai, A.K., Berruti, F., 2001. Modeling of methanol to olefins (MTO) process in a circulating fluidized bed reactor. *Fuel.* 80, 1187–1197.
- Stein, M., Ding, Y.L., Seville, J.P.K., Parker, D.J., 2000. Solids motion in bubbling gas fluidised beds. *Chem. Eng. Sci.* 55, 5291–5300.

- Tanfara, H., Pugsley, T., Winters, C., 2002. Effect of Particle Size Distribution on Local Voidage in a Bench-Scale Conical Fluidized Bed Dryer. *Drying Technol.* 20, 1273–1289.
- Toyohara, H., Kawamura, Y., 1992. Core Type Segregation in a Tapered Fluidized Bed of Binary Particle Mixtures. *Kagaku Kogaku Ronbunshu.* 17 (1), 172-178.
- Uemaki, O. and Tsuji, T., 1986. Gasification of a Sub-bituminous Coal in a Two-stage Jet Spouted Bed Reactor, Fluidization V, Ostergaard K. and Sorensen, A., eds., Engineering Foundation, New York, 497.
- Venkatesh, R.D., Chaouki, J., Klvana, D., 1996. Fluidization of cryogenics in a conical column. *Powder Technol.* 89, 179–186.
- Werther, J., Molerus, O., 1973. The Local Structure of Gas Fluidized Beds. 11: The Spatial Distribution of Bubbles. *Int. J. Multiphase Flow.* 1, 123-138.
- Whitehead, A. B, Gartside, G., Dent, D. C. 1976. Fluidization Studies in Large Gas-Solid Systems, Part III. The Effect of Bed Depth and Fluidizing Velocity on Solids Circulation Patterns. *Powder Technol.* 14, 61-70.
- Wiens, J., Pugsley, T., 2006. Tomographic imaging of a conical fluidized bed of dry pharmaceutical granule. *Powder Technol.* 169, 49–59.
- Wormsbecker, M., Adams, A., Pugsley, T., Winters, C., 2005. Segregation by size difference in a conical fluidized bed of pharmaceutical granulate. *Powder Technol.* 153, 72–80.
- Wormsbecker, M., van Ommen, R., Nijenhuis, J., Tanfara, H., Pugsley, T., 2009a. The influence of vessel geometry on fluidized bed dryer hydrodynamics. *Powder Technol.* 194, 115–125.

Wormsbecker, M., Pugsley, T., Tanfara, H., 2009b. Interpretation of the hydrodynamic behaviour in a conical fluidized bed dryer. Chem. Eng. Sci. 64, 1739–1746.





Chapter 2

Radioactive Particle Tracking (RPT) Technique

Scope

In this chapter, various flow measurement techniques used for solid velocity measurement in the fluidized bed are discussed. The implementation of the radioactive particle tracking (RPT) technique is described. Further, the processing RPT data is described. In addition, the time series and chaos analysis of RPT data are discussed.

2.1 Introduction

The design and scale-up of the fluidized bed are still majorly based on developed empirical correlations restricted to a small range of operating conditions. Therefore, the dynamic properties such as mean velocities and volume fraction are of great importance for the better design and scale-up. These parameters play a major role in determining the reactor performance. Therefore, the measurement techniques used should be able to provide results at both the local and global level. Detailed methodology about various measurement techniques is explained by Nieuwland et al. (1996), Chaouki et al. (1997), Boyer et al. (2002), van Ommen and Mudde (2008), Upadhyay (2010). A brief description of these measurement techniques, used in the fluidized bed are presented here. These techniques are classified as invasive and non-invasive, depending on the tool of measurement.

Invasive techniques

In Invasive flow measurement technique, a probe is inserted into the system to measure the flow field. However, this probe can disturb the flow field during measurement.

Further, the probe can get damaged due to the particle motion around it. Though this technique has disadvantages, they are mostly used for flow measurement due to their easy handling. The Invasive techniques used frequently/commonly for flow measurement are optical fiber probes, pitot tube, and capacitance probes.

Optical fiber probe

Optical fiber probe is used to measure the velocity as well as volume fraction (Aradhya, 2013; Zaid, 2013; Taofeeq et al., 2018). The probe consists of a number of fibers and works based on light reflection by solids. The central fiber emits light that reflects back when solid passes near the probe. For velocity measurement, the distance between two probes and the time taken by the solid to touch both probes is measured. The reflected light signals are then collected by the photodiode and converted into the voltage and amplified before sending it to the computer. By using cross-correlation the time difference is calculated. The probe co-ordinates are measured for the distance calculation.

Figure 2.1 shows the schematic of a typical optical fiber probe.

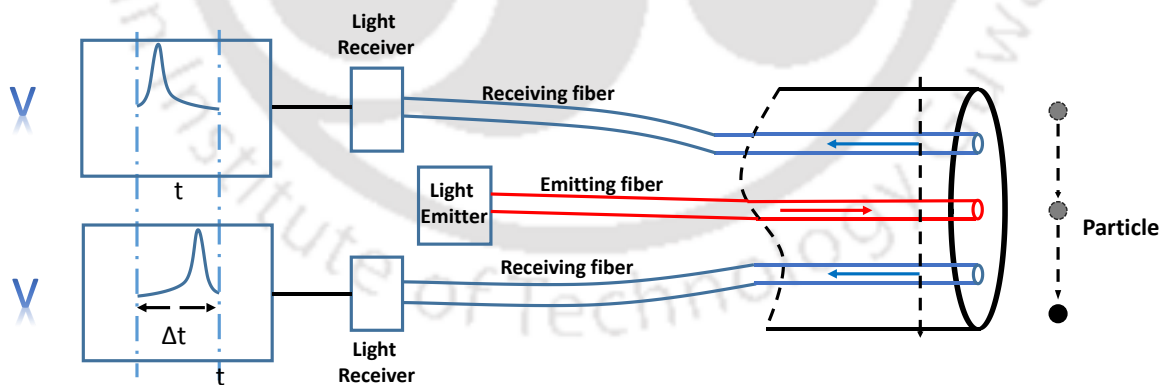


Figure 2.1 Schematic of optical fiber probe technique (Werther and Molerus, 1973)

Noninvasive techniques

The measurement techniques which do not disrupt the flow are called non-invasive techniques. The non-invasive technique used for velocity measurement in fluidized bed

systems are laser Doppler velocimetry (LDV / LDA), particle image velocimetry (PIV), positron emission particle tracking (PEPT) and radioactive particle tracking (RPT). A brief description of each technique is given below.

Laser Doppler velocimetry (LDV)

Laser Doppler velocimetry (LDV) uses Doppler shift of a moving particle to measure the particle velocity. LDV can be used to measure solid velocity, fluctuation velocity, size, and concentration. In LDV laser (5W, Argon-Ion), transmitting and receiving optics, detector, signal processor, and data analysis system is used. For measurement, LDV uses a laser beam as a light source which is divided into two equal intensity coherent beams. The two beams are then directed to intersect at a point that results in a fringe pattern with a series of light and dark alternative fringes. When a particle flows across these fringes, it scatters light while crossing light fringe and it does not scatter any light while crossing dark fringe. The fringe spacing depends on the angle between incident beams and the wavelength of the beam. When the particle passes through the fringes, they scatter light. The scattered light is measured by a photodetector/receiver. The frequency of scattered light (Doppler shift) depends on the velocity of seed particles. The velocity is calculated by multiplying the Doppler frequency with the fringe spacing. Figure 2.2 shows the schematic diagram of the LDA setup.

LDA has the advantage of providing high spatial and temporal resolutions. It also does not require calibration. But unfortunately, this technique can only be used in the low solids fraction (not more than 5%) and also it provides velocity only at a point. Further, the arrangement of the LDA setup is tedious. It can only be used in a transparent column.

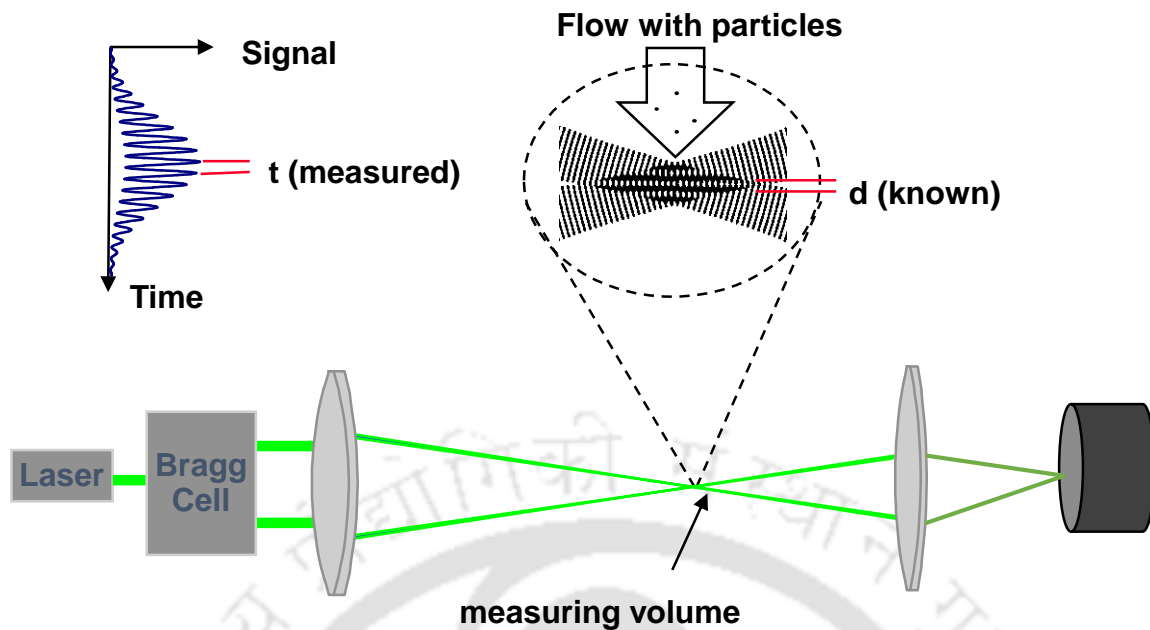


Figure 2.2 Schematic of LDA technique (Durst et al., 1981)

Particle image velocimetry (PIV)

Particle image velocimetry (PIV) is also based on optical measurement. The components of PIV systems are laser light, image recorder. In PIV, seeded particles are used for the experiment. Laser lights are used to form a laser sheet that illuminates the seeded particles, which scatters light when they pass through the measurement zone. The light scattered by the particles are recorded by cameras (i.e. CCD (Charge Coupled Device) or CMOS (Complementary Metal Oxide Semiconductor) in the form of images. These images are later processed by suitable image processing software to track the seed particles. PIV is mostly used in 2D systems; however, 3D PIV is also introduced to multiphase systems nowadays. The disadvantage of PIV is that in opaque systems, such as fluidized bed it cannot be used as it works on laser light. Further, its observations are limited to the layers closest to the wall of the column. The schematic of the PIV is presented in Figure 2.3.

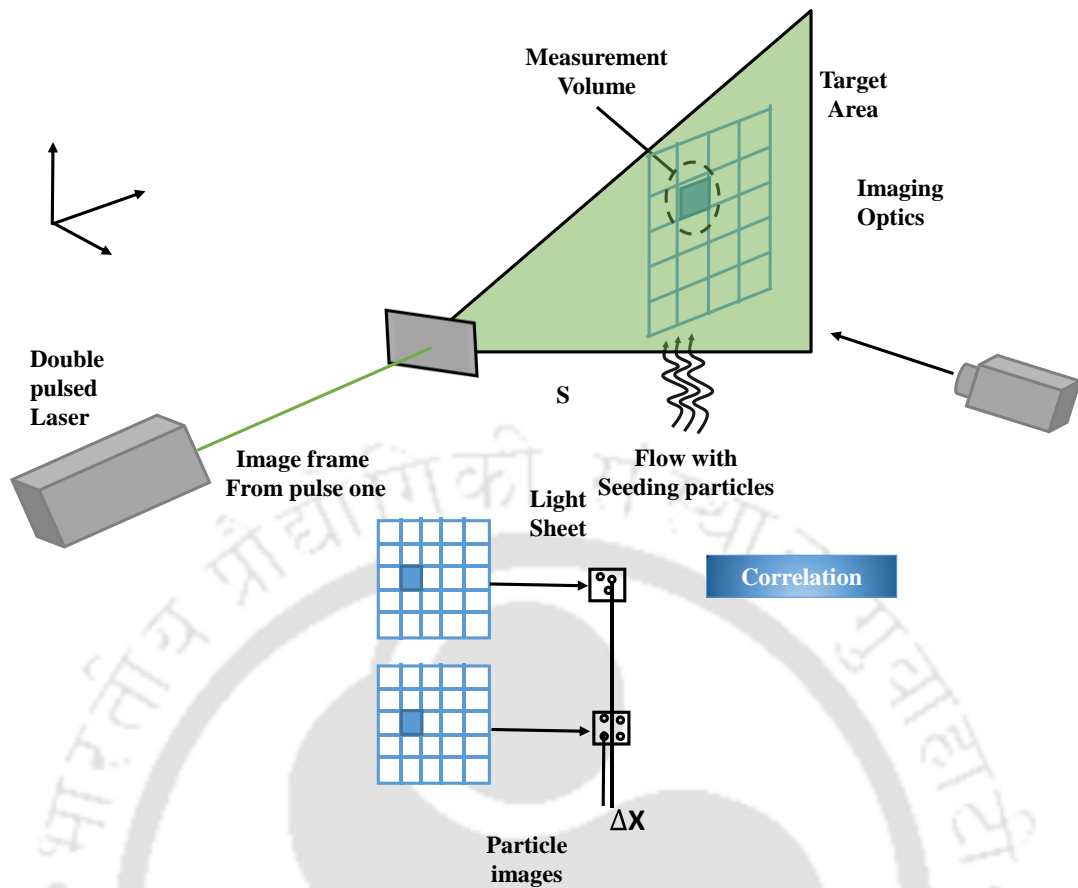


Figure 2.3 Schematic of the PIV technique (Prasad, 2000)

Positron emission particle tracking (PEPT)

PEPT is a radiation-based measurement technique. In PEPT, a single radioactive particle is tracked and its trajectory inside the system is used to obtain information on the solid motion. PEPT used positron emitting isotopes such as ^{18}F , ^{61}Cu , ^{66}Ga as the tracer. These tracers emit positron that annihilates with the free electron present in the surrounding and produces a pair of back to back gamma rays. These gamma rays travel in the opposite direction and are detected by positron cameras placed on either side of the column. The tracer position is determined by detecting a number of such gamma-ray pair by triangulation. The accurate position of tracer can be determined using PEPT. Another advantage is that PEPT does not require pre-calibration like RPT. The disadvantage of PEPT is that it takes a longer time to get sufficient data for a single set of experiment.

Moreover, the energy of the produced gamma ray is limited (512 KeV) and the cost of PEPT is also high. Figure 2.4 shows the schematic of the PEPT technique.

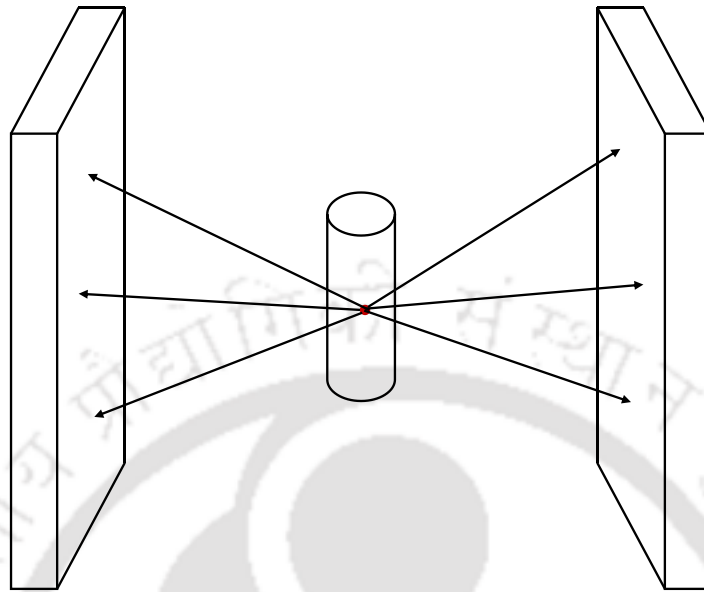


Figure 2.4 Schematic of PEPT technique (Parker et al., 1997)

Radioactive particle tracking (RPT)

Radioactive particle tracking (RPT) is also a radiation-based measurement technique like PEPT but with a different methodology. In RPT, a single radioactive particle is used as a tracer and its motion is tracked by a number of scintillation detector placed around the column (Figure 2.5). During the experiment, the intensity of radiation (count) emitted by the radioactive particle is recorded by detectors. The intensity recorded by each detector depends on the distance between tracer particle and detector, phases present between them, wall material and solid angle made by tracer particle on the detector. .

Radioactive particle releases energy in the form of photons. The number of photons received by the detector is measured by taking the distance between the radioactive particle and detector as the radius of a sphere whose center is the actual detector position and surface is particle location. The intersection point of these surfaces, corresponding to different detectors, is the position of the particle. Three detectors are sufficient to

determine particle position, but to measure particle position with the change of time, a minimum of four detectors are required. The increased number of detectors increases the accuracy of the measurement. Therefore, a number of detectors are placed outside the column, from top to bottom, to track the whole path of the moving tracer particle.

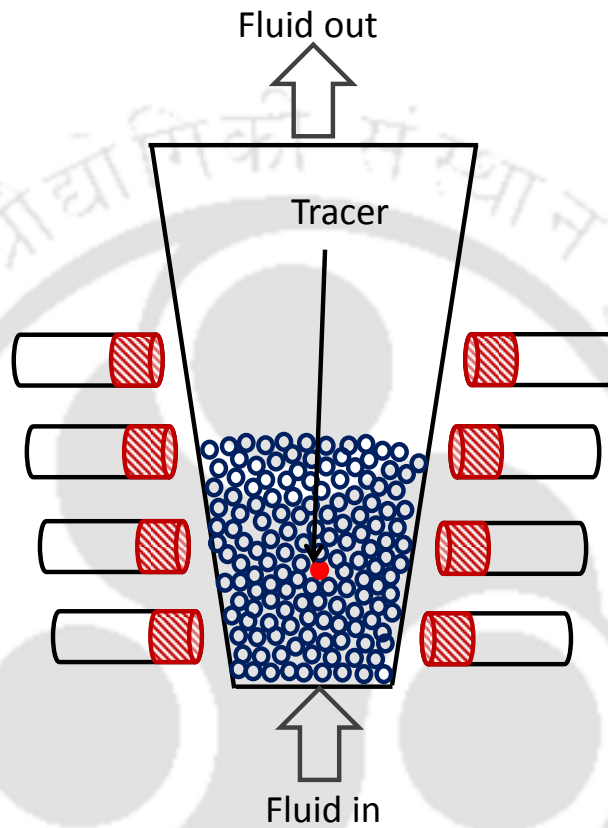


Figure 2.5 Schematic of RPT technique

Unlike PEPT this technique needs calibration prior to the experiment. During calibration, the tracer is placed at various known locations and the counts recorded on each detector are noted down. This gives a distance count map for each detector. Then, the actual experiment is performed where the tracer is placed inside the column with other moving particles. After the experiment, the position of the tracer is reconstructed by comparing the experimentally obtained count with calibrated one. It gives the Lagrangian position time series of the tracer particle. Time differentiation of two successive Lagrangian positions gives the instantaneous velocity of the tracer. The tracer is prepared to be

neutrally buoyant in case of liquid tracking and of same size, shape, and density of the solid present in the bed for solid tracking. NaI (TI) scintillation detectors are mainly used for RPT. The main advantage of RPT is that it is a versatile technique as it can be used in both transparent and opaque techniques. It can be implemented for both dense and dilute systems with the similar accuracy. Further, it can be implemented at different scales without any major issues. The drawback of RPT is that it needs calibration. RPT can provide a spatial resolution of less than 1 mm at 50 Hz (Upadhyay, 2010) and temporal resolution up to 200 Hz (Bhusarapu et al., 2006).

Selection of experimental technique for measurements in the conical fluidized bed

The selection of measurement technique majorly depends on its spatial and temporal resolutions with versatility. The technique should be capable of measuring the flow phenomena at different time and length scale for better understanding. Further, the technique should be applicable to laboratory, pilot and industrial scale systems with the almost same accuracy. However, none of the above-mentioned technique has all the required quality. Though the optical techniques have high spatial and temporal resolutions compared to the radiation-based technique they are limited to the transparent column. Even if one makes column wall of the glass or any other transparent material, the high solid fraction makes it dense and optical based technique can only resolve the flow near the wall. Further, PEPT is restricted to the scanning of a small diameter system, so it cannot be used for the scale-up study. RPT satisfies all the requirement needed for the present work. Further, the accuracy of the RPT is already established by various researchers for low velocity and high velocity systems at different scales (both laboratory and pilot plant scale). Therefore, RPT is selected for the experimental investigation.

2.2 Radioactive particle tracking technique

RPT has been used by many researchers to investigate fluidized bed. Kondukov et al. (1964) have used RPT for the first time in gas-solid fluidized bed for flow measurement. Later, RPT has been used and developed by many researchers such as Meek (1972), Lin et al. (1985), Devanathan (1991), Moslemian et al. (1992), Larachi et al. (1997), Degaleesan (1997), Chen et al. (1999), Roy et al. (2000), Limtrakul et al. (2005), Upadhyay (2010), and Al-Dahhan et al., 2014. Upadhyay (2010) have discussed the development of RPT technique in detail with various post-processing methodologies. Khane and Al-Dahhan (2017) developed hybrid RPT technique to eliminate calibration for RPT. In the present work, RPT is briefly explained with the current state of the art instrumentation.

2.2.1 Methodology

In radioactive particle tracking (RPT), a radioactive particle emitting γ -ray is used which follow the same path as that of the phase of interest. The radioactive particle should resemble the shape, size, and density of the solids to be followed (Lin et al., 1985). The radioactive particle in case of liquid should be neutrally buoyant. The radioactive particle is allowed to move freely inside the column with other particles. A number of scintillation detectors are placed outside of the column which measures the radiation emitted by the radioactive particle. The intensity recorded by each detector depends on the distance between tracer particle and detector, phases present between them, wall material and solid angle made by tracer particle on the detector. The experiment is followed by a calibration procedure for estimating the position of the particle. The calibration is made at the desired operating condition to mimic the composition of the phases and materials between the radioactive particle and the detectors. During calibration, the radioactive particle is placed

at different known locations and the emitted counts are recorded. Using this information, a calibration curve is plotted which relates the intensity of radiation recorded at a detector to the distance between that detector and tracer. From this curve, the coordinates of the particle are determined by using appropriate reconstruction algorithm. This curve provides a set of position data of the particle with respect to time, differentiation of which gives the instantaneous velocity of the particle as a function of space and time (Lin et al., 1985; Larachi et al., 1995). Figure 2.6 shows the flowchart of measurement principle using RPT technique. The ensemble average velocity is calculated by discretizing the whole column into a number of cells, the same as the grid in computational fluid dynamics (CFD). The fluctuation velocity is calculated from the difference between instantaneous velocity and ensemble average velocity. RPT also provides various turbulence parameters such as root-mean-square (RMS) velocity, the kinetic energy of fluctuations, Reynolds stresses etc. (Limtrakul et al., 2005; Upadhyay, 2010). In addition, time series data such as diffusivity (Yang et al., 1993; Degaleesan, 1997; Roy, 2000), and autocorrelation (Yang et al., 1993; Degaleesan, 1997; Johnsson et al., 2000; Roy, 2000) can also be acquired from RPT data.

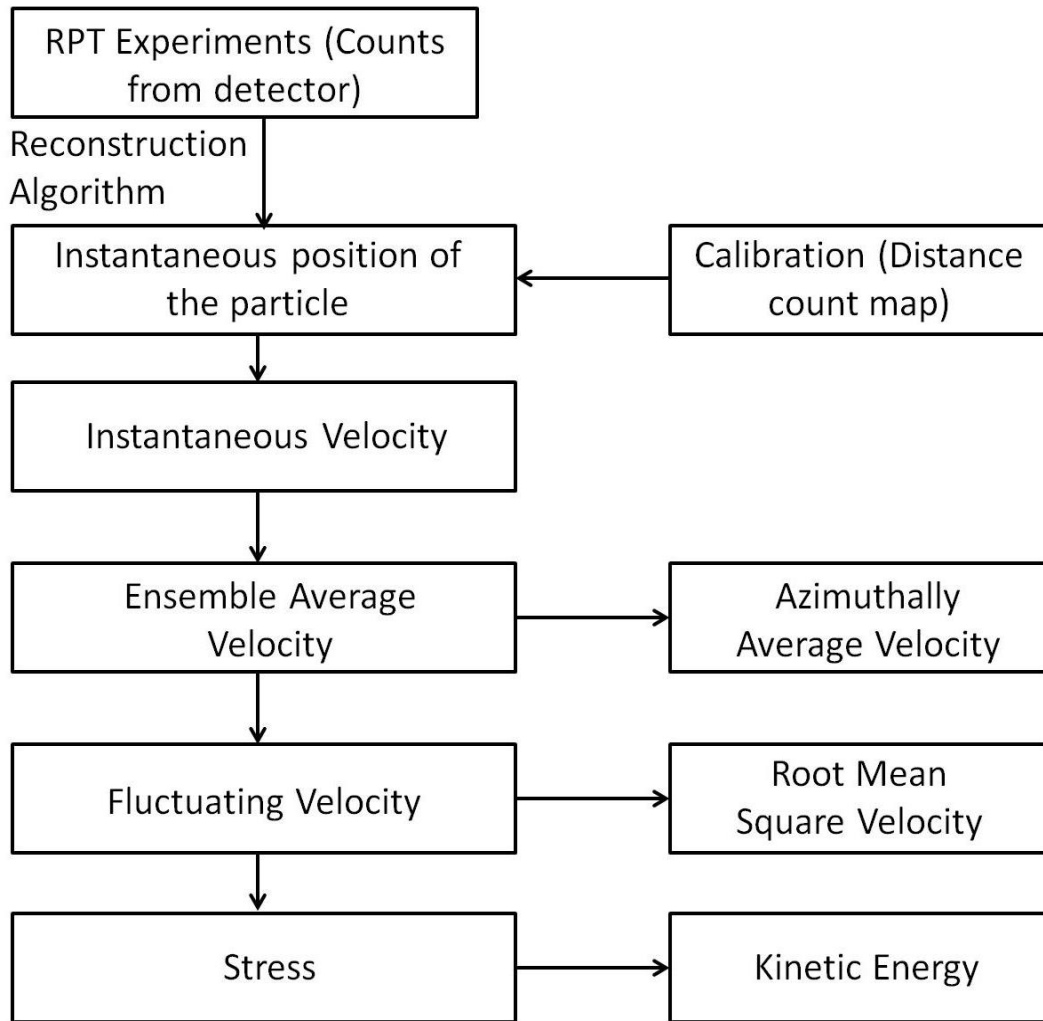


Figure 2.6 Flow chart of measurement principle (Limtrakul et al., 2005)

The various hydrodynamic parameters obtained from RPT data are given in the following equations.

The instantaneous velocities in r , θ and z direction are given by equations 2.1, 2.2 and 2.3.

Instantaneous velocity

$$v_r = \frac{2}{\Delta t} [r_2 \cos(\theta_2 - \theta_1) - r] \quad (2.1)$$

$$v_\theta = \frac{2}{\Delta t} [r_2 \sin(\theta_2 - \theta)] \quad (2.2)$$

$$v_z = \frac{\Delta z}{\Delta t} \quad (2.3)$$

Where,

$$r = \frac{1}{2} \sqrt{r_1^2 + r_2^2 + 2r_1 r_2 \cos(\theta_1 - \theta_2)}$$

The average velocities measurements are given by equations 2.4 to 2.7.

Ensemble average velocity

$$\langle v_q(i, j, k) \rangle = \frac{1}{N(i, j, k)} \sum_{n=1}^{N(i, j, k)} v_{q,n}(i, j, k) \quad (2.4)$$

Where q refers the polar coordinates r, θ, z

Fluctuating velocity component

$$v'_q(i, j, k) = v_q(i, j, k) - \langle v_q(i, j, k) \rangle \quad (2.5)$$

Azimuthal average velocity component

$$\langle v_q(i, k) \rangle^{az} = \frac{\sum_{j=1}^{T_{dim}(i)} \langle v_q(i, j, k) \rangle N(i, j, k)}{\sum_{j=1}^{T_{dim}(i)} N(i, j, k)} \quad (2.6)$$

RMS velocity

$$\langle v_q \rangle^{RMS} = \sqrt{\langle v_q'^2 \rangle} \quad (2.7)$$

The granular temperature is given by equation 2.8

Granular temperature

$$\theta = \frac{1}{3} [\langle v_r'^2 \rangle + \langle v_\theta'^2 \rangle + \langle v_z'^2 \rangle] \quad (2.8)$$

2.2.2 Implementation of RPT

In this section, various hardware and electronics used in RPT are discussed, with the mechanism involved in the photon detection and approximations involved in the implementation are explained.

Radioactive tracer particle

The radioactive particle used to track the solid phase is selected based on criteria given by Roy et al. (2002) and Upadhyay (2010). The radioactive particle used as tracer should be highly radioactive to reduce errors in the number of counts. But, it should not be so high that the detector will get saturated whenever the particle comes close. As the instantaneous position of the particle is calculated, the sampling interval should not be shorter than the time taken by the particle to move a certain distance. Usually, Scandium 46 is used as the tracer particle. The half-life of scandium is around 83 days. It exhibits two photopeaks at 889 KeV and 1120 KeV. The density of scandium is 2990 kg/m^3 which is closer to 2500 kg/m^3 which is the density of solids used in this study, i.e. glass beads.

However, the procedure followed to prepare the tracer varies in literature. Liquid tracking is performed by hollow polypropylene or polystyrene balls embedded with the small amount of scandium-46. The particle is made neutrally buoyant by keeping some air gap inside the ball (Devanathan, 1991; Degaleensan, 1997; Upadhyay, 2010). For solid tracking, a small amount of scandium-46 powder is doped inside the solid particle and the shape, size, and density is matched. Lin (1981), Moslemian et al. (1989), Upadhyay (2010), Zaid (2013), Efhaima and Al-Dahhan (2017) tracked solid particle in gas-solid fluidized bed whereas Limtrakul et al. (2005), Jain et al. (2014) and Jain et al. (2017) tracked solid particle in the liquid-solid fluidized bed. Further, Ali et al. (2017) and Al-Juwaya et al. (2019) tracked solid particle in gas-solid spouted bed. Lin (1981) used

scandium ball coated with epoxy as tracer particle. Moslemian et al. (1989) used tracer particle made up of scandium-46 and matched its density and diameter closely with the glass beads, used in their experiment. Upadhyay (2010) used Scandium powder doped in glass bead and polystyrene as a tracer in order to match the density of tracer with glass beads and sago used in the experiment. Limtrakul et al. (2005) and Jain et al. (2014 and 2017) used Scandium doped into a particle of the same size and density as the solids used in the experiment. Hence, in the present work, scandium powder is doped in the glass bead and is irradiated in a nuclear reactor (situated in BARC, Mumbai) to make it radioactive. In this way, both the size and density of the tracer will be close to the solids being traced.

Photon detection and counting

The pulse processing system processes the signals from the detector. The instrument is known as Multi-Input Data Acquisition System (MIDAS) or pulse processing unit, designed by Electronic Enterprises (I) Pvt. Ltd., for tracer experiment like RPT. It supports communication through the USB port. The information acquired during the experiment is transferred to PC on the USB port and stored on PC. Figure 2.7 shows the photograph of MIDAS.



Figure 2.7 Photograph of MIDAS®

This instrument (MIDAS[®]) comprises of

- Power Supply
- Amplifier and SCA circuit for each detector
- Interface Module

The power supply has been designed to provide sufficient current to all the modules. This power supply gives +5V to $\pm 12V$ outputs. The input of the amplifier and SCA is the output of the detector. The amplifier amplifies up to 1000 times as the signal is in the millivolt range. The single channel analyzer eliminates noise to remove unwanted pulses. The noise gets amplified with the amplification of signals while amplified by the amplifier. The single channel analyzer selects the useful signals and eliminates the unwanted signals by using a threshold. It removes the data below LLD (Low-level discriminator) threshold and above ULD (Upper-level discriminator) threshold. The schematic diagram of the pulse processing system is given in Figure 2.8.

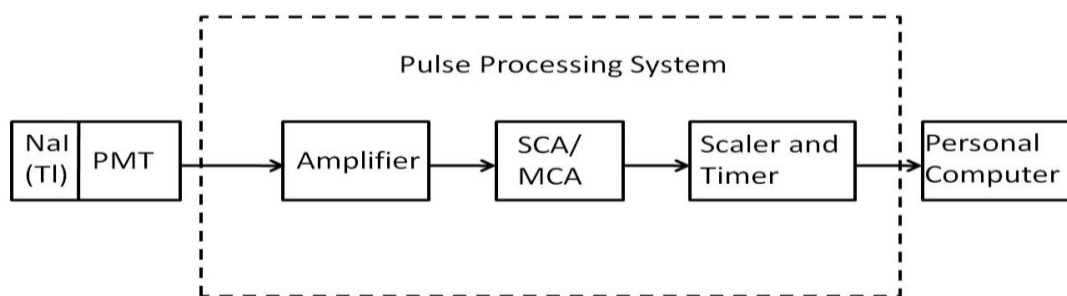


Figure. 2.8 Schematic diagram of the pulse processing system

Multi-Channel Analyzer (MCA) converts the analog signal from the detector to digital signal to process by the computer. It separates the incident photons based on their energy level and bins them. Figure 2.9 shows the photograph of MCA.



Figure 2.9 Photograph of MCA

Scintillation detectors

Scintillation detectors are used to record the radiations emitted by the radioactive particle. These scintillating materials produce light when radiation or photon falls on them. When radiation falls on scintillating material it transfers its energy to the material which results in excitation of scintillation molecule. These scintillating molecules during de-excitation process emit light photons. The scintillation detector consists of two components coupled together. The first one is scintillator which is a solid sodium iodide crystal and the second one is a photomultiplier tube, which converts light pulse into electric current. The attached photomultiplier tube (PMT) has 14 pins. The PMT is an amplifier; it can amplify 10^6 times or more in a time of 10^{-9} second. It is a glass tube that contains photocathode which is followed by several dynodes. The photocathode is very sensitive to light. The photons produced by the detector enter the PMT and hit the photocathode which then emits low energy electron. These electrons when hit dynode, it emits secondary electrons. These secondary electrons move from one dynode to other which results in amplification of the signal. Each dynode is maintained at a higher potential than the previous one to attract the electrons to next dynode. This potential difference is maintained by supplying high voltage to the PMT. After hitting the last dynode, the amplified signal is collected on

the anode of PMT. The number of photopeak photon counts recorded by a detector can be calculated by using equation 2.9 (Larachi et al., 1994).

$$C = \frac{T \nu A \varepsilon_{abs} \phi}{1 + \tau \nu A \varepsilon_{abs} \phi} \quad (2.9)$$

In equation 2.9 three parameters are unknown, viz., dead time (τ), source strength (A) and medium attenuation coefficient (μ). To know these unknown parameters, calibration is performed where the radioactive particle is placed at different known locations so that they can be used in the Monte Carlo algorithm.

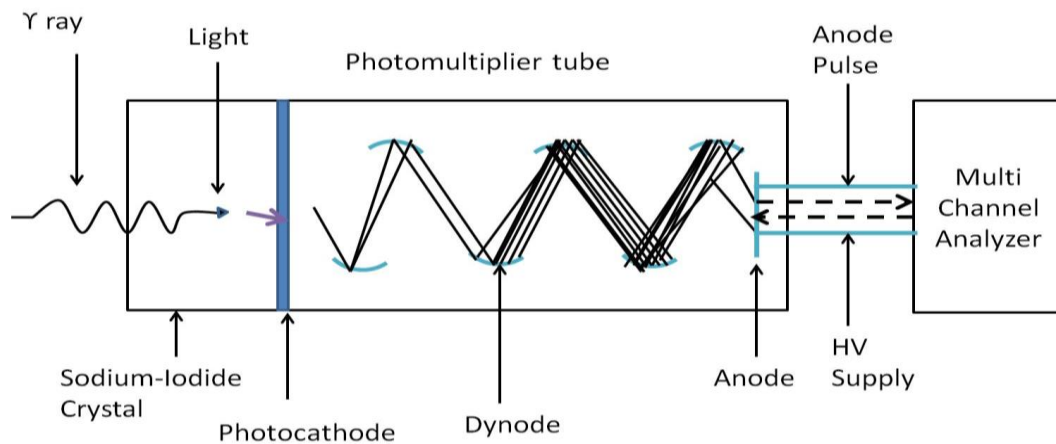


Figure 2.10 Schematic diagram of NaI(Tl) scintillation detector



Figure 2.11 Photograph of NaI(Tl) scintillation detector

NaI(Tl) scintillation detector is a commonly used detector for this technique. The size of the crystal used in this detector is $2'' \times 2''$. The schematic diagram and photograph of the NaI (Tl) scintillation detector are shown in Figures 2.10 and 2.11, respectively. These

detectors are durable and relatively inexpensive. These detectors have high detection efficiency and can be operated at room temperature.

Arrangement of detectors

The positioning of the detectors plays an important role in RPT experiment and it should be known accurately. The detector should not be placed close to the column, as it can cause blinding of the detector, due to the recording of excessive counts and also the detector should not be placed far from the column which reduces the spatial resolution and solid angle of the detector. Hence the detector should be placed at an optimal position.

2.2.3 Calibration

Calibration is done prior to the experiment where the tracer particle is placed at various known locations and its intensity (count rate) is recorded at each detector. Calibration is performed at the in-situ condition. During calibration, the particle is placed at known locations and the detectors around the column record the intensity of the radiation (counts). The intensity recorded by each detector depends upon the distance between tracer particle and detector, phases present between them, wall material and solid angle made by tracer particle on the detector. The intensity of radiation recorded at each detector decreases exponentially with increase in the distance between the tracer particle and the detector. Using this information, the calibration curve is plotted which relates the intensity of radiation recorded at a detector to the distance between the tracer and detector. For high accuracy, the number of positions during calibration should be such that the particle covers the whole column. However, this process is not possible as it is a tedious job and will require huge time and effort. To reduce this effort, Monte Carlo code developed by Larachi et al. (1994) is used for photon emission, transmission, and

detection, which was later on modified by Upadhyay (2010) to generate the counts recorded on the detector for a known particle location. However to optimize the unknown fitting variables of Monte Carlo code, ‘in – situ’ calibration at few points is required (Upadhyay, 2010). In the current work, the Monte Carlo program is used to plot the position – count map using a limited set of calibration data.

Monte Carlo method (Beam et al., 1978; Upadhyay, 2010)

Monte Carlo method is used to generate the counts recorded on the detector for a known particle location. It is used to generate the distance-count map using calibration data and efforts needed for calibration. The efficiency of the detector effects the photon counting. This also depends on the solid angle of the detector (angle created by the tracer particle with the detector). When the tracer moves, most of the time it goes out of the detector vision (front face) and is exposed to the side face of the detector.

The absolute efficiency ε_{abs} is calculated by equation 2.10 (Roy, 2000).

$$\varepsilon_{abs} = \iint_{\Omega} \frac{r \cdot n}{r^3} \exp\left(-\sum_{j=1}^N \mu_j l_j\right) (1 - \exp(-\mu_D d)) d\Sigma \quad (2.10)$$

In equation 2.10, the three unknowns are mass attenuation coefficient of the detector crystal (μ_D), the penetration depth of photons in the detector crystal (d) and solid angle subtended the detector surface and tracer (Ω). The solid angle is calculated by tracking the particle histories in all directions through the Monte Carlo method. The solid angle subtended by the detector to the tracer particle is measured based on the possible tracer position with respect to the detector. There can be three possible positions of a tracer particle with respect to detector position. Figure 2.12 shows the schematic diagram of the positioning of source and detector when the source is outside detector flat face and within the detector flat face.

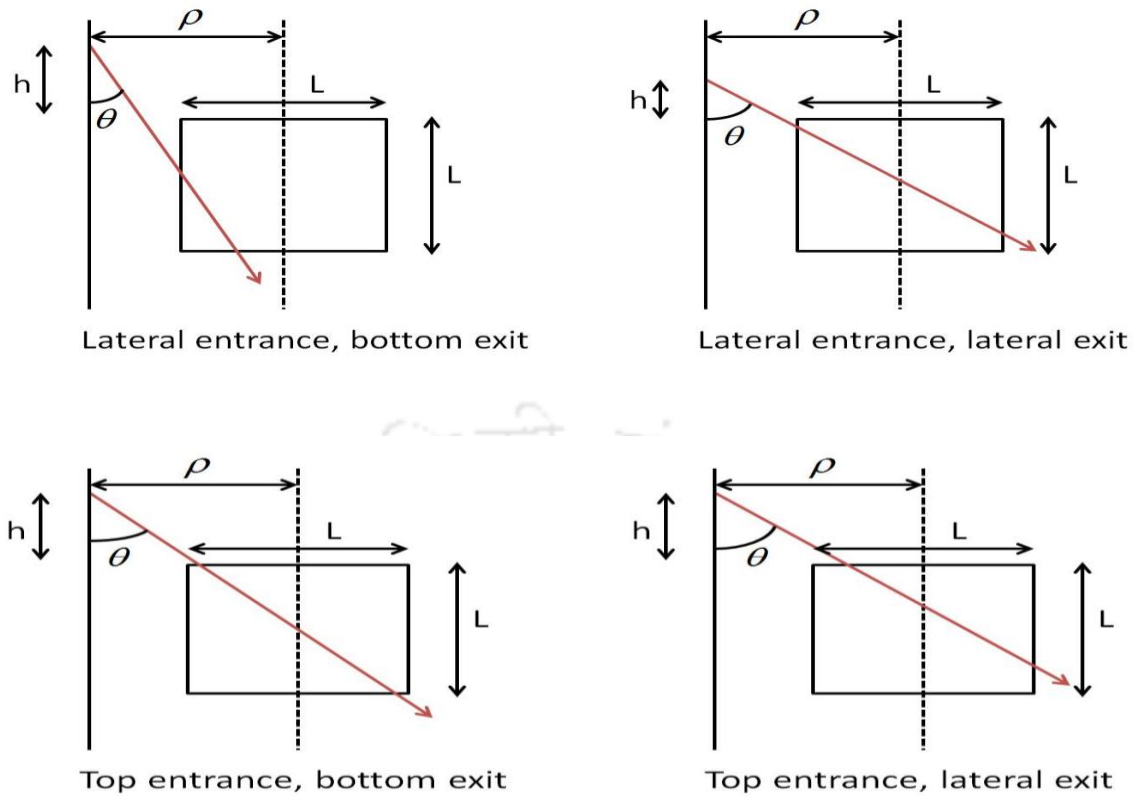


Figure 2.13 Schematic diagram of possibilities of the photon travelling path through the detector (Beam et al., 1978)

2.2.4 Reconstruction algorithm

During RPT, the tracer moves throughout the column emitting radiation which is recorded by the scintillation detector placed around the column. The path of the tracer particle is reconstructed by using the counts recorded by the scintillation detectors. Four types of reconstruction algorithm are used in the literature. They are

- Weighted Least Square Regression Method
- Monte Carlo Method
- Feed Forward Neural Network Method
- Cross Correlation Method

The above mentioned methods have already been explained in Upadhyay (2010). In the current work, the Monte Carlo method is used for particle position reconstruction. In this

method, first the calibration is performed. The calibrated counts are used to calculate the model parameter like dead time and medium attenuation coefficient. Then by using equation 2.10, counts are generated for every possible position of the tracer. Table 2.1 is the look up table for tracer position and count recorded by each detector.

Table 2.1 Look up table of calibration data

X	Y	Z	C1	C2	C3	C4	C5	C6	C7	C8
0	0	0	400	370	300	280	100	90	50	35
0	0.5	0								

X, Y, and Z are the co-ordinates of the tracer and C1, C2....C7 are the counts for respective detectors. To reconstruct the unknown position of tracer Chi square test is performed which compares the experimental and simulated calibration counts. The value of chi square must be less than 10^{-4} .

$$\chi^2(j) = \sum_{i=1}^{N_D} \frac{(C_i - M_i)^2}{\sigma_i} \quad (2.11)$$

Where j is the jth calibration node

$$\sigma_i^2 = C_i^2$$

2.3 Advanced post processing techniques (time series analysis)

The time series analysis is used when the system is complex and cannot be characterized completely by time-averaged quantities, like mean and RMS velocities. Various time series analysis components, such as Hurst exponent, autocorrelation and segregation index and, the chaos analysis components, such as Kolmogorov entropy and correlation

dimension are calculated by post-processing of RPT data, the procedures are explained below:

Rescaled range (R/S) analysis

Rescaled range analysis (R/S analysis) is performed on instantaneous velocities to investigate the solid phase turbulence inside the column. The R/S analysis has been put forward by Hurst (1951) and applied by Mandelbrot to describe the so-called fractional Brownian motion, which indicates super or sub-dispersion of moving particles. It can be represented by equation 2.12 as below

$$\frac{R(t, \tau)}{S(t, \tau)} \propto \tau^H \quad (2.12)$$

Where the exponent 'H' is called the Hurst exponent and is obtained from the slope of the log-log graph of R/S versus τ .

If $v(t)$ denotes the variation of Lagrangian velocity with time then

$$\xi(t) = v(t + dt) - v(t) \quad (2.13)$$

Where dt denotes data acquisition time and $\xi(t)$ denotes the signal increment. For a selected time window τ the cumulative departure of the increment from the average increment $\langle \xi \rangle_\tau$ is given by equation 2.14

$$y(t, \tau) = \sum_{i=t+1}^{t+\tau} (\xi(i) - \langle \xi \rangle_\tau) \quad (2.14)$$

The range of signal y and the standard deviation of the signal increment are calculated by equations 2.15 and 2.16, respectively.

$$R(t, \tau) = \max_{t < i \leq t + \tau} y(i, \tau) - \min_{t < i \leq t + \tau} y(i, \tau) \quad (2.15)$$

$$S(t, \tau) = \sqrt{\frac{1}{\tau} \sum_{i=t+1}^{t+\tau} (\xi(i) - \langle \xi \rangle_{\tau})^2} \quad (2.16)$$

Hurst exponent greater than 0.5 points to ‘persistence’ or ‘super dispersive solid motion’. It indicates that there is a positive correlation between the velocities of the particle, thus, statistically maintaining the current trend in time. If the value of H is less than 0.5, it represents negative correlations of the particle velocities, anti-persistence or sub dispersive solid motion. Hence, the particle velocities have a tendency to reverse/oppose the trend in future. If Hurst exponent value is equal to 0.5, it means there is no correlation between the velocity fluctuations, which indicates a particle motion resembling a Brownian motion or a diffusion-type mixing mechanism. Thus, the process is Markovian having no correlation between the velocity fluctuations. Hurst exponent is capable of distinguishing both long and short-term memory of the system (Drahoš et al., 1992).

Autocorrelation

The autocorrelation function is represented by correlating the particle fluctuation velocity to itself after a certain time interval. Autocorrelation function decays to zero after some time indicating a loss of memory of initial state. The expression used to calculate the autocorrelation function is given in equation 2.17 (Yang et al., 1993).

$$AC(\tau) = \frac{\sum_{t=0}^n (v(t) - \langle v \rangle)(v(t + \tau) - \langle v \rangle)}{\sum_{t=0}^n (v(t) - \langle v \rangle)^2} \quad (2.17)$$

In a gas-solid cylindrical fluidized bed where motion is primarily in the axial direction, axial autocorrelation shows a strong correlation and decays slowly, whereas, the radial autocorrelation decays rapidly. The periodic peak in axial autocorrelation indicates the timescales when the particle is more likely to return to the same axial location, thus indicating recirculation time (Halow et al., 2012). For the strongly periodic process, the

autocorrelation function exhibits oscillation, while for the stochastic process it will decay faster to zero with time.

Segregation index

Segregation index can help to determine the regime transition and mixing nature of the column. Usually, the column is divided into k sub-volumes. Then the probability of occurrences of the particle in each sub-volume is determined. The probability P_i of the 1 mm or 0.6 mm tracer particle entering a cell of the volume V_i is calculated as

$$P_i = \frac{N_i}{N} \left(\frac{V_i}{V} \right) \quad (2.18)$$

The Segregation index 'SI' is calculated as given in equation 2.19

$$\text{Segregation index (SI)} = 1 - \sum_{i=1}^k |P_i(1\text{mm}) - P_i(0.6\text{mm})| \quad (2.19)$$

For the binary bed RPT experiments, motions of both particles (1 mm and 0.6 mm) were tracked individually. The individual particle motion was tracked for 8 hours for all the velocities to acquire sufficient statistics. Hence, for calculating the probability of finding the tracer particle in any region, total numbers of occurrences of both the tracer particles were used. The value of S will be 1 for a completely mixed bed and -1 for a completely segregated bed.

Kolmogorov entropy (KE)

Kolmogorov entropy characterizes the rate of loss of information or degree of unpredictability of a system. It indicates the rate at which two close initial states of the system depart from each other. KE can be used as a tool for flow regime prediction. The Kolmogorov entropy of a system can be calculated from a single characteristic variable (Takens, 1981). A positive value of Kolmogorov entropy indicates that the system is

chaotic. $KE = 0$ represents a constant, regular or cyclic phenomena and $KE = \infty$ indicates a stochastic system (random or unpredictable systems from which no information can be retrieved) (Grassberger and Procaccia, 1983). A low value of KE indicates that the system is more regular and high value of KE signifies irregular dynamics. In current work, the method proposed by Schouten et al. (1994a) is used to calculate the maximum-likelihood estimate of Kolmogorov entropy (given by equation 2.20).

$$KE = -\frac{1}{dt} \ln \left(1 - \frac{1}{b} \right) \quad (2.20)$$

And \bar{b} is expressed by equation 2.21

$$\bar{b} = \frac{1}{m_c} \sum_{i=1}^{m_c} b_i \quad (2.21)$$

Correlation dimension (CD)

Correlation dimension is used to measure the complexity of a signal and can be calculated as the derivative of correlation integral with respect to distance. CD provides an indication of the degrees of freedom of any dynamic system (i.e. the number of variables needed to describe the asymptotic state of the system). Correlation dimension is calculated by using the procedure put forward by Schouten et al. (1994b). Equation 2.22 shows the expression used for calculating the correlation integral value.

$$C(l) = \lim_{m \rightarrow \infty} \frac{1}{m^2} \sum_{i,j=1}^m \Theta(l - |x_i - x_j|) \quad (2.22)$$

CD is calculated from a power law as shown in equation 2.23 in the limit $l \rightarrow 0$ and the number of points $m \rightarrow \infty$

$$C(l) \approx l^D \quad (2.23)$$

The correlation dimension (D) is evaluated from the scaling region of $\ln(C)$ vs $\ln(l)$.

Notations

A	Source strength, Ci
$AC(\tau)$	Autocorrelation Function, -
b	Number of time intervals required for the distance of a pair of two initial states x_i and x_j on the attractor to exceed for the first time the considered maximum distance, l , -
\bar{b}	Average of all the b values, -
C	Photo peak count, -
C_i	Counts registered by the i^{th} detector for the tracer particle at j^{th} node, -
$c(l)$	Correlation integral, -
d	Penetration depth of photons in the detector crystal, m
dt	Data acquisition time, s
D	Correlation dimension of the attractor, -
H	Hurst exponent, -
k	Number of sub-volumes in which the column is divided to calculate the probabilities, -
KE	Maximum-likelihood estimate of the entropy, -
l	Distance between the pair of states on the attractor, m
l_j	Length of the intervening medium between source and detector, m
m_c	Number of samples of b values taken into account, -

m	Number of data points in the reconstructed attractor, -
M_i	Counts measured by the i^{th} detector for unknown particle position, -
n	Length of the time series, -
N_D	Number of the detector, -
N_i	Number of occurrences of the particle in the i^{th} sub volumes, -
N_t	Total number of occurrences of the particle, -
$P_i(1mm)$	The probability of 1 mm particle entering a cell of volume V_i , -
$P_i(0.6mm)$	The probability of 0.6 mm particle entering a cell of volume V_i , -
r	Radius at which data is plotted, m
$R(t, \tau)$	Range of signal y , m/s
S	Segregation Index, -
$S(t, \tau)$	Standard deviation of the signal, m/s
t	Time, s
T	Sampling time, s
v_r, v_θ, v_z	Velocity in r, θ, z direction respectively, m/s
v_q	q^{th} component of instantaneous velocity, m/s
v_q'	q^{th} component of fluctuating velocity, m/s
$\langle v_q \rangle$	q^{th} component of ensemble average velocity, m/s
$\langle v_q \rangle^{az}$	q^{th} component of azimuthal average velocity, m/s

$\langle v_q \rangle^{RMS}$	q^{th} component of RMS velocity, m/s
$v(t)$	Variation of Lagrangian velocity with time, m/s
$\langle v \rangle$	Average Lagrangian velocity, m/s
V	Total volume of the bed, m^3
V_i	Volume of the i^{th} sub volume, m^3
$y(t, \tau)$	Cumulative departure of increment, m/s
ε_{abs}	Absolute efficiency of the detector, -
θ	Angle in the osculating plane formed by the source and detector curved surface, radian
ϕ	Photo peak fraction, -
Θ	Heaviside function employed to count the pairs of states $[x_i, x_j]$ on the attractor whose distance is smaller than l , -
$\xi(t)$	Signal increment, m/s
$\langle \xi \rangle_\tau$	Average increment, m/s
τ	Time window, s
ν	Number of gamma ray photons emitted per disintegration, -
ϕ	Photo peak fraction, -
μ_D	Mass attenuation coefficient of the detector crystal material, m^{-1}
μ_j	Mass attenuation coefficient of all the materials that come in the path of photons between the source and the detector, m^{-1}

ρ_p Particle density, kg/m³

Subscripts

r, θ, z Cylindrical co-ordinate

x, y, z Cartesian co-ordinate

References

- Ali, N., Al-Juwaya, T., Al-Dahhan, M.H., 2017. An advanced evaluation of the mechanistic scale-up methodology of gas–solid spouted beds using radioactive particle tracking. *Particuology* 34, 48-60.
- Al-Dahhan, M., Aradhya, S., Zaid, F., Ali, N., Al-Juwaya, T., 2014. Scale-up and on-line monitoring of gas–solid systems using advanced and non-invasive measurement techniques. *Procedia Eng.* 83, 469–476.
- Al-Juwaya, T., Ali, N., Al-Dahhan, M.H., 2019. Investigation of hydrodynamics of binary solids mixture spouted beds using radioactive particle tracking (RPT) technique. *Chem. Eng. Res. Des.* 148, 21-44.
- Aradhya, S.B., 2013. Scaleup and hydrodynamics study of gas-solid spouted beds. Ph.D. thesis, Missouri University of Science and Technology, USA.
- Beam, G.B., Wielopolski, L., Gardner, R.P., Verghese, K., 1978. Monte Carlo calculation of efficiencies of right-circular cylindrical NaI detectors for arbitrarily located point sources. *Nucl. Instruments and Methods* 154, 501–508.
- Bhusarapu, S., Al-Dahhan, M.H., Duduković, M.P., 2006. Solids flow mapping in a gas–solid riser: Mean holdup and velocity fields. *Powder Technol.* 163, 98–123.

- Boyer, C., Duquenne, A.M., Wild, G., 2002. Measuring techniques in gas-liquid and gas-liquid-solid reactors. *Chem. Eng. Sci.* 57, 3185–3215.
- Chaouki, J., Larachi, F., Dudukovic, M.P., 1997. Noninvasive Tomographic and Velocimetric Monitoring of Multiphase Flows. *Ind. Eng. Chem. Res.* 5885, 4476–4503.
- Chen, J., Kemoun, A., Al-Dahhan, M.H., Dudukovic, M.P., Lee, D.J., Fan, L., 1999. Comparative hydrodynamics study in a bubble column using computer-automated radioactive particle tracking (CARPT)/ computed tomography (CT) and particle image velocimetry (PIV). *Chem. Eng. Sci.* 54, 2199–2207.
- Degaleesan, S., 1997. Fluid dynamic measurements and modeling of liquid mixing in bubble columns. D. Sc. thesis. Washington University St. Louis.
- Devanathan, N., 1991. Investigation of Liquid Hydrodynamics in Bubble Columns via Computer Automated Radioactive Particle Tracking (CARPT). D.Sc. thesis, Washington University in St. Louis, USA.
- Drahoš, J., Bradka, F., Punčochář, M., 1992. Fractal behaviour of pressure fluctuations in a bubble column. *Chem. Eng. Sci.* 47, 4069–4075.
- Durst, F., Melling, A., Whitelaw, J.H., 1981. Principles and practice of laser Doppler anemometry. Academic press, London.
- Efhaima, A., Al-Dahhan, M.H., 2017. Assessment of Scale-up Dimensionless Groups Methodology of Gas-Solid Fluidized Beds using Advanced Non-Invasive Measurement Techniques (CT and RPT). *Can. J. Chem. Eng.* 95, 656–669.
- Grassberger, P., Procaccia, I., 1983. Characterization of strange attractors. *Phys. Rev. Lett.* 50, 346-349.

- Halow, J., Holsopple, K., Crawshaw, B., Daw, S., Finney, C., 2012. Observed mixing behavior of single particles in a bubbling fluidized bed of higher-density particles. *Ind. Eng. Chem. Res.* 51, 14566–14576.
- Hurst, H.E., 1951. Long-Term Storage Capacity of Reservoirs. *Trans. Am. Soc. Civil. Eng.* 116, 770-808.
- Jain, S., Saraswat, P., Jain, V., Pant, H.J., Upadhyay, R.K., 2014. Investigation of liquid-solids fluidized bed of different particle size through radioactive particle tracking techniques. *J. Radioanal. Nucl. Chem.* 302, 1309–1313.
- Jain, V., Kalo, L., Kumar, D., Pant, H.J., Upadhyay, R.K., 2017. Experimental and numerical investigation of liquid–solid binary fluidized beds: Radioactive particle tracking technique and dense discrete phase model simulations. *Particuology.* 33, 112-122.
- Johnsson, F., Zijerveld, R.C., Schouten, J.C., van den Bleek, C.M., Leckner, B., 2000. Characterization of fluidization regimes by time-series analysis of pressure fluctuations. *Int. J. Multiphase Flow* 26, 663-715.
- Khane, V., Al-Dahhan, M.H., 2017. Hybrid dynamic radioactive particle tracking (RPT) calibration technique for multiphase flow systems. *Meas Sci Technol.* 28, 055904 (16pp).
- Kondukov, N.B., Kornilaev, A. N., Skachko, I. M., Akhromenkov, A.A., and Kruglov, A.S., 1964. An Investigation of the Parameters of Moving Particles in a Fluidized Bed by a Radioisotopic Method. *Int. Chem. Eng.* 4, 43–47.

- Larachi, F., Kennedy, G., Chaouki, J., 1994. A γ -ray detection system for 3-D particle tracking in multiphase reactors. Nucl. Instrum. Methods Phys. Res., Sect. A 338, 568-576.
- Larachi, F., Chaouki, J., Kennedy, G., 1995. 3 D Mapping of Solids Flow Fields in Multiphase Reactors with RPT. AIChE J. 41, 439–443.
- Larachi, F., Chaouki, J., Kennedy G., and Dudukovic, M.P., 1997, Radioactive Particle tracking in Multiphase Reactors: Principles and Applications. in Non-Invasive Monitoring of Multiphase Flows, eds., Chaouki, J., Larachi, F., and Dudukovic, M. P., 335- 406.
- Limtrakul, S., Chen, J., Ramachandran, P.A., Dudukovic, M.P., 2005. Solids motion and holdup profiles in liquid fluidized beds. Chem. Eng. Sci. 60, 1889–1900.
- Lin, J., 1981. Particle-Tracking Studies for Solids Motion in a Gas Fluidized Bed. Ph.D. thesis, University of Illinois, Urbana, Illinois.
- Lin, J.S., Chen, M.M., Chao, B.T., 1985. A novel radioactive particle tracking facility for measurement of solids motion in gas fluidized beds. AIChE J. 31, 465–473.
- Meek, C.C., 1972. Statistical Characterization of Dilute Particulate Suspensions in Turbulent Fluid Field. Ph.D. thesis, University of Illinois. Urbana, IL.
- Moslemian, D., Chen, M.M., Chao, B.T., 1989. Experimental and Numerical Investigations of Solids Mixing in a Gas Fluidized Bed. Part. Sci. Technol. 7, 335-355.
- Moslemian, D., Devanathan, N., Dudukovic, M.P., 1992. Radioactive particle tracking technique for investigation of phase recirculation and turbulence in multiphase systems. Rev. Sci. Instrum. 63, 4361–4372.

- Nieuwland, J.J., Meijer, R., Kuiper, J.A.M., Van Swaij, W.P.M, 1996. Measurements of solids concentration and axial solids velocity in gas-solid two-phase flows. Powder Technol. 87, 127-139.
- Parker, D.J., Dijkstra, A.E., Martin, I.T.W., Seville, J.P.K, 1997. Positron emission particle tracking studies of spherical particle motion in rotating drums. Chem. Eng. Sci. 52, 2011-2022.
- Prasad, A.K., 2000. Particle image Velocimetry. Curr Sci. 79, 51-60.
- Roy, S., 2000. Quantification of Two-Phase Flow in Liquid-Solid Risers. Ph.D. thesis, Washington University, USA.
- Roy, S., Larachi, F., Al-Dahhan, M.H., Duduković, M.P., 2002. Optimal design of radioactive particle tracking experiments for flow mapping in opaque multiphase reactors. Appl. Radiat. Isot. 56, 485–503.
- Schouten, J.C., Takens, F., van den Bleek, C.M., 1994a. Maximum-likelihood estimation of the entropy of an attractor. Phys. Rev. E 49, 126-129.
- Schouten, J.C., Takens, S., Bleek, C.M., 1994b. Estimation of Dimension of a Noisy Attractor. Phys. Rev. E. 50, 1851-1861.
- Takens, F., 1981. Detecting strange attractors in turbulence. Lecture Notes in Mathematics 898, 366–381.
- Taofeeq, H., Aradhya, S., Shao, J., Al-Dahhan, M., 2018. Advance optical fiber probe for simultaneous measurements of solids holdup and particles velocity using simple calibration methods for gas-solid fluidization systems. Flow Meas. Instrum. 63, 18–32.

- Upadhyay, R. K., 2010. Investigation of multiphase reactors using radioactive particle tracking. Ph.D. thesis, IIT Delhi, India.
- van Ommen, J.R., Mudde, R.F., 2008. Measuring the Gas-Solids Distribution in Fluidized Beds - A Review. *Int. J. Chem. React. Eng.* 6, 1-29.
- Werther, J., Molerus, O. 1973. The local structure of gas fluidized beds. II The spatial distribution of bubbles. *Int. J. of Multiphase Flow* 1, 123-138.
- Yang, Y.B., Devanathan, N., Duduković, M.P., 1993. Liquid backmixing in bubble columns via computer-automated radioactive particle tracking (CARPT). *Experiments in Fluids* 16, 1-9.
- Zaid, F.M., 2013. Gas-solid fluidized bed reactors: scale-up, flow regimes identification and hydrodynamics. Ph.D. thesis, Missouri University of Science and Technology, USA.



Chapter 3

Experimental Investigation of Gas-Solid Conical Fluidized Bed

Scope

In this chapter, radioactive particle tracking (RPT) technique is used to investigate the behavior of gas-solid conical fluidized bed. The data obtained are used to analyze the mean solid velocity of particles for mono and binary dispersed beds of different compositions. Further effect of gas velocity on solid mean velocity, RMS velocity, and granular temperature are studied. Further, to understand the mixing characteristic of the bed, time series analysis is performed and Hurst exponent, autocorrelation function, segregation index are calculated. Finally, chaos analysis is used to calculate Kolmogorov entropy and correlation dimension for each case.

3.1 Introduction

Gas-solid fluidized beds are extensively used in various industries for their excellent gas-solid contact with high heat and mass transfer capability. They are widely used for many industrial operations such as drying (Pugsley et al., 2007, Khanna, 2008, Wormsbecker et al., 2009), granulation (Schaafsma et al., 2006), crystallization (Ishii, 1973; Golubkovich, 1975; Dighe et al., 1981), coating (Depypere et al., 2009; Hampel et al., 2013), etc. The performance of the gas-solid conical fluidized bed reactor strongly depends on the gas inlet velocity, particle size, shape, density, and type (Geldart's classification), and cone angle. Further, gas-solid and solid-solid interactions also play a vital role in determining the flow characteristics of the conical fluidized bed or for the matter of any gas-solid fluidized bed. These interactions become more critical when poly-disperse solids are used, which is often the case for most of the above-mentioned applications, compared to

mono-dispersed solids (Upadhyay and Roy, 2010; Jain et al., 2014). Further, the length and time scales of these interactions changes with the change in inlet gas velocity and/or particle type. Several authors have reported the change in the regime of cylindrical as well as the conical fluidized bed with gas inlet velocity for monodispersed bed (Kunii and Levenspiel, 1991; Peng and Fan, 1997). However, in poly-dispersed bed, or more commonly studied binary bed, with a change in gas inlet velocity both change in fluidization regime and, mixing and segregation pattern of the bed is reported for gas-solid cylindrical fluidized bed (Upadhyay and Roy, 2010). Such studies are largely missing in conical fluidized bed due to the lack of sufficient data. Most of the studies reported in binary conical fluidized beds are limited to overall pressure drop measurement, calculation of minimum fluidization velocity and finding the global mixing/segregation pattern of the bed through visual observation or off-line measurements (Maruyama and Koyanagi, 1993; Kwant et al., 1995; Sau et al., 2008). The flow regime transition and mixing/segregation pattern of the gas-solids bed largely depends on their local hydrodynamics which is initiated due to the complex interaction take place between gas-solid and solid-solid. Hence, for detailed analysis of the gas-solid conical fluidized bed analysis of both time-averaged and local fluctuation data are required (Schouten and van den Bleek, 1992; Cassanello et al., 1995; Dudukovic, 2009; van Ommen et al., 2011). The fluctuation data can be for pressure, solid/void fraction or gas/solid velocity. The time series analysis and chaos analysis of such data can reveal the detailed insight of the bed which can be useful for better operation, design, and scale-up of these beds.

3.2 Literature on G-S conical fluidized bed

Monodispersed bed

The conical fluidized beds have been used as monodispersed bed during the initial investigation. These beds have been introduced to reduce pressure fluctuations and provide better particle mixing (Ridgway, 1965; Babu et al., 1973). More vigorous circulation of solid can be obtained in the conical fluidized bed, which improves uniformity in size distribution and mixing compared to cylindrical bed due to the angled wall (Kim et al., 2000). Usually, in a cylindrical column, the smaller particle gets entrained and large particles get defluidized near the bottom for broad size distribution. However, in conical fluidized bed column diameter changes with the height of the column. Therefore, a higher gas velocity is maintained at the bottom that fluidizes the bigger particle and a lower velocity on top prevents entrainment of the smaller particles (Shi et al., 1984; Kwauk, 1992; Singh et al., 1992; Jones, 1994). Hence, this behavior of conical bed is very important for operation where particle size changes (e.g. granulation, coal combustion, crystallization, microbial growth, etc.). The conical fluidized bed also allows smooth fluidization of broad size distribution of solid, which is not possible in case of the deep cylindrical bed where the existence of large pressure difference between top and bottom, causes expansion of bed and agitation of particles and elutriation at the top as gas rises. The cross-sectional area of the conical fluidized bed increases upward and enables it to accommodate the increase in the gas volume providing smooth fluidization (Ridgway, 1965). Moreover, the modified geometry provides better mixing characteristics than the cylindrical fluidized bed at a lower velocity which reduces gas consumption and prevents elutriation of fine particles (Shi et al., 1984). The solid back mixing in the axial direction in case of cylindrical fluidized bed can be prevented in conical bed due to the inclined wall (Singh et al., 1992; Schaafsma et al., 2006). Many

investigators also compared cylindrical and conical geometry (Kim et al., 2000; Wormsbecker et al., 2009; Molnar et al., 2013) and observed improvement in solid distribution and mixing in a conical fluidized bed. The initial studies of the conical fluidized bed are mainly on regime transition (Kwauk, 1992; Toyohara and Kawamura, 1992; Olazar et al., 1994; Peng and Fan, 1997; Jing et al., 2000). Further, the development of empirical correlation on minimum fluidization velocity (Gelperin et al., 1960; Nishi, 1979; Biswal et al., 1985; Venkatesh et al., 1996; Peng and Fan, 1997; Sau et al., 2010) and pressure drop (Maruyama, 1993; Jing et al., 2000; Sau et al., 2008; Sau et al., 2010; Khani, 2011) are also added to the literature. The hydrodynamics of conical fluidized bed is needed for their design, scale up and their numerical validation and also can be useful for industrial applications and research purpose. Several invasive and non-invasive experimental techniques are also available to predict the flow pattern and mixing behavior in gas-solid conical fluidized bed. Schaafsma et al. (2006) have observed solids ascending in the center and descending near wall using positron emission particle tracking (PEPT) in a shallow bed of Geldart B particles. Tanfara et al. (2002) identified a lean core flow in the center and a denser annular flow similar to a spouted bed. Similar circulation pattern reported by Toyohara and Kawamura (1992). Khanna et al. (2008) and Wormsbecker et al. (2009) used radioactive particle tracking (RPT) technique to study the flow pattern of dry pharmaceutical granule and observed the same type of circulation pattern. Depypere et al. (2009) also observed similar circulatory motion using positron emission particle tracking (PEPT) inside a laboratory-scale GPCG-1 fluidized bed coater. They have plotted radial mean velocity at four different bed heights and found that the radial particle movement in conical bed is comparatively stronger than the cylindrical bed. The particles move towards the wall on upper part of bed and towards center near the distributor. Pugsley et al. (2007) reported circulatory motion from dilute core to dense

annulus region using transient electrical capacitance tomography (ECT) images. Bahramian and Mansour (2010) modeled conical fluidized bed and observed that solids are carried upwards in the center reaches the top and then drop down in the annular region due to gravity. This motion of solid in conical fluidized bed formed a circulation pattern of solid known as gulf-effect. Their observation shows that with increasing fluid velocity the height of solid distribution increases and become more homogeneous. At a velocity of 1.43 m/s, the particle reaches its maxima in the zone $-0.05 < r/R < 0.05$ and reaches its minima in the zone $r/R < -0.28$ and $r/R > 0.28$. They have shown for a static bed height of 6.1 cm, the axial solid velocity is low near bottom and highest at 10 cm which keeps on decreasing with the axial level of the column. Duangkhamchan et al (2010) simulated gas-solid tapered fluidized bed coater using Euler-Euler approach to select the suitable drag coefficient model and compared with PEPT results of Depypere (2005) and Depypere et al. (2009). They have employed various drag models available in FLUENT and developed by many researchers in the CFD simulations to obtain the suitable drag coefficient for modeling the hydrodynamics of tapered fluidized bed coaters. The simulation shows that the bed mean volume fraction is high at the bottom and reduces before it reaches the static bed height for two and four-phase flow.

Binary dispersed bed

For any industrial application where gas-solid fluidized beds are used, it is impossible to use uniform sized (monodispersed) particles. However, these fluidized bed characteristics have been always represented by a mean size of the particle, though the particle size distribution has a strong impact on fluidization behavior. Sutar and Das (2012) have observed that the mixing and segregation depend on the fraction of solids present in the mixture completely. Addition of dissimilar solids to the bed changes the behavior of the fluidized bed and different mixing and segregation pattern occurs in these beds. Further,

the design and operation of these reactors depend on the mixing and segregation behavior of the solids used. Thus, it is very important to understand the effect of particle size distribution on the performance of conical fluidized bed. However, it is quite impossible to take into account a broad size distribution of solid in the experiments. Hence, many researchers have accounted for the mixing and segregation behavior of binary dispersed bed. Mainly four stages have been observed in a binary dispersed fluidized bed (Kwant et al., 1995). Figure 3.1 is a representation of various stages in a binary dispersed conical fluidized bed. The effect of particle size distribution has been unfolded by many researchers in cylindrical fluidized bed (Cheung et al., 1974; Roew and Nienow, 1976; Rice and Brainovich, 1986; Noda et al., 1986; Nienow et al., 1987; Peeler et al., 1989; Fan et al., 1990; Formisani, 1991; Hoffmann et al., 1993; Wu and Baeyens, 1998; Rasul et al., 1999; Marzocchella et al., 2000; Formisani et al., 2001). Besides, the information available on the binary cylindrical fluidized bed, the study on binary conical fluidized bed need to be broadened as its behavior differs from cylindrical due to the changing geometry.

Toyohara and Kawamura (1992) have found that horizontal segregation of bed occurs. At low flow rate while the core bed is fluidized while the annular region is still static. As the gas velocity increases the annular region starts moving with horizontal segregation. Very few studied have included binary dispersed mixture in a conical geometry. Maruyama and Koyanagi (1993) proposed a model to predict bed height and pressure drop, independent of cone angle. Mixing and segregation in tapered bed have been performed by Kwant et al. (1995). Kim et al. (2000) compared the behavior of solids with the binary composition in various geometries and observed that a critical angle is needed to reduce segregation. Wormsbecker et al. (2005) observed improvement in particle mixing with an increase in superficial gas velocity and a decrease in tracer size. Wiens et al. (2006) used electrical

capacitance tomography in conical bed investigation. Schaafsma et al. (2006) have calculated the concentration of granules throughout the bed for various solid loadings by dividing the central section of the column in one part and the tapered section in another part. Further, PEPT technique is also used. They have observed homogeneous mixing in the center part of the column compared to the annulus. They have stated that the granule fraction in the bed has a significant effect on granule segregation. They have observed that the flotsam behavior of granule at low granule fraction changes to jetsam at high granule fraction. No clear segregation observed by them. They have also used PEPT for their investigation. Sau et al. (2008) have developed an empirical correlation based on dimensionless analysis for the calculation of critical fluidization velocity and maximum bed pressure drop for a binary mixture of group B and D. Khanna et al. (2008) have observed poor mixing of solids in the case of wide particle size distribution (PSD) bed compared to the bed with narrow PSD. Gernon et al. (2010) focused on the various regimes formed in conical binary dispersed fluidized bed with changing velocity. Their observation shows at low flow rate the bed is completely fixed and just above u_{mf} of mixture vertical segregation occurs. At a higher gas flow rates horizontal segregation occurs and at a sufficiently high gas flowrate complete mixing occurs.

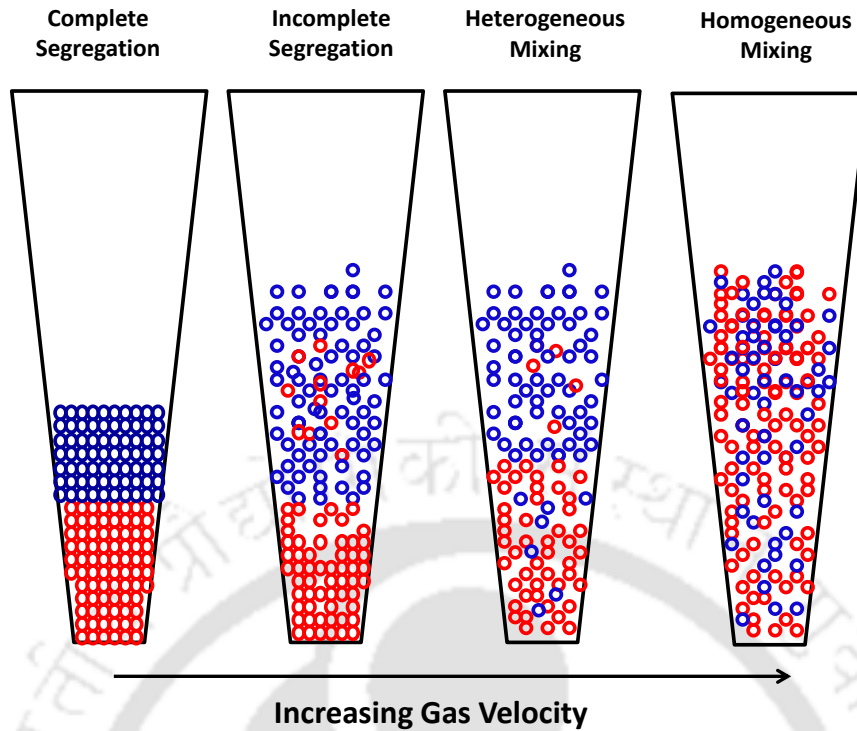


Figure 3.1 Regimes in binary conical fluidized bed (Kwant et al., 1995)

3.3 Experimental setup

A laboratory scale gas-solid conical fluidized bed was used for the hydrodynamics study in the present work. The conical bed used for the experiment was made up of stainless steel. The setup was designed with a number of calibration ports to conduct radioactive particle tracking (RPT) technique experiments. The present study used RPT technique for experimental investigation. Scandium-46 was used as the radioactive particle in all experiments. The particle has been prepared to match the size, shape and density of other solids in the bed before irradiation to reduce the error during tracking of particle.

Figure 3.2 shows the conical gas-solid setup installed for the current study. The bottom diameter of the conical column was 0.05 m and the top diameter was 0.2 m with a tapering of 5.4° . Glass beads of two different diameters, 0.6 mm (Geldart-B) and 1 mm (Geldart-D), and density 2500 kg/m^3 were used as the solid phase and compressed air was used as the gas phase. Rotameter was used at the inlet to control the air velocity. A mesh

of 200 size was used at the bottom of the bed just above the distributor (sieve plate). The fluidized bed was operated at three different velocities, i.e., 3.8 m/s, 5.7 m/s and 7.6 m/s, which are 2, 3 and 4 times the minimum fluidization velocity of the bigger (1 mm) particle. The bed composition was maintained as 0:100, 75:25, 50:50, 25:75 and 100:0 by mass for the binary mixture of 1 mm and 0.6 mm particles, respectively. The total amount of solid used for all experiments was kept constant, i.e., 1.36 kg. Total 12 scintillation detectors were used to track the motion of the tracer particle. While investigating binary bed, the motion of both particles was tracked individually for each set of experiments. Table 3.1 shows the operating conditions of monodispersed bed. The different bed compositions and operating conditions of binary bed are shown in Table 3.2. The schematic diagram of the conical fluidized bed is depicted in Figure 3.3.



Figure 3.2 Experimental setup of gas-solid conical fluidized bed for RPT

Table 3.1 Operating conditions in gas-solid conical bed

Material	Size of solid (mm)	u_{mf} (m/s)	Gas velocity (m/s)
Glass beads	1	1.97	3.8, 5.7, 7.6
Glass beads	0.6	1.1	3.8, 5.7, 7.6

Table 3.2 Different bed compositions and operating velocities in gas-solid conical bed

Bed composition	Gas velocity (m/s)
100% 1 mm glass beads	3.8, 5.7, 7.6
75% 1 mm and 25% 0.6 mm glass beads	7.6
50% 1 mm and 50% 0.6 mm glass beads	3.8, 5.7, 7.6
25% 1 mm and 75% 0.6 mm glass beads	7.6
100% 0.6 mm glass beads	3.8, 5.7, 7.6

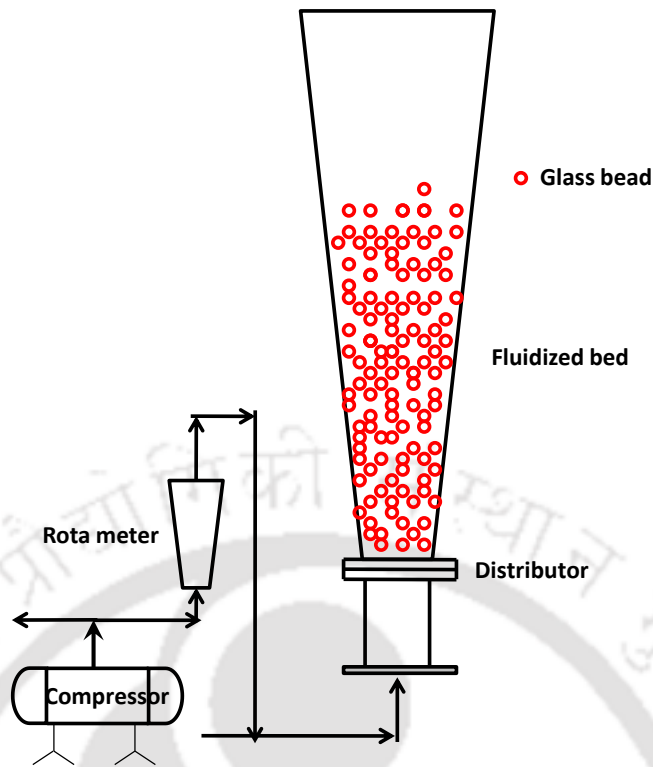


Figure 3.3 Schematic diagram of experimental setup

3.4 Results and discussions

3.4.1 Lagrangian track of particle position

In RPT as the tracer moves along with the bed of solid, its motion gets tracked. Thus, the Lagrangian position of the particle is computed. In an ergodic system, the trajectory of a single particle tracked for a long time can represent the trajectory of the entire particle in the column. A typical trajectory of a tracer of 1 mm size at 7.6 m/s in r-z and the x-y axis is shown in Figures 3.4 and 3.5, respectively. The trajectory of the particle is shown after 1, 2, 5, 10 and 20 seconds as the tracer flows during the experiment.

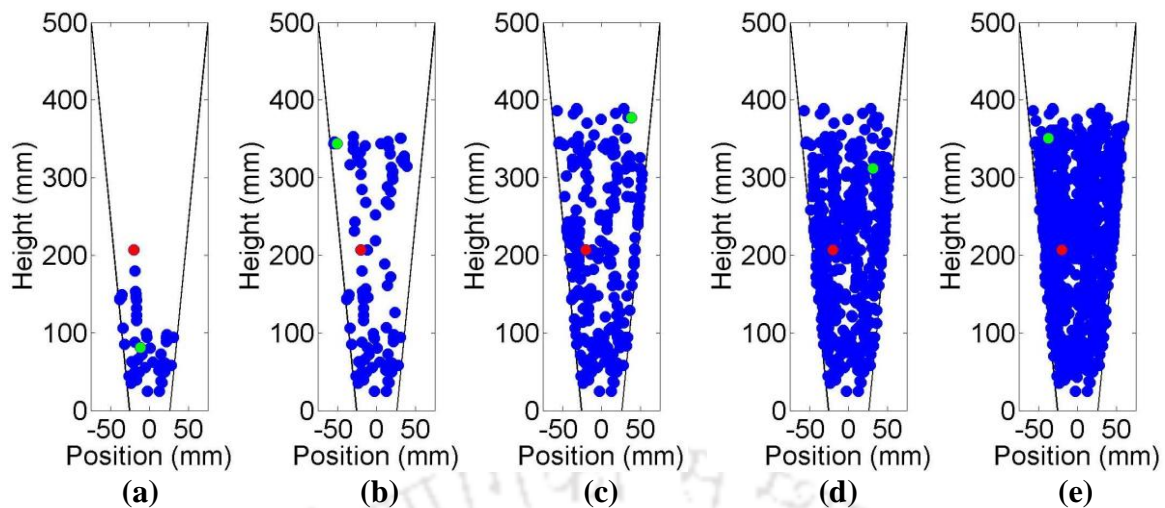


Figure 3.4 Trajectory of 1 mm tracer at 7.6 m/s with time in r-z plane at: (a) 1 sec, (b) 2 sec, (c) 5 sec, (d) 10 sec, and (e) 20 sec

The initial and final positions of the tracer are marked in red and green, respectively. The trajectory has been presented for various time durations to observe the dispersion of the particle inside the column. It has been observed that within 20 seconds of time the particle covered almost the entire volume of the column. After running the experiment for 8 hours, the tracer particle visited all positions in the column and hence it can represent the motion of the solid phase as a whole as it moved throughout the system. Further, the particle trajectory in the x-y axis also shows that the tracer covers all the location.

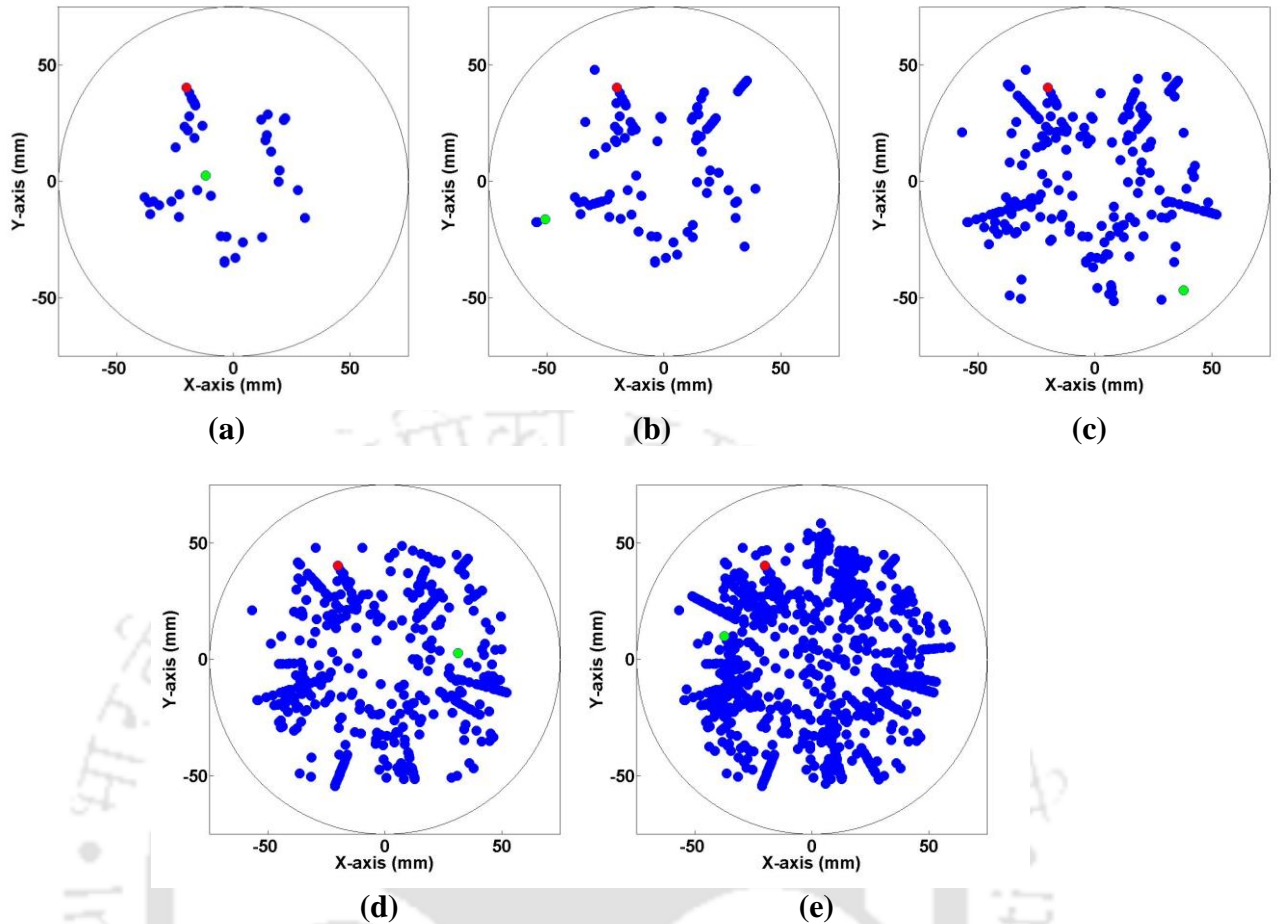


Figure 3.5 Trajectory of 1 mm tracer at 7.6 m/s with time in x-y plane at:(a) 1 sec, (b) 2 sec, (c) 5 sec, (d) 10 sec, and (e) 20 sec

3.4.2 Lagrangian velocity of the solids

Instantaneous Lagrangian velocity was calculated by time differentiation of two successive positions of the tracer particle. The axial instantaneous Lagrangian velocity of the solids with time is shown in Figure 3.6. It is seen that the particle is moving in both an upward and downward directions which was expected. Even though there was small fluctuation observed in the axial direction, it's not significant. Figure 3.7 shows the radial instantaneous Lagrangian velocity of the solids with time. Figure 3.7 indicated that there exist a radial motion of solid in the column though it is too low compared to axial velocity. The axial velocity was observed to be almost 10 times of the radial velocity.

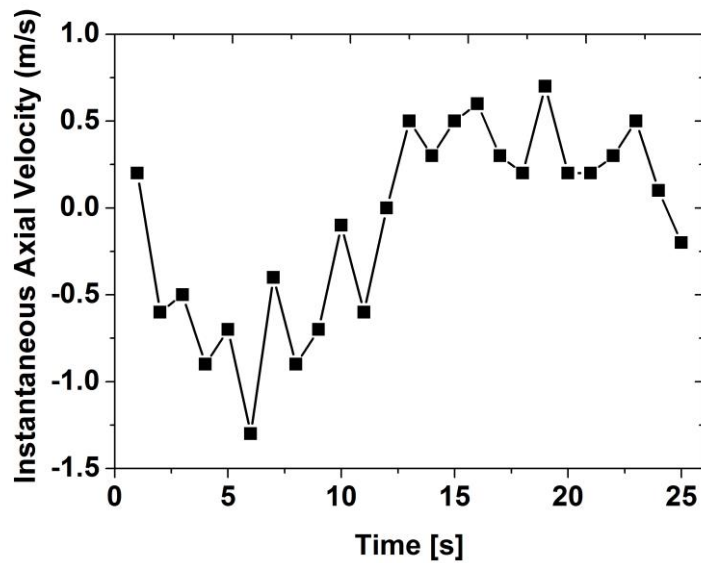


Figure 3.6 Axial Lagrangian velocity of 1 mm solid at 7.6 m/s

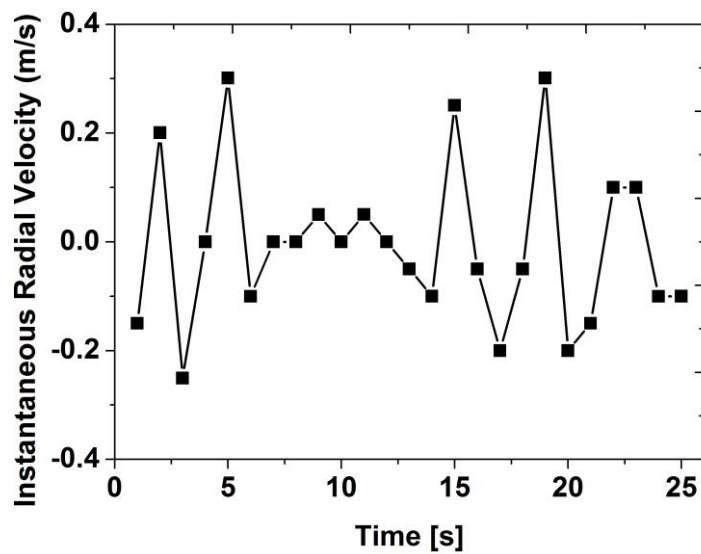


Figure 3.7 Radial Lagrangian velocity of 1 mm solid at 7.6 m/s

To understand the trend of the whole particle inside the bed it is necessary to convert the Lagrangian data to the Eulerian frame of reference. This can be obtained by ensemble averaging the trajectory of tracer for a particular control volume invoking ergodicity (Bendat and Piersol, 2000). The time average of a sample function is equal to the ensemble average for an ergodic system (Bendat and Piersol, 2000). This concept of ensemble averaging invoking ergodicity has been applied to many RPT experiments

(Roy, 2000; Bhusarapu, 2005; Upadhyay, 2010). The Eulerian velocity was obtained by forming a number of virtual grid similar to mesh generation in modeling. The ensemble average was calculated by summation of all the instantaneous velocities in the cell divided by the number of occurrence in the cell. Further, the ergodic system should satisfy stationary condition (i.e. the condition where the system behavior does not change over the time series). It means if the system is stationary the moment will not change with an increase in the number of occurrences in case of RPT experiment.

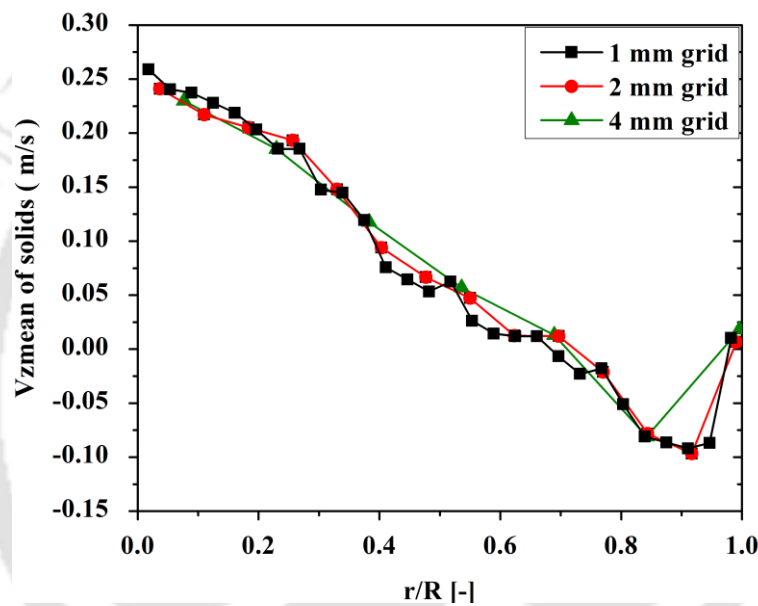


Figure 3.8 Effect of grid on mean axial velocity at $h/H = 0.25$ and 7.6 m/s (1 mm solid)

In order to obtain the moment of the solid at any height, the ensemble average moments of each cell at that particular height is calculated. Therefore, to calculate this, sufficient statistics is needed (i.e. the particle should visit all the position inside the column). This will take a large amount of time. Therefore, to reduce the experimental time finite volume grid was used to satisfy the stationary conditions in each cell. Many discretization methods were referred in the literature with a constant volume of each cell (Devanathan, 1991; Degaleesan, 1997; Roy, 2000) in the assertion that the number of occurrences in each cell will be constant. In the current work, r and z directions were uniformly divided

and theta division was increased with r , as the area increases with radius. Figure 3.8 shows a comparison of three grids. 4 mm grid ($\Delta r = 4$ mm, $\Delta z = 20$ mm), 2 mm grid ($\Delta r = 2$ mm and $\Delta z = 20$ mm) and 1 mm grid ($\Delta r = 1$ mm and $\Delta z = 20$ mm) with theta division varied to match the volume of the cell. Here, ' h ' is the actual height where data was plotted and ' H ' is the expanded bed height during fluidization. The figure shows there is no significant difference observed between all the three grids. Hence, in this work, 2 mm grid was used, as it provides better resolution in the r direction. Therefore, the radial direction (r) was divided into 14 divisions and the axial direction (z) was divided into 20 divisions. Further, the moments were ensemble averaged on the basis of the number of occurrences to maintain stationarity.

Further, to validate the reproducibility and stationarity, the mean axial velocity and RMS velocity with 50%, 75% and 100% of total acquired data are plotted in Figure 3.9. Figure 3.9a and 3.9b show validation of stationarity for axial mean velocity and axial RMS velocity on top at 7.6 m/s. There was no remarkable change obtained in the plot of mean axial velocity and RMS velocity, even though the number of occurrences increases with increase in the number of data points. This confirmed the reproducibility and stationarity of the RPT experiments. In order to confirm this, stationarity for all the operating condition was verified.

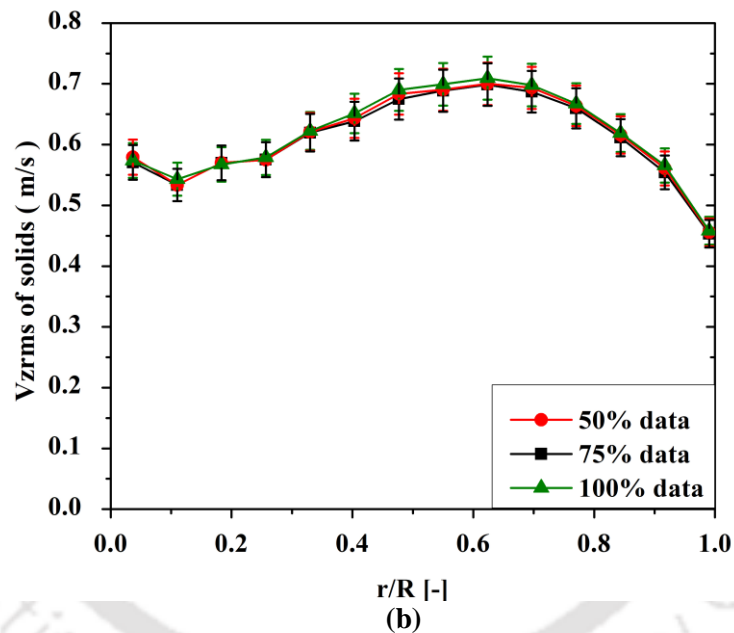
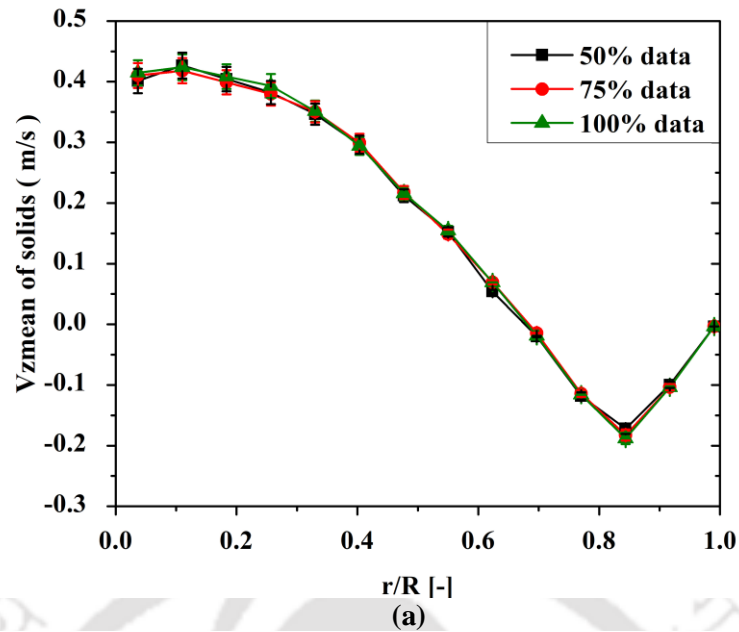


Figure 3.9 Validation of stationarity of 1 mm solid at $h/H = 0.75$ at 7.6 m/s (a) V_{zmean} (b) V_{zrms}

3.5 Effect of gas velocity on monodispersed bed

3.5.1 Velocity vector plots

Figures 3.10 and 3.11 show the mean axial velocity vector plot with superficial velocity for 1 mm and 0.6 mm particles, respectively. The vector plots are shown at 3.8, 5.7 and 7.6 m/s which correspond to 2, 3 and 4 u_{mf} of 1 mm solid. The azimuthally time-averaged

data was used to plot the results. It was observed that one circulation cell exists in the bed with a similar flow pattern for all the operating velocities. The particles were moving upward in the center going towards the wall and moving downward near wall going towards center near the distributor. It is obvious from the figure that the presence of a bubble in the central region tends to move the solid particle upward in the center at a higher velocity. However, near wall region due to the absence of bubble higher concentration of solid was moving downward at a relatively lower velocity than the central region. This kind of single circulation with ascending solid in center and descending near wall profile was observed at high velocity, i.e. above $4u/u_{mf}$ in case of the cylindrical column (Lin et al., 1985; Baeyens and Geldart, 1986). This indicates even at low u/u_{mf} in conical fluidized bed, i.e. at $2 u/u_{mf}$, the velocity of solid is comparatively higher compared to the cylindrical column.

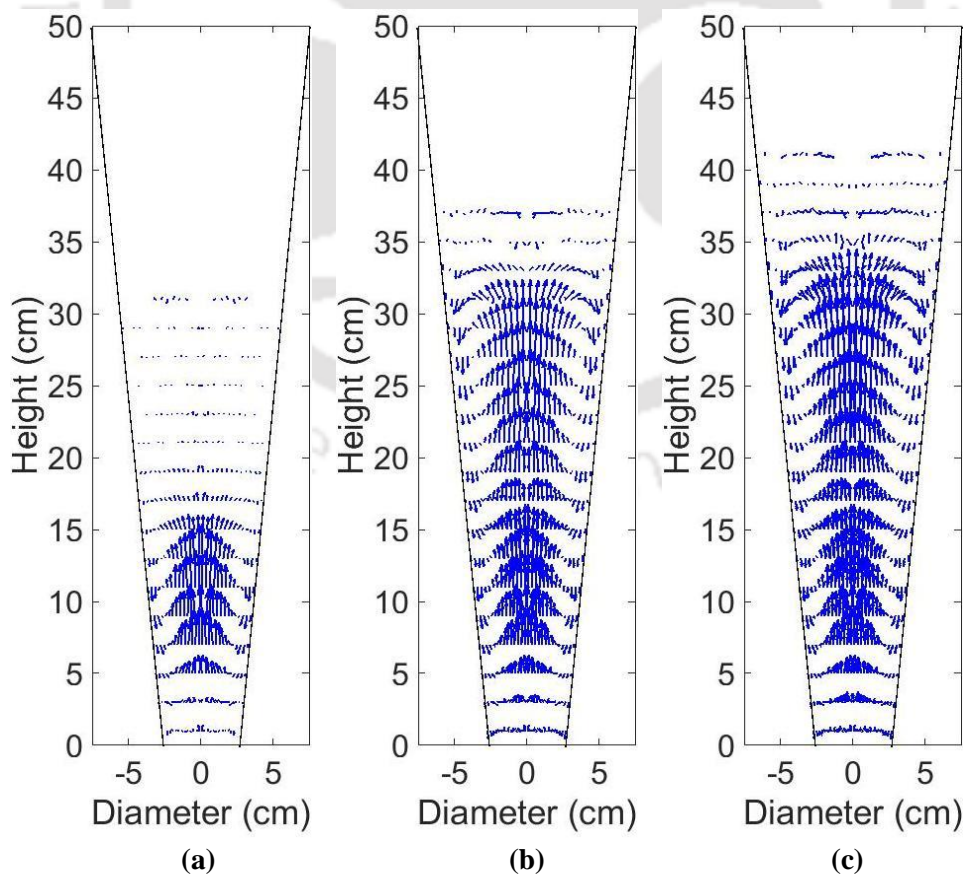


Figure 3.10 Mean axial velocity vectors of 1 mm solids at (a) 3.8, (b) 5.7, and (c) 7.6 m/s

Further, the magnitude of solid velocity was seen to increase with an increase in inlet velocity which is similar to the cylindrical one.

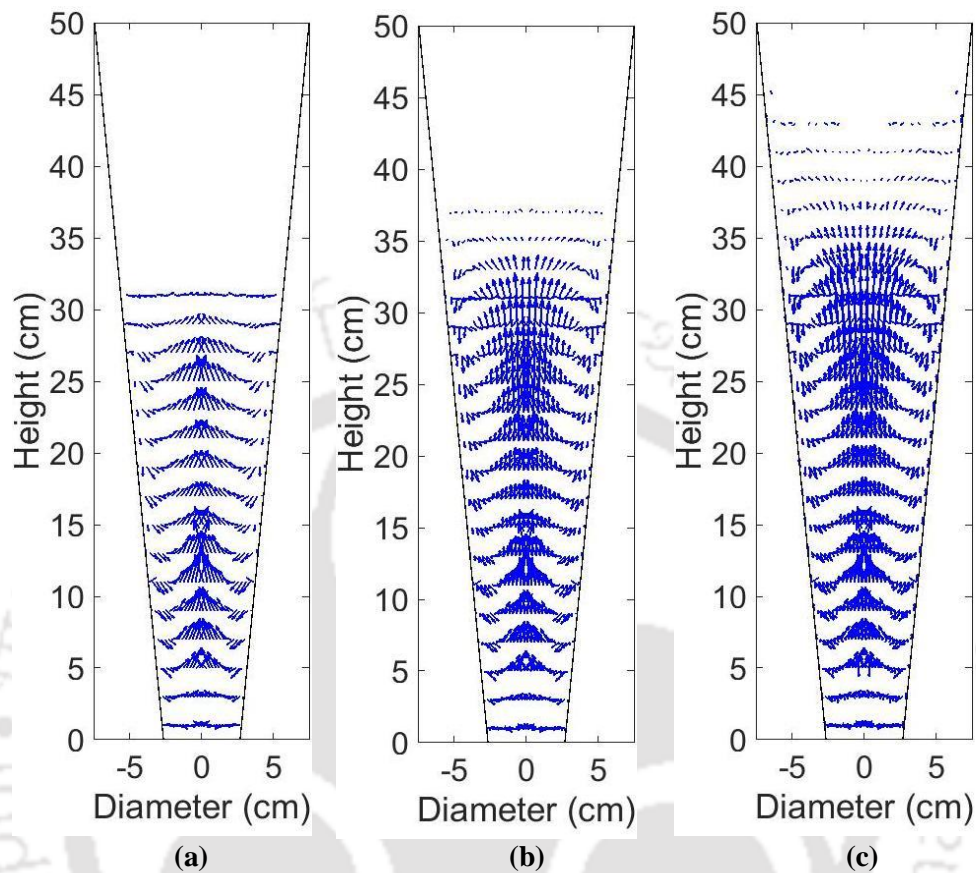


Figure 3.11 Mean axial velocity vectors of 0.6 mm solids at (a) 3.8, (b) 5.7, and (c) 7.6 m/s

3.5.2 Number of occurrences

In RPT, the experiment was performed for an extended period of time to calculate the statistically independent time-averaged quantities. Hence, the tracer particle visited the same location multiple times. This tracer particle occurrences information can also be used to get the time-averaged solid distribution profile. The cumulative tracer particle occurrences will be higher at those locations where the solid fraction is high. Figures 3.12a and 3.12b show respective contour map of occurrence of 1 mm and 0.6 mm solid at 7.6 m/s velocity. The trend of NOC plots for both particles remained similar. Solid fraction for both particles was increasing from bottom to the top of the bed. This is the

special feature of the conical fluidized bed where gas velocity is higher at the bottom of the column and reduces with the height due to the increase in bed diameter. Further, for all the height NOC was increasing steeply with radius from center to wall. This plot can only give an idea about the solid distribution qualitatively. However, quantitative analysis will give a better insight into the conical fluidized bed. Therefore, qualitative analysis of velocity and fluctuation was presented in the next section of this chapter.

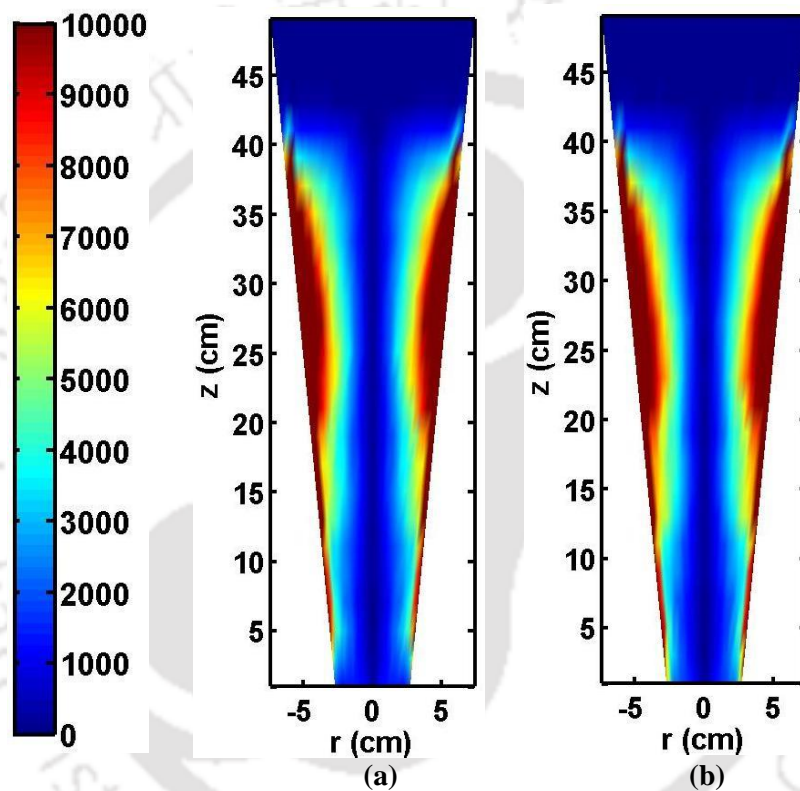


Figure 3.12 Contour map of occurrence of 1 mm and 0.6 mm solid at 7.6 m/s velocity

3.5.3 Ensemble averaged velocity

Figure 3.13 shows the mean axial solid velocity profiles in monodispersed bed as a function of air velocity. Figures 3.13a and 3.13b show the radial variation of the mean axial velocity of 1 mm and 0.6 mm solid with dimensionless radius for the top section, respectively. Similarly, Figure 3.13c and 3.13d show the plot of the mean axial solid velocity of 1 mm and 0.6 mm particle with dimensionless radius at the bottom section, respectively. The data has been obtained at $h/H = 0.75$ for the top section and at h/H

= 0.25 for the bottom section. The velocity profile in all operating condition showed that the particles are ascending in the center and descending near the wall. The vector plots also showed a similar profile. In fluidized bed, as the gas moves through the distributor, bubble formation takes place in the annulus. As the bubbles move upward, they move to center and coalesce and forms a bigger bubble. These bubble carry solids either in their wake or in emulsion phase till top and as the bubble break on top, the solids move downward to the bottom near the wall. Once these solids reach the bottom, the same phenomena repeat resulting in the mean circulation of solids. This is known as “gulf streaming” of solids. Similar ‘gulf effect’ observed in Bahramian and Mansour (2010). The figure shows the axial mean velocity of solid is higher on the top section for 5.7 and 7.6 m/s compared to the bottom section. This is because as the bubbles move upward coalescence takes place which results in faster motion of bubble with axial level. Thus the particles being carried up in the bubble wake tends to move faster near the top section. This contradicts the phenomena of the existence of velocity gradient in the conical fluidized bed. As it has been explained in the literature that the gas velocity in conical column decreases along height (Shi et al., 1984; Kwauk, 1992; Singh et al., 1992; Jones, 1994). Therefore, the solid velocity should also decrease along the height. This indicates that though the drag force on the solid decreases with height, the slip velocity between the gas and solid increases along the height. The reason behind this behavior is not clear at this point. Further, Webster and Perona (1988) explained that the downward flow near the wall decreases the cross-sectional area available for upward flow and increases the upward flow rate of the fluid. Therefore, the upward flow rate becomes larger on top than the flow rate entering the column.

At a fixed velocity of 3.8 m/s, the mean solid axial velocity of 1 mm was lower on top than bottom section also observed in vector plot. This may occur as the minimum velocity

of full fluidization for 1 mm particle is 3.4 m/s, which means that the bed was operated at $1.1 u/u_{mf}$. It satisfies the minimum fluidization condition, where all particles move though there is no significant mean axial velocity. The solid velocity profile for 0.6 mm particles which belongs to Geldart group B also shows the same ascending trend in the center and descending near the wall. It also shows an increase in solid velocity with an increase in operating velocity. However, the solid velocity for 0.6 mm particle is higher than 1 mm particle as u/u_{mf} of 0.6 mm is higher for a particular operating velocity. Further 0.6 mm does not show the low velocity of solid at 3.8 m/s on top as it is operated at more than u/u_{mf} .

The radial mean solid velocity of 1 mm and 0.6 mm particle is represented by Figure 3.14a and 3.14b on the top section of the column and the radial mean solid velocity of both solids is shown in Figures 3.14c and 3.14d at the bottom section, respectively. The figure indicates the radial components of mean solid velocities are too small compared to axial velocity irrespective of the particle size and velocity. No significant variation was observed for radial mean velocity in all cases. It implies that the motion of the particle is mainly in the axial direction. The positive radial velocity indicates outward motion of solid and negative velocity indicates inward motion of solids.

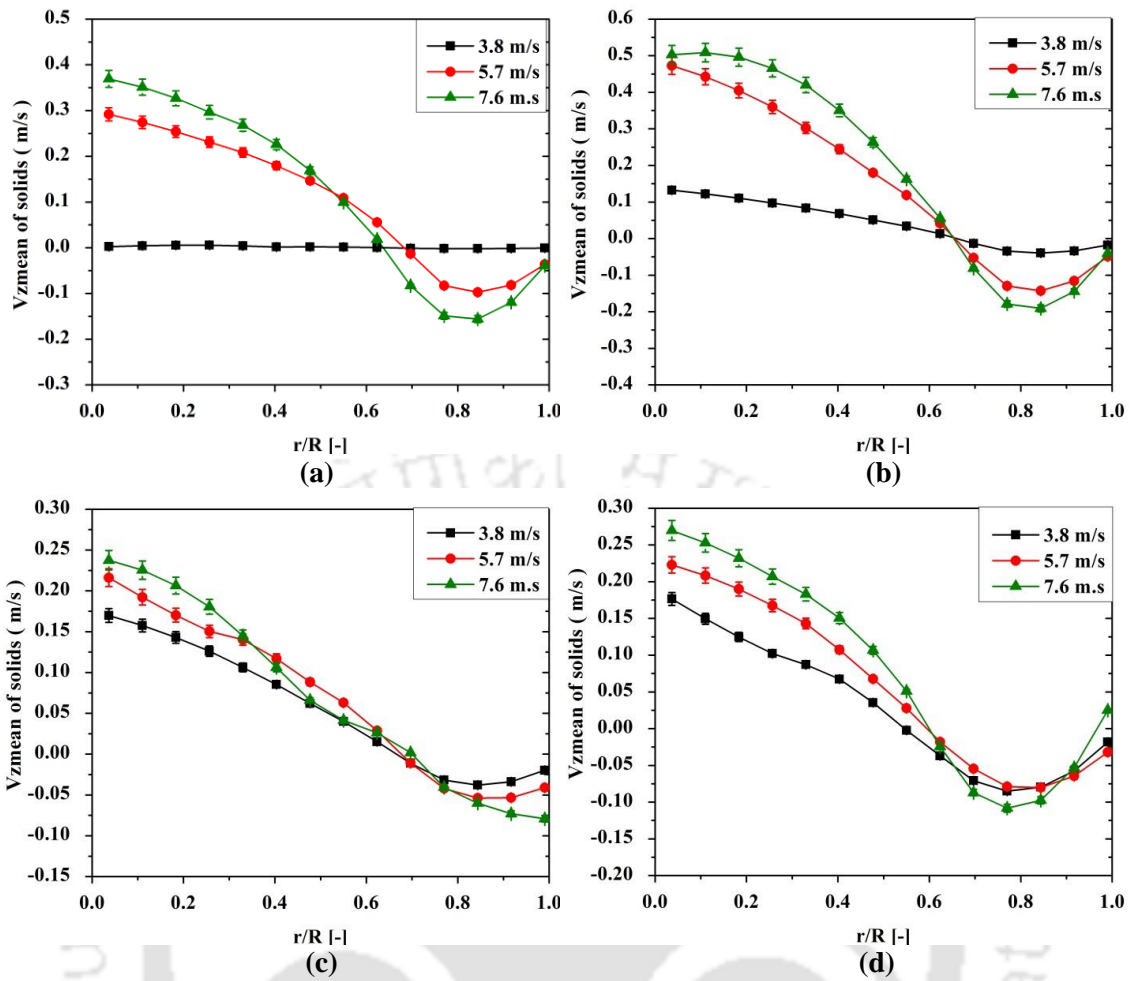


Figure 3.13 Variation of mean axial velocity of solid at different velocities: (a) 1 mm particle on top section, (b) 0.6 mm particle on top section, (c) 1 mm particle at bottom section, and (d) 0.6 mm particle at bottom section

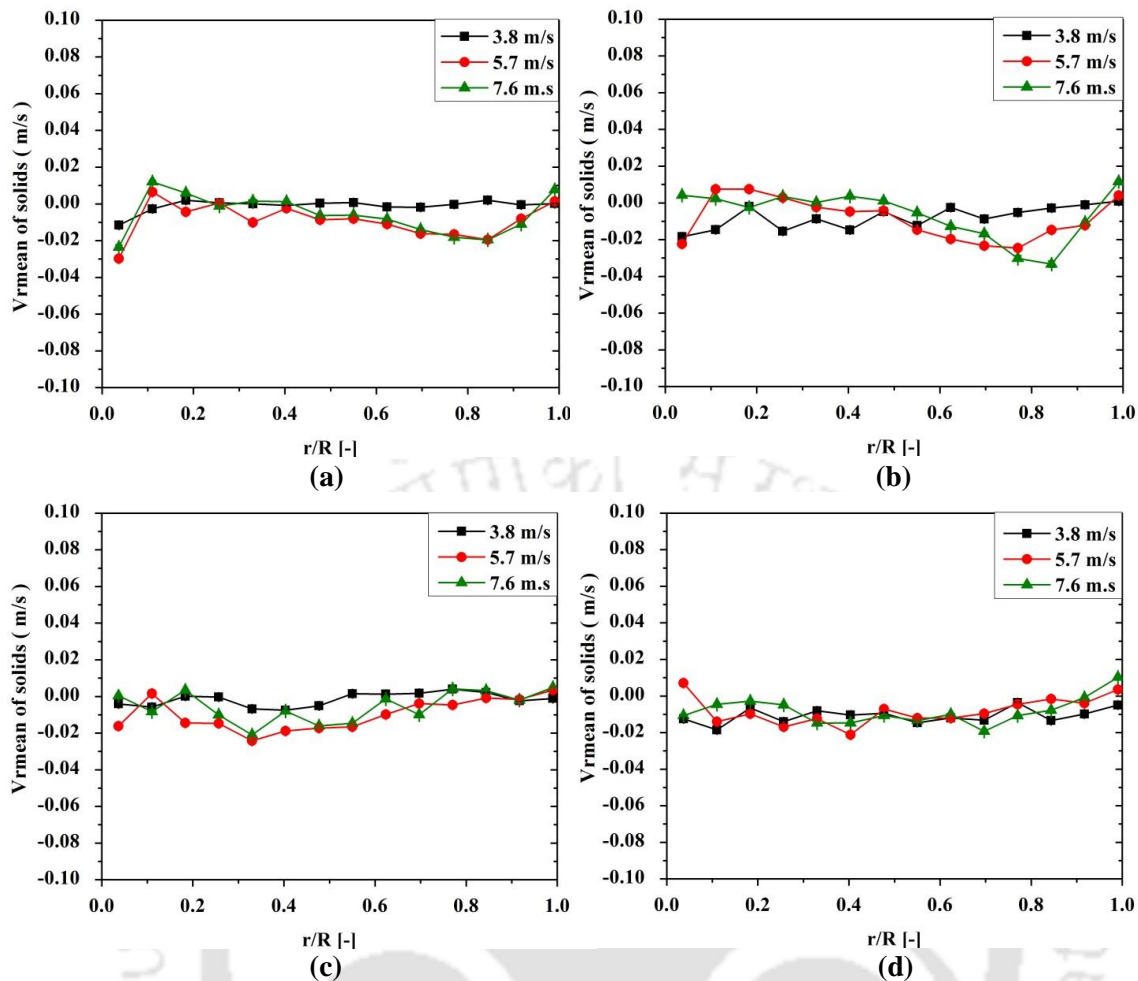


Figure 3.14 Variation of mean radial velocity of solid at different velocities: (a) 1 mm particle on top section, (b) 0.6 mm particle on top section, (c) 1 mm particle at bottom section, and (d) 0.6 mm particle at bottom section

3.5.4 Solid velocity fluctuations

The axial root-mean-square (RMS) velocity (second moment) was calculated by subtracting the mean Eulerian solid velocity from the instantaneous Eulerian solid velocity. Figures 3.15a and 3.15b are plot of mean RMS velocity of 1 mm and 0.6 mm particle at top sections respectively. It represents that there is fluctuation on the top section of the bed at a velocity of 3.8 m/s, confirming the solid movement on the bed surface. This assured the minimum fluidized bed condition at 3.8 m/s for 1 mm. Figures 3.15c and 3.15d represent the plot of mean axial RMS velocity of 1 mm and 0.6 mm

particles at bottom section. As the velocity was high at the center the mean motion of the particle was high and thus, the fluctuation was less in the center. However, the motion of solids near the wall constituted a downward moving packed bed, which reduced the mean free path for the particle and reduces the fluctuation. In addition, the lower gas velocity and higher particle–wall friction also reduced the RMS near the wall. The figure shows that fluctuation is decreasing with height, though solid mean velocity seems to increase with height. This behavior can be achieved as the mean motion of the particle was high and thus, the fluctuation was less in the bottom and vice-versa. Increase in fluctuating motion was observed with increasing velocity. This happens as the increase in velocity increases energy input and thus dissipates more energy by particle collision/fluctuation. The trend remained the same for 0.6 mm particle. The axial RMS of 0.6 mm shows a higher value than 1 mm due to high u/u_{mf} . The plots shown in Figure were obtained by azimuthally averaging the results.

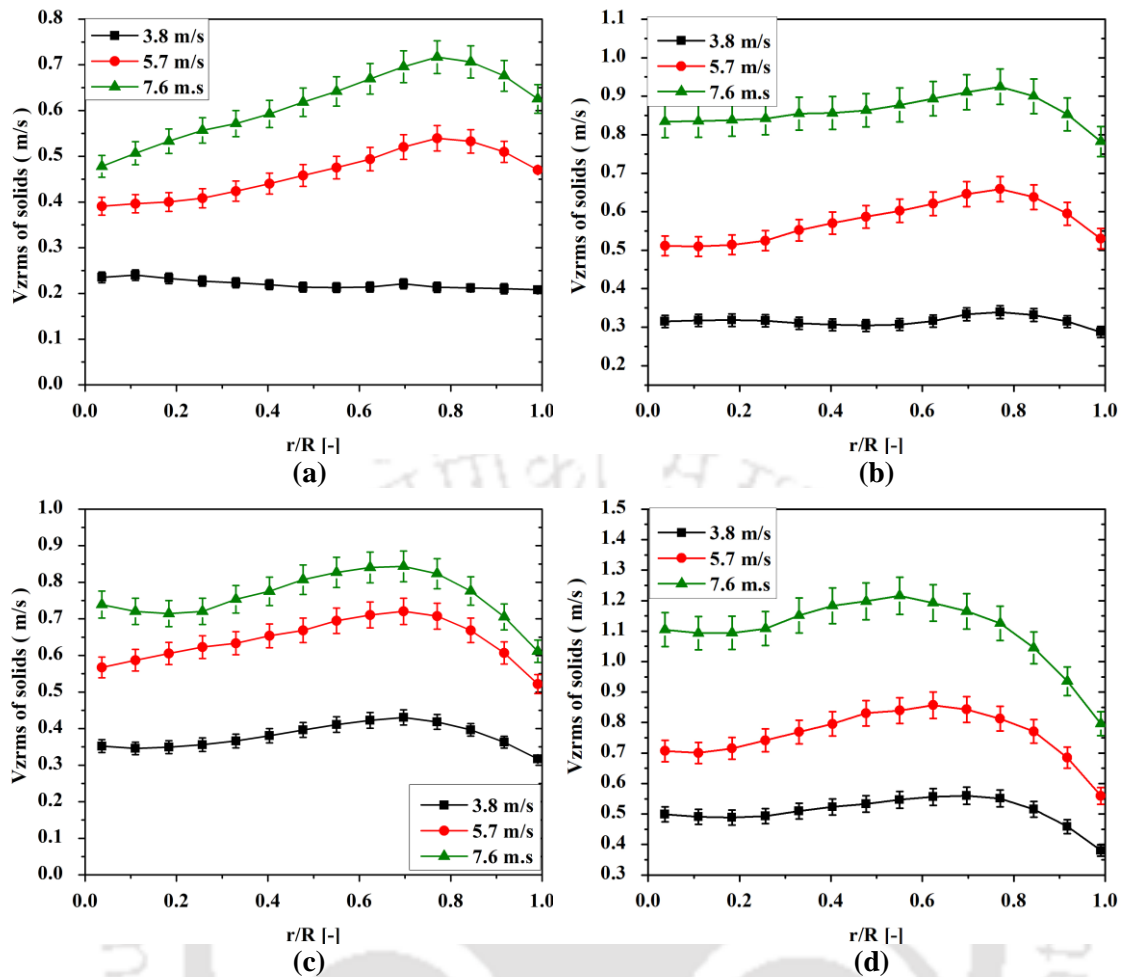


Figure 3.15 Variation of V_{zrms} of solid at different velocities: (a) 1 mm particle on top section, (b) 0.6 mm particle on top section, (c) 1 mm particle at bottom section, and (d) 0.6 mm particle at bottom section

Figures 3.16a and 3.16b give the variation of radial RMS of 1 mm and 0.6 mm solid at upper sections at various gas velocities whereas Figures 3.16c and 3.16d give the variation of radial RMS of 1 mm and 0.6 mm solid at lower sections. Radial RMS showed almost constant fluctuation in the center which decreased near wall due to restriction near the wall. The radial fluctuation showed an increase in value with an increase in velocity and decrease in value with an increase in height. The similar profile obtained for 0.6 mm particle with higher RMS value at a particular velocity. This happened as the u/u_{mf} ratio of the smaller particle is higher compared to the bigger particle for any particular

velocity. Radial RMS velocities were comparable to axial value, unlike radial mean velocities. However, the radial RMS velocities were less than half of the axial RMS velocity. The fluctuation was observed to be anisotropic in nature for both solids irrespective of the gas velocity.

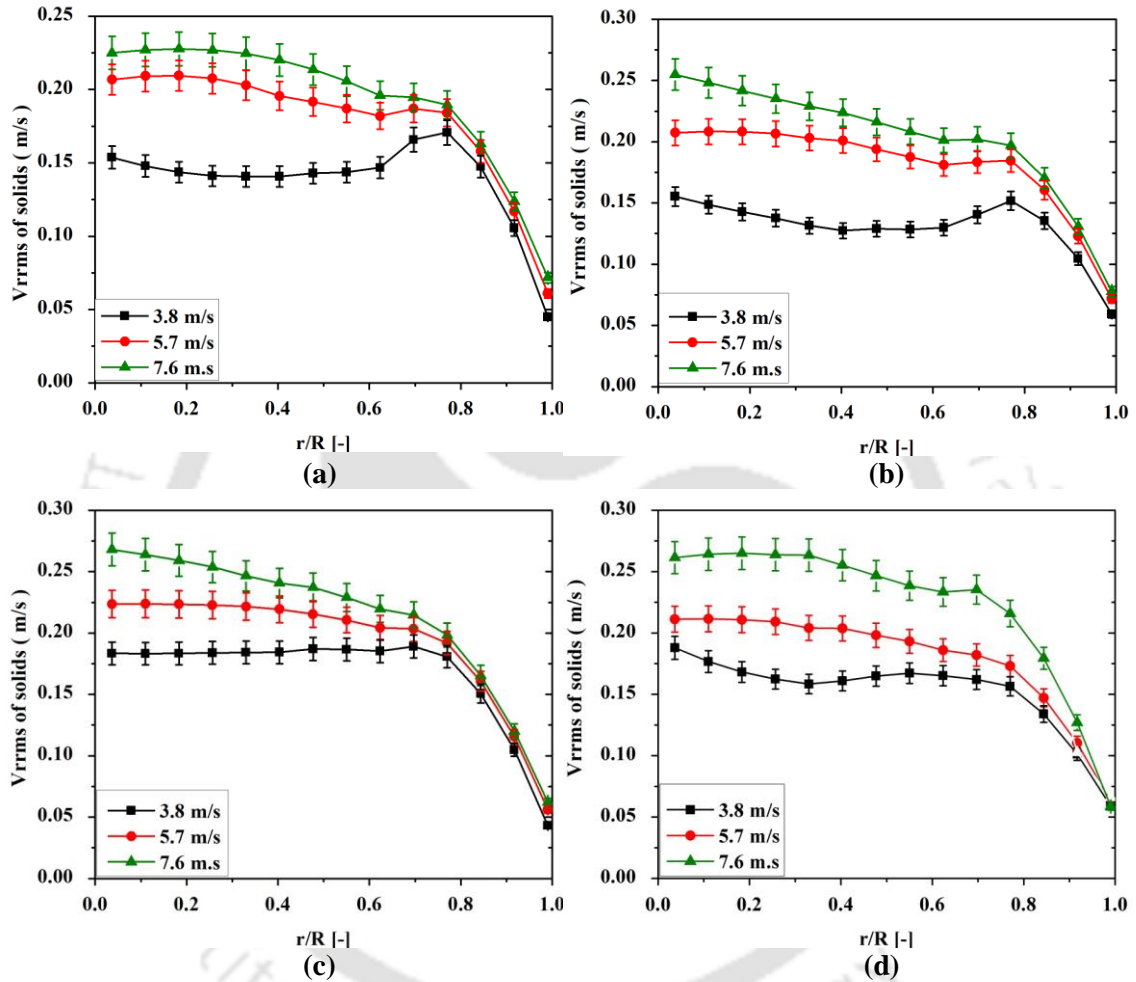


Figure 3.16 Variation of V_{rrms} of solid at different velocities: (a) 1 mm particle on top section, (b) 0.6 mm particle on top section, (c) 1 mm particle at bottom section, and (d) 0.6 mm particle at bottom section

3.5.5 Granular temperature

Granular temperature is the energy due to the fluctuation, as a result of turbulence in the fluidized bed. The granular temperature of 1 mm and 0.6 mm particle is illustrated in Figure 3.17. Figures 3.17a and 3.17c show the granular temperature trends for 1 mm solid

on top and the bottom sections, and Figures 3.17b and 3.17d show the granular temperature trends for 0.6 mm solid on top and bottom sections. The figures show that granular temperature has a similar trend as axial RMS velocity. Results indicate that granular temperature was higher at the bottom than the top section for a particular air velocity. This happens due to the low solid fraction at the bottom that tends to increase mean free path which increases the oscillation of particles contributing to a higher granular temperature at the bottom. The granular temperature value was reduced near wall due to the restriction of solid motion.

The granular temperature seems to increase with an increase in gas inlet velocity. This was expected as the increase in gas inlet velocity increases the energy input to the system. Hence, resulting in an increase in the granular temperature. The granular temperature of 0.6 mm was higher compared to 1 mm solids as 0.6 mm solids were operated at higher u/u_{mf} .

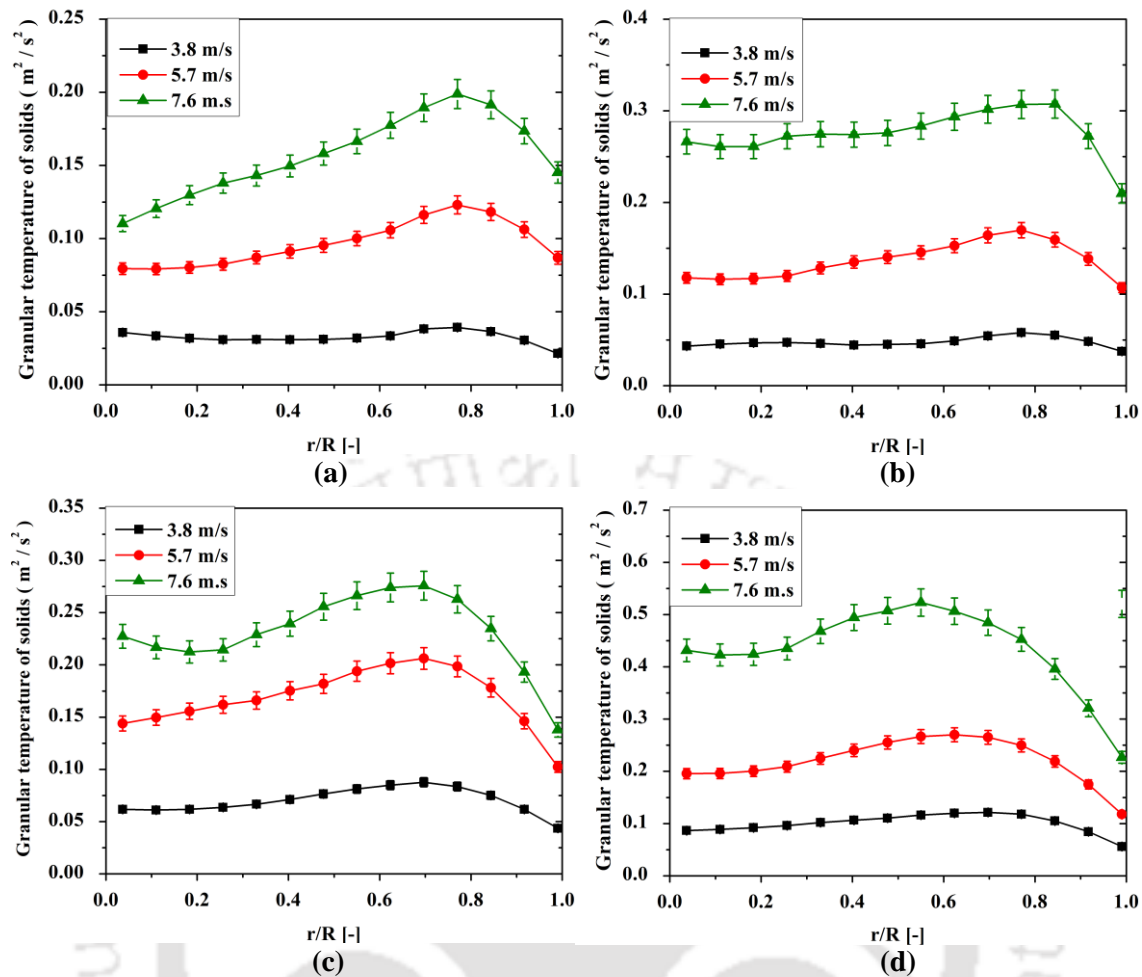


Figure 3.17 Variation of granular temperature of solid at different velocities: (a) 1 mm particle on top section, (b) 0.6 mm particle on top section, (c) 1 mm particle at bottom section, and (d) 0.6 mm particle at bottom section

3.5.6 Hurst exponent

Hurst exponent values were calculated through R/S analysis of Lagrangian particle velocity of the solids. Figures 3.18a and 3.18b show a typical pox diagram obtained through R/S analysis for 1 mm and 0.6 mm particles, respectively in a mono bed at 7.6 m/s gas inlet velocity. For both solids the Hurst exponent value for lower time lag, where the periodicity affects less, were found to be around 0.9. This indicates that the solid motion in the gas-solid conical fluidized bed is ‘persistent’ as the solid motion largely depends on gas velocity for both solids. Table 3.3 shows the Hurst exponent value for

mono bed for both solids at all the operating velocities. It clearly indicates that Hurst exponent value for both solids was higher than 0.5 for all velocities which mean solids motion is ‘persistent’ in-case-of gas-solid conical fluidized bed and for all the velocity it largely depends on gas/bubble motion. It should be noted that Hurst exponent value reported here is for entire column and not for any particular section.

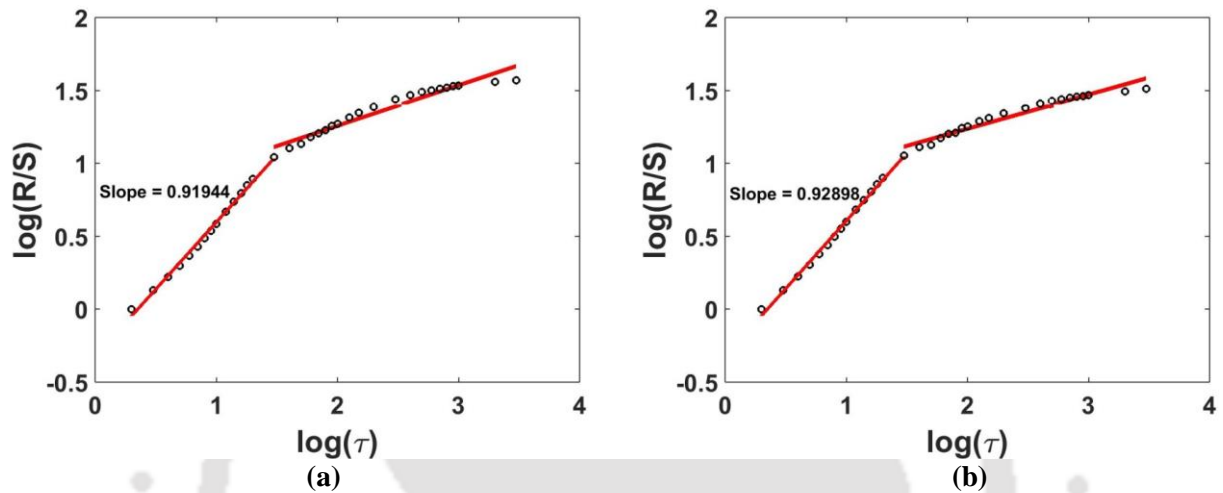


Figure 3.18 Hurst exponent at 7.6 m/s gas velocity for (a) 1 mm solid, and (b) 0.6 mm solid

Table 3.3 Hurst exponents at different operating conditions for 1 mm and 0.6 mm particle in mono bed

Gas velocity	Bed composition	Hurst exponent
3.8 m/s	Mono 1 mm	0.59
5.7 m/s	Mono 1 mm	0.89
7.6 m/s	Mono 1 mm	0.91
3.8 m/s	Mono 0.6 mm	0.8
5.7 m/s	Mono 0.6 mm	0.9
7.6 m/s	Mono 0.6 mm	0.92

3.5.7 Autocorrelation

Autocorrelation function represents the self-correlation with time. The axial autocorrelation is represented by Figure 3.19. Figures 3.19a, 3.19b, and 3.19c represent the axial autocorrelation function of 1 mm solids at 3.8, 5.7 and 7.6 m/s gas inlet velocity in monodispersed bed. Figures 3.19d, 3.19e, and 3.19f represent the axial autocorrelation function of 0.6 mm solids at 3.8, 5.7 and 7.6 m/s gas inlet velocity in monodispersed bed. Results show that for both particles axial autocorrelation coefficient decay very fast. A typical axial autocorrelation plot (shown in Figure 3.19) first decay to zero and then dips to below zero to a negative value and thereafter oscillate for a long time before it finally settles down to a stationary value of zero. The oscillation increases with an increase in gas inlet velocity. Such type of profile was observed mainly due to the gross circulation of the particle as solids were in batch and their motion was bounded between the lower wall and top boundary of the bed. With an increase in gas inlet velocity the rate of circulation increases due to the the increase in solid velocity. Further, with an increase in gas inlet velocity rate of formation and coalescence of the bubbles also increases which produces periodic signals and results in terms of oscillation in axial autocorrelation value with increasing velocity. Figure 3.20 displays the radial autocorrelation with increasing inlet velocity for both solids. The radial autocorrelation trends for both solids remain same. However, as the motion was primarily in axial direction the radial autocorrelation decay at a much faster rate for all the velocities compared to axial autocorrelation coefficient.

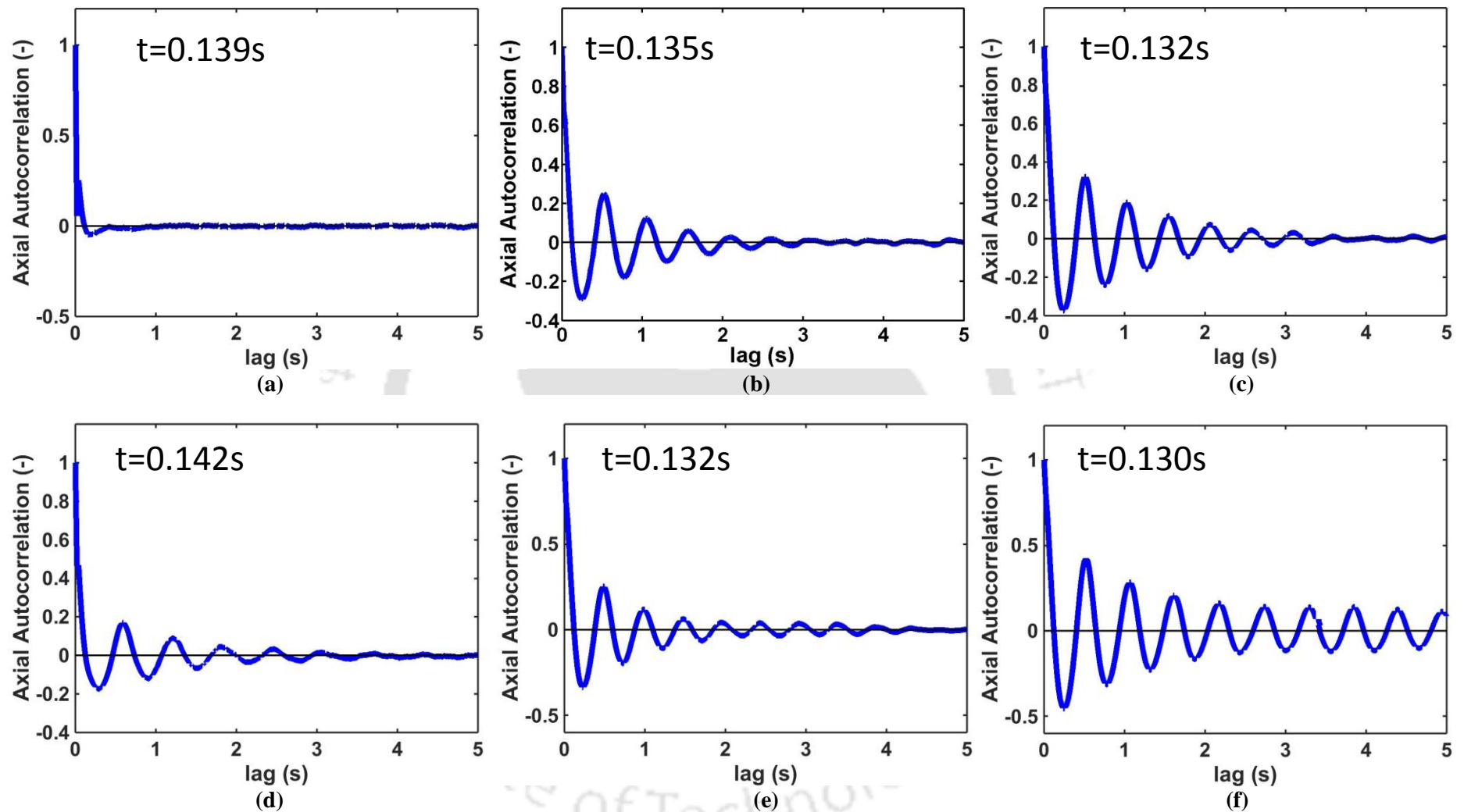


Figure 3.19 Variation of axial autocorrelation of solid at different velocities: (a) 1 mm particle at 3.8 m/s, (b) 1 mm particle at 5.7 m/s, (c) 1 mm particle at 7.6 m/s, (d) 0.6 mm particle at 3.8 m/s, (e) 0.6 mm particle at 5.7 m/s, and (f) 0.6 mm particle at 7.6 m/s

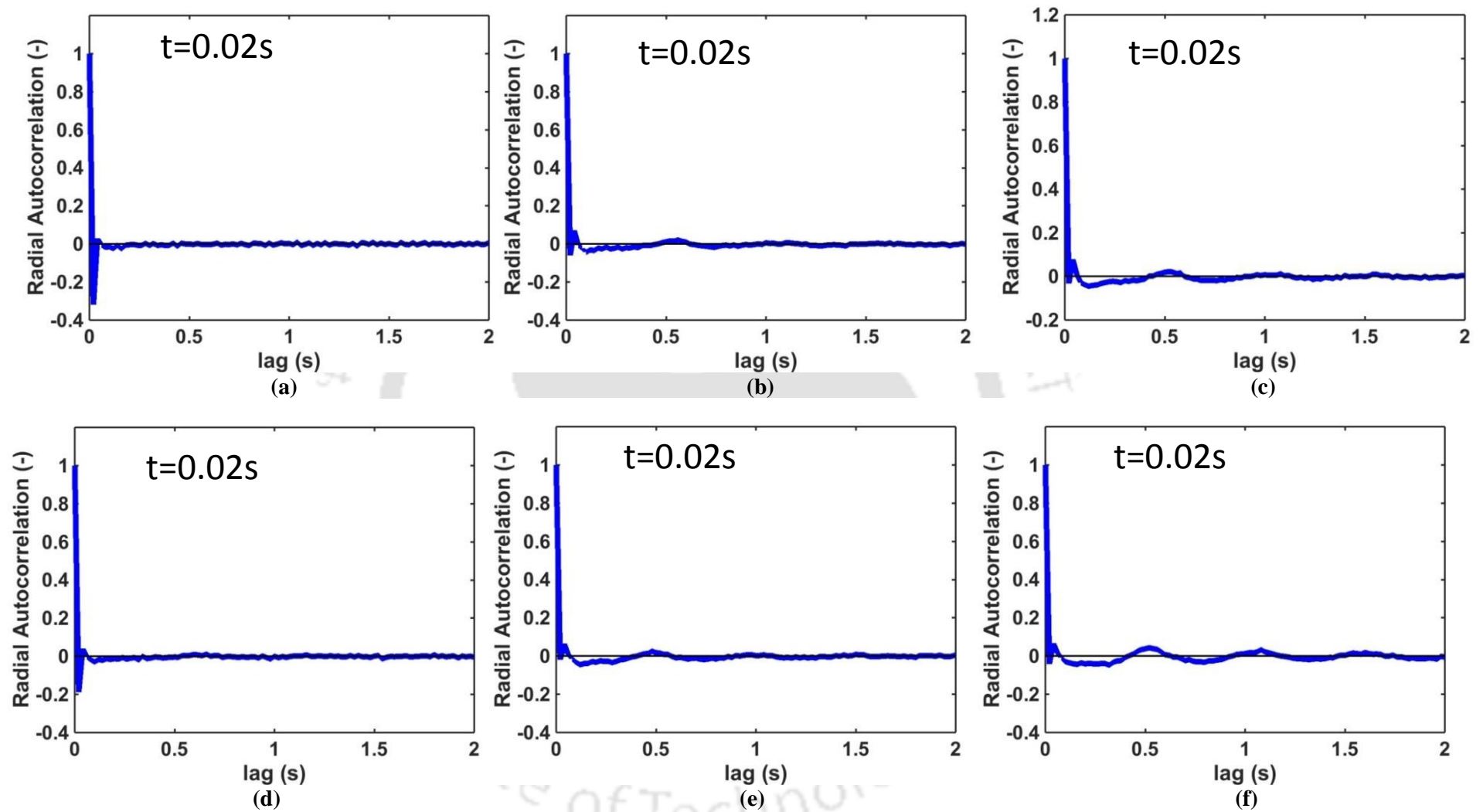


Figure 3.20 Variation of radial autocorrelation of solid at different velocities: (a) 1 mm particle at 3.8 m/s, (b) 1 mm particle at 5.7 m/s, (c) 1 mm particle at 7.6 m/s, (d) 0.6 mm particle at 3.8 m/s, (e) 0.6 mm particle at 5.7 m/s, and (f) 0.6 mm particle at 7.6

3.5.8 Kolmogorov entropy

Figure 3.21 shows the influence of the gas velocity on the Kolmogorov entropy (KE) for both solids. KE has been calculated from the track of the 1 mm (big) and 0.6 mm (small) tracers. KE indicates chaotic behavior for all the experimental conditions examined. Differences in chaotic behavior were marked at low gas velocities for both the solids which reduce when the u/u_{mf} ratio is high. The fluidized bed of 0.6 mm particles showed a higher degree of chaotic behavior than the mono 1 mm bed, likely because the 0.6 mm bed is operated at a higher u/u_{mf} ratio compared to the 1 mm bed. KE shows an increasing trend and reaches highest value at low velocity (i.e at 5.7 m/s) as the bed is more violent due to smaller gas bubbles. Above this velocity the change in KE value is very low. This change in the slope indicates towards the change in flow regime.

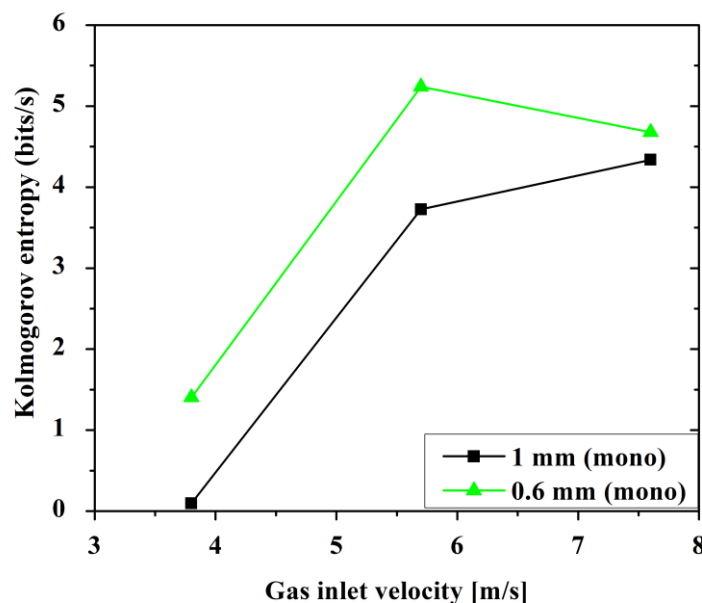


Figure 3.21 Kolmogorov entropy of 1 mm and 0.6 mm particle with gas inlet velocity

3.5.9 Correlation dimension

Figure 3.22 shows the correlation dimension of 1 mm and 0.6 mm particles with gas inlet velocity. CD values for both solids increased initially with gas inlet velocity and decreased thereafter for both solids. This confirms the regime transition for both solids

after 5.7 m/s gas inlet velocity. Initially, as bubble formation starts CD value increases with velocity as the bed is less complex, therefore, less number of variables needed to describe the system. At higher velocity (5.7 m/s) the fluctuation increases hence more number of variables are required to define the system. Further, with increase in velocity the CD value decreases. This indicates change in the flow mechanism/regime transition.

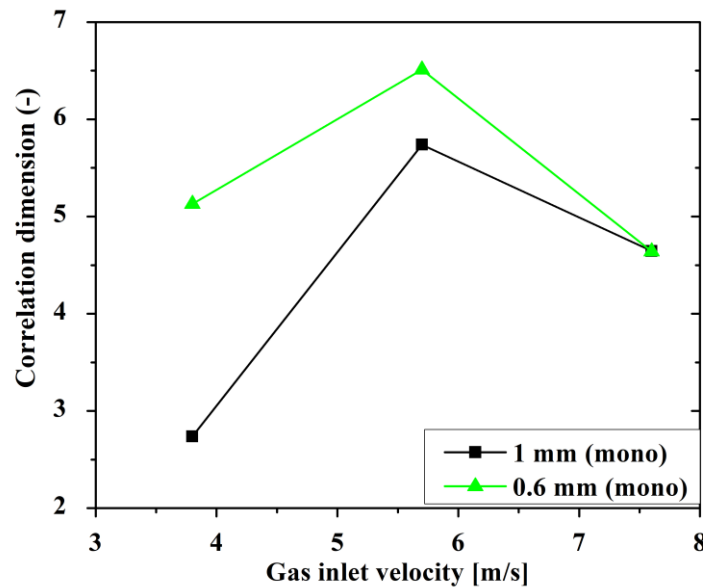


Figure 3.22 Correlation dimension of 1 mm and 0.6 mm particle with gas inlet velocity

3.6 Effect of gas velocity on mono and binary dispersed beds

Experiments were performed for 50b-50s (50% 1 mm and 50% 0.6 mm particle mixture by mass) binary bed. The bed was operated at 3.8, 5.7 and 7.6 m/s, respectively, for both mono and binary beds to understand the effect of velocity and composition of the flow characteristic of the conical fluidized bed. It is to be noted that in the binary fluidized bed, the motion of both particles was tracked individually.

3.6.1 Ensemble averaged velocity

Figures 3.23a, b, and c represent the axial solid velocity on the top section of bed while Figures 3.23d, e, and f represent the solid velocity at the bottom section for three different gas inlet velocities. The mean axial velocity of the binary bed was bounded between the

two mono dispersed beds of 0.6 mm and 1 mm particles at the top section for all the gas velocities. The velocity of 0.6 mm mono dispersed bed was maximum and velocity of 1 mm mono dispersed bed was minimum. In binary bed, mean axial velocity of 1 mm particle was higher and velocity of 0.6 mm particle was lower compared to their mono dispersed bed. This shows that particle-particle interaction plays an important role in binary gas-solid conical fluidized bed. Smaller particles transferred some of their momenta to the bigger particles in the binary bed through particle-particle interaction. The difference between the mean axial solid velocities of two mono dispersed beds was reduced with the increase in gas inlet velocity. This was mainly due to enhanced gas-solid interaction with increased gas velocity. The similar phenomenon was observed in binary bed where both solids tried to equalize their axial velocity with the increase in gas inlet velocity. Therefore, it can be concluded that particle-particle interactions are more dominating for lower gas velocity. At higher gas velocity both particle-particle and gas-particle interactions are critical. Figures 3.23d, e, and f show the mean axial velocity of solid particles at the bottom section of the column for monodispersed and binary bed. It was observed that velocities of both 1 mm and 0.6 mm solids were same at the bottom section for both monodispersed and binary fluidized bed. This clearly indicates that at high gas velocity, fluid-particle interaction becomes dominating. As the diameter of the column was lower at the bottom section, the gas velocity was higher which resulted in higher fluid-particle interaction. However, near the wall, (where gas velocity is low) the downward velocity of the smaller particle in monodispersed bed was considerably high for all velocities.

Further, it was observed from Figure 3.23a that velocity of the solid particle at the top section is almost zero for 1 mm mono dispersed bed operated at 3.8 m/s gas inlet velocity. However, for the binary bed noticeably high velocity of 1 mm solids was observed. This

was mainly due to momentum exchange between the two solids (1 mm and 0.6 mm) via particle-particle interactions. It was also interesting to note that for lower gas inlet velocity (3.8 m/s), solids velocity in both monodispersed and binary beds is lower at the top section and higher near the bottom section of the column. This was due to the higher solid fraction at the top section of the column compared to the bottom section (shown in Figure 3.13). However, with the increase in gas inlet velocity, solid velocities for both beds (mono and binary dispersed beds of both solids) were higher at the top section compared to the bottom section of the column. This indicates the occurrences of the large bubbles (due to bubble coalescence) at the top section of the column for higher gas inlet velocity. With these results, it can be clearly stated that the dynamics of the gas-solid conical bed are very complex. The governing physics and underline phenomena take place at various length and time scales and strongly depend on the operating condition. Therefore, a detailed analysis is needed to understand the behavior of the bed.

Figure 3.24 is the plot of the mean radial velocity of 1 mm and 0.6 mm particles in monodispersed and binary dispersed beds of 50b-50s composition. The magnitude of radial solid velocity was negligible at low velocity and the behavior remains similar even at a higher velocity. There was no variation observed in the solid velocity in the radial direction on top as well as on the bottom. The mean radial velocity trend and value remained same irrespective of the bed composition.

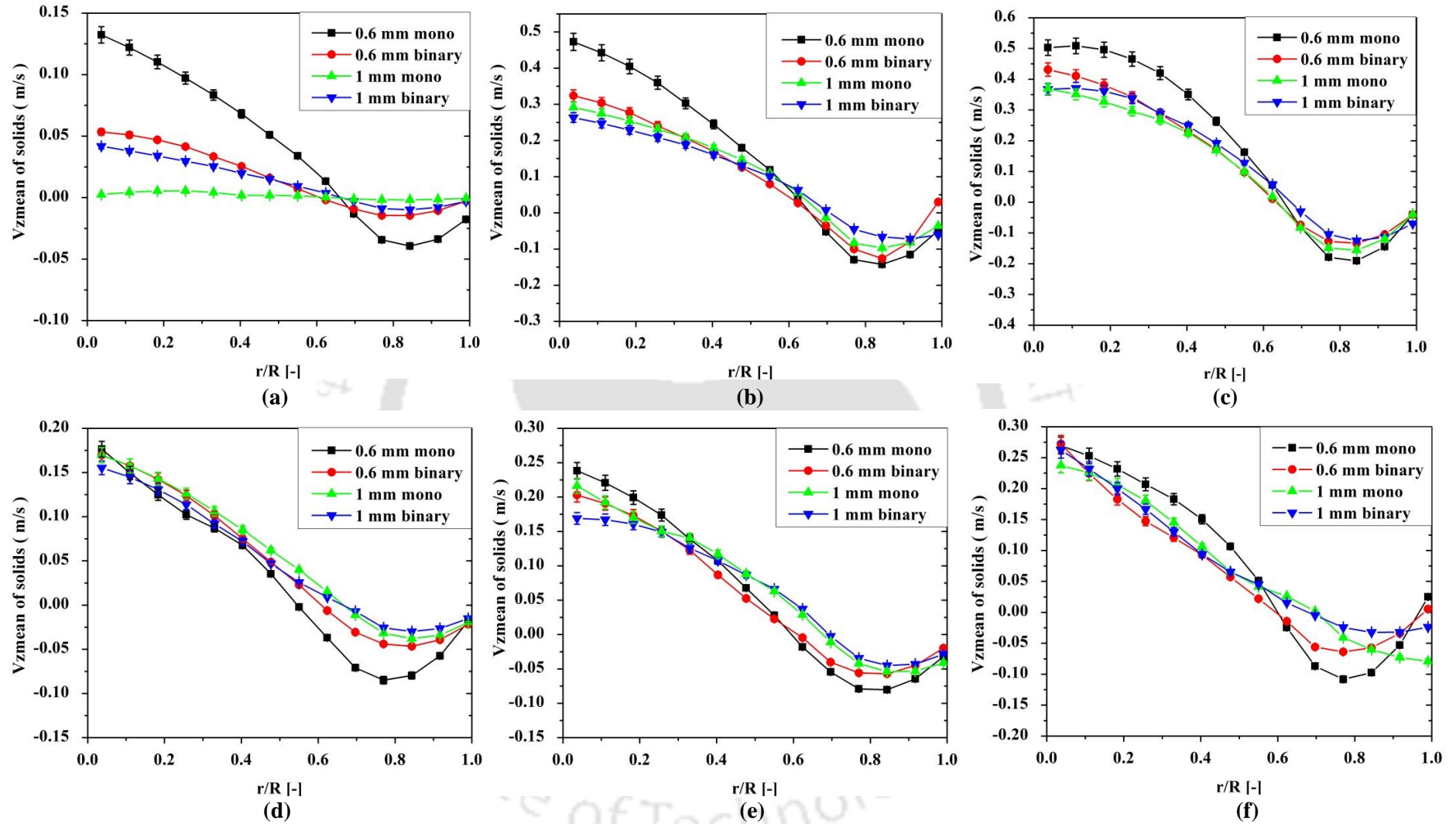


Figure 3.23 Variation of mean axial velocity of solid at different velocities with composition: (a) top section at 3.8 m/s, (b) top section at 5.7 m/s, (c) top section at 7.6 m/s, (d) bottom section at 3.8 m/s, (e) bottom section at 5.7 m/s, and (f) bottom section at 7.6 m/s

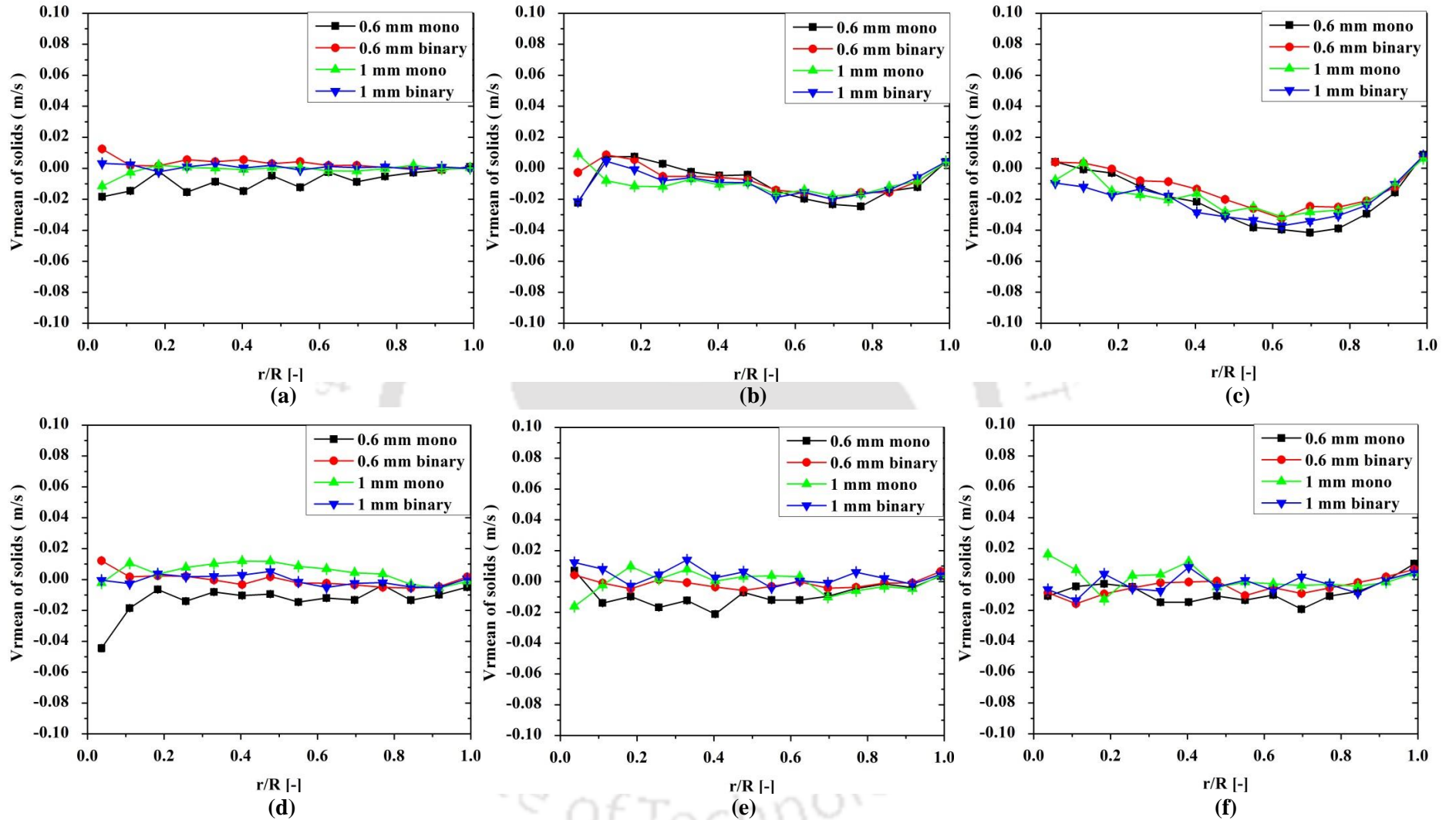


Figure 3.24 Variation of mean radial velocity of solid at different velocities with composition: (a) top section at 3.8 m/s, (b) top section at 5.7 m/s, (c) top section at 7.6 m/s, (d) bottom section at 3.8 m/s, (e) bottom section at 5.7 m/s, and (f) bottom section at 7.6 m/s

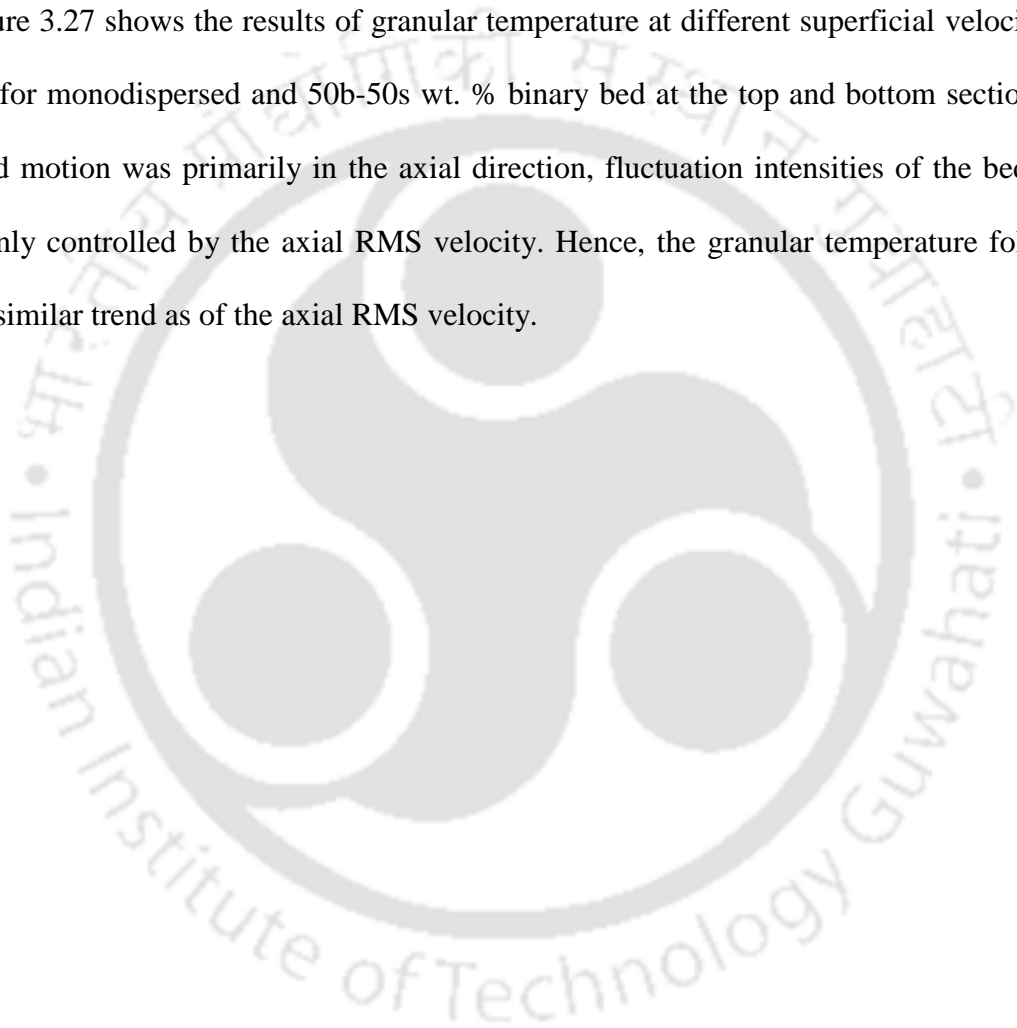
3.6.2 Solid velocity fluctuations

The axial root mean square (RMS) velocity of the solids is illustrated in Figure 3.25 for monodispersed and binary beds at 3.8, 5.7 and 7.6 m/s gas inlet velocity. RMS velocities of both solids were higher at the bottom section of the column compared to the top section for all velocities. This was contrary to the mean axial velocity trend where solid velocity was higher at the top section (other than 3.8 m/s velocity). For both monodispersed and binary beds, the solid fraction was lower at the bottom section of the column (shown in Figure 3.13). Hence, a higher mean free path was available to solids at the bottom section compared to the top section, which resulted in higher fluctuation. Further, RMS velocities for both solids were increasing with an increase in gas inlet velocity at both the sections. This showed that bed becomes more violent at higher velocity due to higher gas phase turbulence. However, for all cases axial RMS velocity of 0.6 mm mono dispersed bed was higher. It was observed that in binary bed, RMS velocity of 0.6 mm particle was always higher than the 1 mm particle. At bottom section for (3.8, 5.7 m/s gas inlet velocity) RMS velocities of solids in binary bed remained close to the RMS velocities of their respective mono dispersed beds. However, at the top section, RMS velocities of solids were bounded between the monodispersed beds of the same solids. Hence, at lower gas inlet velocity fluid-solid interaction was critical near the bottom section and solid-solid interaction was dominating at the top section. At higher velocity (7.6 m/s), the trend of the solids RMS velocity remained same both for the top and bottom sections of the column. The solid RMS velocity was bounded between the values of the monodispersed beds of the same solids. The observation pointed to a change in the interaction mechanism at a higher gas velocity which may be due to a change in the flow regime. Figure 3.26 shows the mean radial RMS velocity for various operating conditions and different mixtures. Figure 3.26a -3.26c represents the radial RMS velocity

on the top section of bed while Figure 3.26d -3.26f represents the bottom section results. The trend of binary bed is equal as the monodispersed bed on top section. However, only for low velocity at the bottom, it is same as the mono bed. Further, the radial RMS also becomes high at higher inlet velocity due to increase in input energy as other parameters.

3.6.3 Granular Temperature

Figure 3.27 shows the results of granular temperature at different superficial velocities of gas for monodispersed and 50b-50s wt. % binary bed at the top and bottom sections. As solid motion was primarily in the axial direction, fluctuation intensities of the bed were mainly controlled by the axial RMS velocity. Hence, the granular temperature followed the similar trend as of the axial RMS velocity.



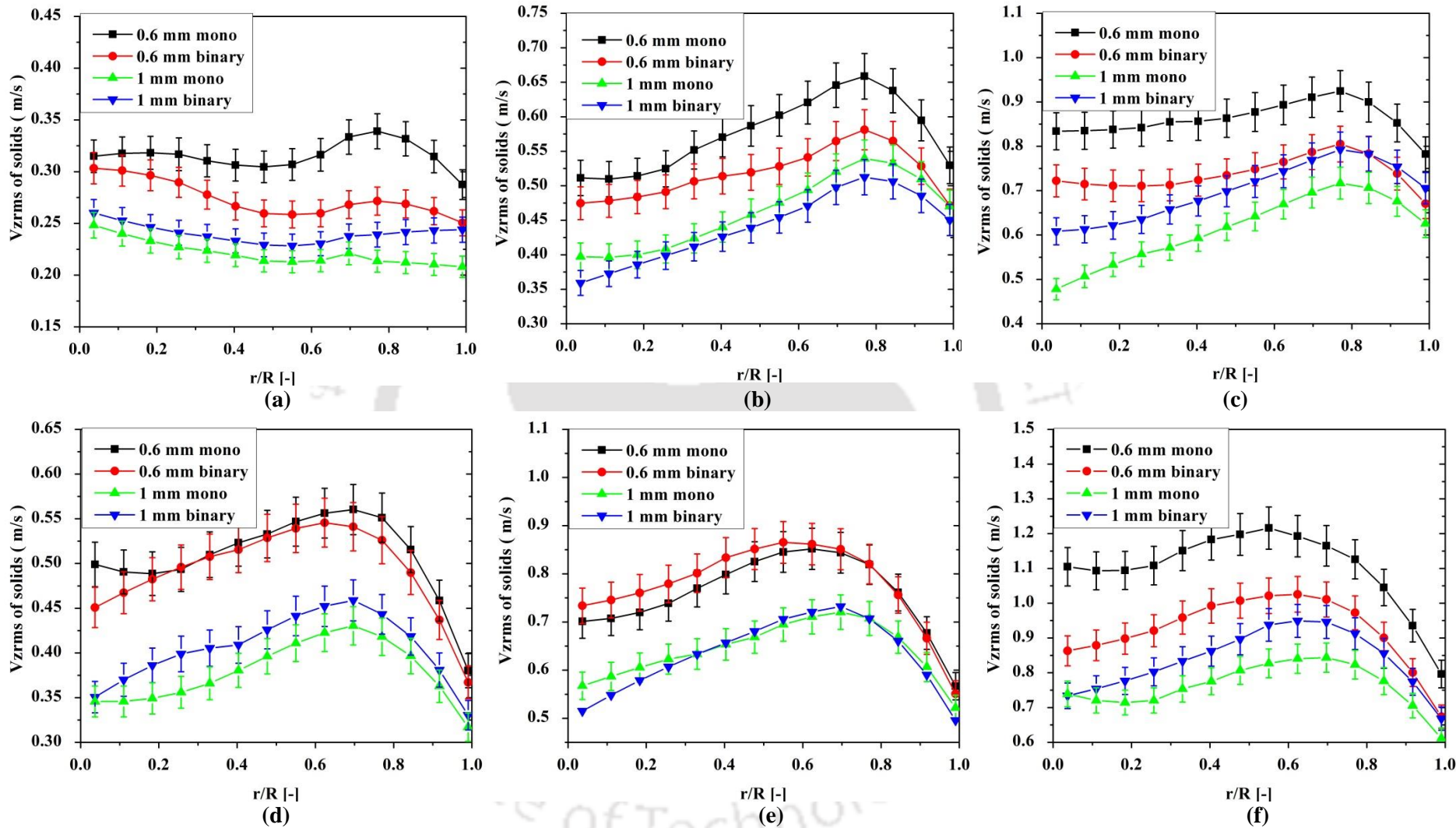


Figure 3.25 Variation of V_{zrms} of solid at different velocities with composition: (a) top section at 3.8 m/s, (b) top section at 5.7 m/s, (c) top section at 7.6 m/s, (d) bottom section at 3.8 m/s, (e) bottom section at 5.7 m/s, and (f) bottom section at 7.6 m/s

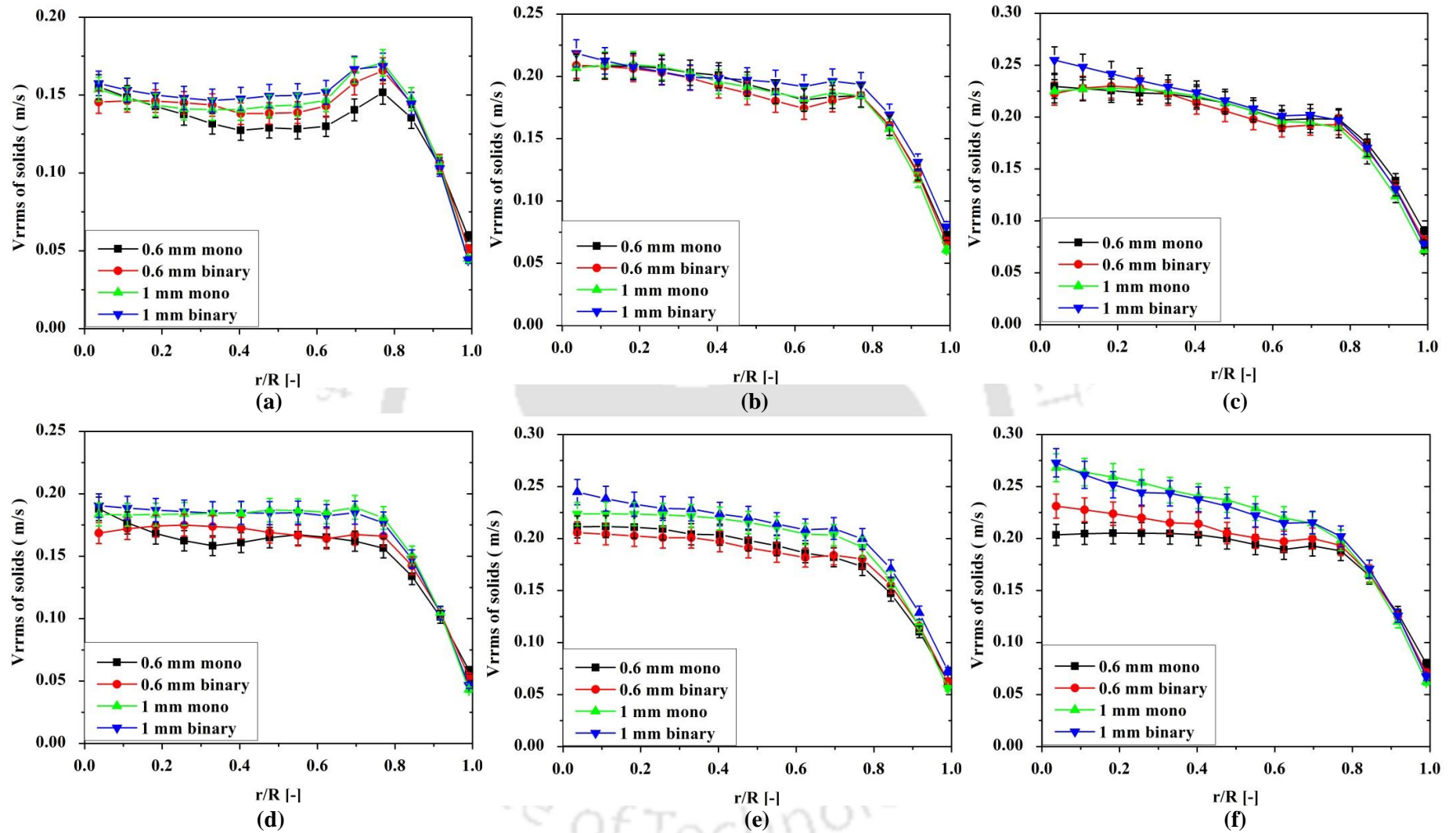


Figure 3.26 Variation of V_{rms} of solid at different velocities with composition: (a) top section at 3.8 m/s, (b) top section at 5.7 m/s, (c) top section at 7.6 m/s, (d) bottom section at 3.8 m/s, (e) bottom section at 5.7 m/s, and (f) bottom section at 7.6 m/s

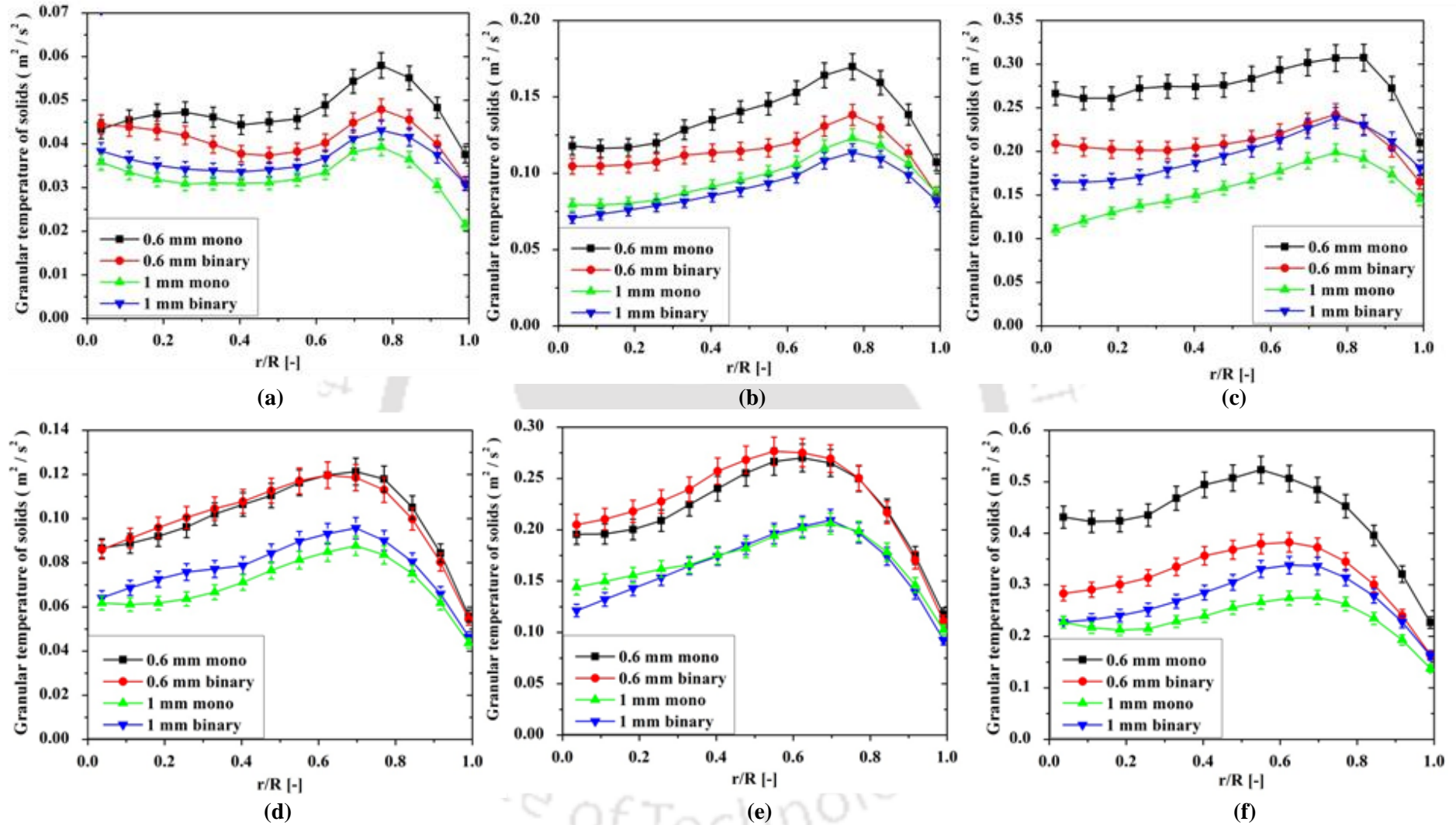


Figure 3.27 Variation of granular temperature of solid at different velocities with composition: (a) top section at 3.8 m/s, (b) top section at 5.7 m/s, (c) top section at 7.6 m/s, (d) bottom section at 3.8 m/s, (e) bottom section at 5.7 m/s, and (f) bottom section at 7.6 m/s

3.6.4 Hurst Exponent

Table 3.4 shows the Hurst exponent value for binary bed for both the solids at all the operating velocities. It clearly indicates that Hurst exponent value for both solids are higher than 0.5 for all velocities which means solids motion is 'persistent' in-case-of gas-solids conical fluidized bed and for all velocities, it largely depends on gas/bubble motion. Figure 3.28 shows the change in Hurst exponent values for both solids in the binary conical fluidized bed with gas inlet velocity. The change in slope around gas inlet velocity of 5.7 m/s indicates a change in flow regime.

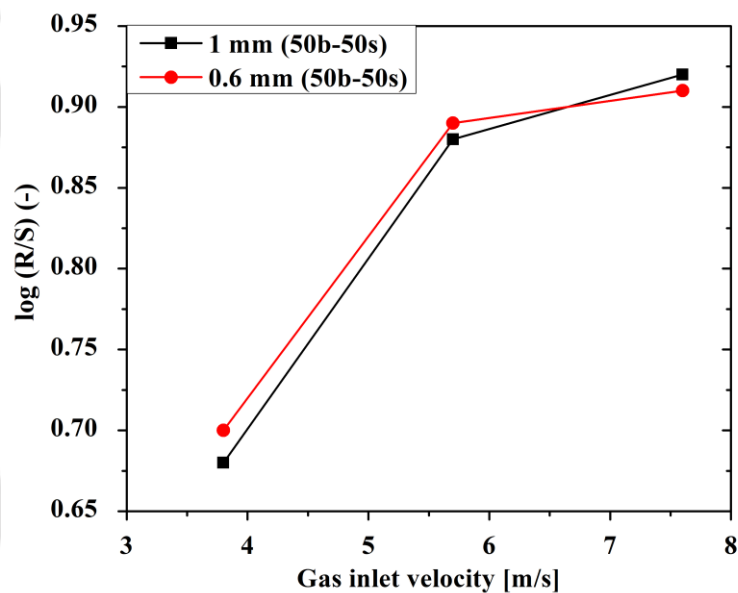


Figure 3.28 Hurst exponent versus gas inlet velocity

Table 3.4 Hurst exponents at different operating conditions for 1 mm and 0.6 mm particle in 50b-50s bed

Gas velocity	Bed composition	Hurst exponent
3.8 m/s	50b-50s 1 mm	0.68
5.7 m/s	50b-50s 1 mm	0.88
7.6 m/s	50b-50s 1 mm	0.92
3.8 m/s	50b-50s 0.6 mm	0.70
5.7 m/s	50b-50s 0.6 mm	0.89
7.6 m/s	50b-50s 0.6 mm	0.91

3.6.5 Autocorrelation

The axial autocorrelation is represented by Figure 3.29. Figures 3.29a, 3.29b, and 3.29c represent the axial autocorrelation function of 1 mm solids at 3.8, 5.7 and 7.6 m/s gas inlet velocity in 50b-50s binary bed. Figure 3.29d, 3.29e, and 3.29f represent the axial autocorrelation function of 0.6 mm solids at 3.8, 5.7 and 7.6 m/s gas inlet velocity in 50b-50s binary bed. Results show that for both particles, axial autocorrelation coefficient decay very fast. A typical axial autocorrelation plot (shown in Figure 3.29) first decay to zero and then dips to below zero to a negative value and thereafter oscillate for a long time before it finally settles down to a stationary value of zero. An increase in oscillation was observed with an increase in gas inlet velocity. Such type of profile was observed mainly due to the gross circulation of the particle as solids were in batch and their motion was bounded between the lower wall and top boundary of the bed. With the increase in gas inlet velocity the rate of circulation increases due to the increase in solid velocity. Further, the rate of formation and death of the bubbles also increases with an increase in gas inlet velocity. These phenomena produce periodic signals and resulted in terms of

oscillation in axial autocorrelation value. Figure 3.30 displays the radial autocorrelation with increasing inlet velocity for both solids. The radial autocorrelation trend for both solids remains similar. However, as the motion is primarily in axial direction the radial autocorrelation decay at a much faster rate for all velocities compared to axial autocorrelation coefficient as the motion was primarily in the axial direction.



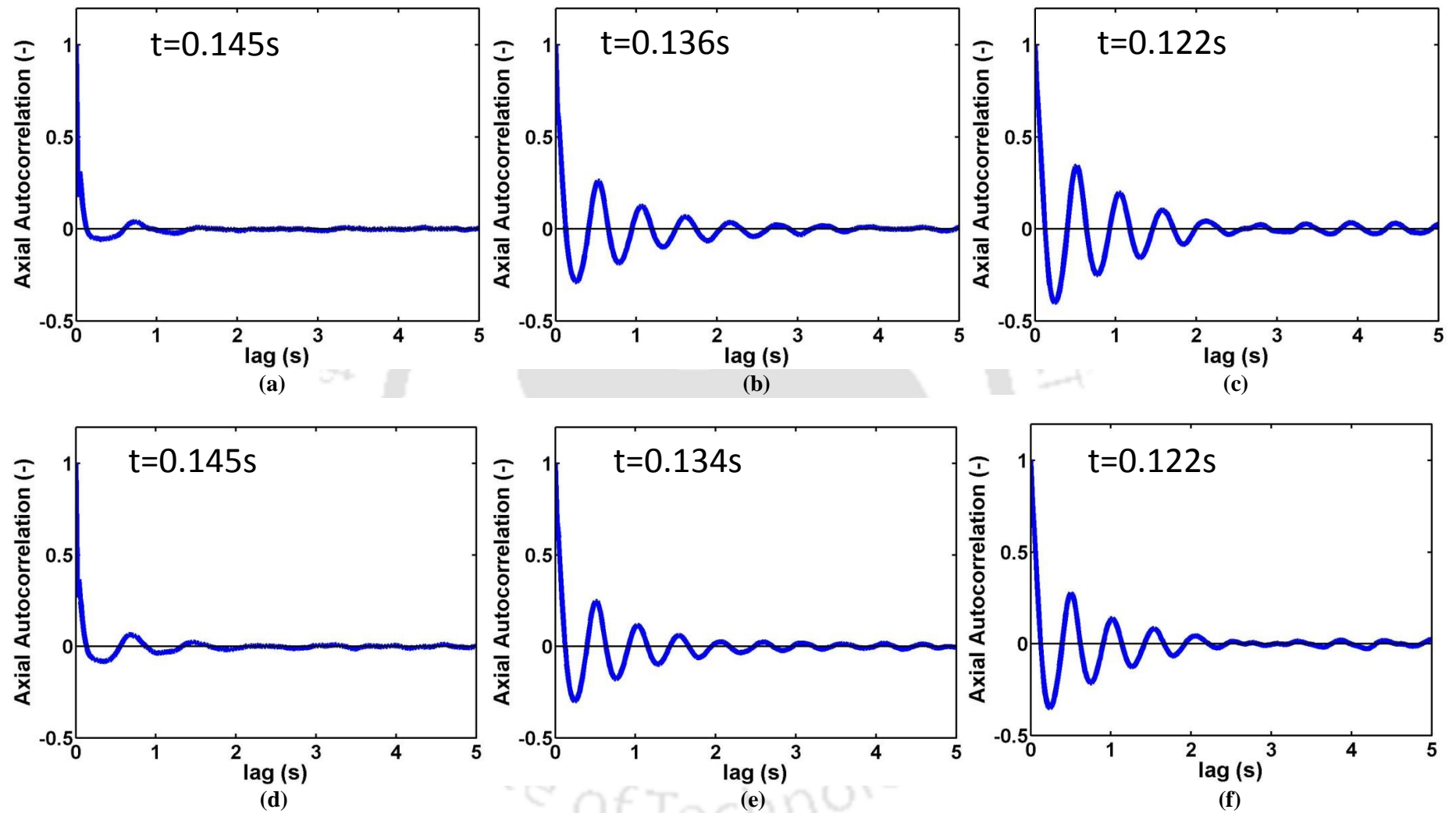


Figure 3.29 Variation of axial autocorrelation of solid at different velocities in binary bed (a) 1 mm particle at 3.8 m/s, (b) 1 mm particle at 5.7 m/s, (c) 1 mm particle at 7.6 m/s, (d) 0.6 mm particle at 3.8 m/s, (e) 0.6 mm particle at 5.7 m/s, and (f) 0.6 mm particle at 7.6 m/s

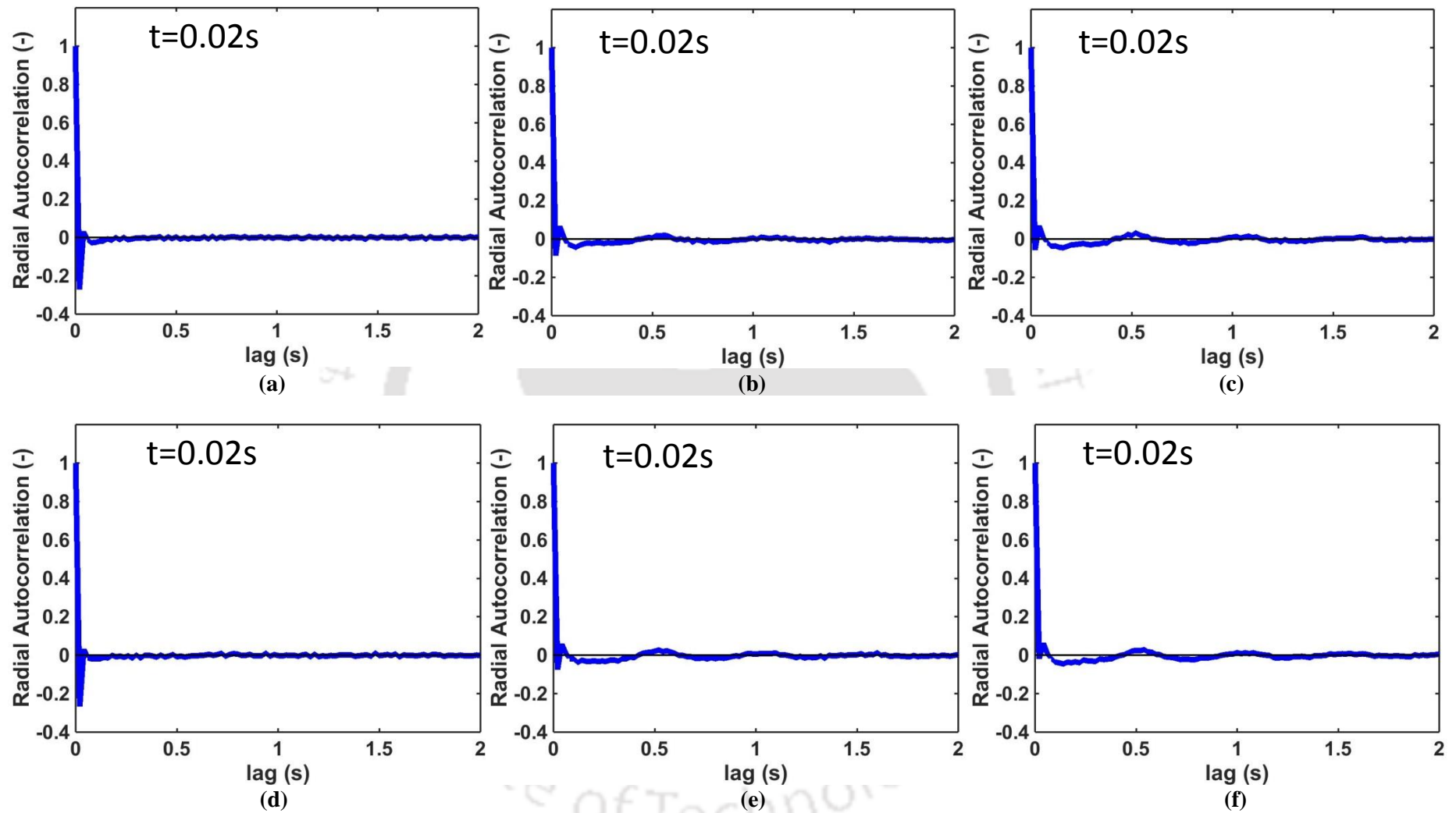


Figure 3.30 Variation of radial autocorrelation of solid at different velocities in binary bed (a) 1 mm particle at 3.8 m/s, (b) 1 mm particle at 5.7 m/s, (c) 1 mm particle at 7.6 m/s, (d) 0.6 mm particle at 3.8 m/s, (e) 0.6 mm particle at 5.7 m/s, and (f) 0.6 mm particle at 7.6 m/s

3.6.6 Segregation index

Further, segregation index values were calculated for both particles for all velocities. To calculate the segregation index, bed was divided into two parts (lower and upper). The probability of occurrences of both solids in each section is calculated. If the solids are perfectly mixed then the segregation index value will be 1 while for completely segregated value the segregation index value will be -1. For the binary bed of 50b-50s composition, segregation index for both solids at the top and bottom sections was found to be more than 0.97. However, Upadhyay (2010) and, Wu and Baeyens (1998) reported the partially segregated bed at a velocity lower than the $2u_{mf}$ of the bigger particle in the cylindrical fluidized bed. Further, van Wachem (2001) reported a value of 0.9 when the bed was operated at $2.7u_{mf}$ of the bigger particle in the cylindrical fluidized bed. Hence, solids were well mixed in a conical fluidized-bed even at a lower gas inlet velocity compared to the cylindrical fluidized bed. Figure 3.31 shows the change in segregation index value with the gas inlet velocity. The change in slope was observed at a velocity above 5.7 m/s. The slope change can be an indication of a regime transition around 5.7 m/s gas inlet velocity, which was also observed with RMS and granular temperature profiles.

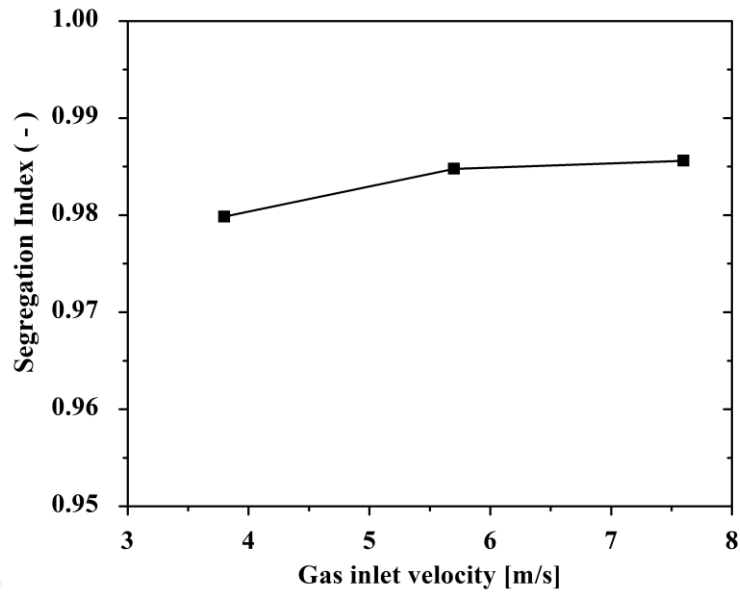


Figure 3.31 Variation of Segregation index of solid with gas inlet velocity for binary dispersed bed

3.6.7 Kolmogorov entropy

The effect of the gas velocity on the Kolmogorov entropy (KE) is depicted in Figure 3.32 for both binary 50b:50s wt. % and mono beds of both solids. Positive values of KE found for both solids indicated the chaotic behavior of the bed for all compositions and velocities. A sharp increase in the degree of chaotic behavior was observed for both solids between gas inlet velocity 3.8 and 5.7 m/s. Thereafter KE value was almost unchanged. This change in slope suggests a different flow regime for velocities above 5.7 m/s. Further, it was observed that KE values for the binary bed were bounded between the monodispersed beds of both solids. For all the velocity KE value of 0.6 mm mono dispersed bed was higher. This confirms that 0.6 mm mono bed was more chaotic and the introduction of the bigger particle changes the dynamics of the bed due to increased particle-particle interactions.

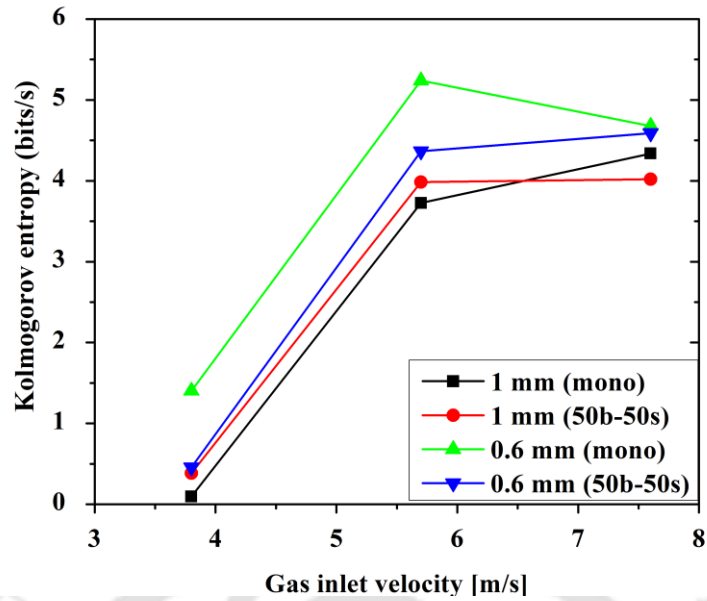


Figure 3.32 Kolmogorov entropy of 1 mm and 0.6 mm particle with gas inlet velocity

3.6.8 Correlation dimension

Figure 3.33 shows the effect of the gas velocity on the correlation dimension (CD), calculated from the position track of the 1 mm and 0.6 mm tracer particle. Initially, an increase in CD value was observed with increase in gas inlet velocity for all the bed compositions. However, beyond 5.7 m/s gas inlet velocity decrease in CD value was observed for both particles. This also supports the existence of a regime transition for both solids around 5.7 m/s gas inlet velocity for all the bed compositions. These results also specify that flow regime transition mainly depends on gas inlet velocity and not on the composition of the bed.

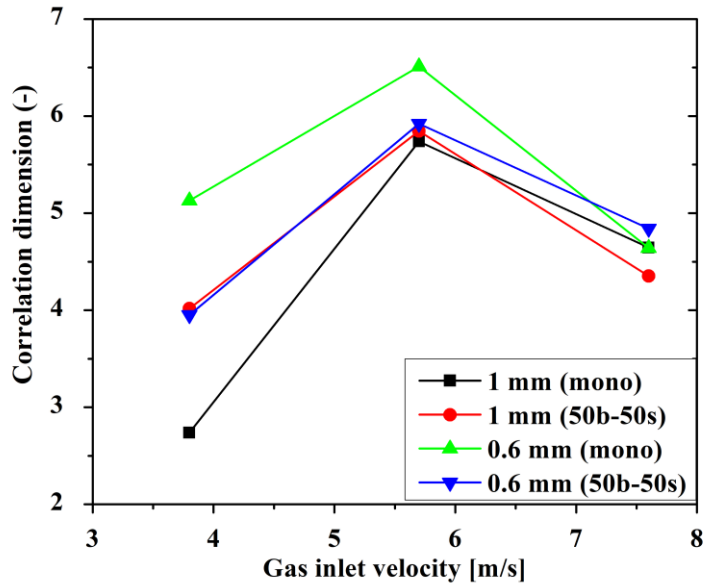


Figure 3.33 Correlation dimension of 1 mm and 0.6 mm particle with gas inlet velocity

3.7 Effect of bed composition

To decipher the effect of bed composition on the behavior of gas-solid conical fluidized bed experiments are performed for various bed composition of solids, i.e. 100:0, 75:25, 50:50 and 25:75 ratios of both solids. The composition of the bed in 50b-50s mixture is 50% bigger particle and 50% smaller particle by weight. Similarly, the 75b-25s mixture contains 75% of bigger particle and 25% of smaller particle and 25b-75s mixture contains 25% of bigger particle and 75% of the smaller particle. The monodispersed bed is 100% bigger particle for 1 mm solid and 100% smaller particle for 0.6 mm solid. The bed is operated at a constant velocity of 7.6 m/s for all cases to determine the composition effect on the bed behavior. At a time only one radioactive particle was used in the experiment. Hence, the motion of both solids is tracked individually (one by one) for each experiment for 8 hours.

3.7.1 Ensemble averaged velocity

The mean axial solid velocity has been plotted for a various composition of binary dispersed and monodispersed beds. Figures 3.34a and 3.34b show the comparisons of mean axial solid velocity plot for mono, 50b-50s, 75b-25s and 25b-75s composition on the top section. Similarly, Figures 3.34c and 3.34d show the comparisons of mean axial solid velocity plot for mono, 50b-50s, 75b-25s and 25b-75s composition at bottom section. At the top section of column 1 mm mono dispersed bed has the lowest axial solid velocity which keeps on increasing with the addition of 0.6 mm solids into the mixture. This indicates that bigger particle gains momentum from the smaller particle and improves its velocity with an increase in smaller particle fraction in the bed. In contrast, the 0.6 mm mono dispersed bed has the highest axial solid velocity which keeps on decreasing with the addition of 1 mm solids into the mixture on the top section. It indicates that in the case of binary dispersed bed particle-particle interaction plays a major role. However, the effect is not significant in the bottom section. The gas-solid interaction plays a vital role in the bottom section of the bed due to the high gas velocity. Therefore, it can be concluded that the fraction of individual solid in any mixture can affect the local velocity and hence, void fraction. Together, this can change the bed dynamics. This can make a huge change at the industrial level which needs to be considered and resolved.

Figure 3.35 presents the variation of mean radial solid velocity for all the compositions. Results do not show any variation with the addition of 1 mm particle to the bed of 0.6 mm particle or vice versa. Figures 3.35a and 3.35b represent the radial solid velocity on the top section of bed while Figures 3.35c and 3.35d represent the velocity at the bottom section of the column. The radial mean solid velocity is negligible compared to mean

axial solid velocity which indicates for all the composition motion of solids were primarily in the axial direction.

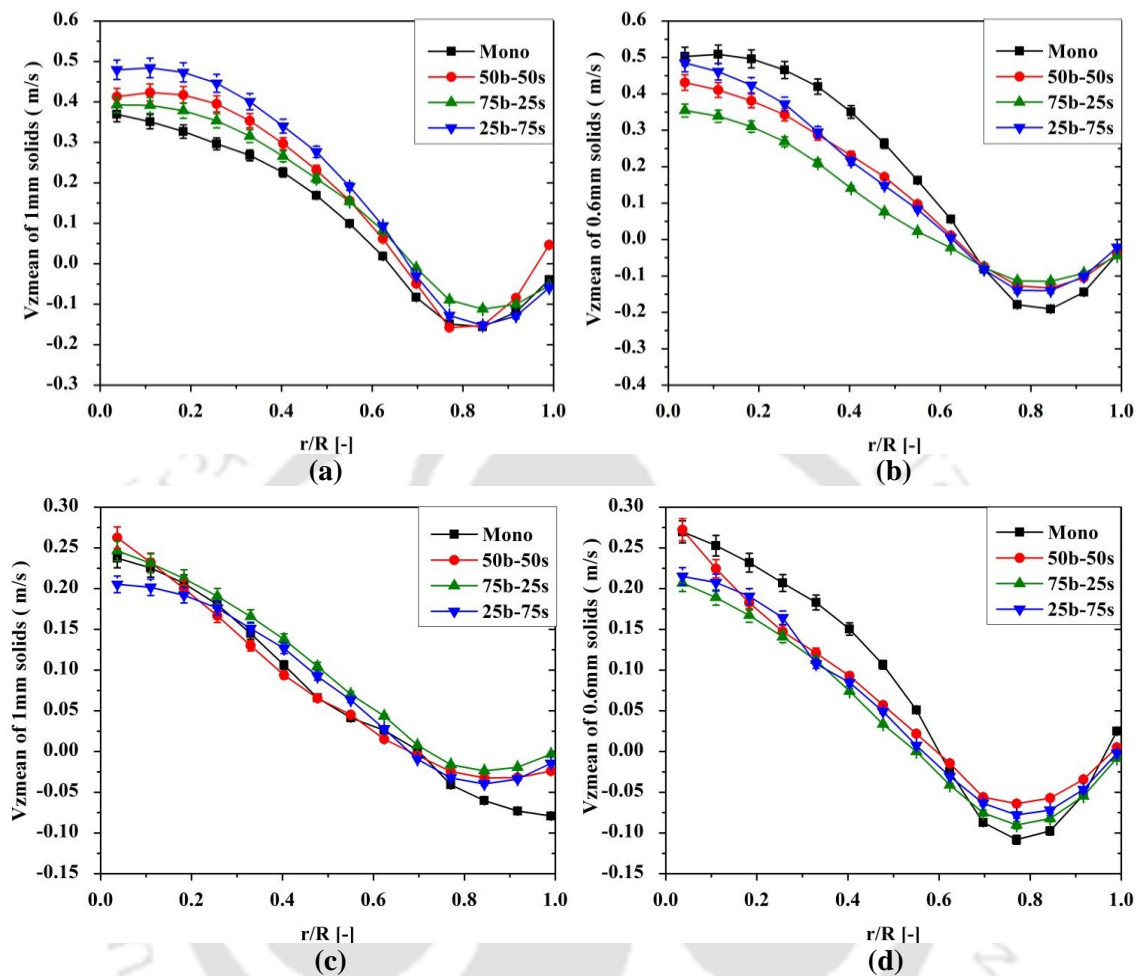


Figure 3.34 Variation of mean axial velocity of solid with different composition: (a) 1 mm particle on top section, (b) 0.6 mm particle on top section, (c) 1 mm particle at bottom section, and (d) 0.6 mm particle at bottom section

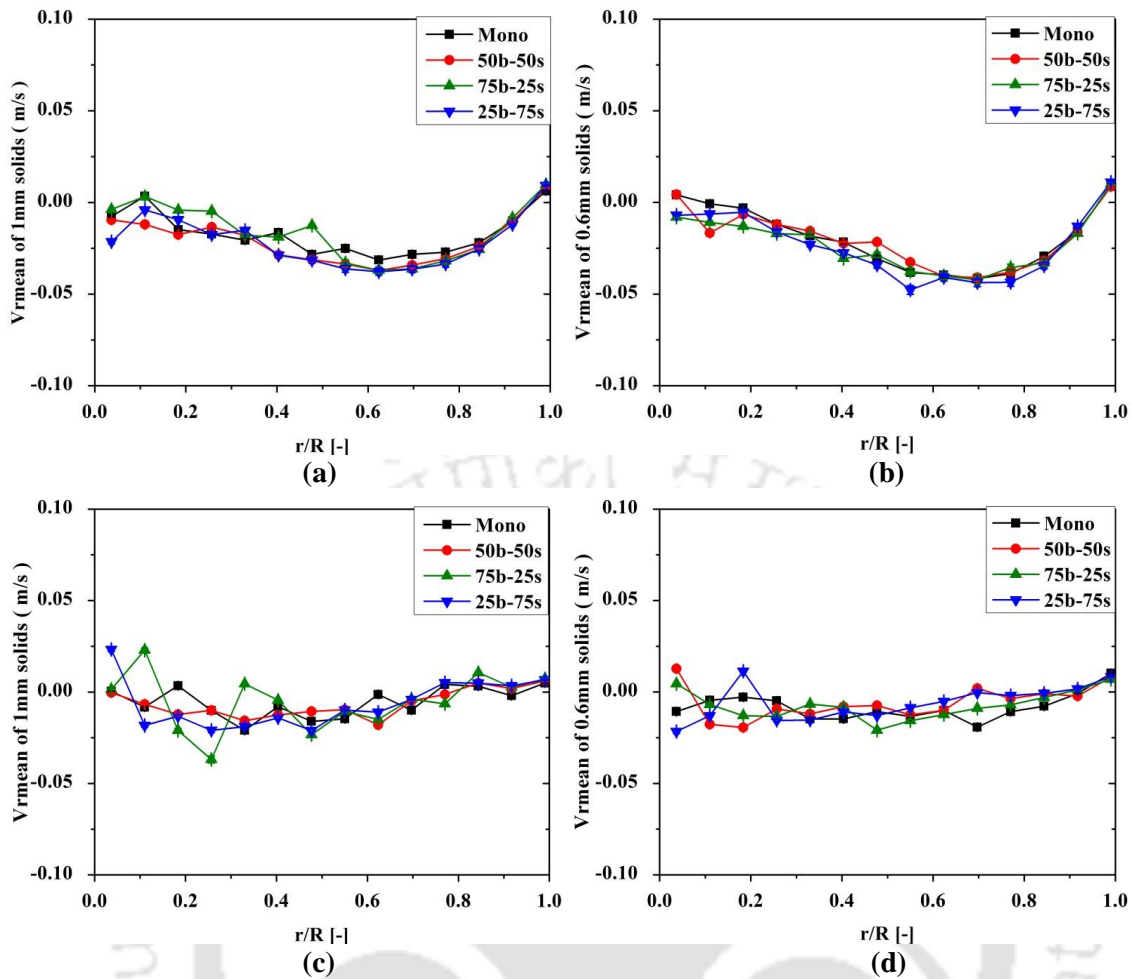


Figure 3.35 Variation of mean radial velocity of solid with different composition: (a) 1 mm particle on top section, (b) 0.6 mm particle on top section, (c) 1 mm particle at bottom section, and (d) 0.6 mm particle at bottom section

3.7.2 Solid velocity fluctuations

The change in fluctuation behavior of both solids with changing composition is depicted in Figure 3.36. Figures 3.36a and 3.36c, respectively are the comparison of mean axial RMS (root mean square) velocity plot of 1 mm solid for mono, 50b-50s, 75b-25s and 25b-75s composition on top and bottom sections. Similarly, Figures 3.36b and 3.36d, respectively are the comparison of mean axial RMS velocity plot of 0.6 mm solid for mono, 50b-50s, 75b-25s and 25b-75s composition on the top and bottom sections. It is observed that the mean axial RMS velocity is lowest for 1 mm solid in mono bed and the

RMS velocity of 1 mm solids keeps on increasing with the addition of smaller particle into the system. For the 25b-75s mixture, axial RMS velocity of 1 mm solid was highest. However, for 0.6 mm solid the highest axial RMS velocity was observed for monodispersed bed and the velocity reduces with bigger particle addition to the bed. Thus, the motion of 0.6 mm solids gets restricted in presence of 1 mm solids in the bed. The axial RMS shows a marginal difference with the composition at both the top and bottom sections of the bed.

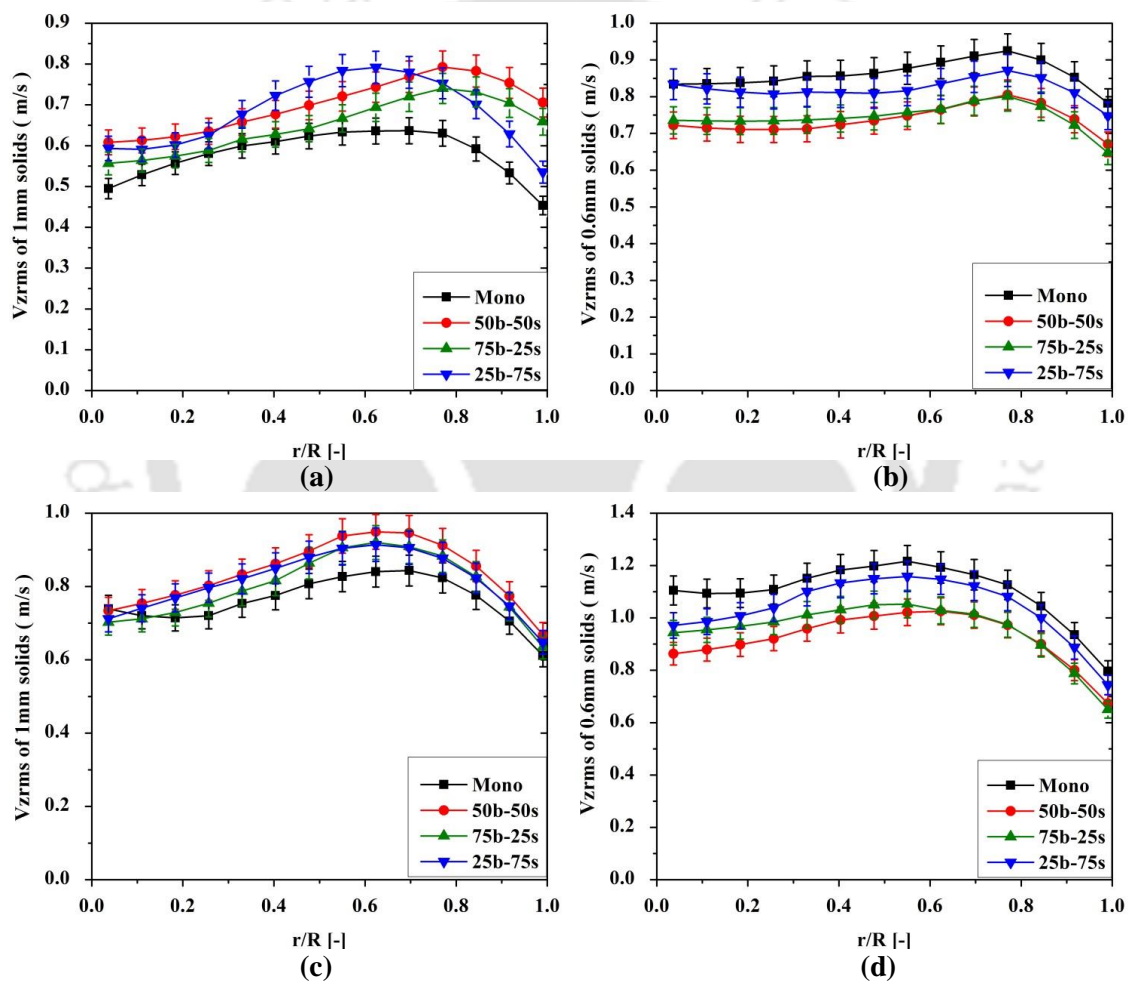


Figure 3.36 Variation of V_{zrms} of solid with different composition: (a) 1 mm particle on top section, (b) 0.6 mm particle on top section, (c) 1 mm particle at bottom section, and (d) 0.6 mm particle at bottom section

The radial RMS velocities are shown in Figure 3.37 for both solids with different compositions and at a constant velocity of 7.6 m/s. The radial RMS velocity was observed to be different in nature compared to axial RMS velocity. The fluctuation in the radial direction was significant, though the mean radial solid motion was negligible in the radial direction. Hence, the radial RMS velocity was mainly observed due to the particle-particle interaction which is higher at the center of the column and restricted near the wall. The radial RMS does not show significant change with the bed composition and height of the column. It shows equal fluctuation for 1 mm and 0.6 mm, irrespective of the varying compositions.

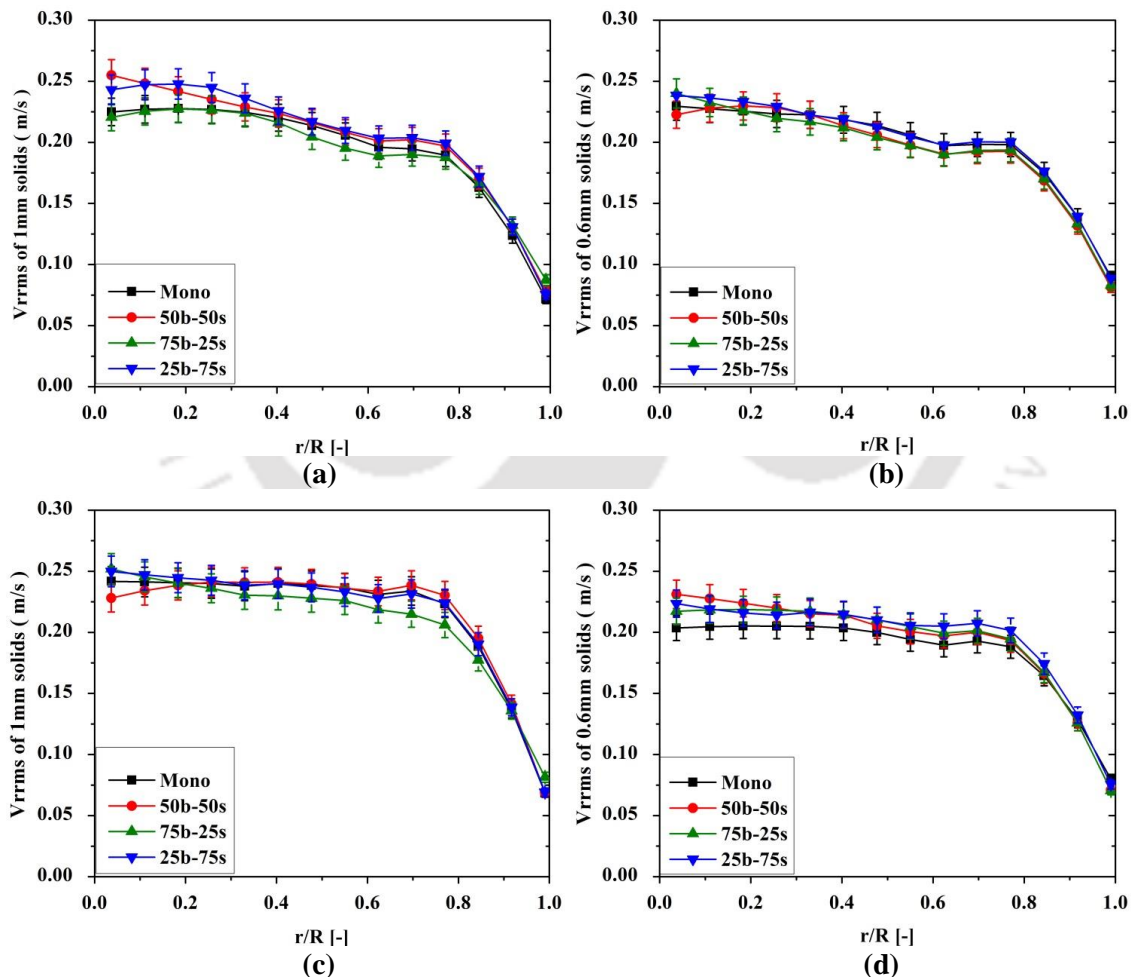


Figure 3.37 Variation of V_{rrms} of solid with different composition: (a) 1 mm particle on top section, (b) 0.6 mm particle on top section, (c) 1 mm particle at bottom section, and (d) 0.6 mm particle at bottom section

3.7.3 Granular temperature

Figure 3.38 presents the granular temperature with the varying composition at 7.6 m/s velocity. The granular temperature shows high variation with composition compared to other parameters. For 0.6 mm particle, the variation is higher compared to 1 mm. In case of 0.6 mm solids, the higher u/u_{mf} results in rigorous bubbling and higher voidage. This gives higher fluctuation in case of 0.6 mm particle than 1 mm particle. The granular temperatures of big and small particles are lower in the upper part of the bed compared to the bottom. The granular temperature shows the same trend as axial RMS velocity.

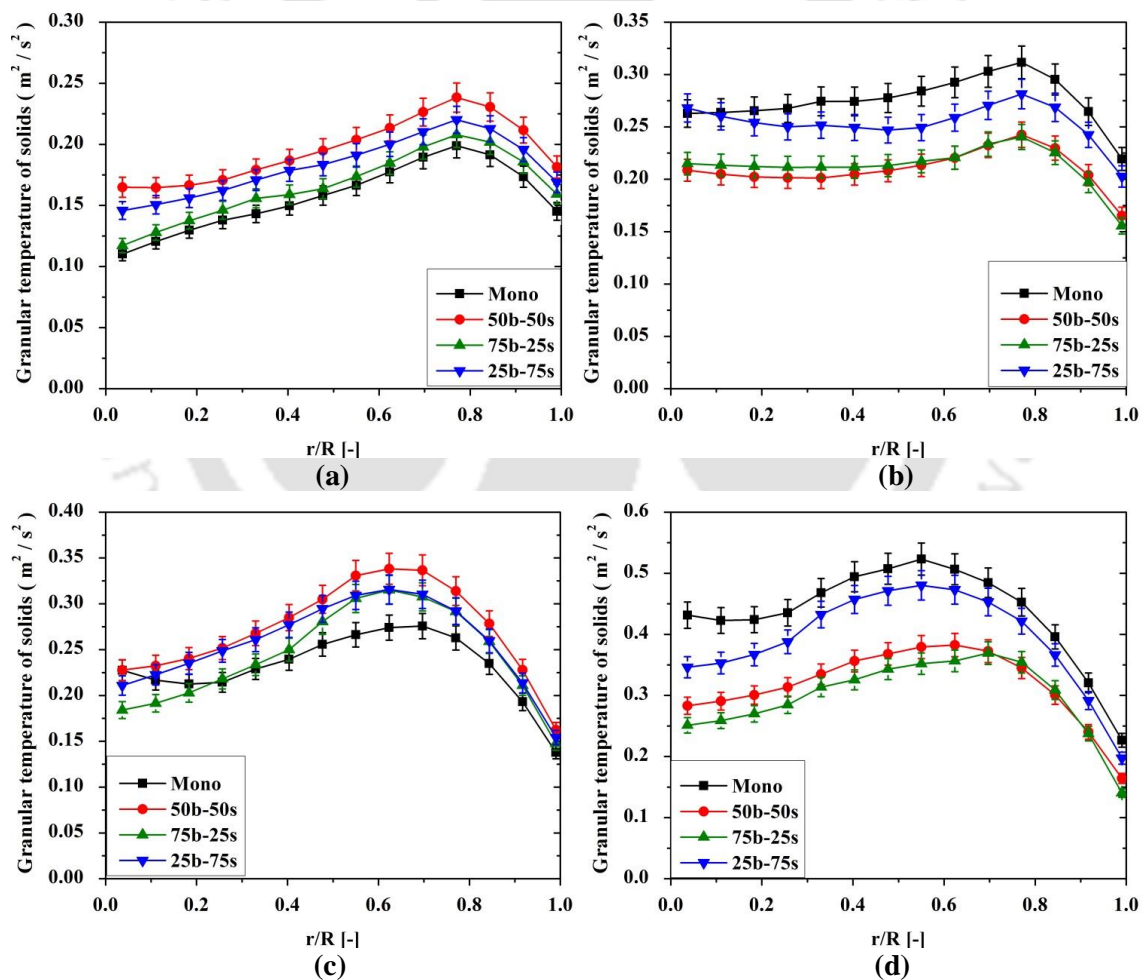


Figure 3.38 Variation of granular temperature of solid with different composition: (a) 1 mm particle on top section, (b) 0.6 mm particle on top section, (c) 1 mm particle at bottom section, and (d) 0.6 mm particle at bottom section

3.7.4 Hurst exponent

Further, Hurst exponent is obtained from Lagrangian particle velocity for all the four compositions. Table 3.5 shows the Hurst exponent values computed for both solids. The Hurst exponent values for all the operating conditions are found to be higher than 0.5. It indicates the persistent nature of the bed for all the operating condition. The result shows no change in Hurst exponent even after varying composition.

Table 3.5 Hurst exponents at different operating conditions for 1 mm and 0.6 mm particles in both mono and binary beds

Fluid velocity	Bed composition	Hurst exponent
7.6 m/s	100b 1 mm	0.92
7.6 m/s	75b-25s 1 mm	0.92
7.6 m/s	50b-50s 1 mm	0.92
7.6 m/s	25b-75s 1 mm	0.92
7.6 m/s	100s 0.6 mm	0.93
7.6 m/s	75b-25s 0.6 mm	0.91
7.6 m/s	50b-50s 0.6 mm	0.91
7.6 m/s	25b-75s 0.6 mm	0.92

3.7.5 Autocorrelation

The axial autocorrelation is illustrated in Figure 3.39 for all the bed compositions. Figures 3.39a-3.39d represent the autocorrelation of 1 mm solid for mono, 75b-25s, 50b-50s and 25b-75s compositions, respectively. Similarly, Figures 3.39e-3.39h represent the

autocorrelation of 0.6 mm solid for mono, 25b-75s, 50b-50s and 75b-25s compositions, respectively. The autocorrelation decays after a certain time and then oscillates before getting constant at zero. It is observed that the autocorrelation decays at 0.12s for both solids for all the bed compositions. For 0.6 mm solid in monodispersed composition the oscillation is highest and continues even after 5s due to higher velocity. The oscillation seems to reduce with the addition of bigger particle to the column as the velocity reduces. However, for 1 mm solid the autocorrelation does not show any variation with composition. It remains same with an increase in the fraction of 0.6 mm solids to the bed.

3.7.6 Segregation index

The segregation index was calculated for all the bed compositions at 7.6 m/s. Figure 3.40 shows the plot of the segregation index with an increase in smaller solid fraction. At low volume fraction of smaller solid, the segregation index is low which is increasing with an increase of smaller solid fraction in the mixture. It indicates that the bed is properly mixed for all the bed compositions as the bed is operated at a very high velocity. Hence, solids are well distributed throughout the column reaching a complete mixing state.

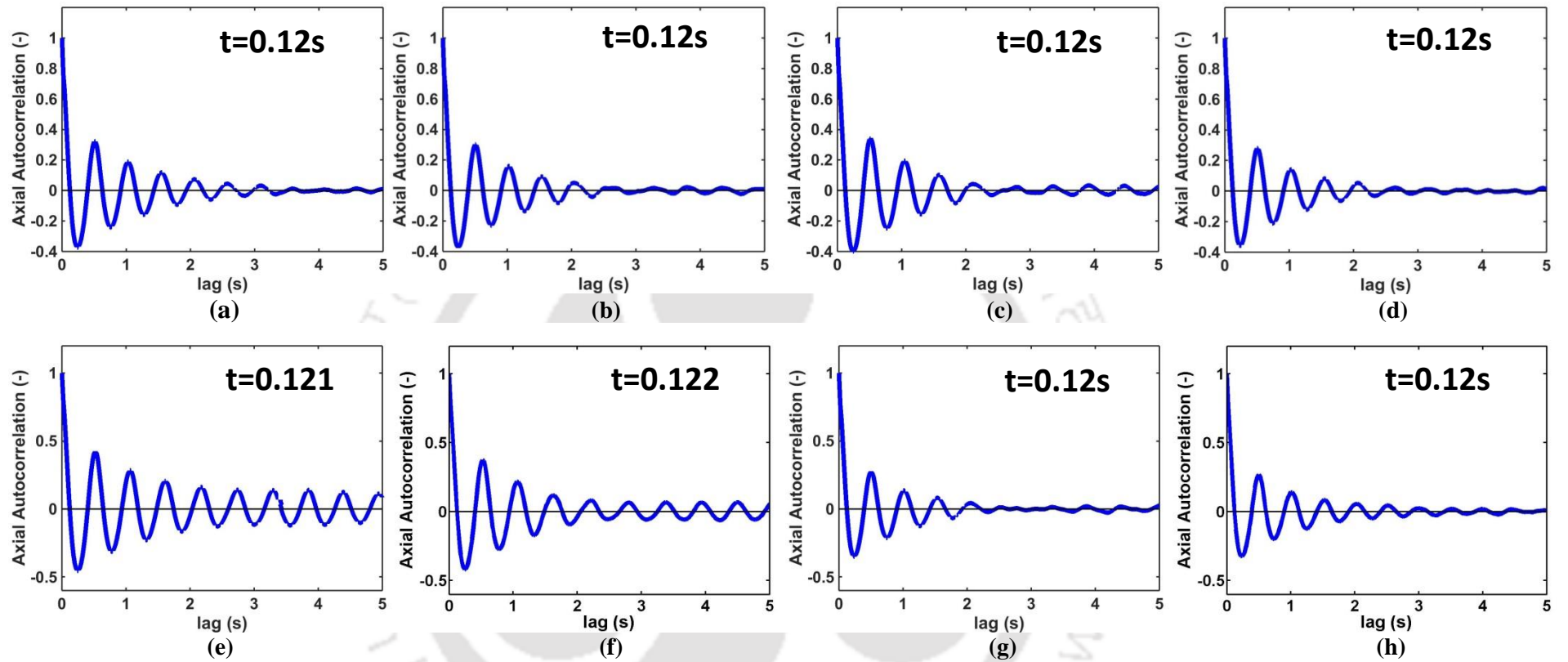


Figure 3.39 Variation of axial autocorrelation of solid with different compositions in binary bed (a) 1 mm particle in mono bed, (b) 1 mm particle in 75b-25s bed, (c) 1 mm particle in 50b-50s bed, (d) 1 mm particle in 25b-75s bed, (e) 0.6 mm particle in mono bed, (f) 0.6 mm particle in 25b-75s bed, (g) 1 mm particle in 50b-50s bed, and (h) 1 mm particle in 75b-25s bed

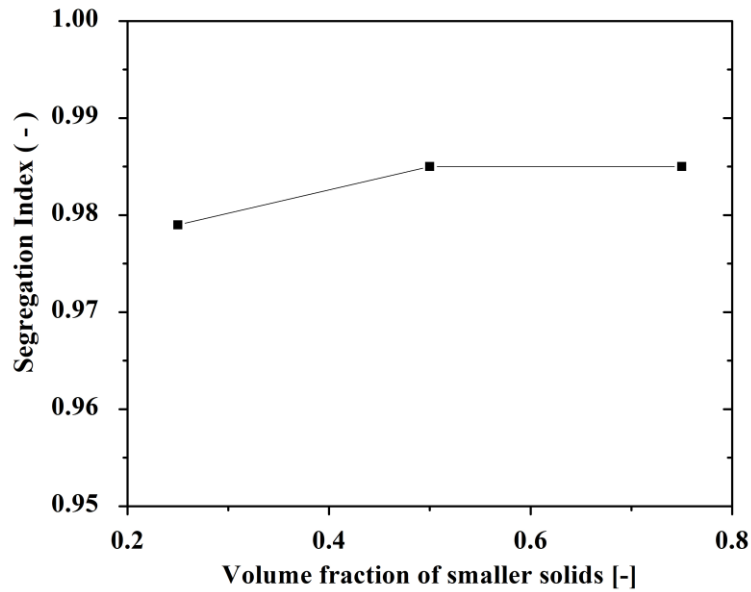


Figure 3.40 Variation of segregation index with different composition in binary bed

3.8 Summary

The results of this chapter are summarized in two parts, viz., monodispersed and binary dispersed bed studies for different gas inlet velocities.

Monodispersed bed study

The following major conclusions can be obtained from the mono dispersed bed study:

- It is observed that the axial mean velocity of the bigger particle is lower than the smaller particle for a particular velocity, as both beds are operated at same inlet velocity. The observation shows solid mean velocity is significant in axial direction compared to the radial direction.
- The fluctuation in case of the smaller particle is more than bigger particle as expected because it indicates high fluctuation in case of the smaller particle.
- Axial autocorrelation shows oscillation in both positive and negative directions before decaying to zero.

- Observed regime transition for both solids at 5.7 m/s from segregation index, as can be seen from KE and CD plots.

Binary dispersed bed studies

- It is found that the hydrodynamics of gas-solid conical bed is chaotic and that the degree of chaotic behavior depends on the gas velocity and bed composition.
- The axial mean velocity of both 1 mm and 0.6 mm particles are found to be approximately similar in 50b-50s wt. % binary bed at a higher velocity, which signifies the homogeneous distribution of solids. It indicates that the mixing and interaction of gas-solids increases with an increase in velocity at the mean level. It was observed that in conical bed two different interaction phenomena dominate the behavior of the bed at the top and bottom sections. At the bottom section, gas-solids interaction plays a dominating role while in top section particle-particle interaction becomes crucial.
- In the conical fluidized bed, the axial autocorrelation takes a longer time to decay, compared to radial autocorrelation which signifies that motion is primarily in the axial direction.
- The segregation index calculated for binary bed indicates good mixing even at a lower gas inlet velocity which is contradictory to the cylindrical column. Hence, it can be stated that conical fluidized bed provides better mixing compared to the cylindrical fluidized bed.
- Correlation Dimension and Kolmogorov Entropy show the chaotic nature of the mono and binary fluidized beds. Further, CD and KE values also indicate a change in flow regime (after 5.7 m/s gas velocity) for both mono and binary

fluidized beds. Finally, it has been found that flow regime transition in conical bed is mainly dependent on gas inlet velocity and not on bed composition.

Notations

h	Actual height where data was plotted, m
H	Expanded bed height during fluidization, m
r	Actual radius where data was plotted, m
R	Radius of the column at that height, m
u	Gas inlet velocity, m/s
u_{mf}	Minimum fluidization velocity, m/s
τ	Time delay, s

References

- Babu, S.P., Leipsiger, S., Lee, B.S., Weil, S.A., 1973. Solids mixing in batch operated tapered bed and non- tapered gas fluidized beds. Fluidized Bed Fundamental Application. AIChE, Symp. Ser., 69, 49-57.
- Baeyens, J., Geldart, D., 1986. Solids mixing, in: D. Geldart (Ed.), Gas Fluidization Technology, John Wiley & Sons Ltd. 97–122.
- Bai, D., Issangya, A.S., Grace, J.R., 1999. Characteristics of gas-fluidized beds in different flow regimes. Ind. Eng. Chem. Res. 38, 803–811.
- Bahramian, A.R., K. Mansour, K., 2010. CFD Modelling of TiO₂nano-agglomerates hydrodynamics in a conical fluidized bed unit with experimental validation. Iran. J. Chem. Chem. Eng., 29(2), 105-120.
- Bendat, J.S., Piersel, A.G., 2000. Random Data: Analysis and Measurement Procedures, 4th Edition, John Wiley & Sons, Inc. New York.

- Bhusarapu, S., 2005. Solids Flow Mapping in Gas-Solid Risers. D.Sc. Thesis.
- Biswal, K.C., Bhowmik, T., Roy, G.K., 1985. Prediction of minimum fluidization velocity for gas-solid fluidization of regular particles in conical vessels. *Chem. Eng. J.* 30, 57–62.
- Cassanello, M., Larachi, F., Marie, M.-N., Guy, C., Chaouki, J., 1995. Experimental Characterization of the Solid Phase Chaotic Dynamics in Three- Phase Fluidization. *Ind. Eng. Chem. Res.*, 34, 2971-2980.
- Cheung, L., Nienow, A.W., Rowe, P.N., 1974. Minimum fluidization velocity of a binary mixture of different sized particles. *Chem. Eng. Sci.* 29, 1301-1303.
- Degaleesan, S., 1997. Fluid dynamic measurements and modeling of liquid mixing in bubble columns. D. Sc. Thesis.
- Depypere, F., Pieters, J.G., Dewettinck, K., 2005. Expanded bed height determination in a tapered fluidised bed reactor. *J. Food Eng.* 67, 353–359.
- Depypere, F., Pieters, J.G., Dewettinck, K., 2009. PEPT visualisation of particle motion in a tapered fluidised bed coater. *J. Food Eng.* 93 (3), 324–336.
- Devanathan, N., 1991. Investigation of liquid hydrodynamics in bubble columns via computer automated radioactive particle tracking, D.Sc Thesis.
- Dighe, S.V., Blinn, M.B., Buggy, J.J., Krasicki, B.R., Pierce, B.L., 1981. Proceedings of the 16th Intersociety Energy Conversion Engineering Conference. ASME, New York, 1059-1067.
- Duangkhamchan, W., Ronsse, F., Depypere, F., Dewettinck, K., Pieters, J.G., 2010. Comparison and evaluation of interphase momentum exchange models for simulation of the solids volume fraction in tapered fluidised beds. *Chem. Eng. Sci.* 65, 3100–3112.
- Dudukovic, M.P., 2009. *Frontiers in Reactor Engineering. Science.* 325, 698-701.
- Fan, L.T., Chen, Y., Lai, F.S., 1990. Recent Developments in Solids Mixing. *Powder Technol.* 61, 255-287.
- Fan, L.T., Neogi, D., Yashima, M., Nassar, R., 1990. Stochastic analysis of a three-phase fluidized bed: Fractal approach. *AIChE J.* 36, 1529–1535.

- Formisani, B., 1991. Packing and Fluidization Properties of Binary Mixtures of Spherical Particles. *Powder Technol.* 66, 259–264.
- Formisani, B., De Cristofaro, G., Girimonte, R., 2001. A fundamental approach to the phenomenology of fluidization of size segregating binary mixtures of solids. *Chem. Eng. Sci.* 56, 109-119.
- Gelperin, N.I., Aynshteyn, V.G., Gelperin, E.N., Lvova, S.D., 1960. Hydrodynamic characteristics of pseudo-liquefaction of granular materials in conical and conico-cylindrical equipment. *Khim. Tekhnol. Topliv Masel (USSR)* 5, 51–57.
- Gernon, T.M., Gilbertson, M.A., Sparks, R.S.J., 2010. Particle Segregation in Tapered Fluidized Beds. *The 13th International Conference on Fluidization-New Paradigm in Fluidization Engineering.* 91.
- Golubkovich, A.V., 1975. Investigation of Fluidized Bed Regimes in Conical Reactors. *Khim. I Neft. Mash.* 3, 21-22.
- Hampel, N., Bück, A., Peglow, M., Tsotsas, E., 2013. Continuous pellet coating in a Wurster fluidized bed process. *Chem. Eng. Sci.* 86, 87–98.
- Hoffmann, A.C., Janssen, L.P.B.M., Prins, J., 1993. Particle Segregation in Fluidized Binary Mixtures. *Chem. Eng. Sci.* 48, 1583–1592.
- Ishii, T., 1973. Multi Particle Crystal Growth Rates in Vertical Cones. *Chem. Eng. Sci.* 28, 1121–1128.
- Jain, S., Saraswat, P., Jain, V., Pant, H.J., Upadhyay, R.K., 2014. Investigation of liquid-solids fluidized bed of different particle size through radioactive particle tracking techniques. *J. Radioanal. Nucl. Chem.* 302, 1309–1313.
- Jing, S., Hu, Q., Wang, J., Jin, Y., 2000. Fluidization of coarse particles in gas–solid conical beds. *Chem. Eng. Process. Process Intensif.* 39, 379–387.
- Jones, D., 1994. Air suspension coating for multiparticulates. *Drug Dev. Ind. Pharm.* 20 (20), 3175–3206.
- Khani, M.H., 2011. Models for prediction of hydrodynamic characteristics of gas– solid tapered and mini-tapered fluidized beds. *Powder Technol.* 205, 224–230.

- Khanna, P., 2008. Particle Tracking in a Lab-Scale Conical Fluidized Bed Dryer, M. Sc. Thesis, University of Saskatchewan, Saskatoon, Saskatchewan.
- Kim, H.G., Lee, I.O., Chung, U.C., Kim, Y.H., 2000. Fluidization Characteristics of Iron Ore Fines of Wide Size Distribution in a Cold Tapered Gas-Solid Fluidized bed. *ISIJ International*. 40 (1), 16-22.
- Kunii, D., Levenspiel, O., 1991. *Fluidization Engineering*, Butterworth-Heinemann, Boston, MA.
- Kwant, G., Prins, W., van Swaaij, W.P.M., 1995. Particle mixing and separation in a binary solids floating fluidized bed. *Powder Technol.* 82, 279-291.
- Kwauk, M., 1992. *Fluidization*. Science and Press, New York.
- Lin, J., Chen, M., Chao, B., 1985. A novel radioactive particle tracking facility for measurement of solids motion in gas fluidized beds. *AIChE Journal*. 31, 465–473.
- Maruyama, T., Koyanagi, T., 1993. Fluidization in tapered vessels. *Chem. Eng. J.* 51, 121–128.
- Marzocchella, A., Salatino, P., Di Pastena, V., Lirer, L., 2000. Transient fluidization and segregation by size difference of binary mixtures of particles. *A.I.Ch.E. J.* 46, 2175-2182.
- Molnar, M., Karri, S., Dehtiar, M., Braun, E., Arrington, Y., Cocco, R., Gelderbloom, S., 2013. Experimental Study on Fluidization Behavior of Geldart B and D Particle Systems in Deep Tapered Beds. *AIChE Annual Meeting*.
- Nienow, A.W., Naimer, N.S., Chiba, T., 1987. Studies of Segregation/Mixing in Fluidised Beds of Different Size Particles. *Chem. Eng. Commun.* 62, 53-66.
- Nishi, Y., 1979. Some considerations on pressure drop and minimum fluidizing velocity of tapered fluidized bed. *Kagaku Kogaku Ronbunshu* 5, 202-204.
- Noda, K., Uchida, S., Makino, T., Kamo, H., 1986. Minimum Fluidization Velocity of Binary Mixture of Particles with Large Size Ratio. *Pow. Tech.* 46, 149-154.
- Olazar, M., San Jose, M.J., Llamas, R., Bilbao, J., 1994. Hydrodynamics of sawdust and mixtures of wood residues in conical spouted beds. *Ind. Eng. Chem. Res.* 33, 993-1000.

- Peeler, J.P.K., Huang, J.R., 1989. Segregation of wide size range particle mixtures in fluidized beds. *Chem. Eng. Sci.* 44, 1113–1119.
- Peng, Y., Fan, L.T., 1997. Hydrodynamic Characteristics of Fluidization in Liquid-Solid Tapered Beds. *Chem. Eng. Sci.* 52, 2277–2290.
- Pugsley, T., Chaplin, G., Khanna, P., 2007. Application of Advanced Measurement Techniques to Conical Lab-scale Fluidized Bed Dryers Containing Pharmaceutical Granule. *Food Bioprod. Process.* 85, 273-283.
- Rasul, M.G., Rudolph, V., Carsky, M., 1999. Segregation potential in binary gas fluidized beds. *Powder Technol.* 103, 175-181.
- Rice, R.W., Brainovich, J.F., 1986. Mixing/Segregation in Two- and Three-Dimensional Fluidized Beds: Binary Systems of Equidensity Spherical Particles. *AIChE J.* 32 (1), 7-16.
- Ridgway, K., 1965. The tapered fluidized bed – a new processing tool. *Chem. Process Eng.* 6, 317 – 321.
- Roew, P.N., Nienow, A.W., 1976. Particle Mixing and Segregation in Gas Fluidized Beds. A Review. *Pow. Tech.* 15, 141-147.
- Roy, S., 2000. Quantification of Two-Phase Flow in Liquid-Solid Risers. Ph.D. thesis, Washington University, USA.
- Sau, D.C., Mohanty, S., Biswal, K.C., 2008. Prediction of critical fluidization velocity and maximum bed pressure drop for binary mixture of regular particles in gas–solid tapered fluidized beds. *Chem. Eng. Process.* 47, 2114-2120.
- Sau, D.C., Mohanty, S., Biswal, K.C., 2010. Experimental studies and empirical models for the prediction of bed expansion in gas-solid tapered fluidized beds. *Chem. Eng. Process.* 49, 418–424.
- Schaafsma, S.H., Marx, T., Hoffmann, A.C., 2006. Investigation of the particle flowpattern and segregation in tapered fluidized bed granulators. *Chem. Eng. Sci.* 61, 4467–4475.

- Schouten, J.C., van den Bleek, C.M., 1992. Chaotic hydrodynamics of fluidization consequences for scaling and modelling of fluid bed reactors. *AIChE Symp. Ser.* 88, 70-84.
- Shi, Y.F., Yub, Y. S., Fan, L. T., 1984. Incipient Fluidization Condition for a Tapered Bed. *Ind. Eng. Chem. Fundam.* 23, 484-489.
- Singh, R.K., Suryanarayana, A., Roy, G.K., 1992. Prediction of minimum velocity and minimum bed pressure drop for gas–solid fluidization in conical conduits. *Can. J. Chem. Eng.* 70 (1), 185–189
- Sutar H, Das, C.K., 2012. Mixing and Segregation Characteristics of Binary Granular Material in Tapered Fluidized Bed: A CFD Study. *Eng.* 215–227.
- Tanfara, H., Pugsley, T., Winters, C., 2002. Effect of particle size distribution on local voidage in a bench-scale conical fluidized bed dryer. *Drying Technol.* 20 (6), 1273–1289.
- Toyohara, H., Kawamura, Y., 1992. Fluidization of a tapered fluidized-bed of a binary particle mixture. *Int. Chem. Eng.* 32 (1), 164–171.
- Upadhyay, R.K., 2010. Investigation of Multiphase Reactors Using Radioactive Particle Tracking. Ph.D. Thesis, IIT Delhi.
- Upadhyay, R.K., Roy, S., 2010. Investigation of Hydrodynamics of Binary Fluidized Beds via Radioactive Particle Tracking and Dual-Source Densitometry. *Can. J. Chem. Eng.* 88, 601-610.
- van Ommen, J.R., Sasic, S., van der Schaaf, J., Gheorghiu, S., Jhonsson, F., Coppens, M.O., 2011. Time series analysis of pressure fluctuations in gas-solid fluidized beds – A review. *Int. J. of Multiphase Flow* 37, 403-428
- Van Wachem, B.G.M., Schouten, J.C., Van den Bleek, C.M., Krishna, R., Sinclair, J.L., 2001. CFD modeling of gas-fluidized beds with a bimodal particle mixture. *AIChE J.* 47, 1292–1302.
- Venkatesh, R.D., Chaouki, J., Klvana, D., 1996. Fluidization of cryogels in a conical column. *Powder Technol.* 89, 179–186.

- Webster, G.H., Perona, J.J., 1988. Liquid Mixing in a Tapered Fluidized Bed. *AIChE J.* 34 (8), 1398-1402.
- Wiens, J., Pugsley, T., 2006. Tomographic imaging of a conical fluidized bed of dry pharmaceutical granule. *Powder Technol.* 169, 49–59.
- Wormsbecker, M., Adams, A., Pugsley, T., Winters, C., 2005. Segregation by size difference in a conical fluidized bed of pharmaceutical granulate. *Powder Technol.* 153, 72–80.
- Wormsbecker, M., van Ommen, R., Nijenhuis, J., Tanfara, H., Pugsley, T., 2009. The influence of vessel geometry on fluidized bed dryer hydrodynamics. *Powder Technol.* 194, 115–125.
- Wu, S.Y., Baeyens, J., 1998. Segregation by Size Difference in Gas Fluidized Beds. *Powder Technol.* 98, 139-150.
- Zarghami, R., Mostoufi, N., Sotudeh-gharebagh, R., 2008. Nonlinear Characterization of Pressure Fluctuations in Fluidized Beds Nonlinear Characterization of Pressure Fluctuations in Fluidized Beds. *Ind. Eng. Chem. Res.* 47, 9497–9507.
- Zijerveld, R.C., Johnsson, F., Marzocchella, A., Schouten, J.C., Van Den Bleek, C.M., 1998. Fluidization regimes and transitions from fixed bed to dilute transport flow. *Powder Technol.* 95, 185–204.



Chapter 4

Experimental Investigation of Liquid-Solid Conical Fluidized Bed

Scope

This chapter includes the hydrodynamic study of the liquid-solid conical fluidized bed. Radioactive particle tracking (RPT) technique is implemented for experimental investigation. The monodispersed and binary dispersed conical bed is investigated for different liquid inlet velocities. The time average behavior of the bed is analyzed using mean solid velocity, RMS velocity, and granular temperature. In order to study the time series behavior Hurst exponent, autocorrelation function and segregation index are calculated. Finally, chaos analysis is performed to calculate Kolmogorov entropy and correlation dimension from data obtained through RPT experiment.

4.1 Introduction

Liquid-solid fluidized bed are used mostly for sedimentation (Chavan and Joshi, 2008), adsorption (Yang and Renken, 2003; Chavan and Joshi, 2008), liquid phase catalytic reactions (Fan et al., 1993), separation and recovery of materials (Fan et al., 1993), biochemical reactions and biological treatment of wastewater (Scott and Hancher, 1976; Pitt et al., 1981; Maruyama et al., 1984) due to their high rates of heat and mass transfer (Morooka et al., 1980; Muroyama et al., 1986; Kang and Kim, 1987). The liquid-solid fluidized bed also gives stability and homogeneous behavior for a wide range of liquid flow-rates unlike gas-solid fluidized bed (Ham et al., 1990). The performance of any liquid-solid fluidized bed reactor is affected by many parameters such as the flow regime (Volpicelli et al., 1966; Kang and Kim, 1988), the motion of discrete phase (Handley et

al., 1966; Kmiec, 1978; Yutani et al., 1983), and void distribution (Fan et al., 1985). The flow regime in the monocomponent bed varies based on inlet velocity in both cylindrical and conical beds (Kunii and Levenspiel, 1991; Peng and Fan, 1997). Further, the particle size distribution plays a major role in any liquid-solid fluidized bed system. However, for simplification, binary and ternary mixtures have been considered in fluidized bed study. Maruyama et al. (1984) have studied the binary component fluidization in the conical fluidized bed for various mixing and segregation conditions. However, detail information regarding solid distribution in the binary dispersed fluidized bed is missing (Kwant et al., 1995). The interaction between the discrete and continuous phases or the interaction within the discrete phase is very critical in case of the fluidized bed in both mono and binary dispersed beds (Jain et al., 2014; Jain et al., 2017). However, the tapered fluidized beds have been used mostly for the study of pressure drop, flow regime, incipient fluidization condition and bed voidage, etc., using off-line measurement techniques (Kolar, 1963; Koloini and Farkas, 1973; Shi et al., 1984). Hence, a detailed study of the liquid-solid conical fluidized bed is needed for their characterization. Further, to understand the long-term behavior, time series analysis, and chaos analysis can be applied to such system.

4.2 Literature on L-S conical fluidized bed

Monodispersed bed

The researches on the liquid-solid conical fluidized bed are rare to find as compared to the gas-solid system. However, the monodispersed liquid-solid fluidized beds have been used since 1960 to investigate the pressure drop, flow regime, incipient fluidization condition and bed voidage, etc. Kolar (1963) has developed a correlation for overall bed voidage as a function of the liquid velocity in a conical mono dispersed fluidized bed for

two different cone angles. Koloini and Farkas (1973) presented a correlation for fixed bed pressure drop, minimum fluidization velocity and bed expansion in conical vessels based on experimental data. Scott et al. (1976) have used the conical fluidized bed for aqueous bioprocess and calculated the pressure drop and total bed volume by using the voidage correlation of cylindrical fluidized bed. Hsu (1978) developed analytical expression to study the effect of cone angle on void fraction and solid distribution in the conical reactor. Pitt et al. (1978) have measured the pressure drop and bed expansion for various apex angle of the column. Maruyama et al (1984) have presented the regime transition of the conical vessel with a diagram that can be used to calculate the bed height and pressure drop on the basis of an empirical voidage which is correlated by a power function of the local superficial liquid velocity. They have compared the calculated bed height and pressure drop with the obtained result of a two-dimensional tapered vessel of various apex angles. They have also used the same method for binary dispersed bed on the basis of the assumption of complete segregation of both species. Bed expansion and mixing behavior were predicted by a voidage correlation and compared with cylindrical bed results. Shi et al (1984) have developed a model based on force balance for the incipient fluidization condition in conical liquid-solid bed. Further, they stated that the existence of velocity gradient in the axial direction in such column to be beneficial in minimizing entrainment and helping in fluidization of denser solid at the bottom. Webster and Perona (1988) calculated residence time and dispersion coefficient by injecting tracer to a conical column and cylindrical column. From residence time calculation they had stated that the tapered fluidized bed is characterized by fluid channeling in the center with a downward flow or stagnant regions at the walls; this flow pattern is markedly different than the flow pattern in the cylindrical fluidized bed. Residence time and dispersion coefficient were found to be larger in conical column compared to cylindrical. Maruyama and Sato (1991)

studied liquid axial mixing based on tracer response measurement. They had calculated solid-particle diffusion coefficient using particle diffusion model. Maruyama and Koyanagi (1993) proposed a model to predict bed height and pressure drop independent of cone angle. Most of the conical fluidized bed studies are performed on the gas-solid system. So, very few literature are available on the liquid-solid conical fluidized bed. For the first time, Peng and Fan (1997) have discussed the regime transition in the conical liquid-solid system using Geldart's group B solids.

Binary dispersed bed

Very few studies are focused on the conical liquid-solid binary system so far. The conical liquid-solid fluidized bed of binary mixture with a size ratio of 5 and cone angle 10° was used by Dathrika et al. (2011). The effect of composition and size ratio on fluidization behavior was investigated and found to be different than mono dispersed bed. They developed correlations for critical fluidization velocity and the minimum velocity for the full fluidization for binary mixture in terms of single component and compared the obtained results with experiment. The bed behavior observed to behave as a monodispersed bed for size ratio 2 and partially segregated bed between size ratio 2 to 3.3 and completely segregated behavior with particle size ratio above 3.3. Similar experiments were extended to three different cone angles by Talapuru et al. (2010). They have also reported similar behavior with size ratio. Figure 4.1 shows the various stages in a binary dispersed conical fluidized bed with increasing velocity.

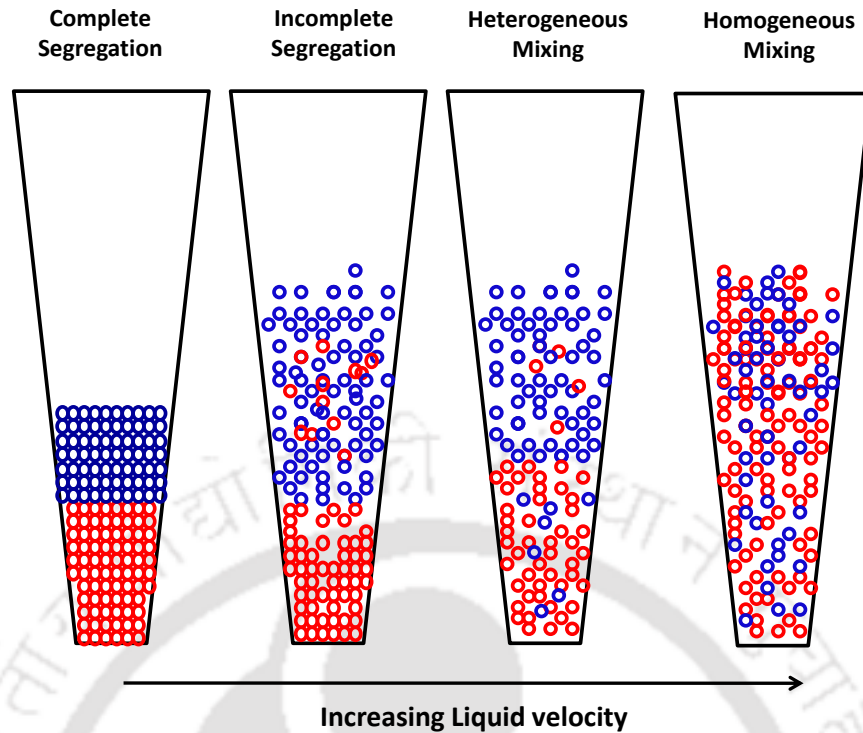


Figure 4.1 Regimes in binary conical fluidized bed (Kwant et al., 1995)

Studies reported on the liquid-solid conical fluidized bed are limited to mainly global bed behavior. Therefore, a detailed study on liquid-solid mono and binary dispersed fluidized beds with state-of-the-art non-invasive technique is still missing which was the main motivation of this chapter.

4.3 Experimental setup

The experimental setup used in the present study consists of 0.05 m bottom and 0.2 m top diameters. The bottom conical section height comprised of 0.8 m with 0.2 m long cylindrical section on top. Experiments have been performed for both mono and binary dispersed beds. Two different sizes (0.6 mm and 1 mm) of glass bead particles with 2500 kg/m³ density have been used. The fluidizing medium was tap water. A 2.5 hp pump was used to pump the water to the inlet of the column. Experiments were performed for different liquid inlet velocities and bed compositions. The composition of these two different sizes of the particle was changed for each set of experiment, keeping the overall

mass of the bed constant as 1.36 kg. The bed composition of 100:0, 25:75, 50:50 and 75:25 were used for the experiment. The bed was operated at three different liquid velocities, i.e. 0.07, 0.1 and 0.14 m/s. The operating conditions of the monodispersed fluidized bed are shown in Table 4.1 while the different bed composition with operating velocity for binary component bed is shown in Table 4.2. Experiments were performed using radioactive particle tracking (RPT) technique. The radioactive particle used in the current work was Scandium-46, which was doped in glass bead of same size and shape. The density of tracer particle was kept same as of the glass beads used in experiments. The experimental set up of the liquid-solid fluidized bed is shown in Figure 4.2. The schematic diagram of the experimental setup is presented in Figure 4.3.

Table 4.1 Operating conditions in conical liquid-solid bed

Material	Size of solid (mm)	u_{mf} (m/s)	Liquid velocity (m/s)
Glass beads	1	0.035	0.07, 0.1, 0.14
Glass beads	0.6	0.016	0.07, 0.1, 0.14

Table 4.2 Different bed compositions and operating velocities in conical liquid-solid bed

Bed composition	Liquid velocity (m/s)
100% 1 mm glass beads	0.07, 0.1, 0.14
75% 1 mm and 25% 0.6 mm glass beads	0.14
50% 1 mm and 50% 0.6 mm glass beads	0.07, 0.1, 0.14
25% 1 mm and 75% 0.6 mm glass beads	0.14
100% 0.6 mm glass beads	0.07, 0.1, 0.14



Figure 4.2 Experimental setup of liquid-solid conical fluidized bed for RPT

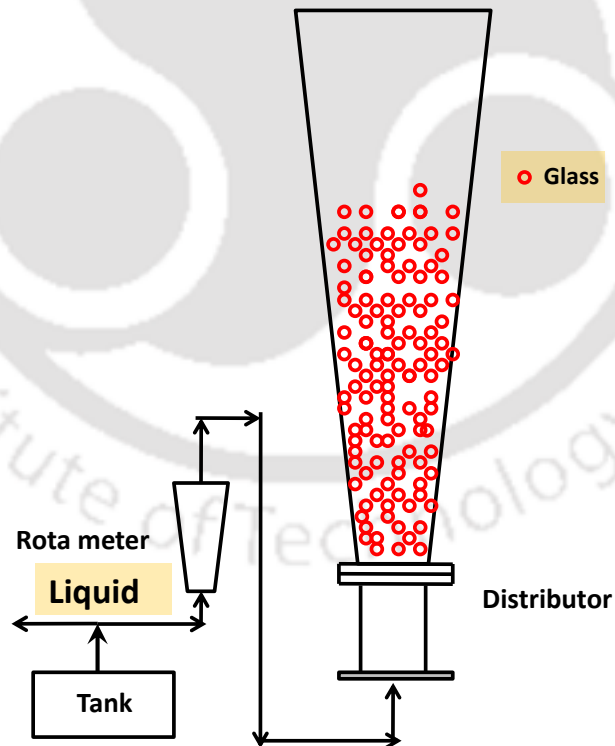


Figure 4.3 Schematic diagram of experimental setup

4.4 Results and discussions

4.4.1 Lagrangian velocity of the solids

Figure 4.4 shows the axial instantaneous Lagrangian velocity of the solids with time. The particle exhibits both positive and negative velocities, indicating up and down movement inside the column. The radial instantaneous Lagrangian velocity of the solids with time is shown in Figure 4.5. Figure 4.5 indicates the existence of radial motion inside the column, though the value is almost half of the axial velocity.

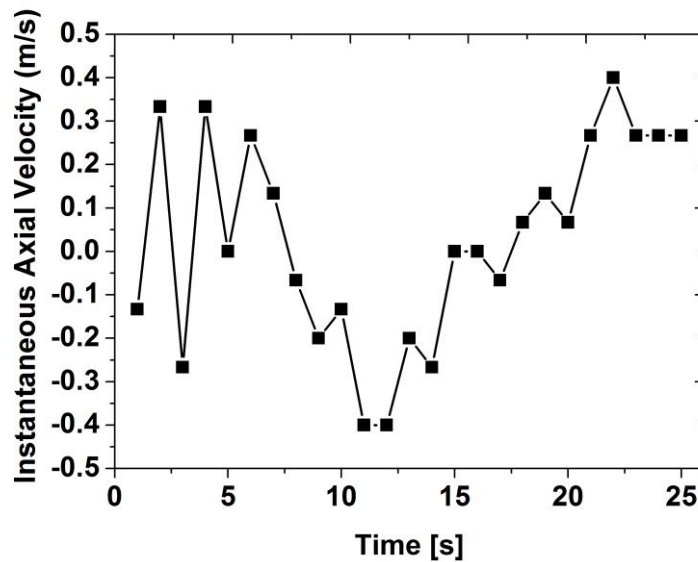


Figure 4.4 Axial Lagrangian velocity of 1 mm solid at 0.14 m/s

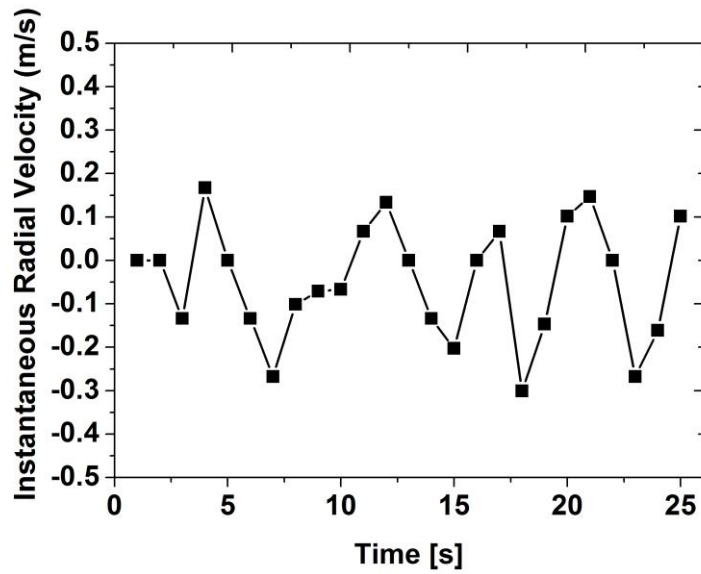


Figure 4.5 Radial Lagrangian velocity of 1 mm solid at 0.14 m/s

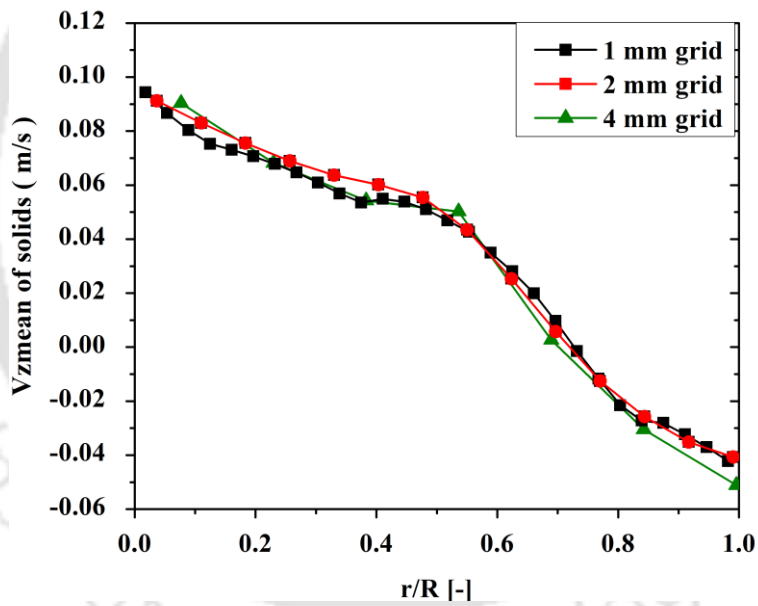


Figure 4.6 Effect of grid on mean axial velocity at $h/H = 0.75$ and 0.14 m/s (1 mm solid)

To validate the stationarity of the data in the conical liquid-solid fluidized bed, three different grids were used. The comparison of all the three grids is shown in Figure 4.6. The grids were 4 mm grid ($\Delta r = 4$ mm, $\Delta z = 20$ mm), 2 mm grid ($\Delta r = 2$ mm and $\Delta z = 20$ mm) and 1 mm grid ($\Delta r = 1$ mm and $\Delta z = 20$ mm) with theta division varied to keep the volume of each cell same at that height. Here, 'h' and 'H' represents the actual height, where data was plotted and the fluidization height, respectively. No significant difference

was observed between the grids. Therefore, 2 mm grid was selected in this work. Further, the number of divisions in the radial direction was used as 14 and axial direction was 20 divisions. Thereafter, the ensemble average was calculated based on the number of occurrence in each cell.

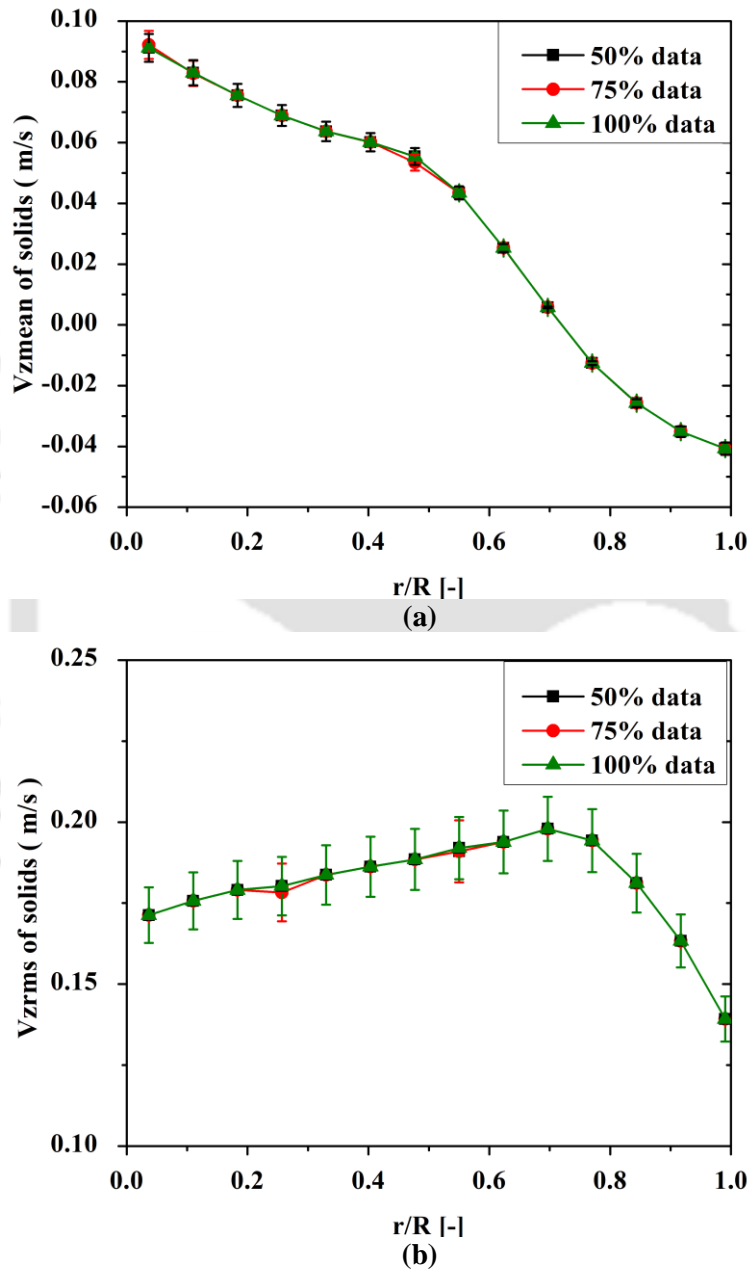


Figure 4.7 Validation of stationarity at $h/H = 0.75$ and 0.14 m/s (1 mm solid) (a) V_{zmean} (b)

V_{zrms}

For the stationarity and reproducibility check, the mean axial solid velocity and mean axial RMS velocity is plotted in Figures 4.7a and 4.7b, using 50%, 75% and 100% of the total acquired data. Results do not show any difference for both mean axial solid and RMS velocities, confirming the reproducibility and stationarity of the RPT data.

4.5 Effect of liquid velocity on monodispersed bed

4.5.1 Velocity vector plots

Figures 4.8a, 4.8b, and 4.8c show the velocity vector plots of 1 mm mono dispersed bed at 0.07, 0.1 and 0.14 m/s liquid inlet velocities. At low liquid inlet velocity (0.07 m/s) one circulation cell exists in the column with an upward motion of solid near wall and downward motion of solid at the center. With the increase in liquid inlet velocity, two circulation cells appear. At the bottom cell, solid moves upward near the wall and downward at the center of the column while at the top cell, solid ascends at the center and descends near the wall. Hence, at the higher liquid inlet velocity of 1 mm, solid velocity vector shows a typical '8' shape. This has been reported by several authors in the cylindrical column for both the gas-solid and liquid-solid fluidized beds (Limtrakul et al., 2005; Upadhyay and Roy, 2010; Jain et al., 2017). The height of the bottom circulation cell either reduces or remains the same with an increase in liquid inlet velocity. In the case of 1 mm mono dispersed bed height of bottom, recirculation cell almost remains the same. Figures 4.8d, 4.8e, and 4.8f show the velocity vector plots of 0.6 mm mono dispersed bed at 0.07, 0.1 and 0.14 m/s liquid inlet velocities, respectively. In the case of 0.6 mm bed, two circulation cells are observed even at lower liquid velocity, 0.07 m/s. This is mainly due to the increased bed height for 0.6 mm bed, which is operated at higher u/u_{mf} ratio, compared to 1 mm bed. Further for 0.6 mm mono dispersed bed, height of bottom recirculation cell reduces with increase in liquid inlet velocity. The bottom recirculation cell completely diminishes at 0.14 m/s liquid inlet velocity and the top

circulation cell dominates the bed. The 0.6 mm bed shows only one circulation cell for 0.14 m/s velocity with solid moving upward in the center and downward near the wall.

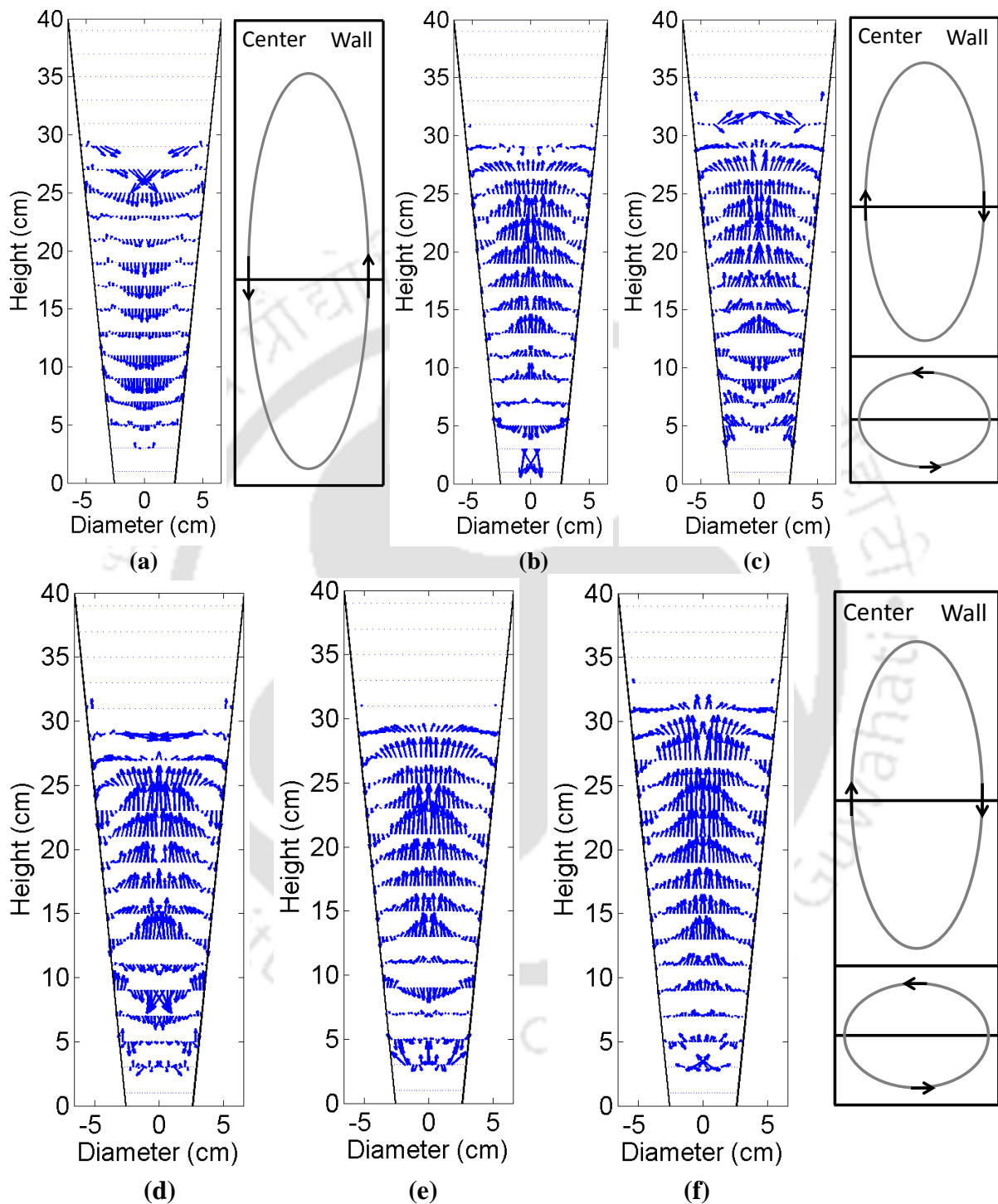


Figure 4.8 Velocity vector plots of mono bed (a) 1 mm solids at 0.07 m/s, (b) 1 mm solids at 0.1 m/s, (c) 1 mm solids at 0.14 m/s, (d) 0.6 mm solids at 0.07 m/s, (e) 0.6 mm solids at 0.1 m/s, and (f) 0.6 mm solids at 0.14 m/s

4.5.2 Number of occurrences

Number of occurrences indicates the total number of time the tracer visits any particular location inside the column. It also indicates the time-averaged solid distribution. A higher value of tracer particle occurrences indicate higher solid fraction at that location. Figure 4.9a and 4.9b show the contour map of occurrence of 1 mm and 0.6 mm solid at 0.14 m/s liquid inlet velocity, respectively. NOC contour of both particles is similar. Increase in solid occurrences was observed from bottom to top. The NOC also increase radially from center to wall. This gives a qualitative picture of the solid fraction in the bed.

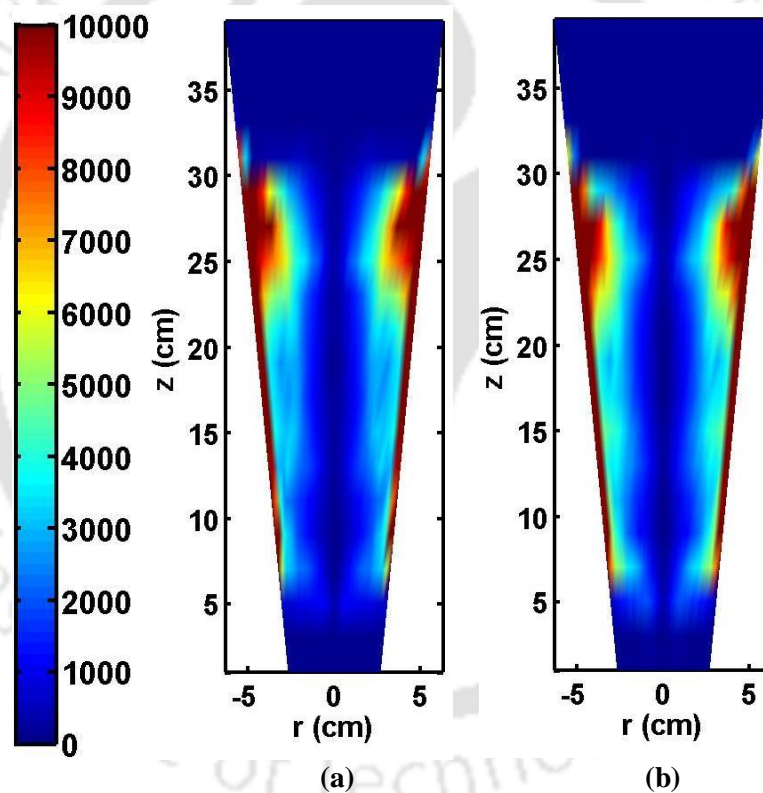


Figure 4.9 Contour map of occurrence of 1 mm and 0.6 mm solids of at 0.14 m/s velocity

4.5.3 Ensemble averaged velocity

Figure 4.10 shows the radial variation of the mean axial velocity of 1 mm and 0.6 mm solid at two different sections. Figures 4.10a and 4.10b show the mean axial solid velocity of 1 mm and 0.6 mm solids with dimensionless radius for top section, respectively.

Similarly, Figures 4.10c and 4.10d show the plot of the mean axial solid velocity of 1 mm and 0.6 mm particles with dimensionless radius at bottom section. The data has been plotted at $h/H = 0.75$ for top section and at $h/H = 0.25$ for bottom section. At low liquid velocity 1 mm solids shows one circulation cell with solids ascending near the wall and descending in the center. However, at a higher liquid velocity at the bottom section solids moves upward near the wall and downward at the center while at the top section opposite flow pattern was observed. 0.6 mm solid shows two circulation cell, even at lower liquid inlet velocity and one circulation cell at higher liquid inlet velocity. For both solids, axial solid velocity was increasing with height. Webster and Perona (1988) have explained that the descending solid motion near wall decreases the cross-sectional area available for ascending solids and increases the upward flow rate of the liquid. This increases the solid velocity on top compared to the bottom section. It was further observed that the velocity of both solids increases with an increase in liquid inlet velocity. However, the increase in mean axial velocity of solid was not significant when liquid velocity was increased from 0.1 m/s to 0.14 m/s. This indicates some shift in the mechanism at high liquid velocity for both solids.

The radial mean solid velocity of both solids are presented in Figures 4.11a and 4.11b on the top section while the radial mean solid velocity of both solids are shown in Figures 4.11c and 4.11d at bottom section, respectively. The radial components of solid velocity were negligible as compared to axial solid velocity for both solids. With an increase in velocity, the radial velocity does not show any increment that indicates that the solid motion is mainly in the axial direction. The positive and negative value of radial velocity indicates outward and inward motion of solids, respectively.

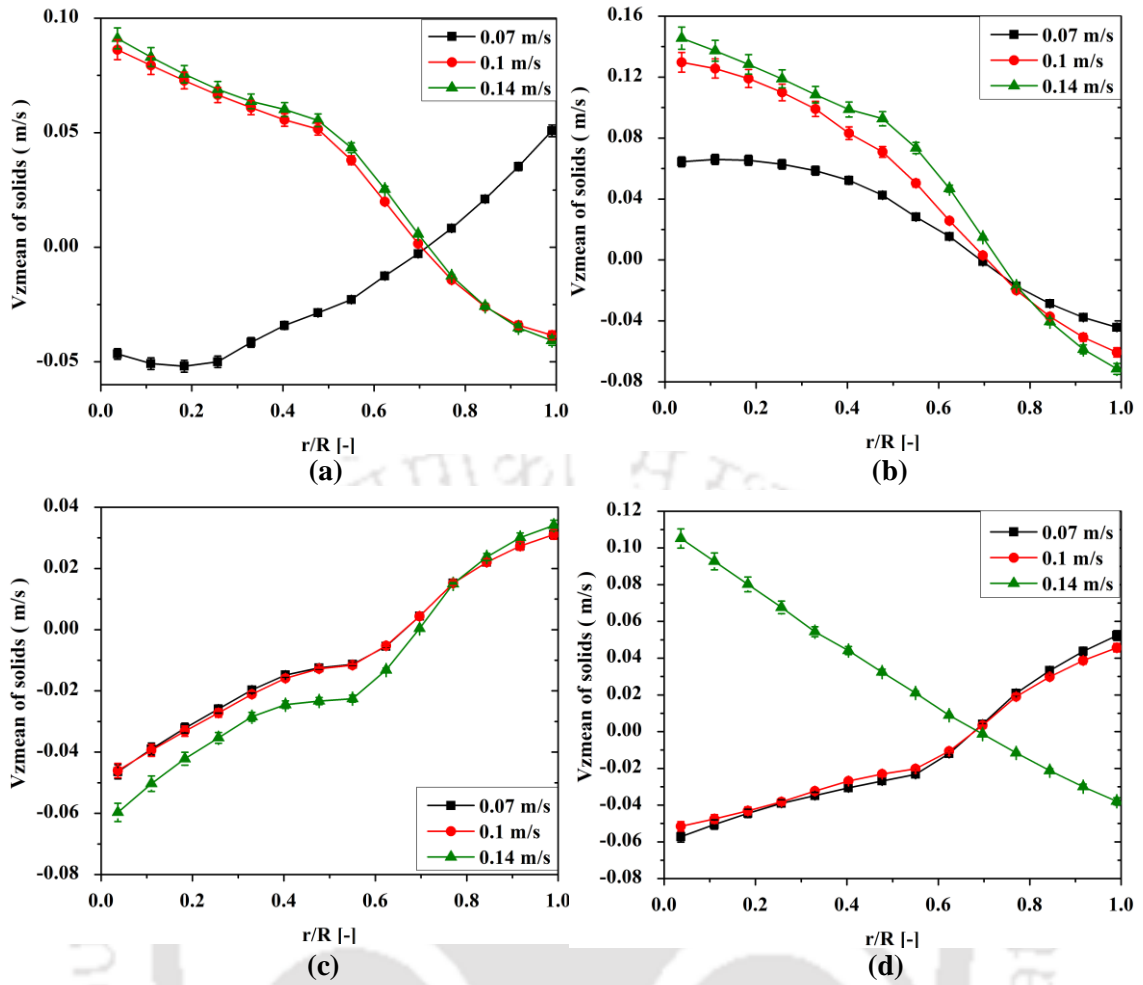


Figure 4.10 Variation of mean axial velocity of solid at different velocities: (a) 1 mm particle on top section, (b) 0.6 mm particle on top section, (c) 1 mm particle at bottom section, and (d) 0.6 mm particle at bottom section

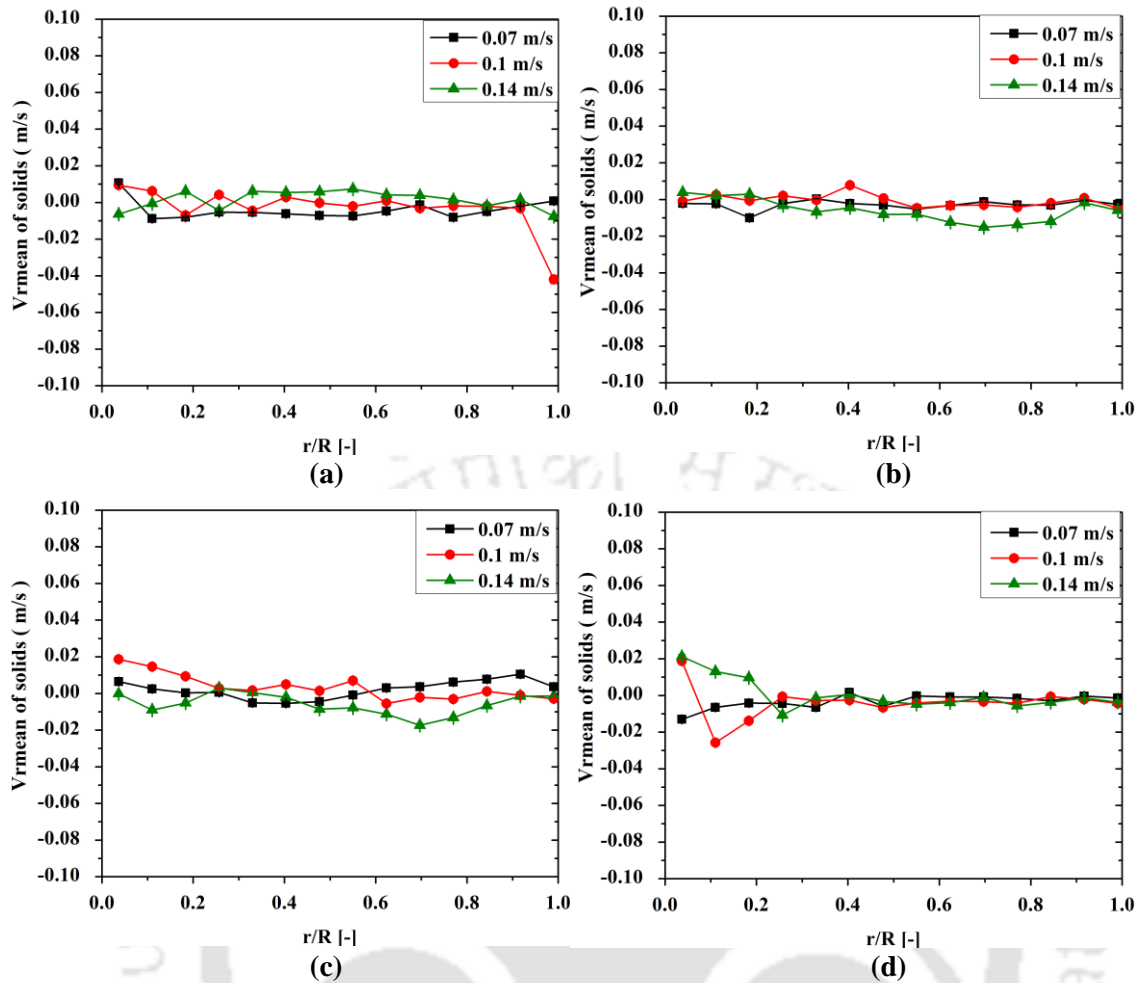


Figure 4.11 Variation of mean radial velocity of solid at different velocities: (a) 1 mm particle on top section, (b) 0.6 mm particle on top section, (c) 1 mm particle at bottom section, and (d) 0.6 mm particle at bottom section

4.5.4 Solid velocity fluctuations

Figures 4.12a and 4.12b show the plot of mean axial RMS velocity of 1 mm and 0.6 mm particles on top section, respectively. Figures 4.12c and 4.12d represent the plot of mean axial RMS velocity of 1 mm and 0.6 mm particles at bottom section, respectively. Higher axial RMS velocity is observed in case of 0.6 mm solids compared to 1 mm solids as it was operated at higher u/u_{mf} . Further, the axial RMS is increasing with an increase in liquid velocity due to an increase in energy input to the system. The axial RMS velocity of both solids are higher in the annular region and lower at the center and near the wall

region. The region where axial RMS velocity is higher corresponds to the boundary where the direction of solid motion changes from upward to downward.

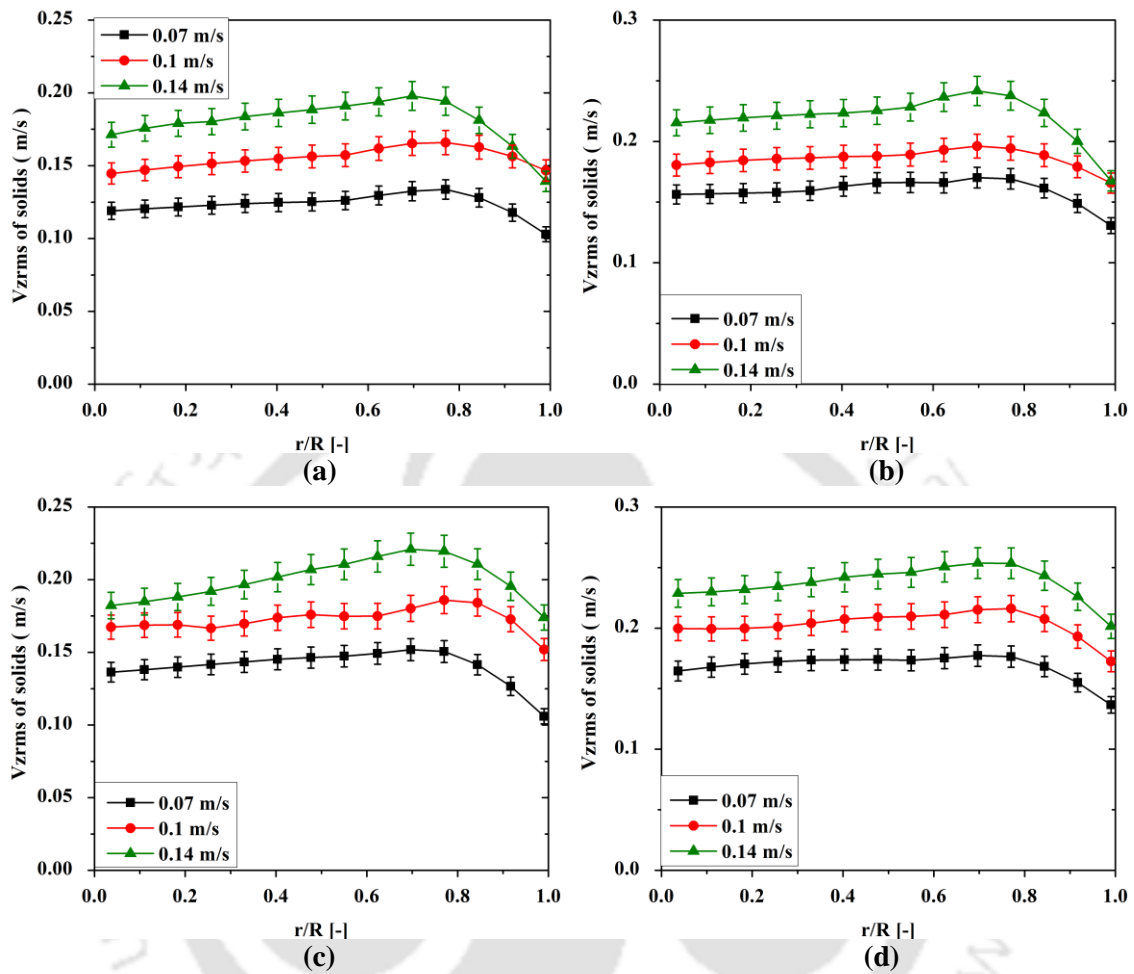


Figure 4.12 Variation of V_{zrms} of solid at different velocities: (a) 1 mm particle on top section, (b) 0.6 mm particle on top section, (c) 1 mm particle at bottom section, and (d) 0.6 mm particle at bottom section

Figures 4.13a and 4.13b show variation of radial RMS velocity of 1 mm and 0.6 mm solids at the top sections for different liquid velocities whereas Figures 4.13c and 4.13d show variation of radial RMS velocity for 1 mm and 0.6 mm solids at bottom sections. The radial RMS velocity shows high fluctuation in the center and low near the wall even though the mean radial velocity was negligible. Further, the magnitude of radial RMS velocity for both solids was approximately same as of the axial RMS velocity. This

indicates the presence of particle-particle interaction in the liquid-solid conical fluidized bed. The low radial RMS velocity near the wall was due to wall restriction. The radial RMS velocity for 0.6 mm solid was more compared to 1 mm solids this was mainly due to the high velocity of 0.6 mm solid compared to 1 mm solid. The axial RMS of liquid-solid bed is observed to be too low compared to gas-solid bed as shown in the previous chapter. However, the radial RMS velocity is equal to the gas-solid system or even higher for 0.6 mm solid.

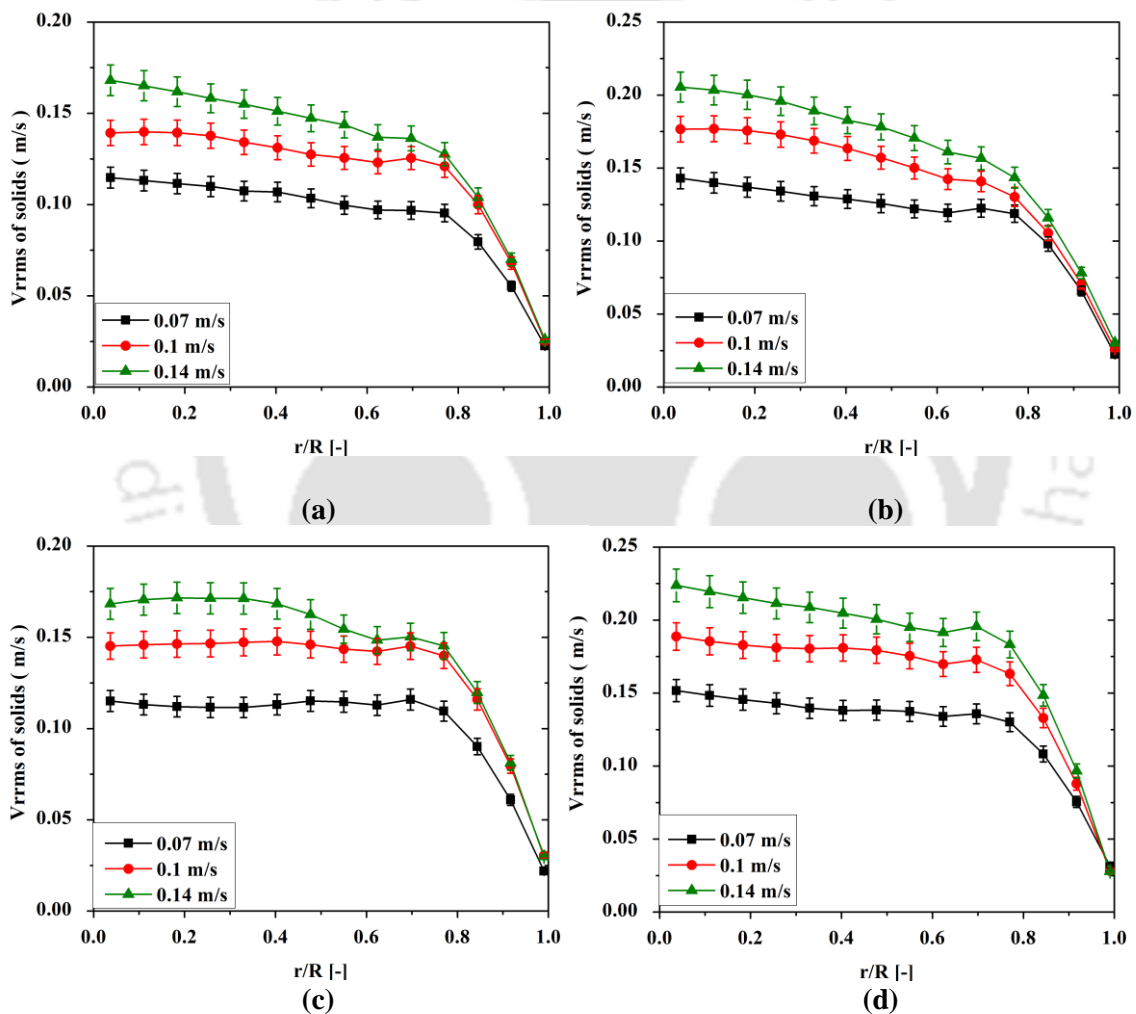


Figure 4.13 Variation of V_{rrms} of solid at different velocities: (a) 1 mm particle on top section, (b) 0.6 mm particle on top section, (c) 1 mm particle at bottom section, and (d) 0.6 mm particle at bottom section

4.5.5 Granular temperature

Figure 4.14 presents the granular temperature of 1 mm and 0.6 mm particles. Figures 4.14a and 4.14c show the granular temperature trends for 1 mm solid on top and the bottom section, and Figures 4.14b and 4.14d show the granular temperature trends for 0.6 mm solid on top and bottom sections. Results indicate that granular temperature was approximately same throughout the column for both solids. This signifies that liquid-solid conical fluidized bed is homogeneous in nature. The value of granular temperature value is decreasing near wall due to restriction.

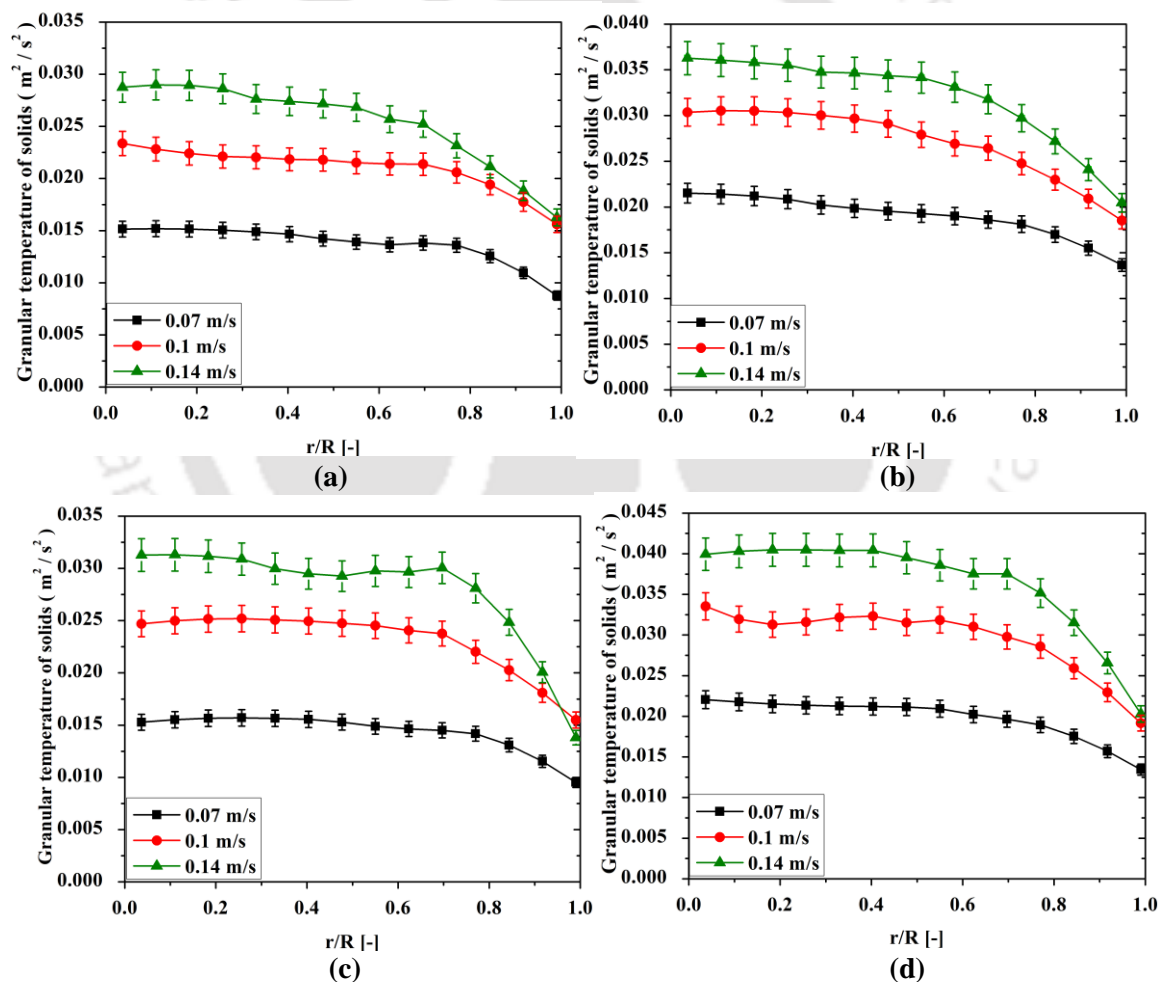


Figure 4.14 Variation of granular temperature of solid at different velocities: (a) 1 mm particle on top section, (b) 0.6 mm particle on top section, (c) 1 mm particle at bottom section, and (d) 0.6 mm particle at bottom section

4.5.6 Hurst exponent

The pox diagram obtained from R/S analysis is illustrated in Figure 4.15a and 4.15b for 1 mm and 0.6 mm particles respectively at 0.14 m/s liquid inlet velocity. The Hurst exponent values for both solids are 0.78 that shows the solid motion is persistent/super dispersive in nature. Table 4.3 shows the Hurst exponent value for both solids for all the operating conditions. The Hurst exponent value for both 1 mm and 0.6 mm solid is higher than 0.5 for all cases indicating persistent behavior of the solid. The Hurst exponent value is increasing with liquid inlet velocity indicating an increase in persistence nature.

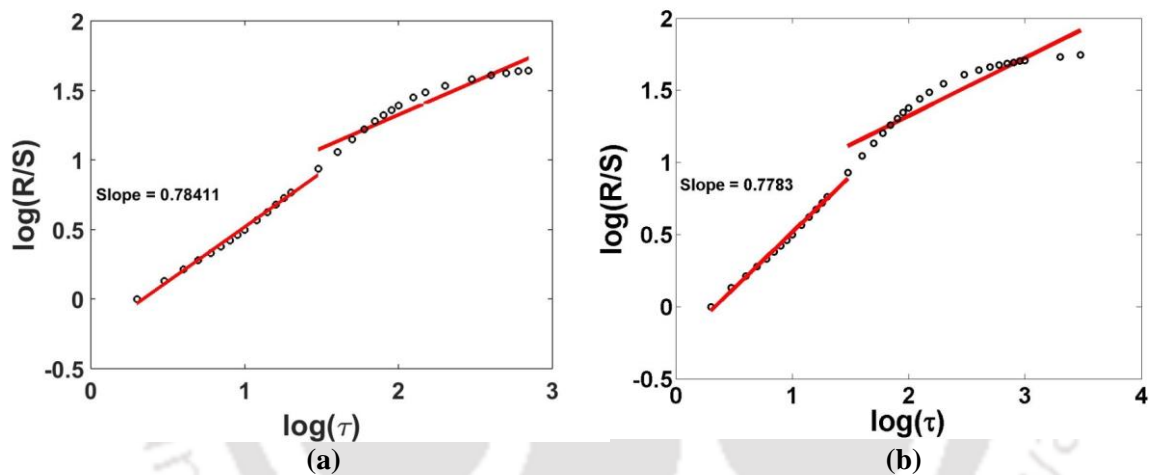


Figure 4.15 Hurst exponent at 0.14 m/s liquid velocity for (a) 1 mm solid, and (b) for 0.6 mm solid

Table 4.3 Hurst exponents at different operating conditions for 1 mm and 0.6 mm particle in mono bed

Fluid Velocity	Bed composition	Hurst exponent
0.07 m/s	Mono 1 mm	0.66
0.1 m/s	Mono 1 mm	0.74
0.14 m/s	Mono 1 mm	0.78
0.07 m/s	Mono 0.6 mm	0.71
0.1 m/s	Mono 0.6 mm	0.76
0.14 m/s	Mono 0.6 mm	0.78

4.5.7 Autocorrelation

Figures 4.16a, 4.16b and 4.16c represent the axial autocorrelation function of 1 mm solids at 0.07, 0.1 and 0.14 m/s liquid inlet velocity, respectively. Figures 4.16d, 4.16e and 4.16f represent the axial autocorrelation function of 0.6 mm solids at 0.07, 0.1 and 0.14 m/s liquid inlet velocity, respectively. The axial autocorrelation first decays to zero and then dips to below zero to a negative value and thereafter it settle down at zero. The axial autocorrelation in liquid-solid fluidized bed decays slowly compared to the gas-solid fluidized bed. Further, it does not show any oscillation due to no bubble activity. The decay time reduces with increase in liquid inlet velocity. Figure 4.17 shows the radial autocorrelation with increasing liquid inlet velocity for both solids. The radial autocorrelation for both solids shows a similar trend. However, the radial autocorrelation decays faster than axial autocorrelation as the motion is primarily in the axial direction for

all velocities. But, the radial autocorrelation decays slower in liquid-solid bed as compared to the gas-solid system.



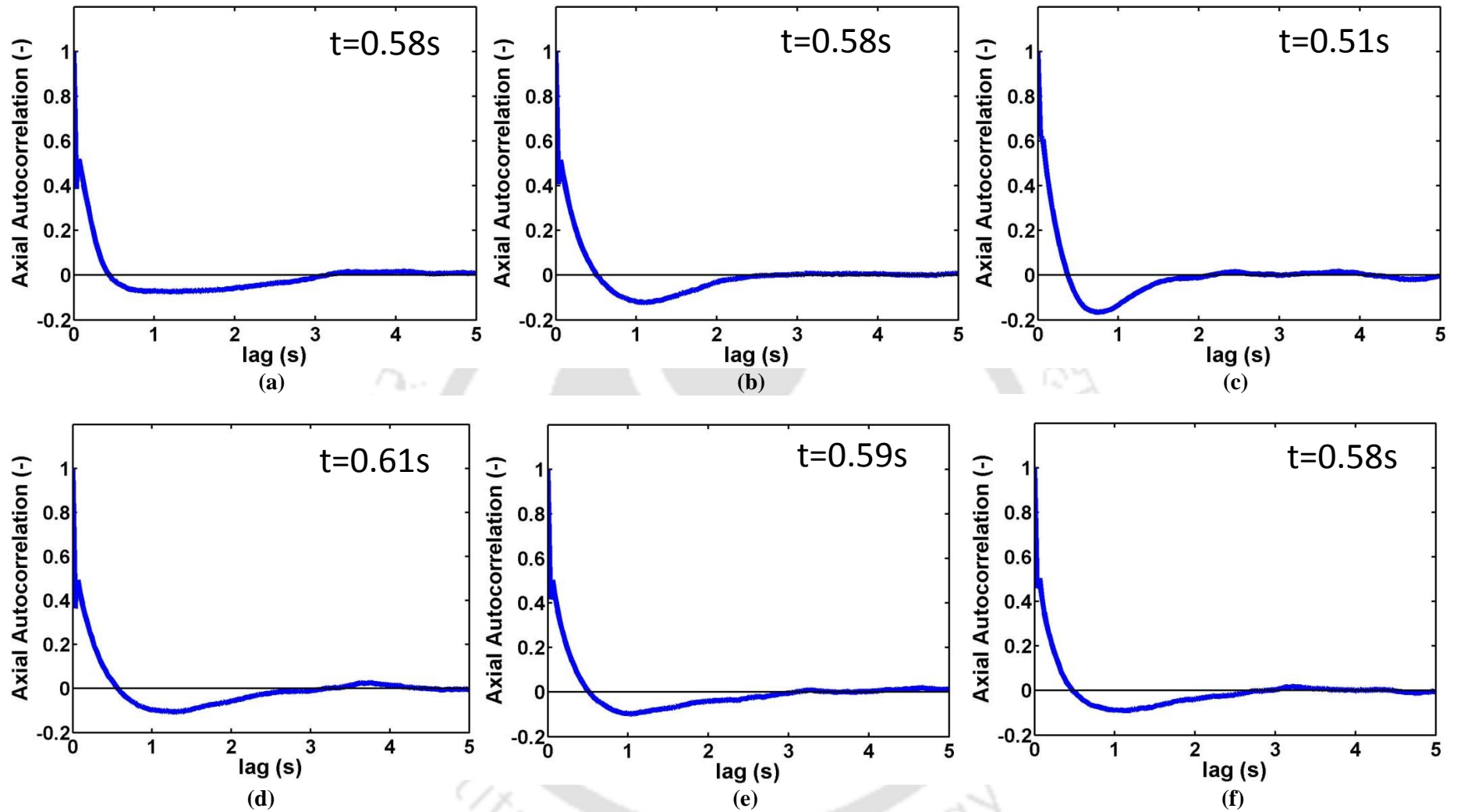


Figure 4.16 Variation of axial autocorrelation of solid at different velocities: (a) 1 mm particle at 0.07 m/s, (b) 1 mm particle at 0.1 m/s, (c) 1 mm particle at 0.14 m/s, (d) 0.6 mm particle at 0.07 m/s, (e) 0.6 mm particle at 0.1 m/s, and (f) 0.6 mm particle at 0.14 m/s

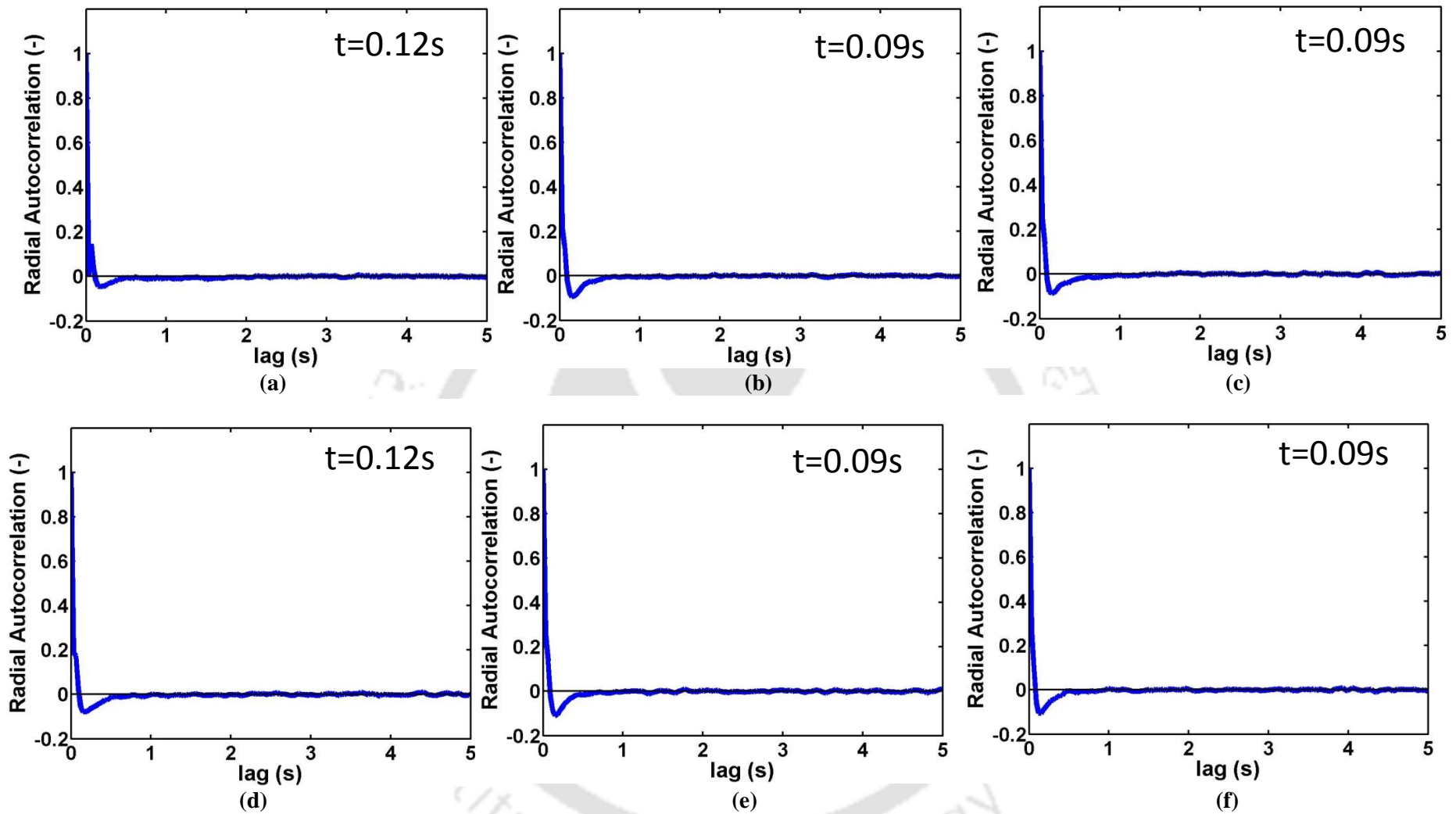


Figure 4.17 Variation of radial autocorrelation of solid at different velocities: (a) 1 mm particle at 0.07 m/s, (b) 1 mm particle at 0.1 m/s, (c) 1 mm particle at 0.14 m/s, (d) 0.6 mm particle at 0.07 m/s, (e) 0.6 mm particle at 0.1 m/s, and (f) 0.6 mm particle at 0.14 m/s

4.5.8 Kolmogorov entropy

Figure 4.18 shows the influence of the liquid inlet velocity on the Kolmogorov entropy (KE) for both solids. The bed was found to be chaotic with a finite value of Kolmogorov entropy for all the experimental operating velocities. The difference in chaotic behavior was observed at high liquid velocities for both solids due to the higher u/u_{mf} ratio. The fluidized bed of 0.6 mm particles shows a higher degree of chaotic behavior than the mono 1 mm bed, likely because the 0.6 mm bed was operated at a higher u/u_{mf} ratio compared to the 1 mm bed. KE shows an increasing trend with inlet velocity for both solids. KE plot shows a change in slope for both solids at 0.1 m/s liquid inlet velocity. This confirms regime transition for both solids at liquid velocity 0.1 m/s.

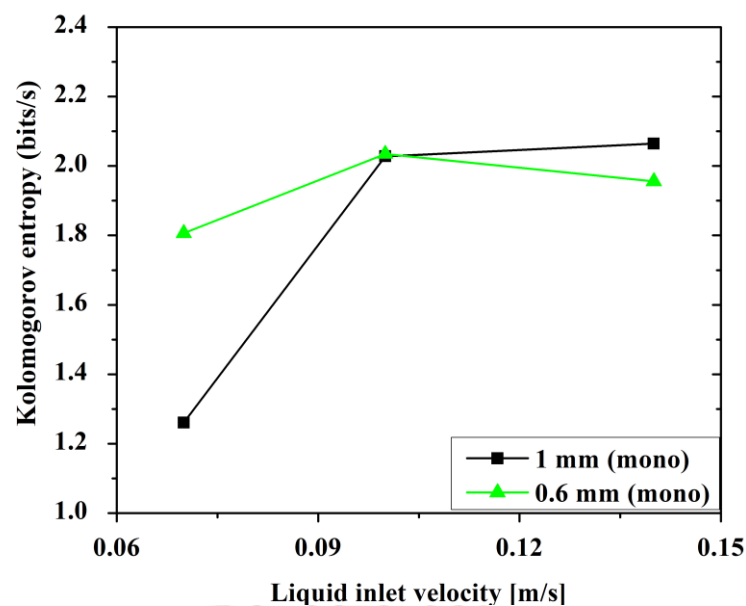


Figure 4.18 Kolmogorov entropy of 1 mm and 0.6 mm particle with liquid inlet velocity

4.5.9 Correlation dimension

Figure 4.19 shows the correlation dimension of 1 mm and 0.6 mm particles with liquid inlet velocity. CD values for both solids increases with liquid inlet velocity for both solids. This confirms that the bed was chaotic for both solids. Further, the CD value

increases with liquid velocity indicating that bed becomes more complex at high velocity. The difference in chaotic behavior was observed at high liquid velocities for both solids due to a higher u/u_{mf} ratio. The fluidized bed of 0.6 mm particles shows a higher degree of chaotic behavior than the mono 1 mm bed, likely because the 0.6 mm bed is operated at a higher u/u_{mf} ratio compared to the 1 mm bed. CD plot shows a change in slope for both solids at 0.1 m/s liquid inlet velocity. This confirms regime transition for both solids at a liquid velocity of 0.1 m/s.

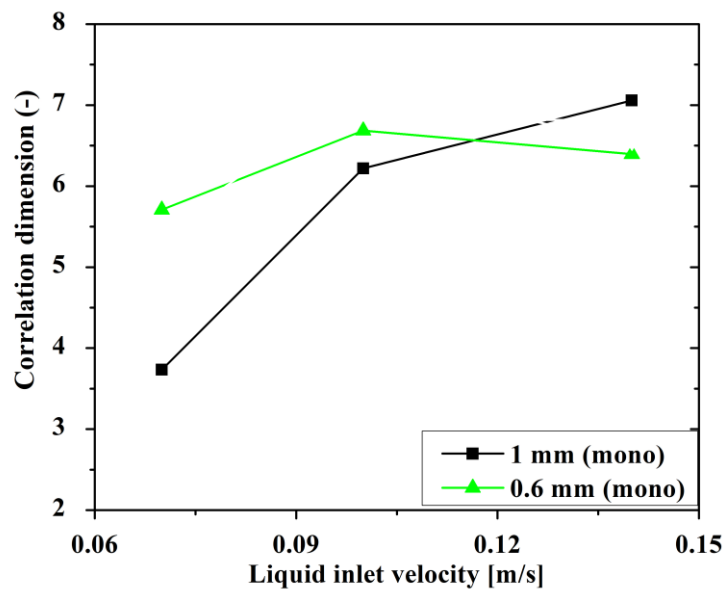


Figure 4.19 Correlation dimension of 1 mm and 0.6 mm particle with liquid inlet velocity

4.6 Effect of liquid velocity on mono and binary dispersed beds

Experiments are performed for mono and 50b-50s mixture binary beds. The bed is operated at 0.07, 0.1 and 0.14 m/s, respectively for both mono and binary beds to understand the effect of velocity and composition of the flow characteristic of the conical fluidized bed. It is to be noted that in binary fluidized bed motion of both particles are tracked individually.

4.6.1 Ensemble averaged velocity

Figure 4.20 shows the mean axial solid velocity profiles of 1 mm and 0.6 mm solids in mono and 50b-50s wt. % binary beds for different liquid inlet velocities. Results were plotted at z/Z of 0.25 and 0.75 and represented here as the bottom and top sections, respectively. Figures 4.20a, 4.20b, and 4.20c illustrate the axial solid velocities on the top section of bed while Figures 4.20d, 4.20e, and 4.20f represent the solid velocities at the bottom section for three different liquid inlet velocities. Results show that for both the bottom and top sections velocity of binary bed solids were bounded between the two mono beds of 0.6 mm and 1 mm solids. The velocity was maximum for 0.6 mm mono bed solid and minimum for 1 mm mono bed. It indicates momentum transfer from smaller to bigger solids in the binary bed of 50b-50s wt. % composition. These particle-particle interactions increased the velocity of 1 mm solid and decreased the velocity of 0.6 mm solid in the binary bed of 50b-50s wt. % composition compared to their mono beds. Similar phenomena were observed in the liquid-solid cylindrical fluidized bed by Jain et al. (2017). Therefore, it can be stated that the behavior of liquid-solid conical fluidized bed is similar to the liquid-solid cylindrical fluidized bed. However, it was observed that for low liquid inlet velocity the solids in binary bed follows the behavior of 0.6 mm mono bed in which at top section particles ascends at the center and descends near the wall. Further, the velocity of 0.6 mm and 1 mm particles in binary bed were close to the velocity of solid in 0.6 mm mono bed. Hence, it can be stated that at low liquid velocity smaller size particle governs the flow pattern of the binary liquid-solid conical fluidized bed. However, at high liquid velocity bigger particle governs the flow behavior of binary bed. The velocity of 0.6 mm and 1 mm solids in binary bed at top section was close to solid velocity in 1 mm mono bed at 0.14 m/s liquid velocity. The bottom section also shows an identical trend, where similar to 1 mm mono bed two circulation cell was

observed for the binary bed of 50b-50s wt. %. The velocity magnitude of 1 mm and 0.6 mm solids in binary bed was also close to the velocity of solid in 1 mm mono bed. At 0.10 m/s liquid velocity the velocity of 0.6 mm and 1 mm particle in binary bed was approximately similar. However, it was not the case for 0.07 and 0.14 m/s liquid inlet velocity which signifies better mixing at 0.10 m/s liquid velocity. These results are different from the cylindrical liquid-solid fluidized bed where solid mixing increases with liquid velocity (Jain et al., 2017). The possible reason may be the regime transition at 0.10 m/s liquid inlet velocity for investigated bed.

Figure 4.21 depicts the plot of the mean radial velocity of 1 mm and 0.6 mm particles in mono and binary dispersed beds of 50b-50s composition. The magnitude of radial solid velocity is negligible for all operating conditions and remains same for both solids. The mean radial solid velocity is not changing with the axial level of the column. The mean radial velocity profile is the same for mono as well as the binary dispersed beds.

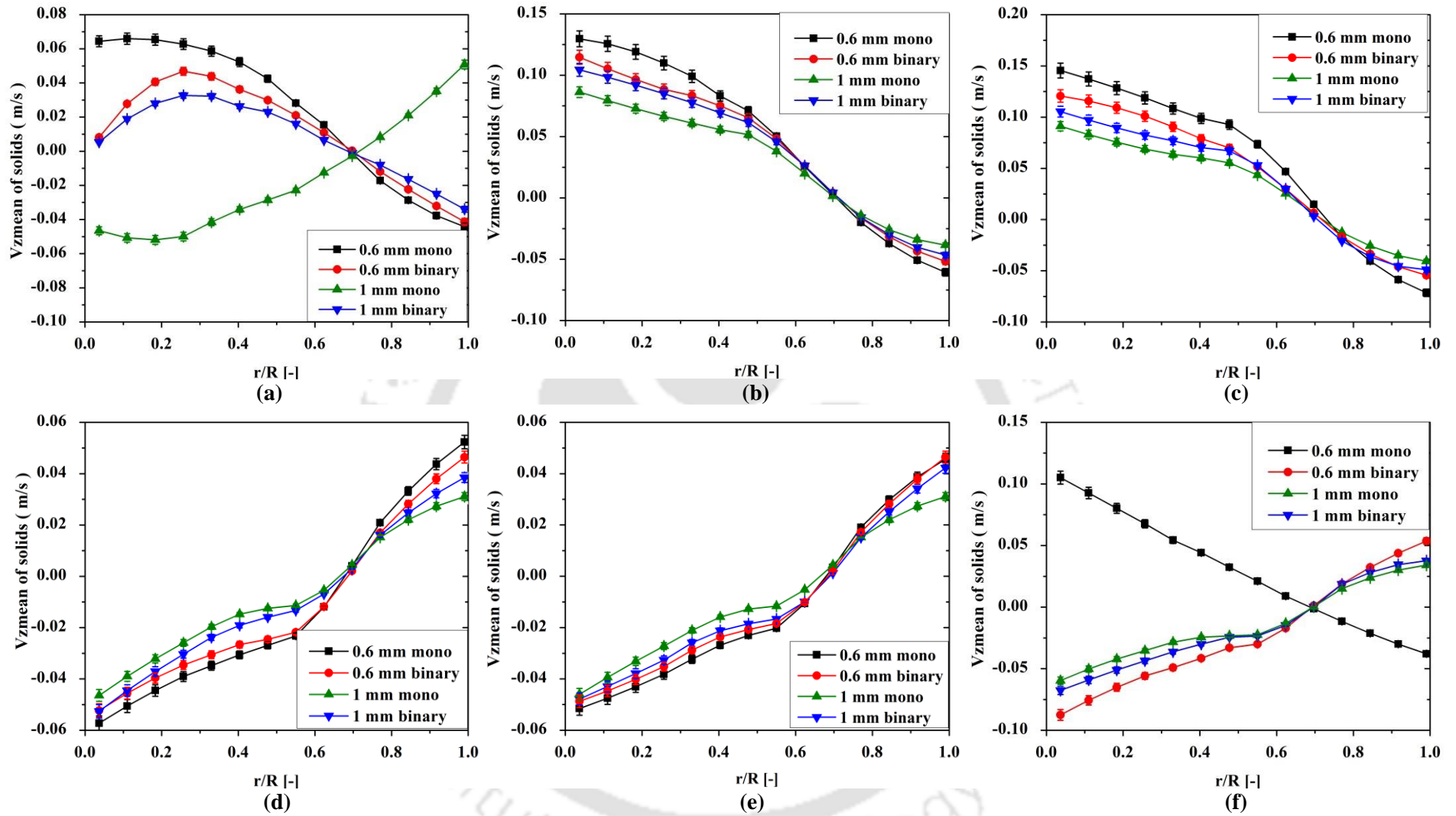


Figure 4.20 Variation of mean axial velocity of solid at different velocities with composition: (a) top section at 0.07 m/s, (b) top section at 0.1 m/s, (c) top section at 0.14 m/s, (d) bottom section at 0.07 m/s, (e) bottom section at 0.1 m/s, and (f) bottom section at 0.14 m/s

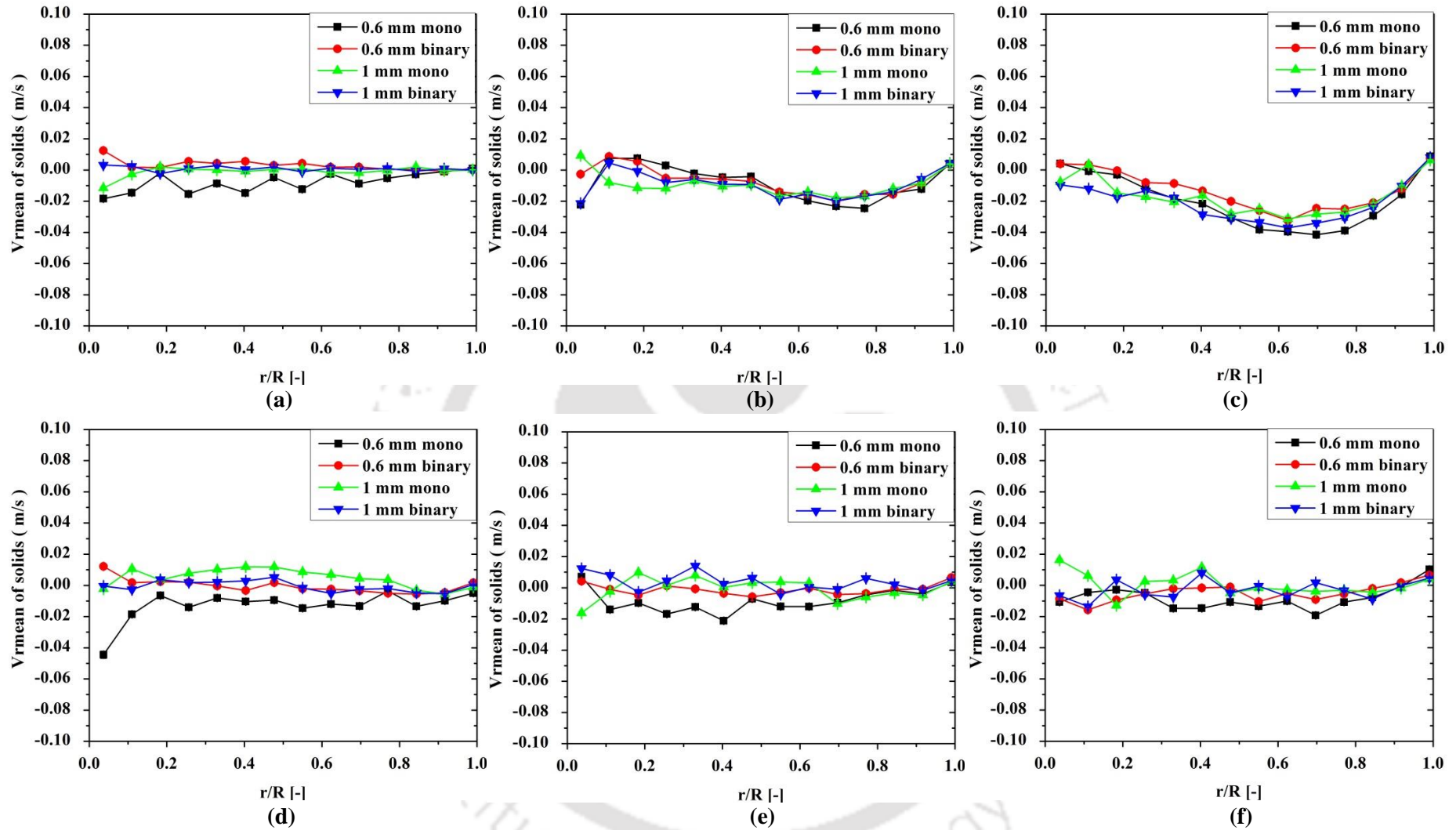


Figure 4.21 Variation of radial velocity of solid at different velocities with composition: (a) top section at 0.07 m/s, (b) top section at 0.1 m/s, (c) top section at 0.14 m/s, (d) bottom section at 0.07 m/s, (e) bottom section at 0.1 m/s, and (f) bottom section at 0.14 m/s

4.6.2 Solid velocity fluctuations

Figure 4.22 presents the radial variation of axial root-mean-square (RMS) velocity of 0.6 mm and 1 mm particles at the top and bottom sections for mono and binary beds. The trend of radial variation of axial RMS velocity remains same for mono and binary dispersed beds at all liquid inlet velocities. In 50b-50s wt. % binary bed, axial RMS velocities of both solids are bounded between two mono dispersed bed of 1 mm and 0.6 mm particle, respectively. The trend remains the same for all the liquid inlet velocities. These results confirm that particle-particle interaction plays a vital role in determining the behavior of liquid-solid conical fluidized bed. The smaller particle which is being operated at higher u/u_{mf} ratio transfer some of its momentum to bigger particle operated at lower u/u_{mf} ratio. These momentum exchange between 0.6 mm and 1 mm particle increases the axial RMS velocity of the bigger particle and reduces the axial RMS velocity for smaller particle compared to their respective mono dispersed bed. The axial RMS for 1 mm solid was lowest and the axial RMS for 0.6 mm solid was highest. The axial RMS velocity of both the solids remains almost the same at the bottom and the top sections of the bed for both mono and binary dispersed beds. This shows liquid-solid conical fluidized bed is more homogeneous compared to liquid solids cylindrical fluidized bed (Jain et al., 2017) and the gas-solid conical fluidized bed (Kalo et al., 2018). The axial RMS velocity of both solids increases with an increase in liquid inlet velocity for both mono and binary dispersed beds. It is mainly due to an increase in energy input with an increase in liquid velocity. At low liquid inlet velocity, 0.07 m/s, the axial RMS velocity of 0.6 mm and 1 mm particles in binary bed was close to their respective mono bed. With the increase in liquid inlet velocity, 0.1m/s, the axial RMS velocity of both solids were almost same which signifies larger particle-particle interaction and mixed bed. However, with further increase in liquid velocity, 0.14 m/s, the value of axial RMS

velocity for both solids in binary bed was different. This signifies the change in mechanism and hence possible regime transition. The trend of axial RMS velocity remains the same for the top and bottom sections of the bed.

Figure 4.23 shows the radial RMS velocity for both mono and 50b-50s wt. % binary bed for three different liquid velocities. Figures 4.23a, 4.23b, and 4.23c present the radial RMS velocity on the top section of bed while Figures 4.23d, 4.23e, and 4.23f present the radial RMS velocity at the bottom section. Though no significant mean radial velocity was observed, the radial RMS velocity shows high fluctuation particularly at the center of the column. The results signify a higher contribution of particle-particle interaction which results in higher radial fluctuation. The magnitude of axial and radial RMS velocity was almost the same at the center of the column. The radial RMS velocity near the wall was less due to wall restriction. The radial RMS velocity of solids was increasing with the increase in liquid inlet velocity. It is mainly due to the higher solid velocity at increased liquid velocity. Further, the radial fluctuation of 0.6 mm mono dispersed bed was always higher than 1 mm mono dispersed bed. For the binary bed, radial RMS velocity of 0.6 mm and 1 mm particle was bounded between their respective mono dispersed beds.

4.6.3 Granular temperature

Figures 4.24a, 4.24b, and 4.24c represent the granular temperature on the top section of bed while Figures 4.24d, 4.24e, and 4.24f represent the bottom section results. Granular temperature shows a similar trend as of axial and radial RMS velocities. The granular temperature of 0.6 mm and 1 mm solids in binary bed was bounded between their respective mono beds. The value of granular temperature was high for higher liquid inlet velocity. The granular temperature of 0.6 mm and 1 mm solids in binary bed was almost

same at 0.1 m/s liquid inlet velocity in 50b-50s wt. % binary bed which signifies better mixing.



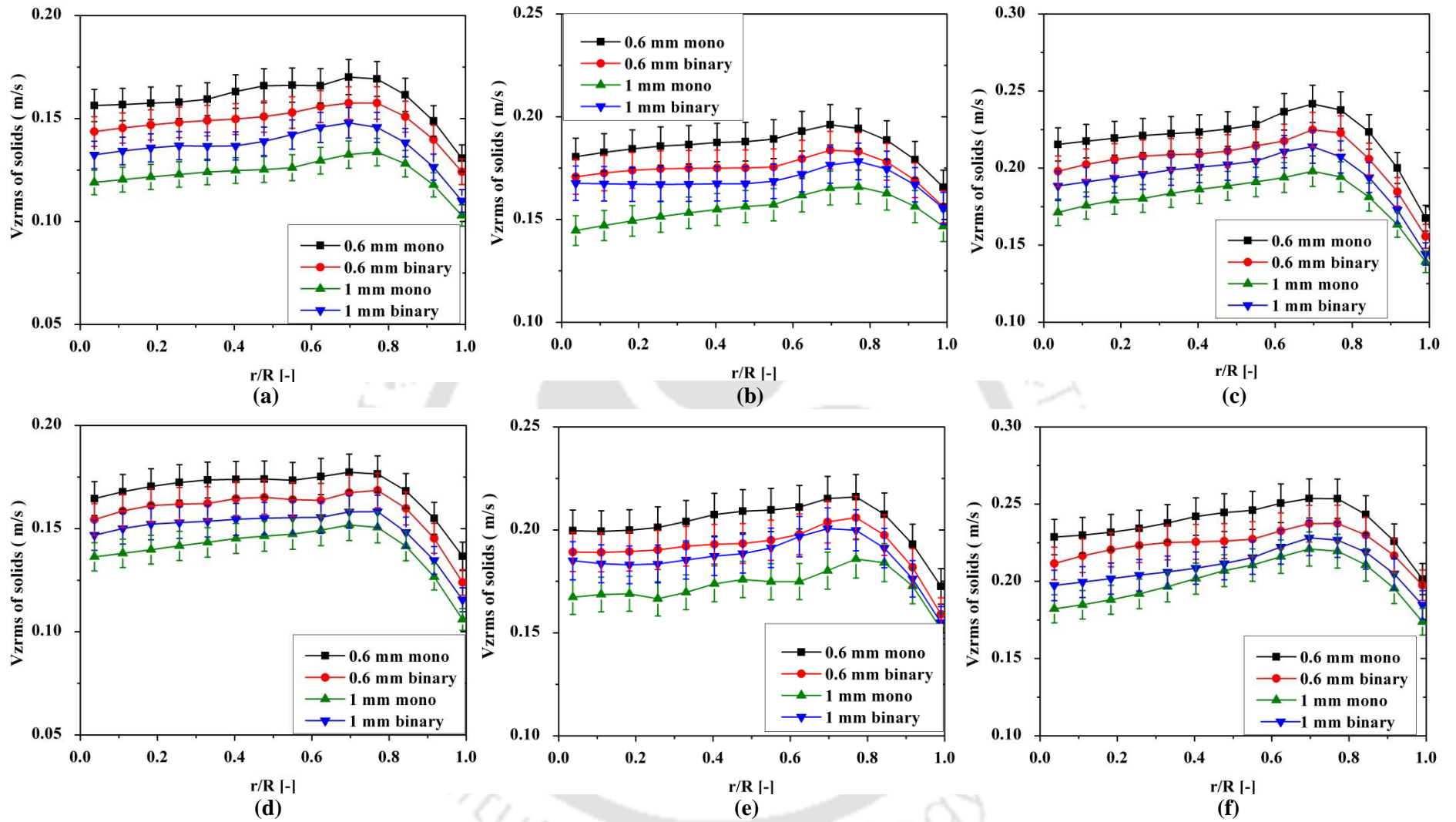


Figure 4.22 Variation of V_{zrms} of solid at different velocities with composition: (a) top section at 0.07 m/s, (b) top section at 0.1 m/s, (c) top section at 0.14 m/s, (d) bottom section at 0.07 m/s, (e) bottom section at 0.1 m/s, and (f) bottom section at 0.14 m/s

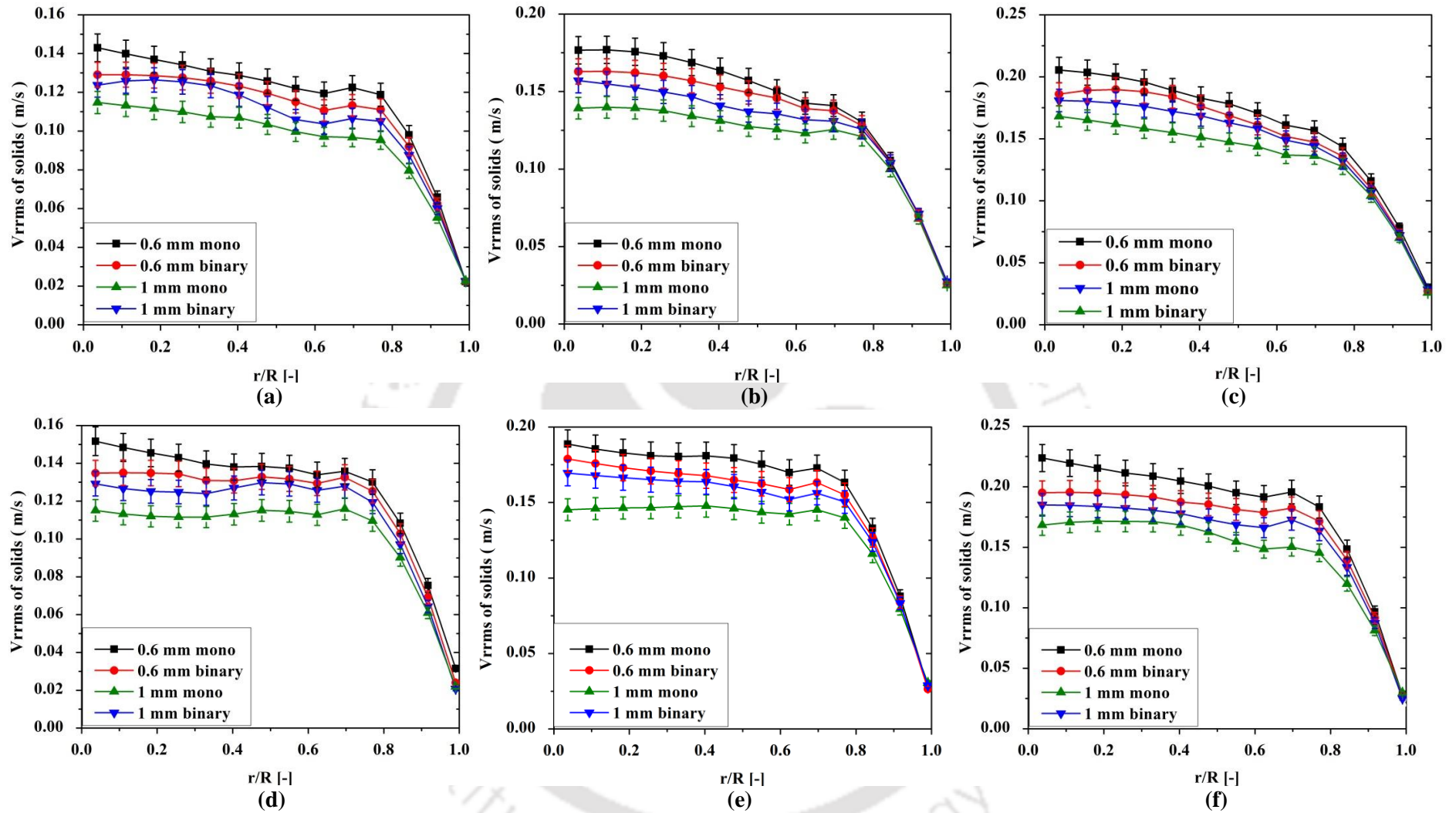


Figure 4.23 Variation of V_{rms} of solid at different velocities with composition: (a) top section at 0.07 m/s, (b) top section at 0.1 m/s, (c) top section at 0.14 m/s, (d) bottom section at 0.07 m/s, (e) bottom section at 0.1 m/s, and (f) bottom section at 0.14 m/s

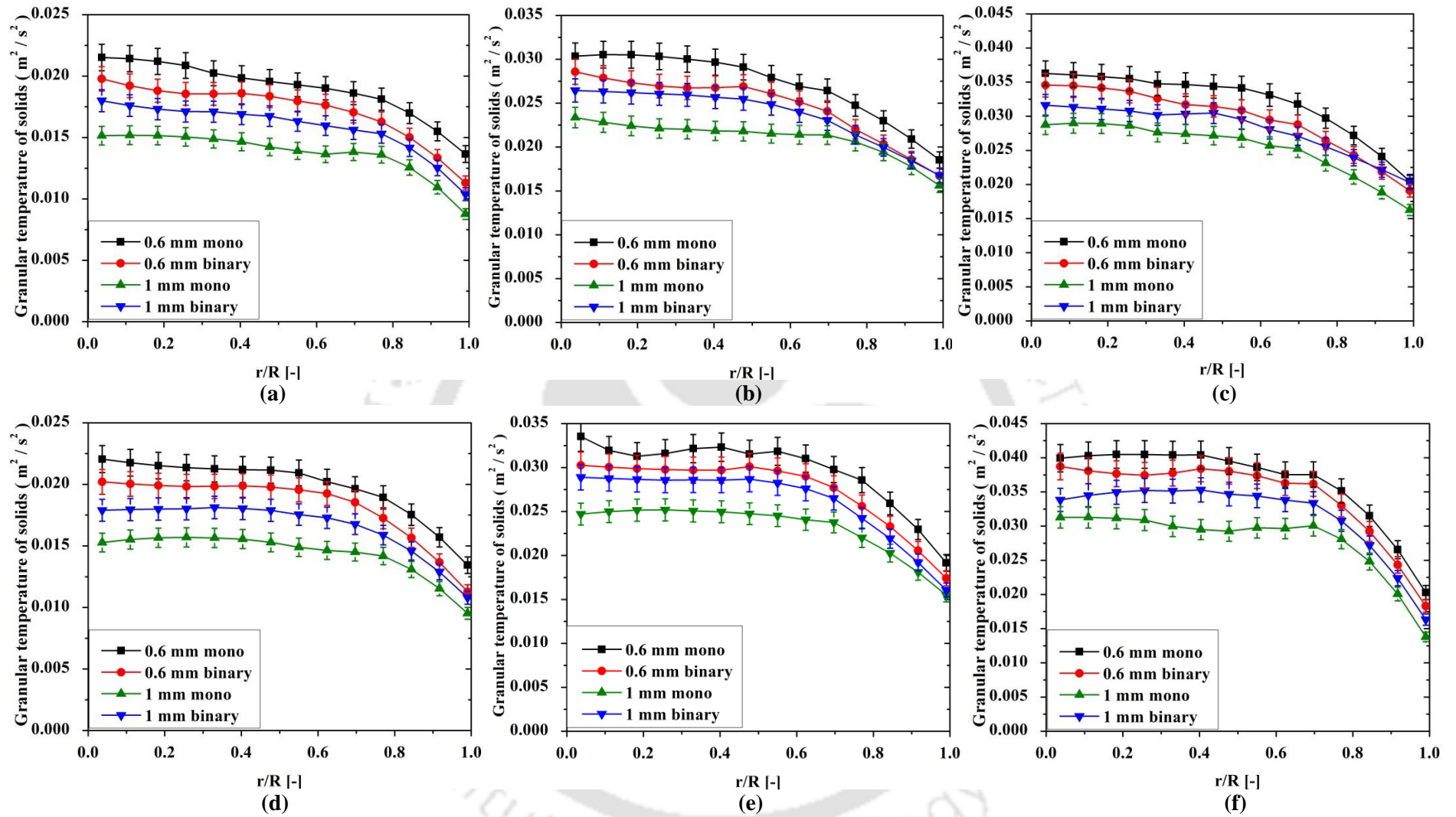


Figure 4.24 Variation of granular temperature of solid at different velocities with composition: (a) top section at 0.07 m/s, (b) top section at 0.1 m/s, (c) top section at 0.14 m/s, (d) bottom section at 0.07 m/s, (e) bottom section at 0.1 m/s, and (f) bottom section at 0.14 m/s

4.6.4 Hurst exponent

Hurst exponent value was obtained from the Rescaled Range analysis of instantaneous velocities. Table 4.4 shows the Hurst exponent value for binary bed at all the operating velocities. The Hurst exponent value for both the solids was higher than 0.5 for all the velocities. It confirms that the solids motion was persistent/super dispersive in the liquid-solid conical fluidized bed. It represents a positive correlation between the velocities of the solids indicating no reversal of the present trend with time. Figure 4.25 shows the Hurst exponent values for both the solids in 50b-50s wt. % binary bed with liquid inlet velocity. A change in slope was observed at 0.1 m/s liquid velocity representing a regime transition. However, further analysis is required to confirm the regime transition.

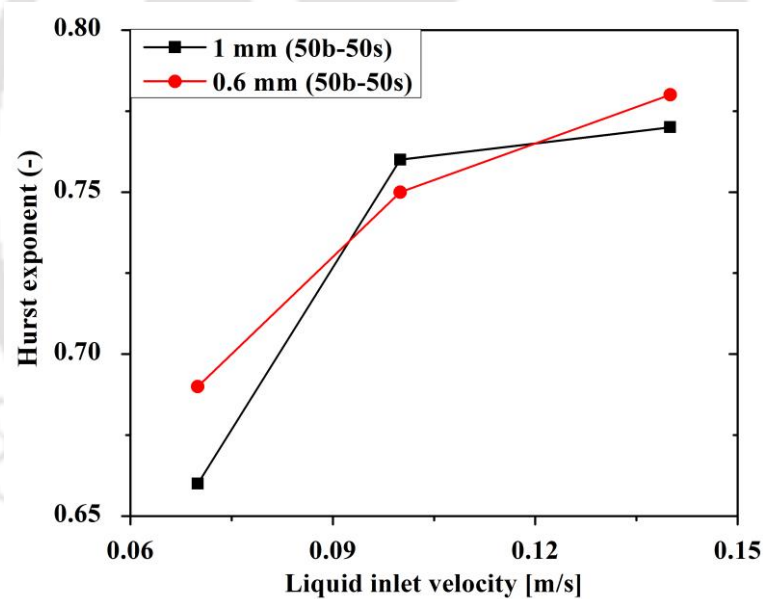


Figure 4.25 Hurst exponent with liquid inlet velocity

Table 4.4 Hurst exponents at different operating conditions for 1 mm and 0.6 mm particle 50b-50s bed

Liquid velocity	Bed composition	Hurst exponent
0.07 m/s	50b-50s 1 mm	0.67
0.1 m/s	50b-50s 1 mm	0.76
0.14 m/s	50b-50s 1 mm	0.77
0.07 m/s	50b-50s 0.6 mm	0.69
0.1 m/s	50b-50s 0.6 mm	0.75
0.14 m/s	50b-50s 0.6 mm	0.78

4.6.5 Autocorrelation

Autocorrelation represents the correlation of a signal to itself. The plot of autocorrelation as a function of time lag shows how long the data is correlated to itself. Figures 4.26a, 4.26b, and 4.26c represent the axial autocorrelation function of 1 mm solids at 0.07, 0.1 and 0.14 m/s liquid inlet velocity in 50b-50s wt. % binary bed. Figures 4.26d, 4.26e, and 4.26f represent the axial autocorrelation function of 0.6 mm solids at different liquid inlet velocity in 50b-50s wt. % binary bed. The autocorrelation function first decayed to zero and became negative before reaching a constant value of zero finally. The trend of autocorrelation function remains the same for both the solids in binary bed for all the investigated liquid velocity. However, the time lag of solids (when it first crosses the zero values) initially decreases with an increase in liquid velocity and then increases. This shows the higher velocity of solids in binary bed at 0.10 m/s liquid velocity compared to 0.07 and 0.14 m/s liquid inlet velocity. This further signifies regime change. The trend remains the same for both the solids. It was also observed that time lag in the liquid-solid conical fluidized bed is higher compared to the gas-solid conical fluidized bed. This

shows the liquid-solid conical bed is calm compared to the gas-solid conical bed. Figure 4.27 shows the radial autocorrelation with increasing liquid inlet velocity for both the solids. The radial autocorrelation shows a similar trend as axial autocorrelation. The trend of radial autocorrelation remains the same for both solids. The decay of radial autocorrelation is faster as compared to axial autocorrelation as the solid motion is primarily in the axial direction.



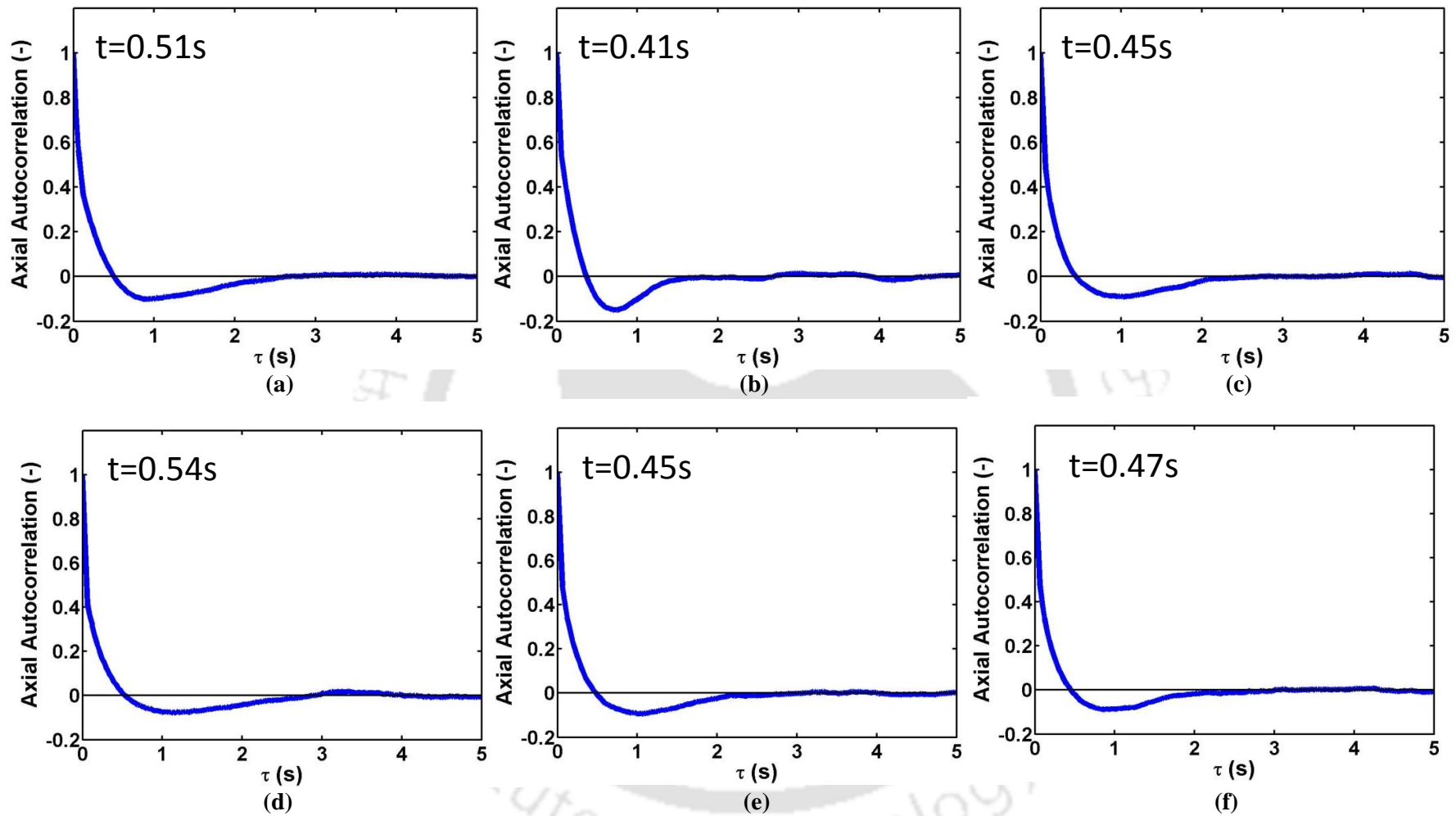


Figure 4.26 Variation of axial autocorrelation of solid at different velocities in binary bed (a) 1 mm particle at 0.07 m/s, (b) 1 mm particle at 0.1 m/s, (c) 1 mm particle at 0.14 m/s, (d) 0.6 mm particle at 0.07 m/s, (e) 0.6 mm particle at 0.1 m/s, and (f) 0.6 mm particle at 0.14 m/s

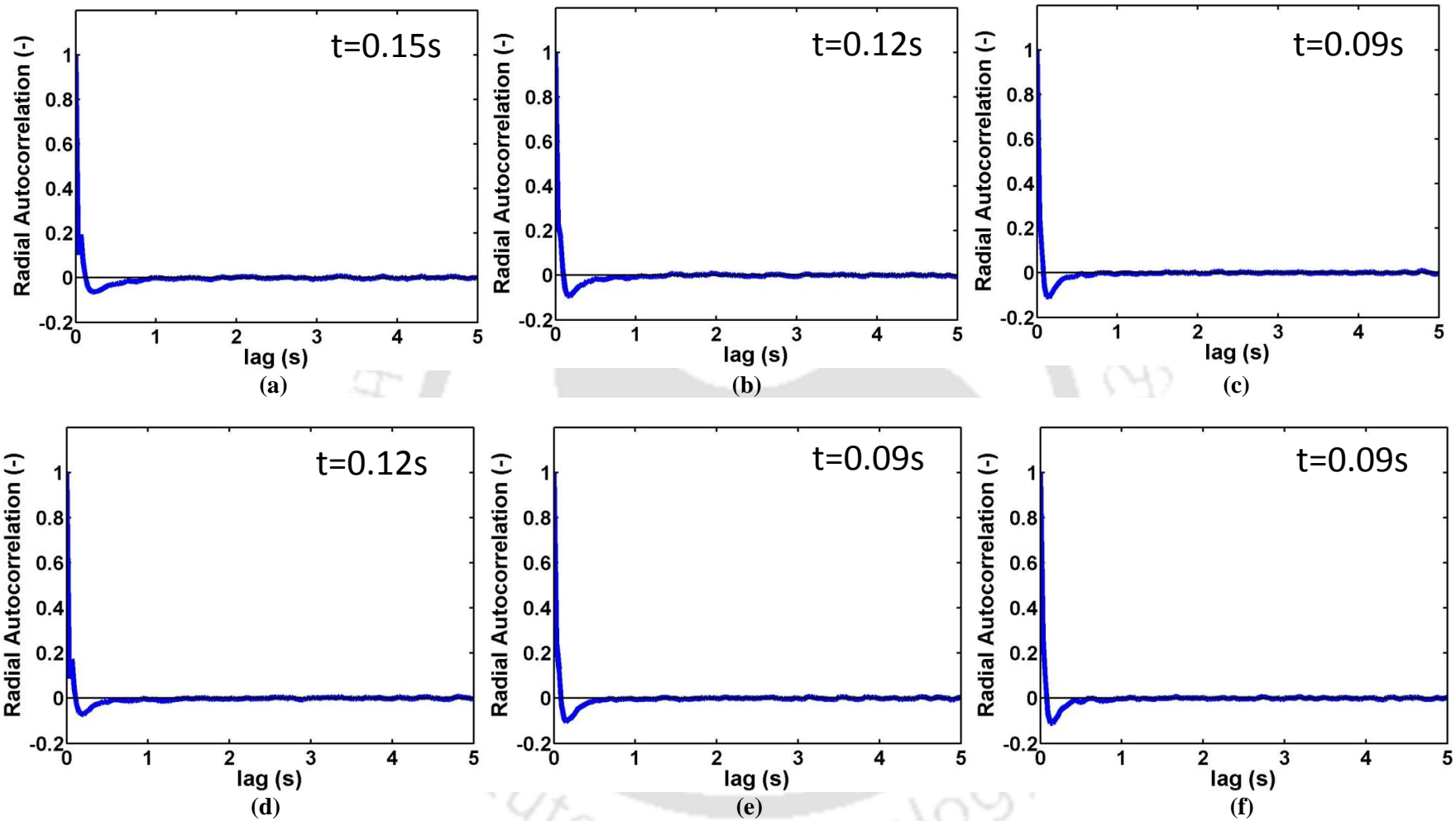


Figure 4.27 Variation of radial autocorrelation of solid at different velocities in binary bed (a) 1 mm particle at 0.07 m/s, (b) 1 mm particle at 0.1 m/s, (c) 1 mm particle at 0.14 m/s, (d) 0.6 mm particle at 0.07 m/s, (e) 0.6 mm particle at 0.1 m/s, and (f) 0.6 mm particle at 0.14 m/s

4.6.6 Segregation index

The segregation index was used to identify the regime change and mixing quality of the fluidized bed in binary bed condition. It was calculated by using the probability of occurrences of both solids in a binary bed composition. The segregation indexes were calculated for both the solids for 50b-50s wt. % binary bed at all the three liquid velocities. The segregation index value for all the liquid velocity was above 0.97 indicating good mixing of the bed even at the low velocity of 0.07 m/s (i.e. $2 u_{mpf}$ of bigger solid). Jain et al. (2017) have observed segregation in cylindrical bed at a low velocity of $1.5 u_{mpf}$ of bigger solid. Hence, it can be concluded that conical bed gives good mixing than cylindrical bed even at low velocity. A plot of segregation indexes vs. liquid inlet velocity is presented in Figure 4.28. Figure 4.28 shows a change in slope at a velocity of 0.1 m/s. This can be again identified as a regime transition around 0.1 m/s inlet velocity.

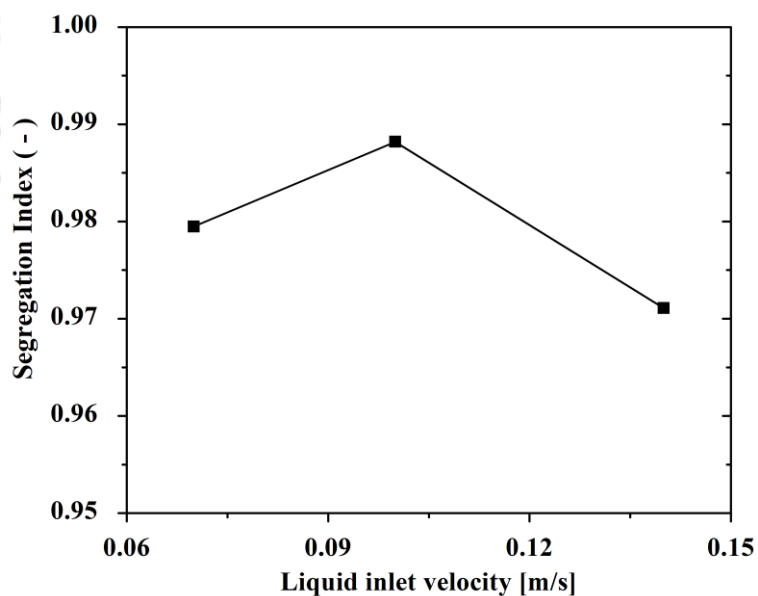


Figure 4.28 Variation of segregation index of solid with liquid inlet velocity for binary dispersed bed

4.6.7 Kolmogorov entropy

Figure 4.29 shows the KE plot of both solids with liquid inlet velocity for both mono and binary dispersed beds. KE indicates the chaotic nature of the bed at both mono and binary dispersed beds for all three velocities. For both 0.6 and 1 mm, solid slope change was observed for mono and binary dispersed bed. Thus, indicating regime transition at 0.1 m/s liquid inlet velocity for both solids. It was also observed that binary bed was more chaotic at higher velocity compared to the monodispersed bed.

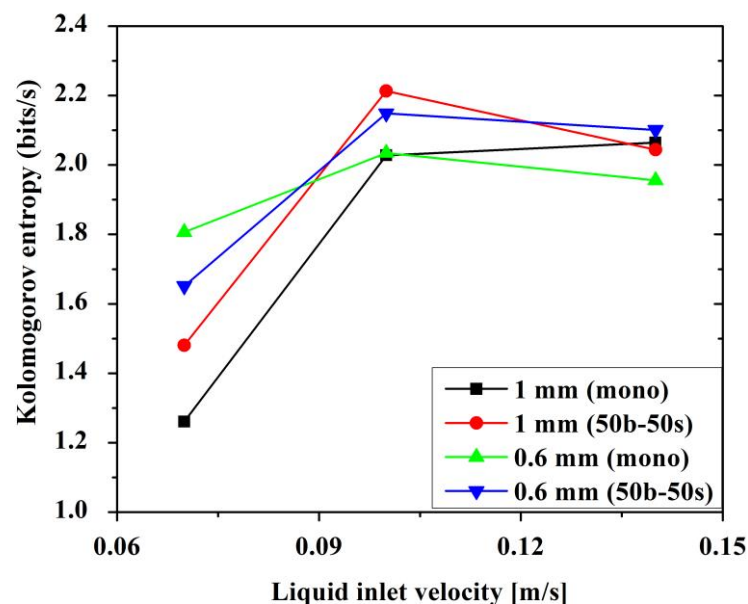


Figure 4.29 Kolmogorov entropy of 1 mm and 0.6 mm particle with liquid inlet velocity

4.6.8 Correlation dimension

The plot of CD vs. liquid inlet velocity for both mono and 50b-50s wt. % binary bed are illustrated in Figure 4.30. CD was calculated from position data of RPT of both solids. CD shows a similar trend as KE for both the solids. For 1 mm mono bed CD value is increasing with liquid inlet velocity though the slope of the curve changes. However, for 0.6 mm mono bed CD value is increasing first and then decreasing with liquid velocity. For both mono and binary dispersed bed regime transition was observed at 0.1 m/s liquid inlet velocity.

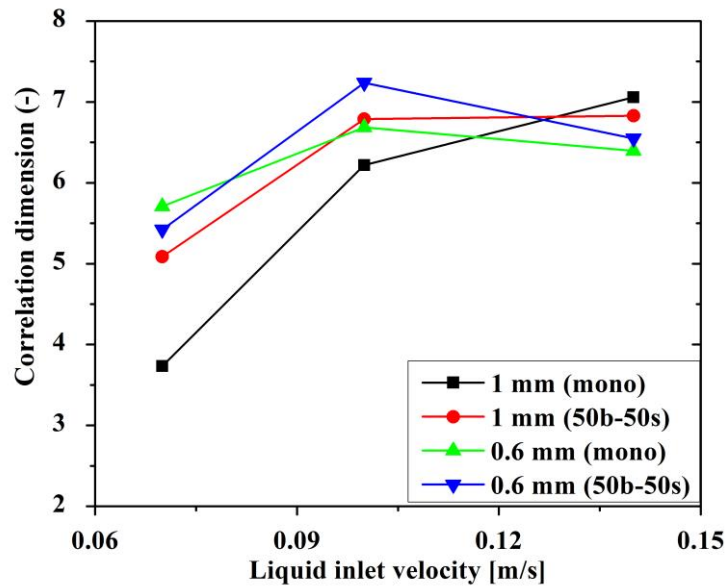


Fig. 4.30 Correlation dimension of 1 mm and 0.6 mm particle with liquid inlet velocity

4.7 Effect of bed composition

Experiments were performed for various bed composition of solid, i.e. 100:0, 75:25, 50:50 and 25:75 ratios of both the solids by weight. The composition of the bed in 50b-50s mixture was 50% bigger particle and 50% smaller particle by weight. Similarly, the 75b-25s mixture contained 75% of bigger particle and 25% of smaller particle and 25b-75s mixture contained 25% of bigger particle and 75% of the smaller particle. The monodispersed bed was 100% bigger particle for 1 mm solid and 100% smaller particle for 0.6 mm solid. The bed was operated at a constant velocity of 0.14 m/s for all the cases to determine the composition effect on the bed behavior. Both solids were tracked individually for each set of experiments for 8 hours.

4.7.1 Ensemble averaged velocity

Figure 4.31 is the comparison plot of solid axial velocity for mono, 50b-50s, 75b-25s and 25b-75s compositions at 0.14 m/s. Figures 4.31a and 4.31b show the solid axial velocity of 1 mm and 0.6 mm solid on top and Figures 4.31c and 4.31d show the solid axial

velocity of 1 mm and 0.6 mm solid on the bottom section. The velocity of 1 mm solid is minimum in mono bed and maximum in 25b-75s mixture bed at both the section. It indicates the solid axial velocity increases with the increasing fraction of 0.6 mm solids in the mixture and vice-versa for 0.6 mm solid. It means the composition of solid has an immense effect on the hydrodynamic parameter.

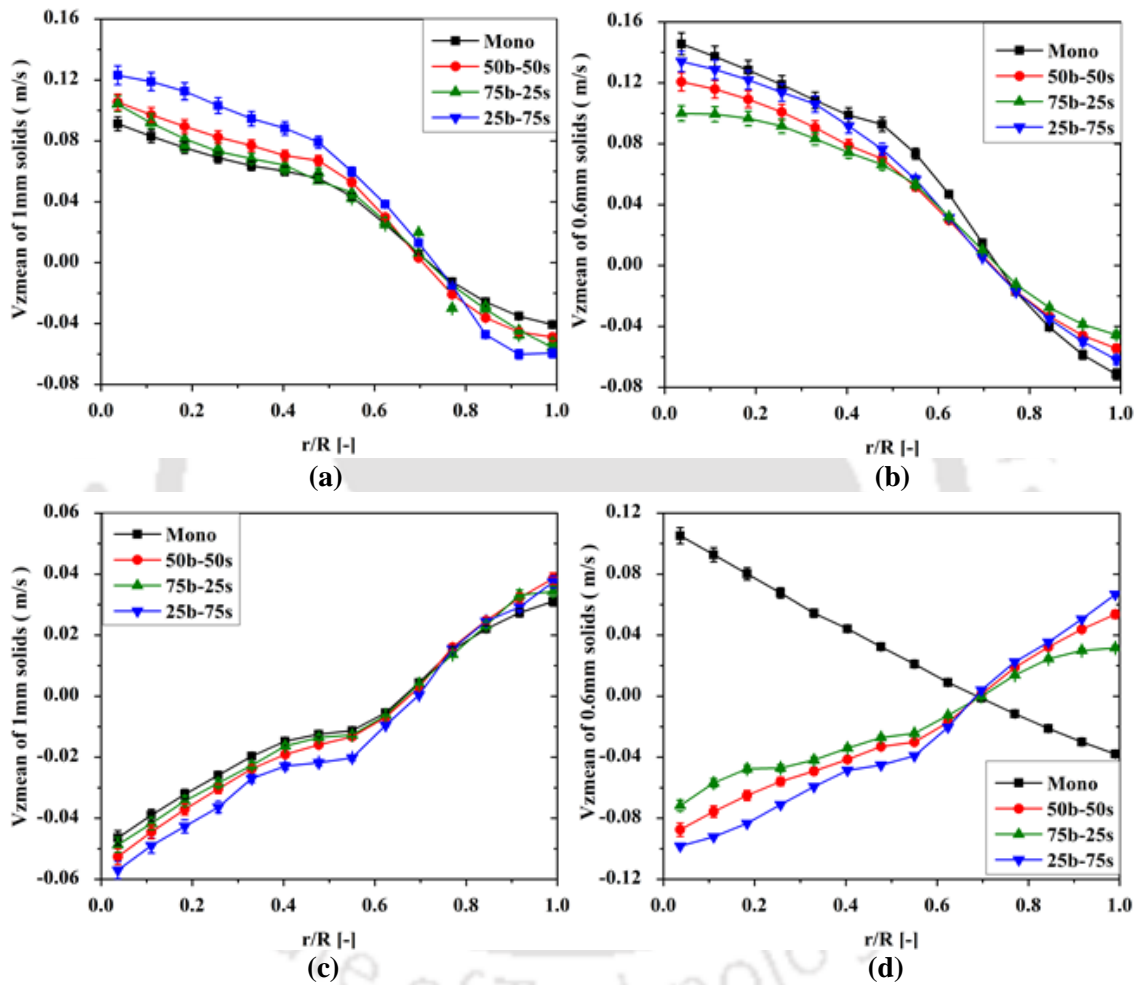


Figure 4.31 Variation of mean axial velocity of solid with different composition: (a) 1 mm particle on top section, (b) 0.6 mm particle on top section, (c) 1 mm particle at bottom section, and (d) 0.6 mm particle at bottom section

Figure 4.32 presents the variation of radial mean solid velocity for all compositions. It does not show any variation with the addition of 1 mm particle to the bed of 0.6 mm particle or vice versa. Figures 4.32a and 4.32b represent the radial solid velocity on the

top section of bed while Figures 4.32c and 4.32d represent the velocity at the bottom section of the column. The radial mean solid velocity is negligible compared to the mean axial solid velocity.

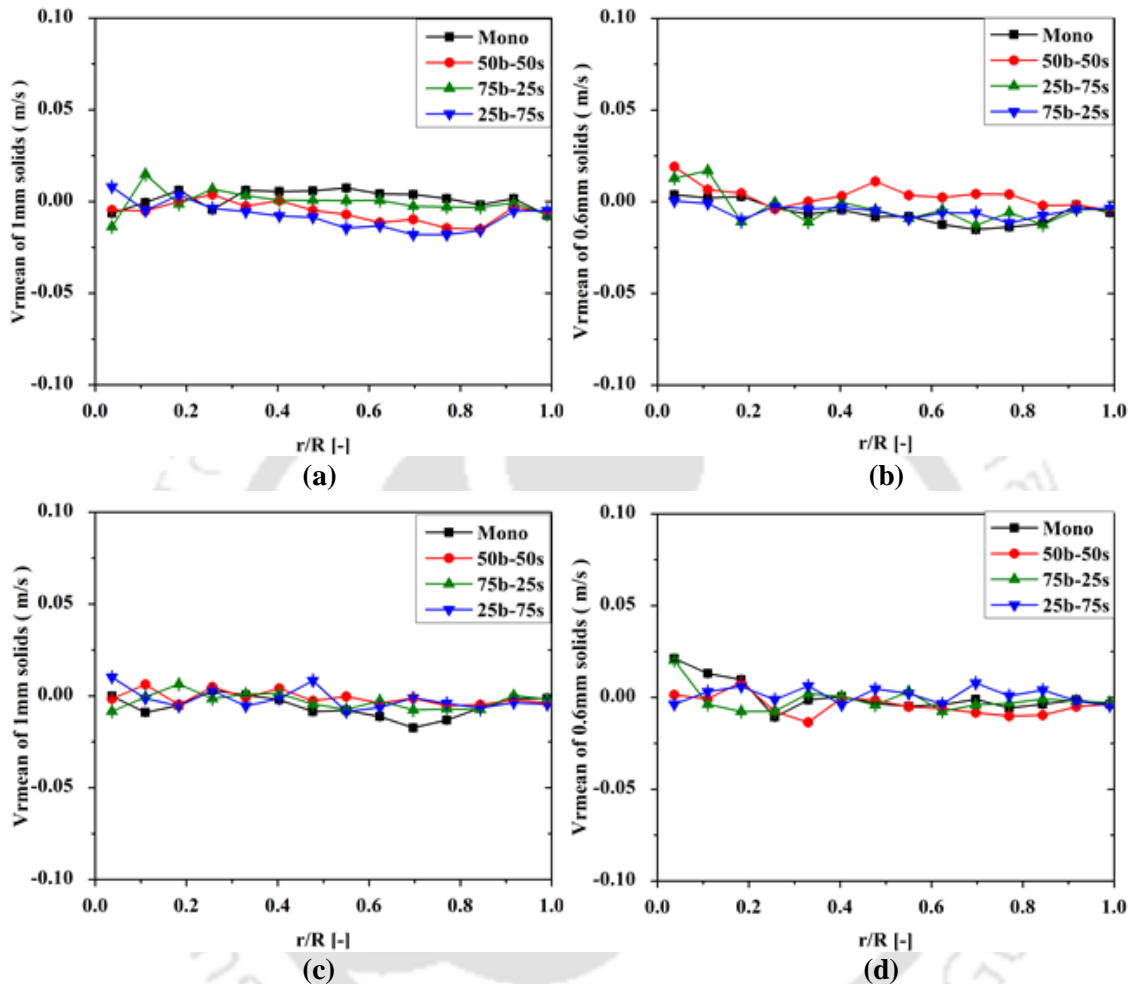


Figure 4.32 Variation of mean radial velocity of solid at different composition: (a) 1 mm particle on top section, (b) 0.6 mm particle on top section, (c) 1 mm particle at bottom section, and (d) 0.6 mm particle at bottom section

4.7.2 Solid velocity fluctuations

The change in fluctuation behavior of both solids with changing composition is depicted in Figures 4.33. Fig. 4.33a and 4.33c, respectively, show the comparison of mean axial RMS velocity plot of 1 mm solid for mono, 50b-50s, 75b-25s and 25b-75s composition on top and bottom section. Similarly, Figures 4.33b and 4.33d, respectively, show the

comparison of mean axial RMS velocity plot of 0.6 mm solid for mono, 50b-50s, 75b-25s and 25b-75s composition on the top and bottom sections. It was observed that the mean axial RMS velocity was not changing with the change in the composition of the bed at both sections of the column.

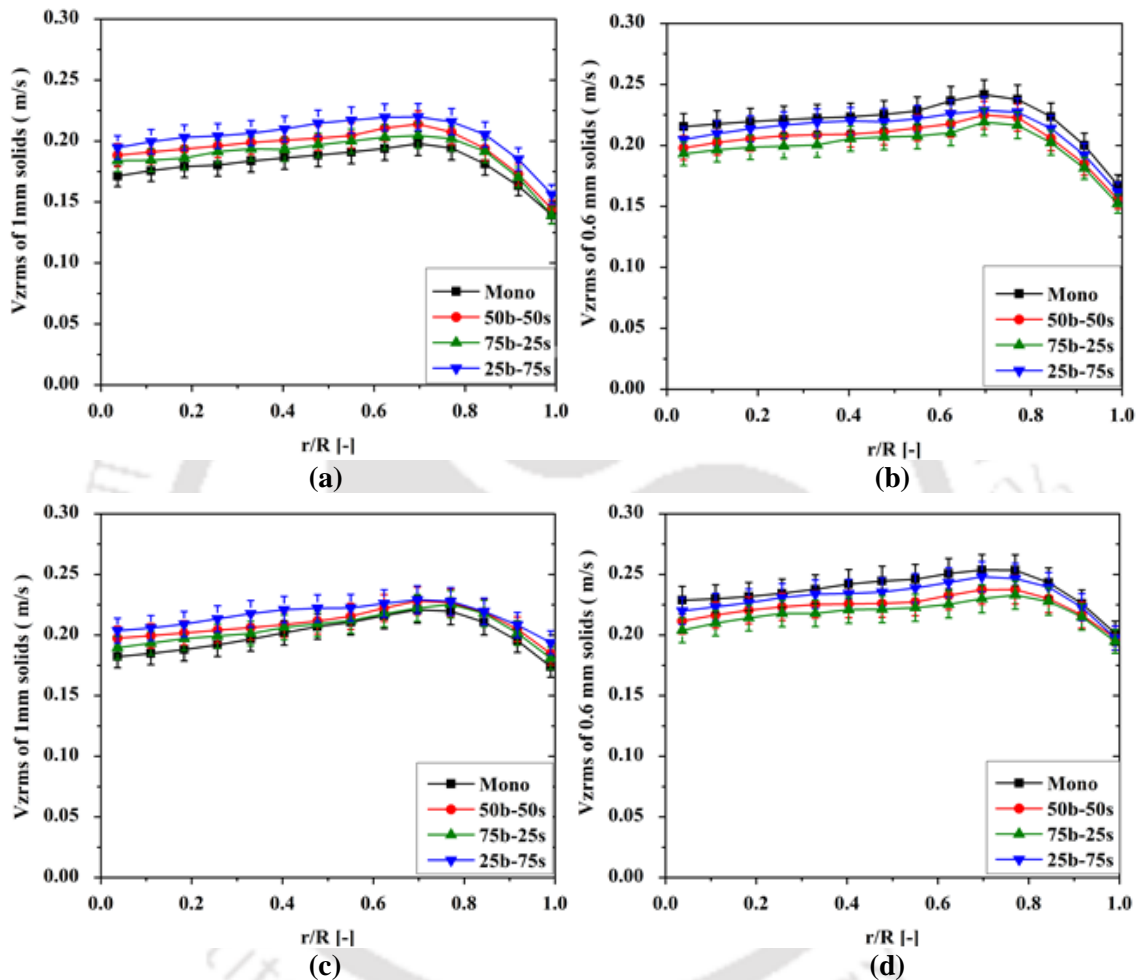


Figure 4.33 Variation of V_{zrms} of solid at different composition: (a) 1 mm particle on top section, (b) 0.6 mm particle on top section, (c) 1 mm particle at bottom section, and (d) 0.6 mm particle at bottom section

The radial RMS velocities are shown in Figure 4.34 for both solids with different compositions and at a constant velocity of 0.14 m/s. The radial RMS shows the difference in magnitude at the bottom section but not on the top section. The profile of radial RMS varies from axial RMS velocity. Though, it shows equal fluctuation for 1 mm and 0.6 mm

irrespective of the varying compositions. It is maximum in the center and minimum near the wall due to restriction near the wall for both solids.

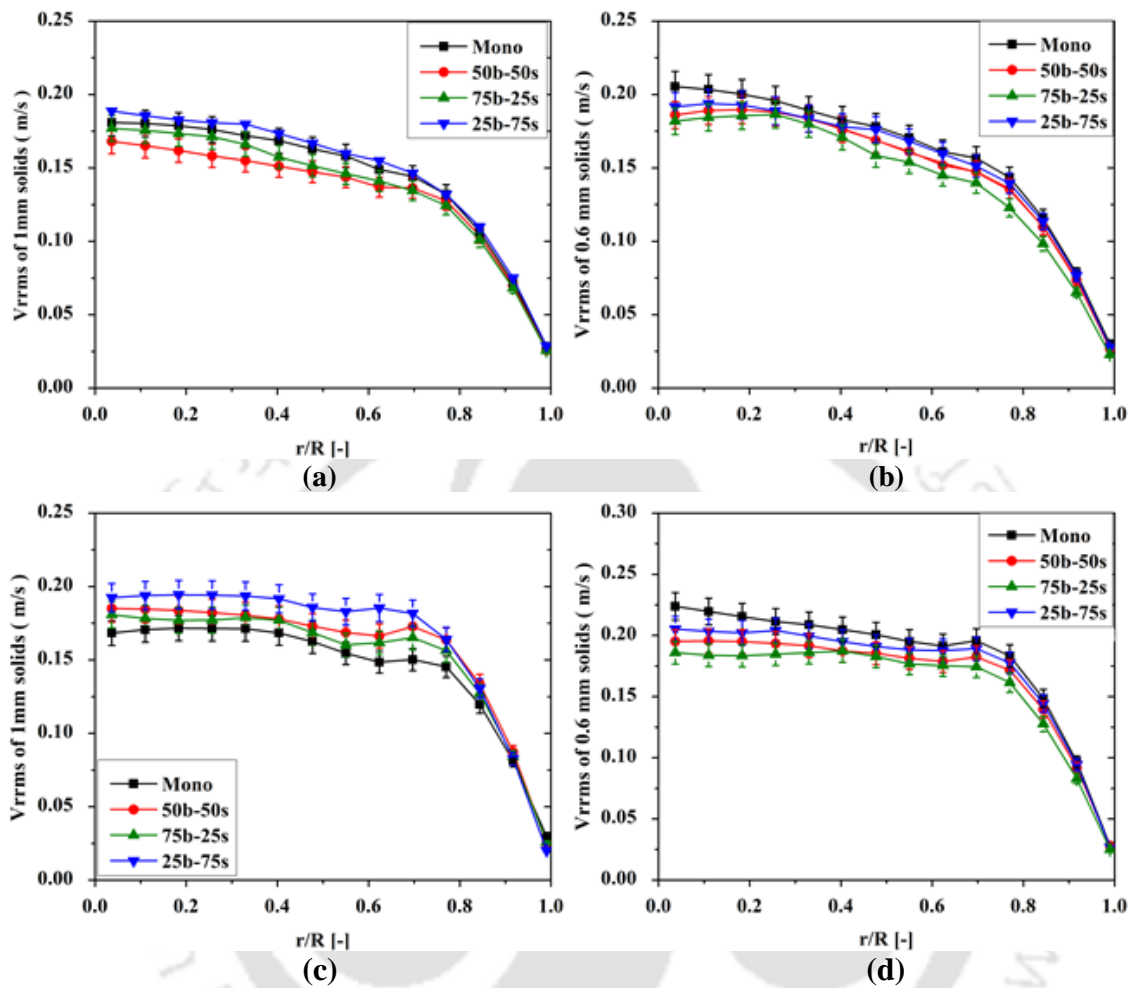


Figure 4.34 Variation of V_{rrms} of solid at different composition: (a) 1 mm particle on top section, (b) 0.6 mm particle on top section, (c) 1 mm particle at bottom section, and (d) 0.6 mm particle at bottom section

4.7.3 Granular temperature

Figure 4.35 presents the granular temperature with the varying composition at 0.14 m/s velocity. The granular temperature shows high variation with composition compared to other parameters. For 0.6 mm particle, the variation is higher compared to 1 mm. In case of 0.6 mm solids the higher u/u_{mf} results in higher voidage. This gives higher fluctuation in case of 0.6 mm particle than 1 mm particle. The granular temperatures of big and small

particles were lower in the top section of the bed compared to the bottom. The granular temperature shows the same trend as axial and radial RMS velocity.

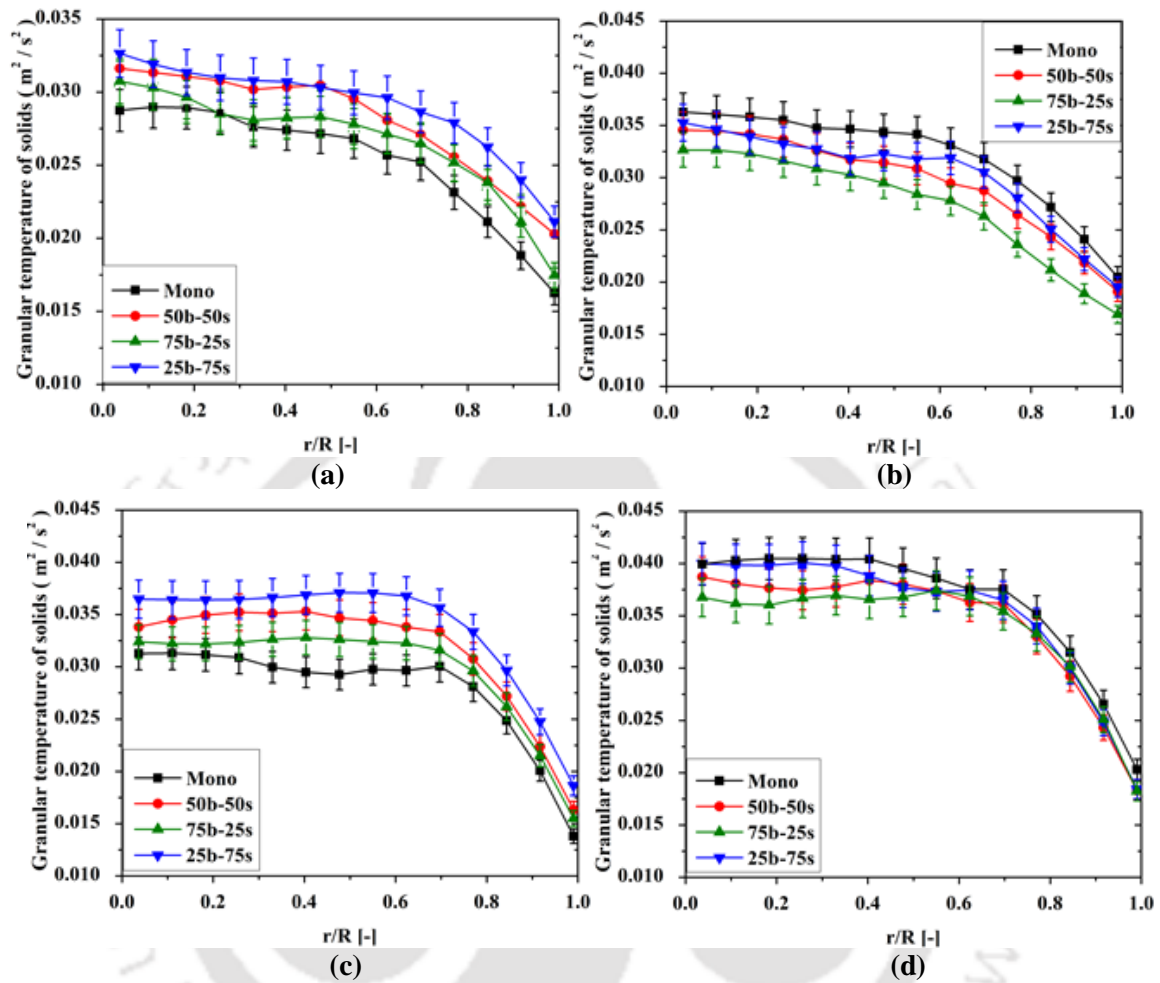


Figure 4.35 Variation of granular temperature of solid at different composition: (a) 1 mm particle on top section, (b) 0.6 mm particle on top section, (c) 1 mm particle at bottom section, and (d) 0.6 mm particle at bottom section

4.7.4 Hurst exponent

Table 4.5 shows the Hurst exponent values computed for both solids at different bed compositions. The Hurst exponent values were found to be higher than 0.5 for all the operating conditions. It means the bed shows persistent behavior for all the operating condition. There was no variation observed in Hurst exponent nature with bed composition.

Table 4.5 Hurst exponents at different operating conditions for 1 mm and 0.6 mm particle in both mono and binary bed

Fluid velocity	Bed Composition	Hurst exponent
0.14 m/s	100b 1 mm	0.78
0.14 m/s	75b-25s 1 mm	0.77
0.14 m/s	50b-50s 1 mm	0.77
0.14 m/s	25b-75s 1 mm	0.76
0.14 m/s	100s 0.6 mm	0.78
0.14 m/s	75b-25s 0.6 mm	0.77
0.14 m/s	50b-50s 0.6 mm	0.78
0.14 m/s	25b-75s 0.6 mm	0.77

4.7.5 Autocorrelation

The axial autocorrelation is illustrated in Figure 4.36 for all the bed compositions. Figures 4.36a, 4.36b, 4.36c and 4.40d represent the autocorrelation of 1 mm solid for mono, 75b-25s, 50b-50s and 25b-75s compositions respectively. Similarly, Figures 4.36e, 4.36f, 4.36g and 4.36h represent the autocorrelation of 0.6 mm solid for mono, 25b-75s, 50b-50s and 75b-25s compositions respectively. The autocorrelation does not show any variation with bed composition.

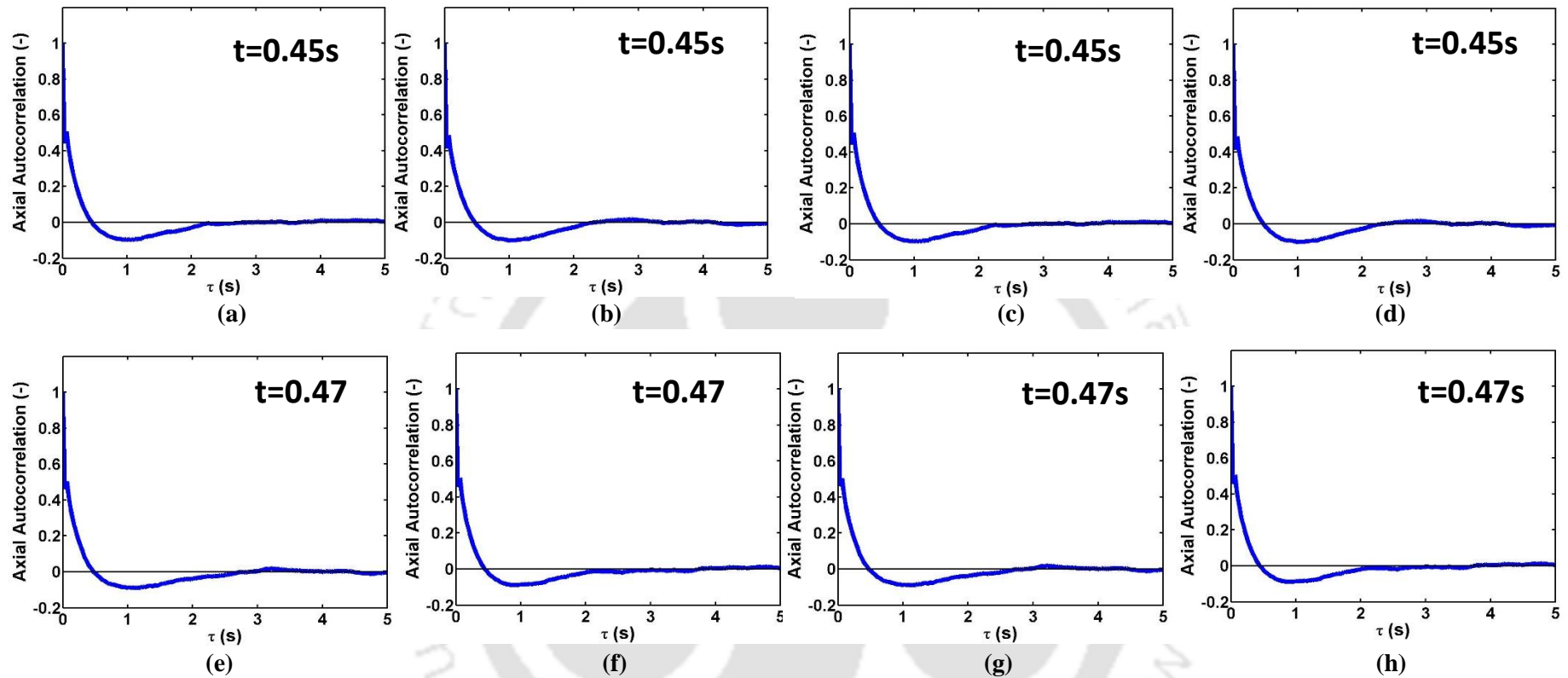


Figure 4.36 Variation of axial autocorrelation of solid with different compositions in binary bed (a) 1 mm particle in mono bed, (b) 1 mm particle in 75b-25s bed, (c) 1 mm particle in 50b-50s bed, (d) 1 mm particle in 25b-75s bed, (e) 0.6 mm particle in mono bed, (f) 0.6 mm particle in 25b-75s bed, (g) 1 mm particle in 50b-50s bed, and (h) 1 mm particle in 75b-25s bed

4.7.6 Segregation index

The segregation index was calculated for all the bed compositions at 0.14 m/s. Figure 4.37 shows the plot of the segregation index with an increase in smaller solid fraction. The segregation index is low at a low volume fraction of smaller solid and increasing with an increase in the smaller solid fraction in the mixture. It indicates that the bed is properly mixed when operated at a very high velocity for all the bed compositions. Hence the solids are well distributed throughout the column reaching a complete mixing state.

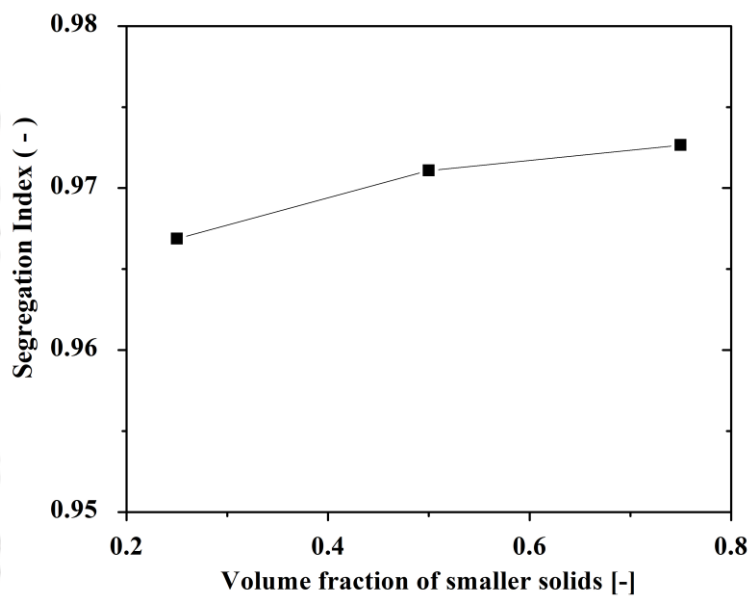


Figure 4.37 Variation of segregation index with different composition in binary bed

4.8 Summary

The results of this chapter are summarized in two parts, viz., mono and binary dispersed bed studies for different liquid inlet velocities.

Monodispersed bed study

The following major conclusions can be drawn from the monodispersed bed study:

- It was observed that the axial mean velocity of the bigger particle was lower than the smaller particle for a particular velocity as both beds were operated at same

liquid inlet velocities. The observation shows solid mean velocity was significant in axial direction compared to the radial direction.

- The fluctuation in case of the smaller particle was more than bigger particle as the bed was operated at higher u/u_{mf} ratio for small particles.
- Radial autocorrelation shows faster decay than axial autocorrelation as the solid motion was mainly in the axial direction.
- KE and CD plots show the regime transition for both the solids at 0.1 m/s liquid inlet velocity.

Binary dispersed bed studies

- It was found that the hydrodynamics of liquid-solid conical bed was chaotic and the degree of chaotic behavior depends on the liquid velocity and bed composition.
- The axial mean velocity of both 1 mm and 0.6 mm particles was found to be approximately same in 50b-50s wt. % binary bed at higher liquid velocity, which signifies the homogeneous distribution of solids. It indicates that the mixing and interaction of liquid-solids increases with an increase in liquid velocity at the mean level.
- It was observed that in conical bed two different interaction phenomena dominate the behavior of the bed at the top and bottom sections. At the bottom section, liquid-solids interaction plays a dominating role while on top section particle-particle interaction becomes crucial.
- In the conical fluidized bed, the axial autocorrelation takes a longer time to decay compared to radial autocorrelation which signifies that motion was primarily in the axial direction.

- The segregation index calculated for binary bed indicates good mixing even at a lower liquid inlet velocity which is contradictory to the cylindrical column. Hence, it can be stated that conical fluidized bed provides better mixing compared to the cylindrical fluidized bed.
- Correlation Dimension and Kolmogorov Entropy shows the chaotic nature of the mono and binary fluidized beds. Further, CD and KE values also indicated a change in flow regime (after 0.1 m/s liquid velocity) for both mono and binary dispersed fluidized beds. Finally, it has been found that flow regime transition in conical bed mainly depends on liquid inlet velocity and not on bed composition.

Notations

h	Actual height where data was plotted, m
H	Expanded bed height during fluidization, m
r	Actual radius where data was plotted, m
R	Radius of the column at that height, m
u	Liquid inlet velocity, m/s
u_{mf}	Minimum fluidization velocity, m/s
τ	Time delay, s

References

Bhusarapu, S., 2005. Solids Flow Mapping in Gas-Solid Risers, D.Sc. Thesis.

Chavan, P.V., Joshi, J.B., 2008. Analysis of Particle Segregation and Intermixing in Solid-Liquid Fluidized Beds. *Ind. Eng. Chem. Res.* 47, 8458–8470.

- Dathrika, S.K., Varma, M.V.K., Akila, G., 2011. Hydrodynamics of Liquid-Solid Fluidization of Binary Mixtures in Tapered Bed. *Int. J. Pharm. Sci. Res.* 2 (1). 91-99.
- Fan, L.S., Kawamura, T., Chitester, D.C., Kornosky, R.M., 1985. Experimental Observation of Nonhomogeneity in a Liquid-Solid Fluidized Bed of Small Particles. *Chem. Eng. Commun.* 37, 141-157.
- Fan, L.T., Kang, Y., Neogi, D., Yashima, M., 1993. Fractal analysis of fluidized particle behavior in liquid-solid fluidized beds. *AIChE J.* 39, 513–517.
- Ham, J.M., Thomas, S., Guazzelli, E., Homsy, G.M., Anselmet, M.C., 1990. An experimental study of the stability of liquid-fluidized beds. *Int. J. Multiph. Flow.* 16, 171–185.
- Handley, D., Doraisamy, A., Butcher, K. L., Franklin, N. L., 1966. A Study of the Fluid and Particle Mechanics in Liquid-Solid Fluidized Beds. *Trans. Inst. Chem. Eng.* 44, T260-T273.
- Hsu, H.W., 1978. Characteristics of Tapered Fluidized Reactors: Two Phase Systems. *Biotechnol. Bioengng. Symp.* 8, 1-11.
- Jain, S., Saraswat, P., Jain, V., Pant, H.J., Upadhyay, R.K., 2014. Investigation of liquid-solids fluidized bed of different particle size through radioactive particle tracking techniques. *J. Radioanal. Nucl. Chem.* 302, 1309–1313.
- Jain, V., Kalo, L., Kumar, D., Pant, H.J., Upadhyay, R.K., 2017. Experimental and numerical investigation of liquid–solid binary fluidized beds: Radioactive particle tracking technique and dense discrete phase model simulations. *Particuology* 33, 112–122.

- Kalo, L., Pant, H. J., Cassanello, M. C., Upadhyay, R. K., 2018. Time Series Analysis of a Binary Gas-Solid Conical Fluidized Bed Using Radioactive Particle Tracking (RPT) Technique Data. Chem. Eng. J. <https://doi.org/10.1016/j.cej.2018.08.193>
- Kang, Y., Kim, S.D., 1987. Heat Transfer Characteristics in Liquid Fluidized Beds. Hwahak Kanghak. 25, 81-89.
- Kang, Y., Kim, S.D., 1988. Solid Flow Transition in Liquid and Three- Phase Fluidized Beds. Particulate Sci. and Technol., 6, 133-144.
- Kmiec, A., 1978. Particle Distributions and Dynamics of Particle Movement in Solid-Liquid Fluidized Beds. Chem. Eng. J. 15, 1-12.
- Kolar, V., 1963. Fluidization of Solid Particles by Liquid in Conical Vessels. Collect. Czech. Chem. Commun. 28, 1224–1231.
- Koloini, T.C., Farkas, E.J., 1973. Fixed Bed Pressure Drop and Liquid Fluidization in Tapered or Conical Vessels. Can. J. Chem. Eng. 51, 499-502.
- Kunii, D., Levenspiel, O., 1991. Fluidization Engineering, Butterworth-Heinemann, Boston, MA.
- Kwant, G., Prins, W., van Swaaij, W.P.M., 1995. Particle mixing and separation in a binary solids floating fluidized bed. Powder Technol. 82, 279-291.
- Limtrakul, S., Chen, J., Ramachandran, P.A., Dudukovic, M.P., 2005. Solids motion and holdup profiles in liquid fluidized beds. Chem. Eng. Sci. 60, 1889–1900.
- Maruyama, T., Maeda, H., Mizushina, T., 1984. Liquid Fluidization in Tapered Vessels. J. Chem. Eng. Jpn. 17 (2), 132-139.

- Maruyama, T., Sato, H., 1991. Liquid fluidization in conical vessels. *Chem. Eng. J.* 46, 15-21.
- Maruyama, T., Koyanagi, T., 1993. Fluidization in tapered vessels. *Chem. Eng. J.* 51, 121-128.
- Morooka, S., Kusakabe, K., Kato, Y., 1980. Mass Transfer Coefficient at the Wall of a Rectangular Fluidized Bed for Liquid-Solid and Gas-Liquid-Solid System. *Int. Chem. Eng.* 20, 433-438.
- Muroyama, K., Fukuma, M., Yasunishi, A., 1986. Wall-to-Bed Heat Transfer in Liquid-Solid and Gas-Liquid-Solid Fluidized Beds: I. Liquid-Solid Fluidized Beds. *Can. J. Chem. Eng.* 64, 399-408.
- Peng, Y., Fan, L.T., 1997. Hydrodynamic Characteristics of Fluidization in Liquid-Solid Tapered Beds. *Chem. Eng. Sci.* 52, 2277-2290.
- Pitt, W.W., Hancher, C.W., Scott, C.D., Hsu, H.W., 1978. The Tapered Fluidized-Bed Bioreactor - an improved Device for Continuous Cultivation. *AIChE National meeting.* 1-19.
- Pitt, W.W., Hancher, C.W., Patton, B.D., 1981. Biological reduction of nitrates in wastewaters from nuclear processing using a fluidized-bed bioreactor. *Nucl. Chem. Waste Manag.* 2, 57-70.
- Roy, S., 2000. Quantification of Two-Phase Flow in Liquid-Solid Risers. *Ph.D. Thesis.*
- Scott, C.D., Hancher, C.W., 1976. Use of a tapered fluidized bed as a continuous bioreactor. *Biotechnol Bioeng.* 18, 1393-1403.
- Shi, Y.F., Yub, Y. S., Fan, L. T., 1984. Incipient Fluidization Condition for a Tapered Bed. *Ind. Eng. Chem. Fundam.* 23, 484-489.

- Talapuru, S., Murthy, J.S.N., Nandana, S., Phani Kiran, S.V.G.R., Ramesh. V., 2010. Hydrodynamic Characteristics of Liquid-Solid Fluidization of Binary Mixtures in Tapered Beds. The 13th International Conference on Fluidization - New Paradigm in Fluidization Engineering. 1-8.
- Upadhyay, R.K., 2010. Investigation of Multiphase Reactors Using Radioactive Particle Tracking. Ph.D. Thesis, IIT Delhi.
- Upadhyay, R.K., Roy, S., 2010. Investigation of Hydrodynamics of Binary Fluidized Beds via Radioactive Particle Tracking and Dual-Source Densitometry. Can. J. Chem. Eng. 88, 601-610.
- Volpicelli, G., Massirilla, L., Zenz, F.A., 1966. Nonhomogeneities in Solid-Liquid Fluidization. Chem. Eng. Prog. Symp. Ser. 62 (67), 42-50.
- Webster, G.H., Perona, J.J., 1988. Liquid Mixing in a Tapered Fluidized Bed. AIChE J. 34 (8), 1398-1402.
- Yang, J., Renken, A., 2003. A generalized correlation for equilibrium of forces in liquid–solid fluidized beds. Chem Eng J. 92, 7–14.
- Yutani, N., Fan, L. T., Too, J. R., 1983. Behavior of Particles in a Liquid-solids Fluidized Bed. AIChE J. 29,101-106.

Chapter 5

Scale up of Conical Gas-solid Fluidized Bed

Scope

In the present chapter, the scale-up study of the conical gas-solid fluidized bed is presented. A state of art RPT technique is used for the hydrodynamic study of the scaled-up conical fluidized bed. The mean and fluctuation behavior of the scaled-up fluidized bed is obtained. Time series and chaos analysis are also presented for the scaled-up conical fluidized bed. Finally, the scaled-up bed results are compared with the smaller one.

5.1 Introduction

The scale-up of multiphase flow reactors is still a challenging task mainly due to the complex interactions involved at different length and time scales in these reactors. In Chapters 3 and 4, it is established that in mono and binary dispersed conical fluidized beds, phenomena are occurring at different length scales. Further depending upon operating conditions interaction mechanism changes from fluid-solid to solid-solid interactions. It is well established in the literature that these interactions not only depends upon the operating conditions but also on the size and geometry of the system. Hence, a considerable difference was observed in the dynamics between laboratory scale and pilot plant/industrial scale setups. Therefore, it is necessary to account the change in flow behavior with the size of the system for any multi-phase flow reactors. The gas-solid fluidized bed is no different and detailed scale-up studies are required to bridge the knowledge gap. In the gas-solids binary fluidized bed, improper scaling results in poor solid mixing, undesirable flow patterns of gas and, operational issues, etc. (Rudisuli et al.,

2012). This can reduce the yield and performance of the scaled-up fluidized bed. Hence, the use of proper scaling criteria is really important in the design of industrial scale fluidized beds.

However, the research is still on for finding the suitable scale-up criteria. Glicksman (1984) have proposed the full set of scaling law based on conservation equations. This scale-up law includes matching Reynolds number, Froude number, density ratio of fluid to solid, length scale ratio, dimensionless particle size distribution, and particle shape. Later, Glicksman found that matching these many dimensionless numbers are difficult to achieve. Hence, Glicksman et al. (1993) have developed the simplified set of scaling law which has lesser dimensionless numbers. Another law of Glicksman et al. (1984) is also available based on high and low Reynolds number of the system. Horio et al. (1986) have proposed a set of scaling parameters based on bubble and gas dynamics equations.

Further, Taofeeq and Al-Dahhan (2018) have stated that the scale-up of any system can be achieved by mainly three ways. First, by using any scale up laws (Glicksman, 1984; Nicastro and Glicksman, 1984; Horio et al., 1986; Glicksman, 1988; Glicksman et al., 1993; Stein et al., 2002), second by matching the Kolmogorov entropy (KE) obtained from pressure signal or by matching the attractor between the small and large scaled column (van den Bleek and Schouten, 1993; van den Bleek and Schouten, 1993; Schouten et al., 1996; van den Bleek et al., 2002; Tahmasebpoor et al., 2017; Taofeeq and Al-Dahhan, 2018) and third by matching the gas hold up/solid velocity profile (Zaid, 2013; Al-Dahhan et al., 2014; Efhaima and Al-Dahhan, 2015; Efhaima, 2016).

However, due to lack of sufficient data on the conical gas-solid fluidized bed, the scale-up study on these systems is still missing. This needs several sets of data at different scales of the conical fluidized bed. The knowledge of local behavior of these systems can be a

great advantage for performing scale-up studies. Therefore, the main objective of the present work is to obtain the local parameters of the bed and compare the results of two different scale beds.

5.2 Present state of the art of scale-up studies

Gas-solid fluidized bed has been investigated by many researchers using different dimensions of bed and type of solid. However, the scale-up study on the conical fluidized bed is yet to be performed. For the first time, Fitzgerald et al. (1984) have used the full set of dimensionless numbers of Glicksman for the scale-up study of the gas-solid cylindrical fluidized bed. They have compared the hydrodynamic of two scaled columns using autocorrelation function obtained through pressure measurement. In one bed they have used cork and in other sand particles for fluidization. They have observed good agreement between both the bed dynamics. The autocorrelation functions were similar for both the columns but were not statistically significant. They stated the reason for mismatching is not considering the forces from electrostatic charge build up.

Nicastro and Glicksman (1984) have applied Glicksman full set of scaling law for scaling-up an atmospheric combustor to a cold bed. The pressure signals were acquired in both hot and cold bed using differential probes placed at different heights. The power spectral density (PSD) and probability density distribution (PDF) of the pressure fluctuations shows good agreement between both beds.

Newby and Kearns (1986) have also applied Glicksman full set of scaling relationship to compare hydrodynamics of two different scale gas-solid fluidized beds. They used a high-speed camera and pressure fluctuations to validate the Glicksman law. They compared the dimensionless bubble frequencies obtained from the high-speed video and found reasonable agreement between the dimensionless amplitudes of the pressure fluctuation.

Stein et al. (2002) used Glicksman simplified set of scaling law for their study. They used the non-invasive technique called positron emission particle tracking (PEPT) technique to acquire the movement of solid particles. Three different columns with 70, 141, and 240 mm diameter were used. They stated that the Froude number plays a major role in scale-up methodology along with the gas-to-particle density ratio which has a lesser effect on scaling.

Knowlton et al. (2005) applied the proposed viscous limit set by Glicksman for scale-up study. They compared the non-dimensional dominant frequency and amplitude of the pressure fluctuations. They found that results are matching for the used set of scaling law.

Further, computational fluid dynamics (CFD) simulations are also used for scale-up studies. Van Ommen et al. (2006) studies scale up through CFD simulations. They used the simplified set of Glicksman, the full set of Glicksman and the full set of Glicksman extended with a dimensionless pressure group. They used two gas-solid fluidized beds with a diameter of 30 cm and 15 cm. They observed the best agreement for the full set extended with the pressure group especially at the lower gas velocity (i.e. at $3u_{mf}$). They also observed that both the simplified and extended sets give reasonable results at $5u_{mf}$. The full set of scaling law performs worse than the simplified set. Though, none of the scaling law gave comparable results between both scales. Sanderson et al. (2007) used the discrete element method (DEM) using the full set and simplified set of scaling law with six 2D and two 3D fluidized beds. They compared the average and standard deviation of the non-dimensionalized pressure drop. They found reasonable agreement for the full-scale set while poor agreement for the simplified set.

Di Maio and DiRenzo (2013) used the full set as well as the simplified set of Glicksman scaling law using DEM-CFD modeling. They compared the mean value of the pressure

drop and the amplitude of its oscillations and found that the results are not matching. The attractors reconstructed from the time series analysis of the pressure signals shows similar results for full set whereas the results vary for the simplified set depending on the scale size.

Zaid (2013) also used Glicksman simplified set of scaling laws for their study. They used two fluidized beds of diameter 14 and 44 cm. Two different types of particles, glass beads and copper particles were used as fluidized material. They used an invasive fiber optical probe for solid velocity and volume fraction measurement. Their experimental outcome showed mismatching of the local hydrodynamics between both the scaled fluidized beds.

Taofeeq and Al-Dahhan (2018) used the chaotic scale-up method with matching the Kolmogorov entropy (KE) proposed by Schouten et al. (1996) with two different scaled columns and confirmed the similarity.

Efhaima and Al-Dahhan (2017) used the non-invasive measurement technique (CT and RPT) for the scale-up study of the gas-solid fluidized bed. They used two fluidized beds of 0.14 m and 0.44 m diameter. In large scale column 210 μm glass bead and in small-scale column 70 μm glass bead used. They used the scale-up methodology proposed by Glicksman et al. (1993). They compared the cross-sectional distribution and radial profile of gas holdup between both the columns using computed tomography (CT) technique. The gas holds up have been compared at four different heights. Further, they compared the velocity vectors; mean axial and radial solid velocity profiles, normal and shear stresses and turbulent kinetic energy. Different gas hold up profile observed for both columns indicating different gas-solid interaction. They observed higher solid axial velocity in large column induced by higher bubble velocity due to larger bubble formation compared to the small-scale column. Further, the normal and shear stresses and

turbulent kinetic energy profiles also show similar trend though there exists a marginal difference between their magnitudes.

Many researchers (Rudisili et al., 2012; Efhaima and Al-Dahhan, 2017) have stated that the use of scaling laws do not give similarity in scaled results as all the dimensionless scaling laws are developed based on the global parameter such as overall measurement of holdups, pressure drop and pressure signal, etc. Further, due to lack of sufficient data on the conical gas-solid fluidized bed the scale-up studies on these systems is still missing. This needs several sets of data at different scales of the conical fluidized bed. The knowledge of local behavior of these systems can be a great advantage for performing scale-up studies. Hence, in this chapter scale-up studies are performed for gas-solid mono and binary dispersed beds by using radioactive particle tracking technique. The data is obtained for two different scale reactor by using the scale-up laws proposed for the gas-solid cylindrical fluidized bed. The mean and RMS velocity profiles along with granular temperature, autocorrelation function, correlation dimensions (CD) and Kolmogorov entropy (KE) are calculated for both scales and matched to find the validity of scale-up laws for gas-solid conical fluidized beds.

5.3 Experimental setup

The large-scale fluidized bed was of twice of inlet diameter of the small column with same cone angle. The large-scale experimental setup dimensions varied from 0.1 m to 0.25 m from bottom to top with the cone angle of 5.4° . The setup was made up of mild steel. Air was used as the fluidizing gas. Rotameters were used to measure the air flow rate. The bed was operated at two different velocities of 5.4 m/s and 8.1 m/s. Two different solids of 1 mm and 2 mm diameters with the equal density of 2500 kg/m^3 (as per scaling law) were used at monodispersed and 50b-50s wt. % binary bed. The mass of the

bed for all the experiment was kept constant. The photograph of the experimental setup is presented in Figure 5.1. The inertia limit set of scaling law (Glicksman, 1984) has been used for the present work. The inertia limit set is used for high Reynolds numbers ($Re_p > 1000$) which is mainly for Geldart group D solids at high gas velocity (Rudisili et al., 2002). The experimental conditions are shown in Tables 5.1. The small-scale bed results have been used from chapter 3.

Solid motion has been investigated in the scaled-up conical fluidized bed using RPT. Sc-46 tracers were used to track the solid motion of the column. Threaded ports have been designed around the column for calibration. Radioactive particles of 1 mm and 2 mm diameter were used to track the solid phases. In a staggered manner, 14 detectors were placed at seven different heights around the column with two detectors at one plane. The experiments have been performed for 12-15 hours at a frequency of 50 Hz.

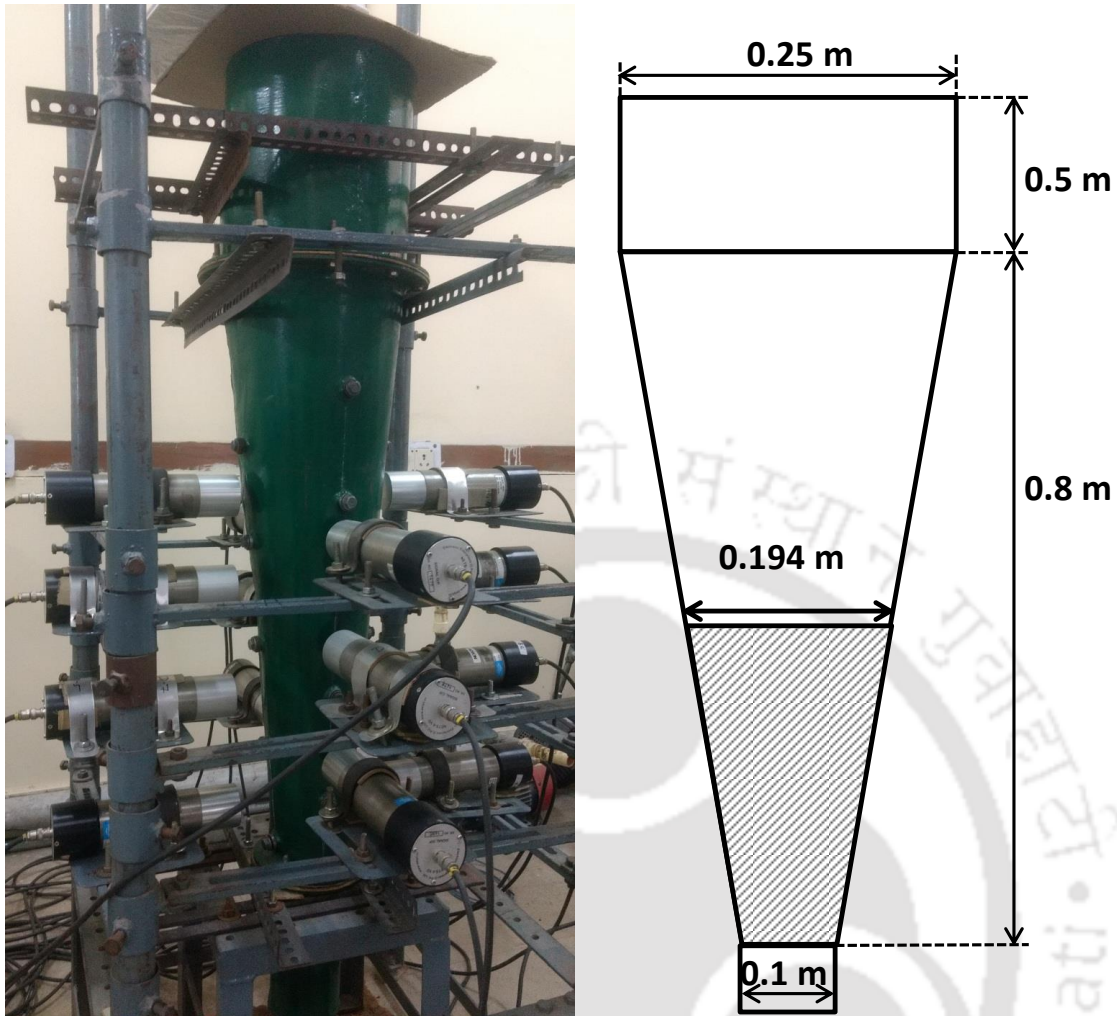


Figure 5.1 Photograph and schematic of scaled experimental setup

Table 5.1 Experimental conditions

$2u_{mf}$ and $3u_{mf}$	Small-scale (Smaller particles)	Large- scale (Smaller particles)	Small-scale (Bigger particles)	Large-scale (Bigger particles)
Column dia, D_c (m)	0.05	0.1	0.05	0.1
Static bed height, h (m)	0.25	0.5	0.25	0.5
Solid	Glass bead	Glass bead	Glass bead	Glass bead

solid diameter, d_p (mm)	0.6	1	1	2				
Particle density, ρ_s (kg/m³)	2500	2500	2500	2500				
Fluid density, ρ_g (kg/m³)	1.225	1.225	1.225	1.225				
Fluid viscosity, μ_g (kg s/m²)	0.0000178	0.0000178	0.0000178	0.0000178				
Inlet velocity, u_g (m/s)	3.8	5.4	3.8	5.4				
u_{mf} (m/s)	1.11	2.18	1.9	3.13				
D_c / d_p	83.3	83.3	50	50				
H / D_c	5	5	5	5				
ρ_s / ρ_g	2041	2041	2041	2041				
u / u_{mf}	3.4	5.7	2.5	3.1	2	3	1.7	2.6
$Fr_s = u^2 / gD_c$	29.4	66.2	29.7	66.8	29.4	66.2	29.7	66.8

5.4 Results and discussions

5.4.1 Lagrangian track of particle position

A typical trajectory of the tracer of 2 mm size at 8.1 m/s in r - z and the r - θ plane is shown in Figures 5.2 and 5.3, respectively. The trajectory of the particle is shown after 1, 2, 5, 10 and 20 seconds as the tracer started moving inside the column. The initial and final position of the tracer is marked in red and green, respectively. The trajectory has been presented for a various time duration to observe the dispersion of the particle inside the column. It has been observed that within 20 seconds of time the particle cover almost the entire volume of the column. Hence, during the whole experimentation time (12-15 hours), tracer visited all the possible locations inside the column multiple times. Further, the particle trajectory in the x - y plane (Figure 5.3) also shows that the tracer covers all the locations within 20 seconds.

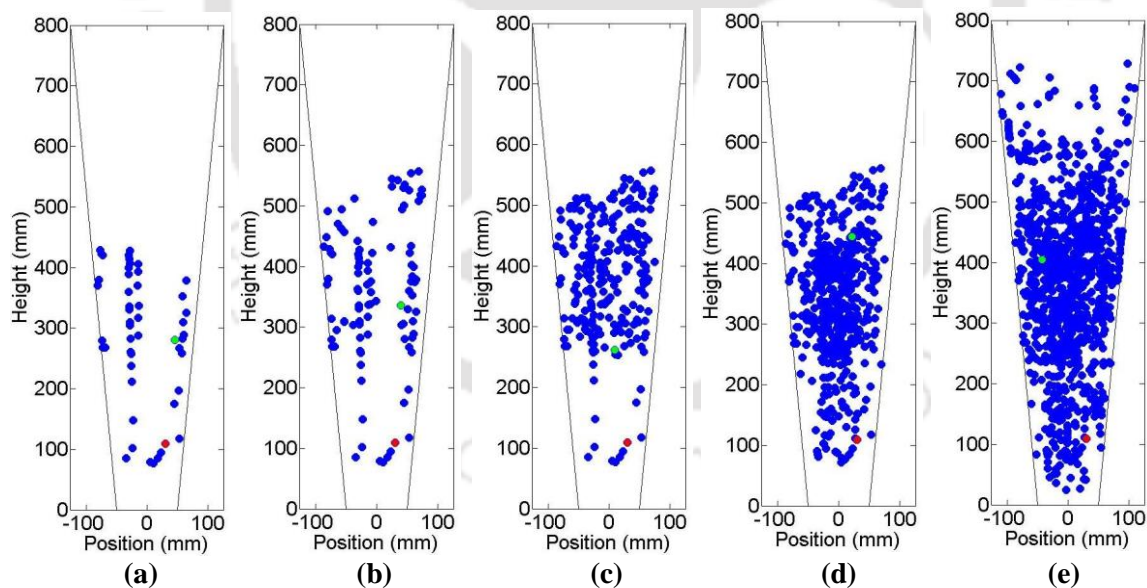


Figure 5.2 Trajectory of 2 mm tracer at 8.1 m/s with time in r - z plane at: (a) 1 sec, (b) 2 sec, (c) 5 sec, (d) 10 sec, and (e) at 20 sec

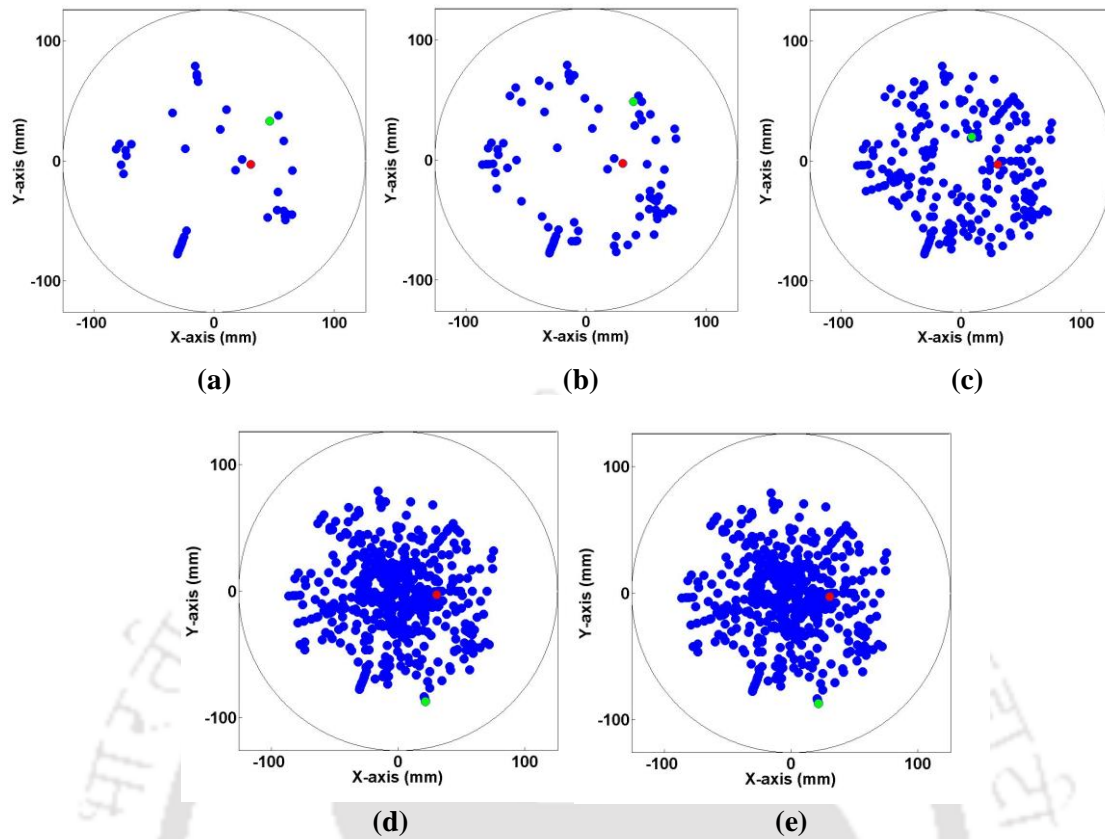


Figure 5.3 Trajectory of 2 mm tracer at 8.1 m/s with time in x-y plane at: (a) 1 sec, (b) 2 sec, (c) 5sec, (d) 10 sec, and (e) at 20 sec

5.5 Effect of scale on monodispersed bed

To find the effect of column dimensions on the behavior of gas-solid mono dispersed fluidized bed, experiments were performed for monodispersed bed. Effect of particle size and gas inlet velocity was studied. Glass beads of two different sizes (1 mm and 2 mm) with the same density (2500 kg/m^3) were used in experiments. The overall mass of the bed was kept constant for both solids. The bed was operated at two different gas velocities, i.e. 5.4 and 8.1 m/s for both 1 mm and 2 mm mono dispersed beds. The results are compared with the data presented in Chapter 3 where experiments were conducted in small diameter column for two different sizes of particles at different gas inlet velocities. The comparison is presented for $2u_{mf}$ and $3u_{mf}$ velocities of bigger particles in both size

column. The L/D ratio in large diameter column is kept same as of the small diameter column.

5.5.1 Ensemble averaged velocity

Figures 5.4a and 5.4b show the solid axial mean velocity for the bigger and smaller particles on top section, respectively for both small (0.05 m diameter at the bottom) and big column (0.1 m diameter at the bottom). The $2 u_{mf}$ and $2 u_{mf}$ scale-up are the plots at low velocity in small and big columns, respectively. Similarly, $3 u_{mf}$ and $3 u_{mf}$ scale-up are the plots at high velocity in small and large columns, respectively. The small-scale refers to 0.05 m diameter bed while large-scale refers to 0.1 m diameter fluidized bed. The results are plotted at two different heights of at z/Z of 0.25 and 0.75, respectively. Qualitatively both columns perform same where solids ascend in the center of the column and descend near the wall for both particles at all the gas velocities. Further, for low gas velocity ($2 u_{mf}$) the top section of both columns show negligible mean axial velocity for bigger solid. However, quantitatively it shows higher axial solid velocity in large diameter column compared to small diameter column for both solids. This was mainly because large diameter column was operated at a higher gas velocity in an absolute sense compared to small diameter column. For $3 u_{mf}$, large diameter column was operated at 8.1 m/s gas velocity while small diameter column was operated at 5.7 m/s gas velocity. Another reason for the difference in solid velocity can be higher bubble coalescence frequency in large diameter column compared to small diameter column. The bigger bubble provides more momentum to solids which results in higher solid velocity for both sizes of solids (Bashiri et al., 2010). However, it is very difficult to conclude anything from Figure 5.4. Hence, a non-dimensional mean axial velocity was plotted for both large and small column diameter. To non-dimensionalize the mean velocity of the solid it was divided by u_{mf} of the respective solids as given in Table 5.1.

Figures 5.5a and 5.5b show the dimensionless mean axial solid velocity for the bigger and smaller particle on the top section while figures 5.5c and 5.5d show the dimensionless mean axial solid velocity for the bigger and smaller particles at bottom section. The profiles of solid velocities for both columns are similar. The dimensionless solid velocities are matching for both columns qualitatively and quantitatively. Hence, it can be stated that the scaling law used in current work is able to predict the mean axial velocity properly. However, for reliable scale-up fluctuations should also be matched.

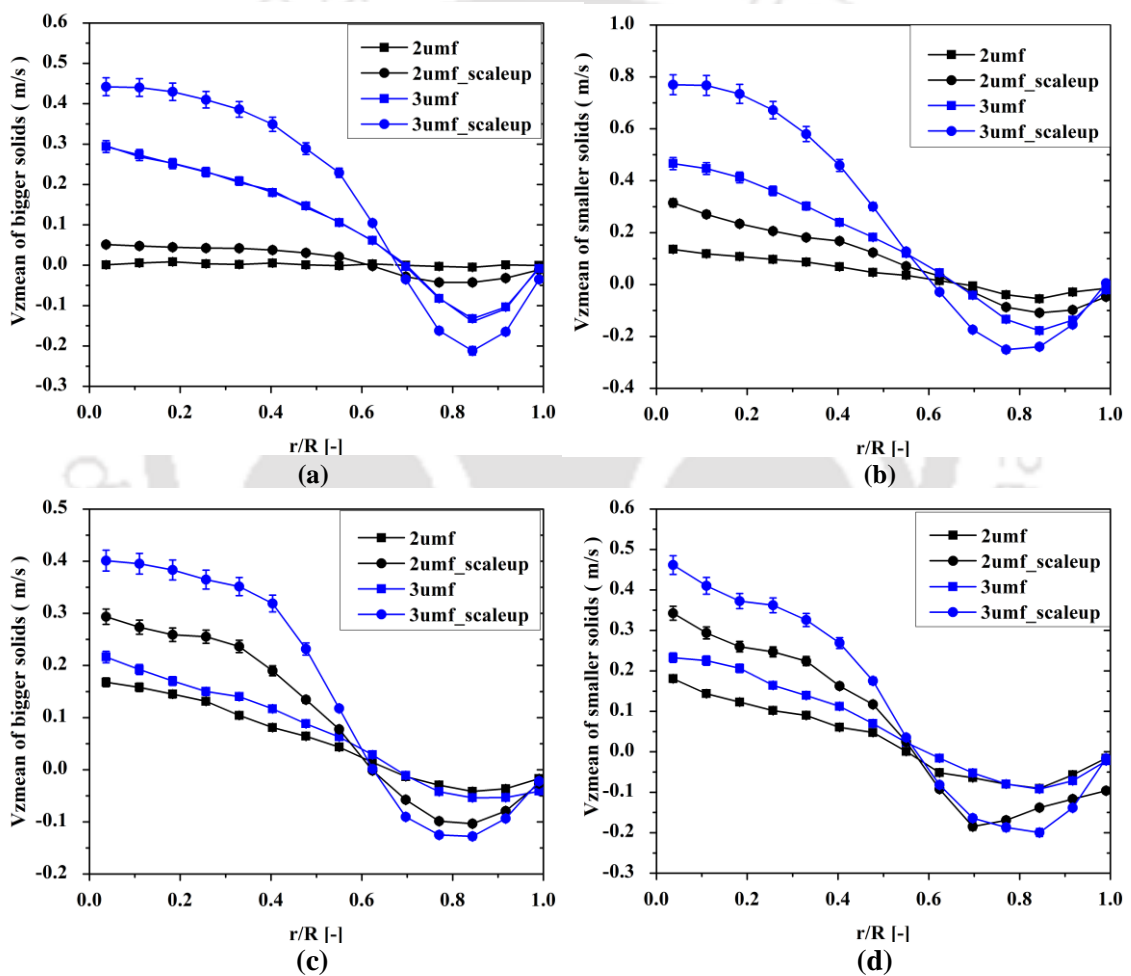


Figure 5.4 Variation of mean axial velocity of solid in mono bed (a) top section bigger solid, (b) top section smaller solid, (c) bottom section bigger solid, and (d) bottom section smaller solid

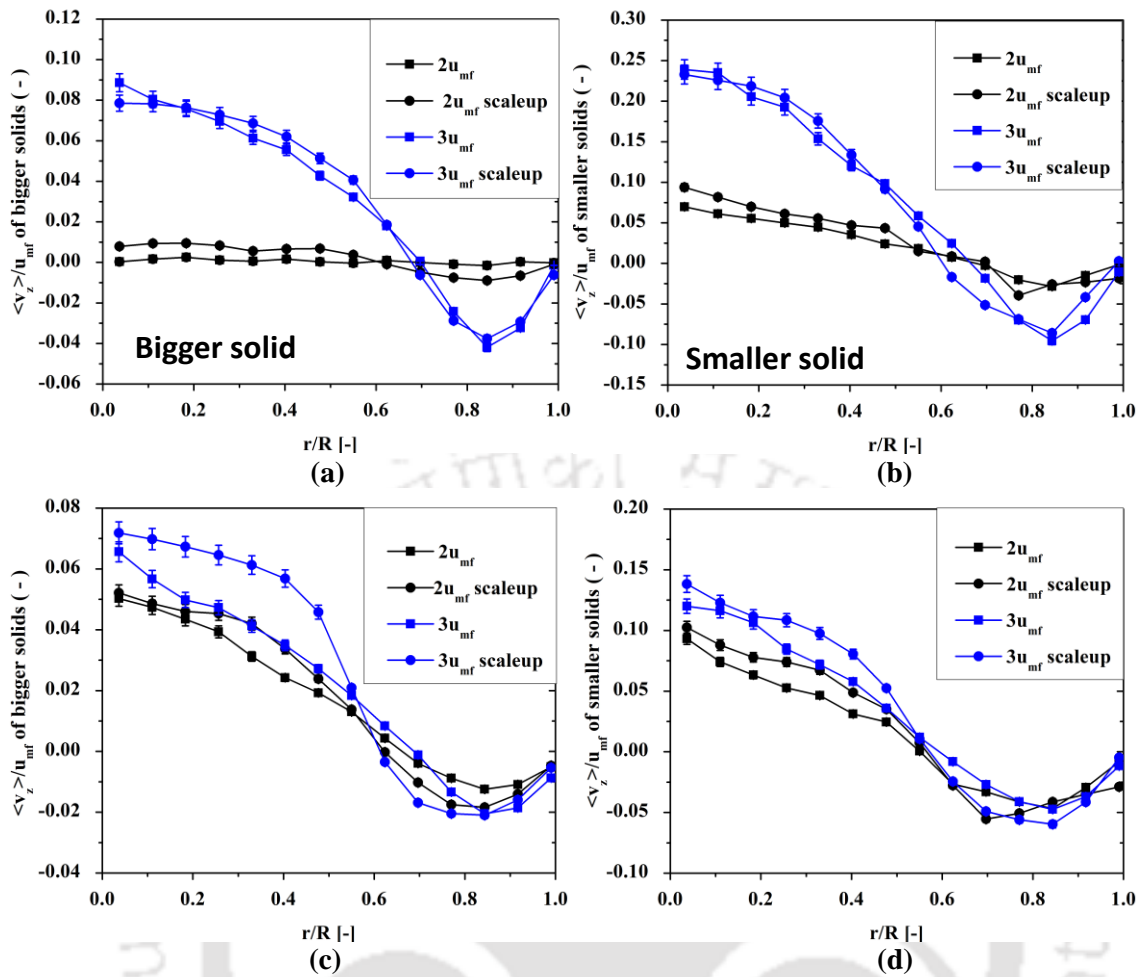


Figure 5.5 Variation of dimensionless mean axial velocity of solid in mono bed (a) top section bigger solid, (b) top section smaller solid, (c) bottom section bigger solid, and (d) bottom section smaller solid

Figures 5.6a, 5.6b show the non-dimensional radial mean solid velocity for the bigger and smaller particles on top section, respectively. Figures 5.6c and 5.6d show the non-dimensional solid radial mean velocity for the bigger and smaller particles at bottom section, respectively. The solid radial velocities are very small compared to their axial velocities in both columns. It indicates that motion is primarily in the axial direction for smaller and bigger solids in both columns.

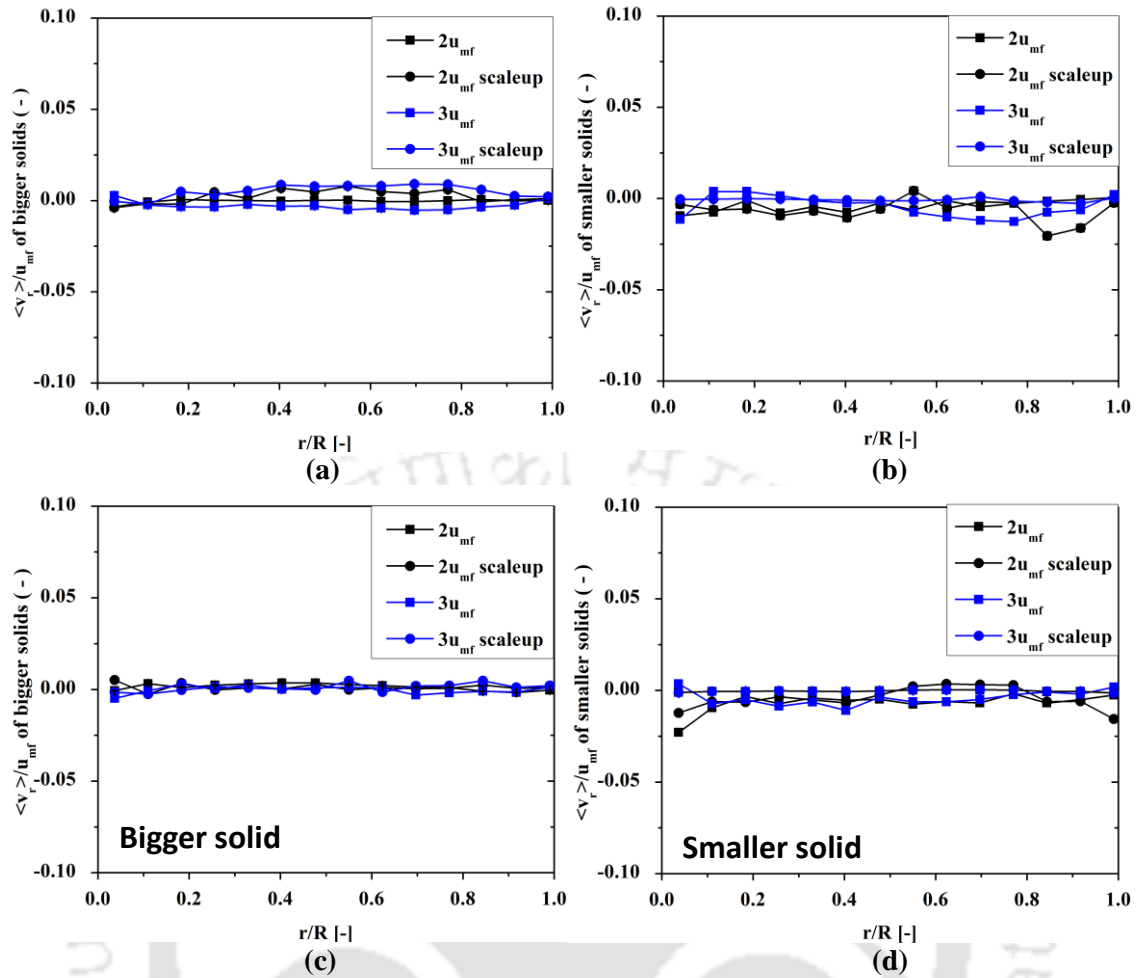


Figure 5.6 Variation of non-dimensional mean radial velocity of solid in mono bed (a) top section bigger solid, (b) top section smaller solid, (c) bottom section bigger solid, and (d) bottom section smaller solid

5.5.2 Solid velocity fluctuations

Similar to mean velocity, the RMS velocity of the solids was non-dimensionalized by dividing the values with u_{mf} of the respective solids. Figures 5.7a and 5.7b depict the dimensionless V_{zrms} of both columns at two different velocities on the top section. Similarly, Figures 5.7c and 5.7d depict the dimensionless V_{zrms} of both columns at two different velocities at the bottom section. Qualitatively the non-dimensional axial RMS velocity was similar for both solids in small and large diameter columns for both the top and bottom sections. However, quantitatively the values were not the same for both

solids. Interestingly reverse trend was observed for small and bigger particle scale up. For the bigger particle, large diameter column shows higher non-dimensional RMS velocity at top section. The trend was just opposite for smaller solids where large diameter column shows lower non-dimensional axial RMS velocity. Further, the non-dimensional axial RMS velocity values were very close for the bigger particle in both columns at bottom section for $2 u_{mf}$ gas inlet velocity. For $3 u_{mf}$, the value of non-dimensional axial RMS velocity is approximately the same at the bottom section. This indicates that the mechanism of transport is almost the same at the bottom section in both the columns for the bigger particle. The smaller particle shows the reverse trend where non-dimensional velocity was very close at the top section compared to bottom section for both columns. This is not surprising as in the case of two geometrically similar fluidized beds also the fluctuation does not make a concordance. This can be possible as the gas-solid contacting pattern changes with the scale-up of bench scale fluidized bed. The same is also reported by Fitzgerald et al. (1984) for the gas-solid cylindrical fluidized bed.

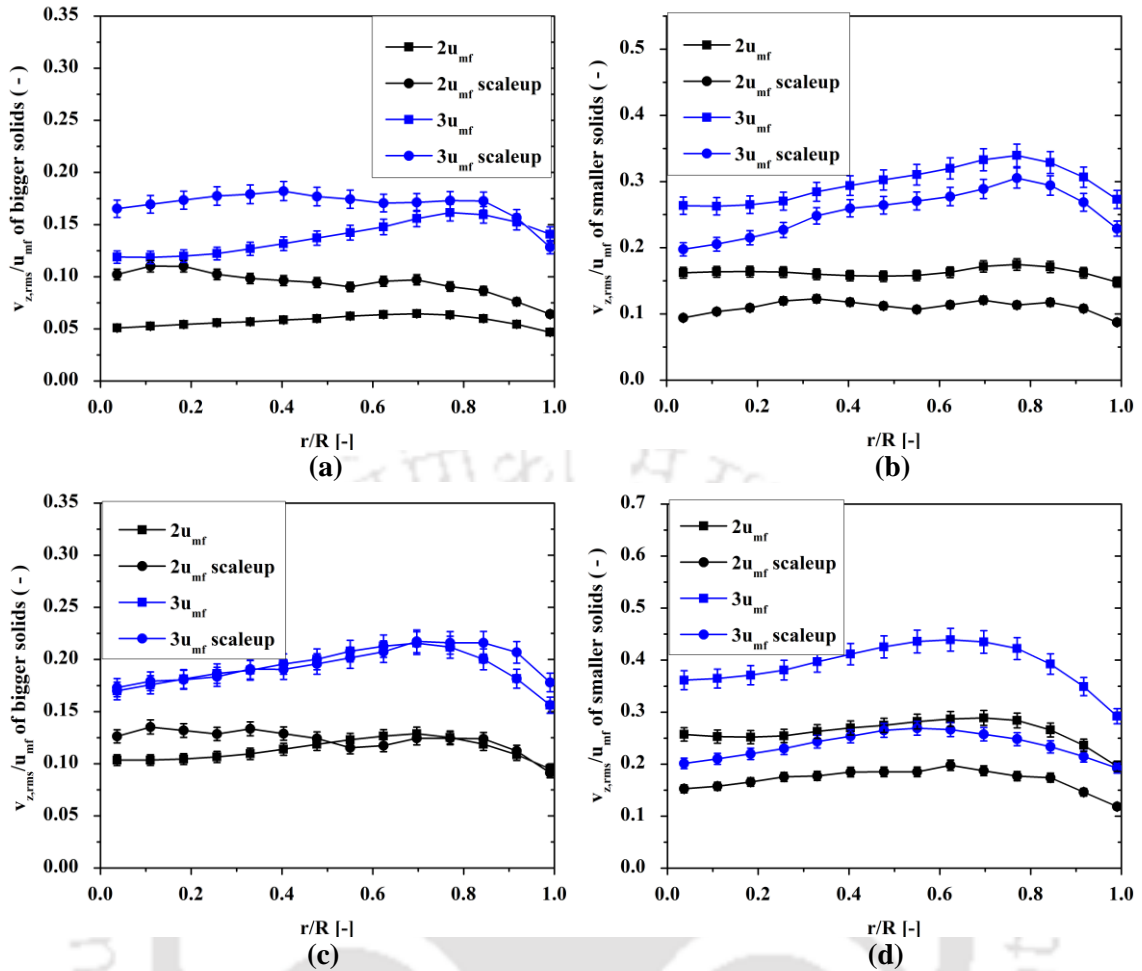


Figure 5.7 Variation of dimensionless $V_{z,rms}$ of solid in mono bed (a) top section bigger solid, (b) top section smaller solid, (c) bottom section bigger solid, and (d) bottom section smaller solid

5.5.3 Granular temperature

The granular temperature (θ) in both small and big columns is non-dimensionalized by dividing them by the square of the minimum fluidization velocity of the respective solids. Figure 5.8 presents the comparison of dimensionless granular temperature for both columns. The qualitative trend of non-dimensional granular temperature was similar to non-dimensional axial RMS velocity for both solids in small and large diameter columns. This indicates that in both columns solids fluctuations are primarily in the axial direction for both solids. However, quantitatively, the values of non-dimensional granular

temperature were different for both solids in small and large diameter columns. Hence, it can be concluded that used scale up law was able to match only mean velocity profile while the fluctuation trends for both columns were different.

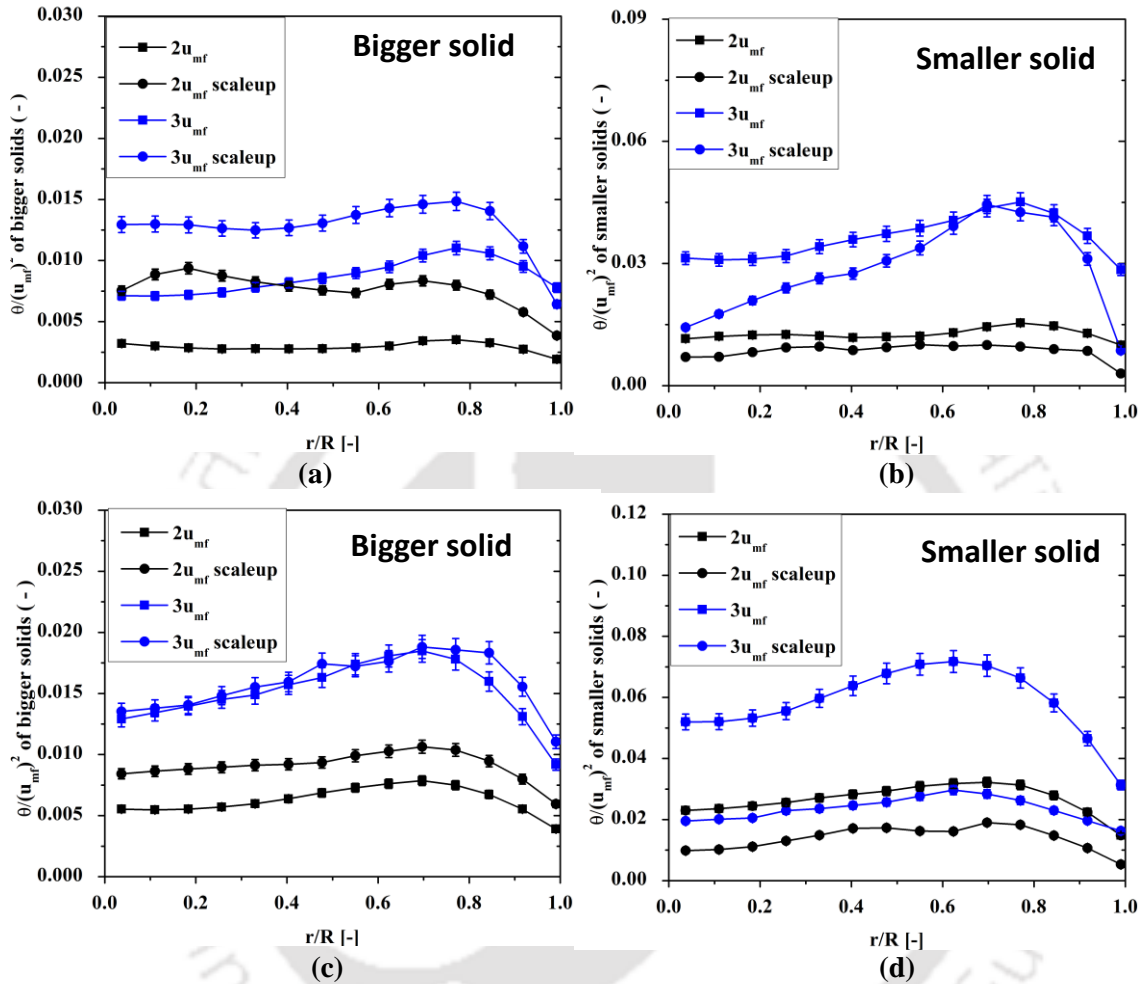


Figure 5.8 Variation of non-dimensionalized granular temperature of solid in mono bed (a) top section bigger solid, (b) top section smaller solid, (c) bottom section bigger solid, and (d) bottom section smaller solid

5.5.4 Hurst exponent

Time series and chaos analysis were performed to understand the dynamics of both solids in small and large diameter columns. Hurst exponent for both the columns was achieved by time series analysis of the instantaneous velocities. Table 5.2 shows the Hurst exponent values for both solids and columns. The ‘ H ’ values for both solids in large and

small diameter columns were greater than 0.5 indicating persistence nature of the solid velocity. Further, the 'H' values are approximately the same for both columns which indicate the dispersive nature of both columns is similar.

Table 5.2 Hurst exponents at different operating conditions for both the columns

u/u_{mf} gas velocity	Type of solid	Hurst exponent	
		Large column	Small column
2	Small	0.89	0.8
2	Big	0.59	0.59
3	Small	0.92	0.9
3	big	0.77	0.89

5.5.5 Autocorrelation

Autocorrelation function represents the correlation of the data with itself with changing time. Figures 5.9a and 5.9b present axial autocorrelation of bigger solids at a different velocity in the large column. Figures 5.9c and 5.9d represent the axial autocorrelation of bigger solids at low and high velocities in the small column. Figure 5.9 shows that the axial autocorrelation decays relatively faster for higher velocity in both columns for the bigger particle. At higher velocity, the axial autocorrelation dips at zero and then exhibit oscillations before converging at zero finally for both columns. An increase in oscillation was observed with an increase in gas inlet velocity for both columns. This indicates the increase in solid circulation rate for both columns with an increase in gas velocity. However, in large diameter column oscillations are taking a longer time to decay. This is because the solid has to travel more distance in large column compared to the small one.

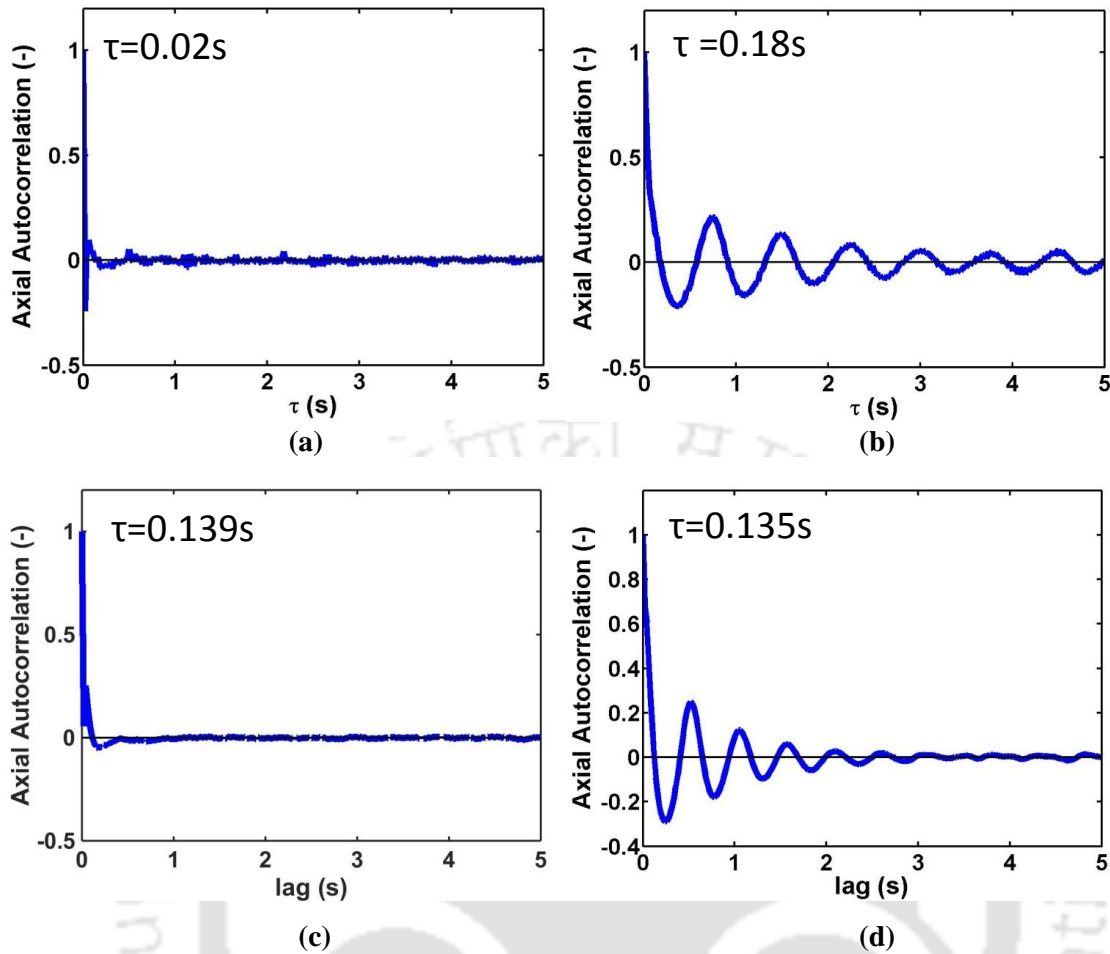


Figure 5.9 Variation of axial autocorrelation of solid in mono bed (a) 2 mm particle at 5.4 m/s in large column, (b) 2 mm particle at 8.1 m/s in large column, (c) 1 mm particle at 3.8 m/s in small column, and (d) 1 mm particle at 5.7 m/s in small column

Figures 5.10a and 5.10b present axial autocorrelation of smaller solids at low and high velocities in the large column. Figures 5.10c and 5.10d represent the axial autocorrelation of smaller solids at low and high velocities in the small column. In case of smaller solids too the autocorrelation function decays faster for higher velocities for both columns. For the smaller particle, axial autocorrelation dips at zero and then exhibit oscillations before converging at zero finally for both columns for all operating conditions. However, an increase in oscillation was observed with an increase in gas velocity for both columns. However, the time of complete decay was higher in the large column which was similar to the bigger particle.

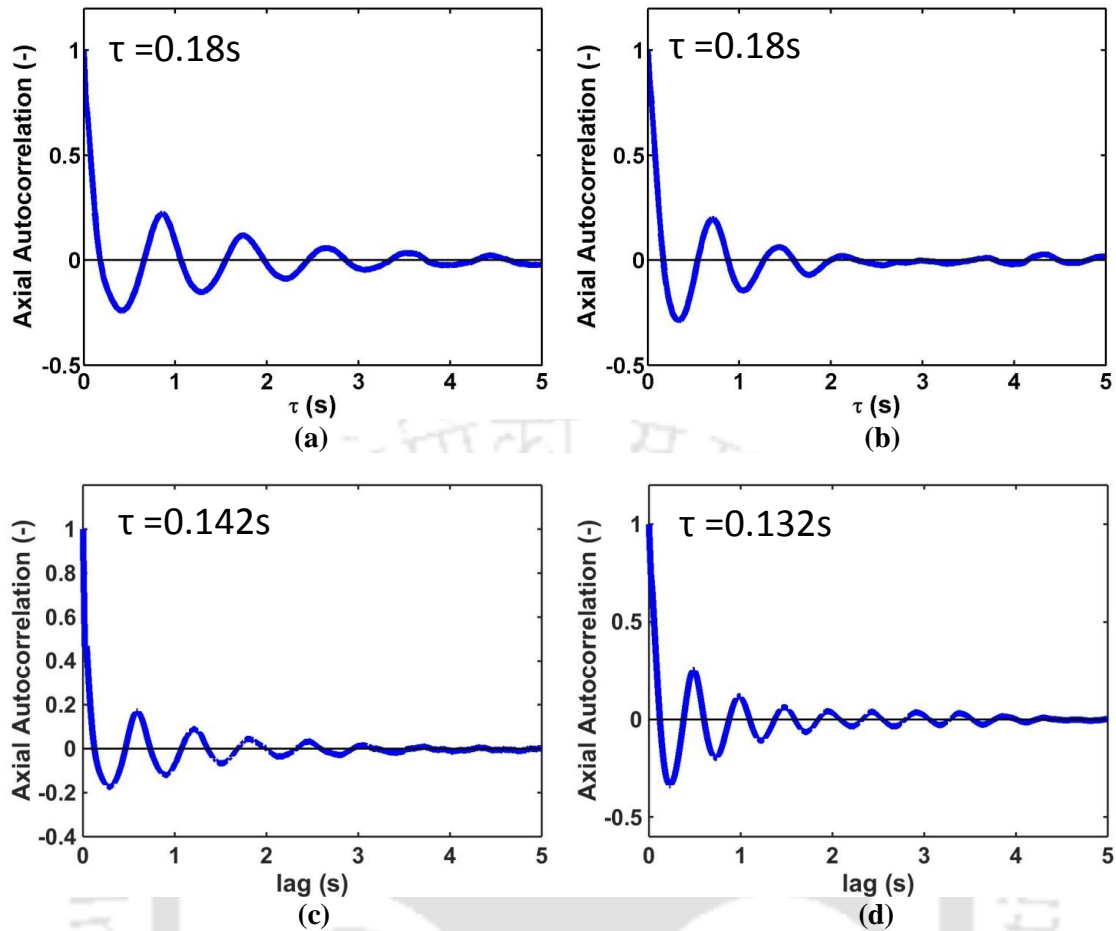


Figure 5.10 Variation of axial autocorrelation of solid in mono bed (a) 1 mm particle at 5.4 m/s in large column, (b) 1 mm particle at 8.1 m/s in large column, (c) 0.6 mm particle at 3.8 m/s in small column, and (d) 0.6 mm particle at 5.7 m/s in small column

5.5.6 Kolmogorov entropy

The Kolmogorov Entropy (KE) is obtained from the chaos analysis of the RPT data. It reveals the rate of information loss for any data. Van den Bleek and Schouten (1993) and Schouten et al. (1996) have stated that any two fluidized bed if scaled properly, their KE value will be the same. Hence, KE values were matched for both the solids in small and large diameter columns. Table 5.3 shows the Kolmogorov entropy values for different conditions in both columns. The Kolmogorov entropy of both columns is not matching which indicates the bed is not properly scaled. However, Schouten et al. (1996) and van der Stappen (1996) have achieved similarity in KE for gas-solid cylindrical fluidized bed

using simplified sets of Glicksman. However, in current work inertia set of Glicksman was used.

Table 5.3 Kolmogorov entropy at different operating conditions for both the columns

u / u_{mf} gas velocity	Type of solid	Kolmogorov entropy	
		Large column	Small column
2	Small	1.99	1.4
2	Big	1.31	0.09
3	Small	3.4	5.23
3	big	2.29	3.72

5.5.7 Correlation dimension

Correlation dimension (CD) reveals the degree of freedom of a system. Table 5.4 shows the Correlation dimension value for different conditions in both columns. The CD values are higher for the large column than the small one. It indicates that the number of parameters needed to explain the bed dynamic for the large column is more than the small column. As the CD values of both the columns are not matching it indicates the gas-solid conical fluidized bed cannot be properly scaled by using inertia set of Glicksman.

Table 5.4 Correlation dimension at different operating conditions for both columns

u/u_{mf} gas velocity	Type of solid	Correlation dimension	
		Large column	Small column
2	Small	6.16	5.12
2	Big	4.1	2.73
3	Small	6.9	6.51
3	big	5.69	5.73

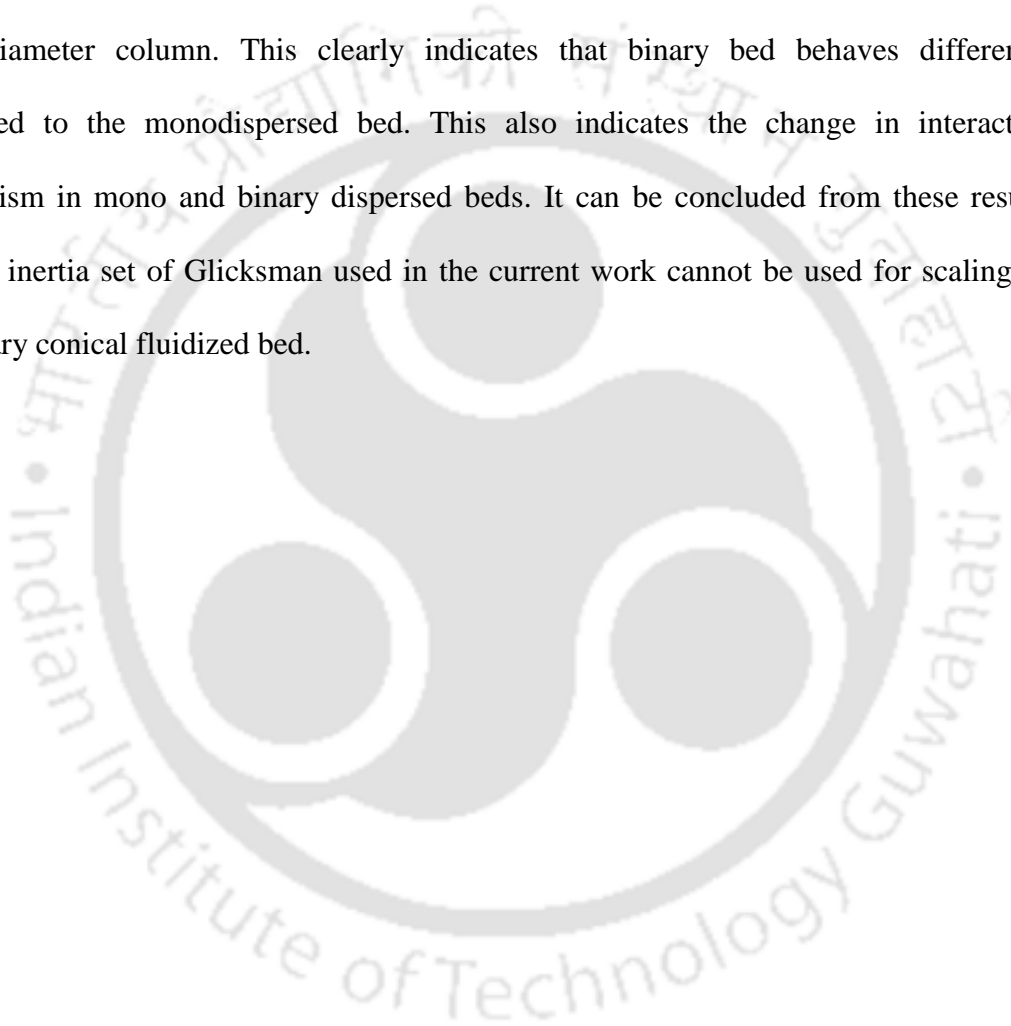
5.6 Effect of scale on binary dispersed bed

In the previous section, scale-up of the monodispersed gas-solid conical fluidized bed of two different sizes were investigated by using inertia set of Glicksman. To the best, no studies are reported in the literature where the same set of the scale-up rule was used for the binary gas-solid conical fluidized bed. Hence, in this section experiments were performed for different gas inlet velocity in 50b-50s wt. % binary bed in large diameter column. Glass beads of two different sizes (1 mm and 2 mm) with same density (2500 kg/m³) were used. The composition of the bed was kept constant for all the experiments. The bed was operated at two different gas inlet velocities, i.e. 5.4 and 8.1 m/s. The results of large diameter bed were compared with results of small diameter bed which are already reported in Chapter 3.

5.6.1 Ensemble averaged velocity

Similar to monodispersed bed in case of binary bed similar methodology was used for non-dimensionalizing the different quantities. The non-dimensional mean axial solid velocity for the bigger and smaller particles on top section is shown in Figures 5.11a and

5.11b and while Figures 5.11c and 5.11d show the same for the bottom section. The velocity profiles in binary bed at the top and bottom sections for both solids are qualitatively same for both columns. Quantitatively the behavior is almost the same for the bigger particle in the top and bottom sections for both velocities. However, they were not the same for smaller solids. On contrary to mono bed, for the smaller particle, the non-dimensional axial velocity was always higher in small diameter column compared to large diameter column. This clearly indicates that binary bed behaves differently compared to the monodispersed bed. This also indicates the change in interaction mechanism in mono and binary dispersed beds. It can be concluded from these results that the inertia set of Glicksman used in the current work cannot be used for scaling up the binary conical fluidized bed.



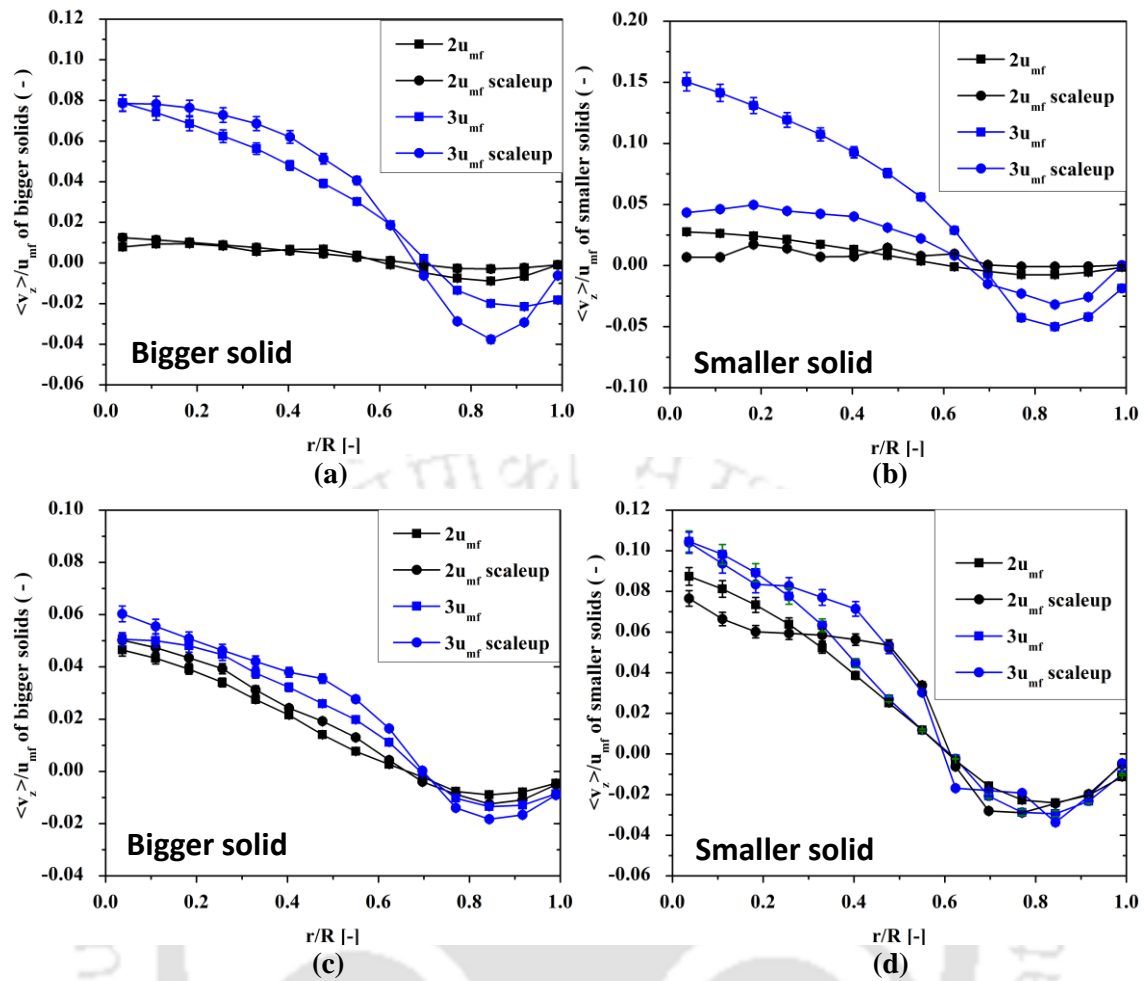


Figure 5.11 Variation of dimensionless mean axial velocity of solid in 50b-50s bed (a) top section bigger solid, (b) top section smaller solid, (c) bottom section bigger solid, and (d) bottom section smaller solid

5.6.2 Solid velocity fluctuations

Figure 5.12 depicts the dimensionless V_{zrms} of both columns at two different velocities at the top and bottom section. The V_{zrms} values are non-dimensionalized by dividing them by the minimum fluidization velocity of the corresponding solids. The V_{zrms} shows the difference in magnitude for both columns. This change may be due to the difference in the interaction of phases for both columns.

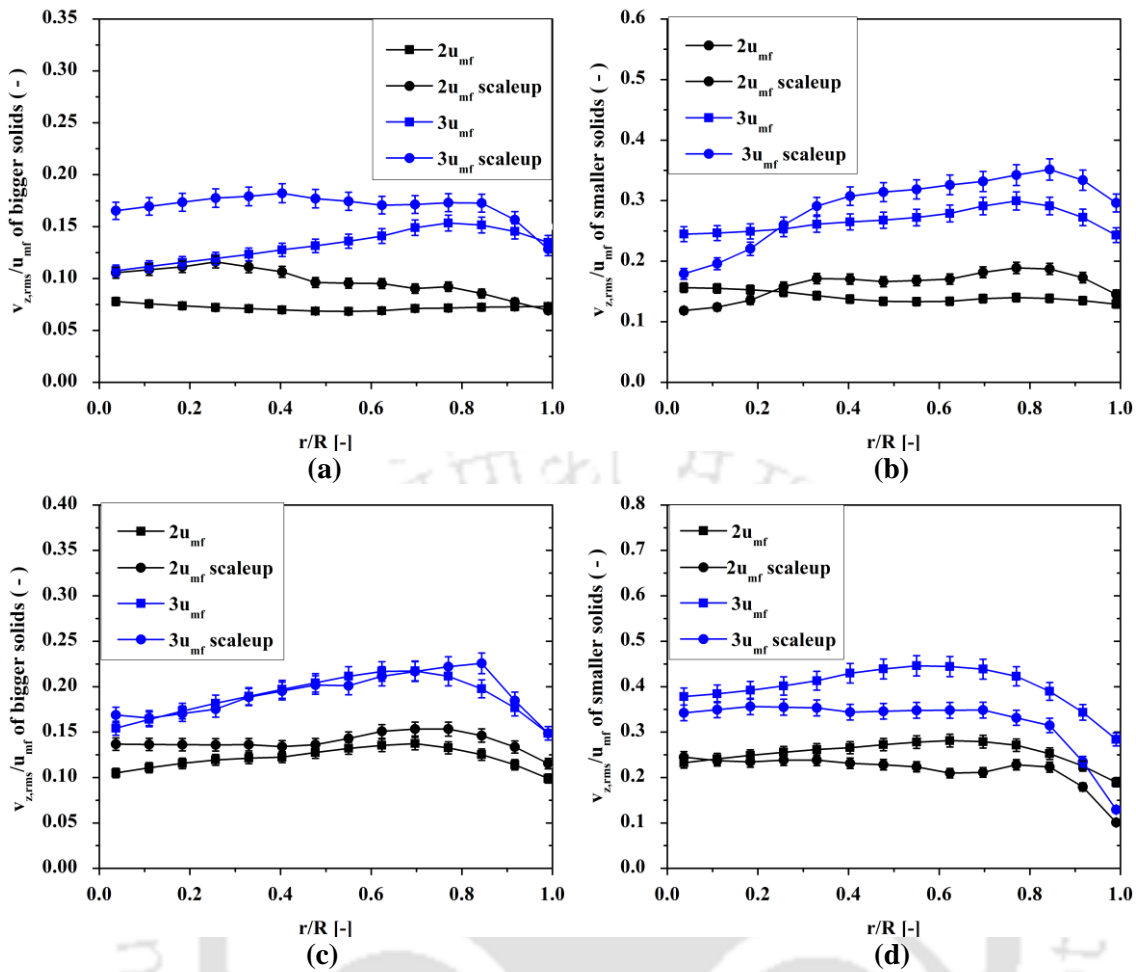


Figure 5.12 Variation of dimensionless V_{zrms} of solid in 50b-50s bed (a) top section bigger solid, (b) top section smaller solid, (c) bottom section bigger solid, and (d) bottom section smaller solid

5.6.3 Granular temperature

The granular temperature in both small and big columns is non-dimensionalized by dividing them by the square of the minimum fluidization velocity. Figure 5.13 presents the comparison of dimensionless granular temperature for both columns. Figure 5.13 shows that the profiles were similar but the magnitudes were different for both columns. This indicates there is a difference in the hydrodynamics of the two different dimensions fluidized beds.

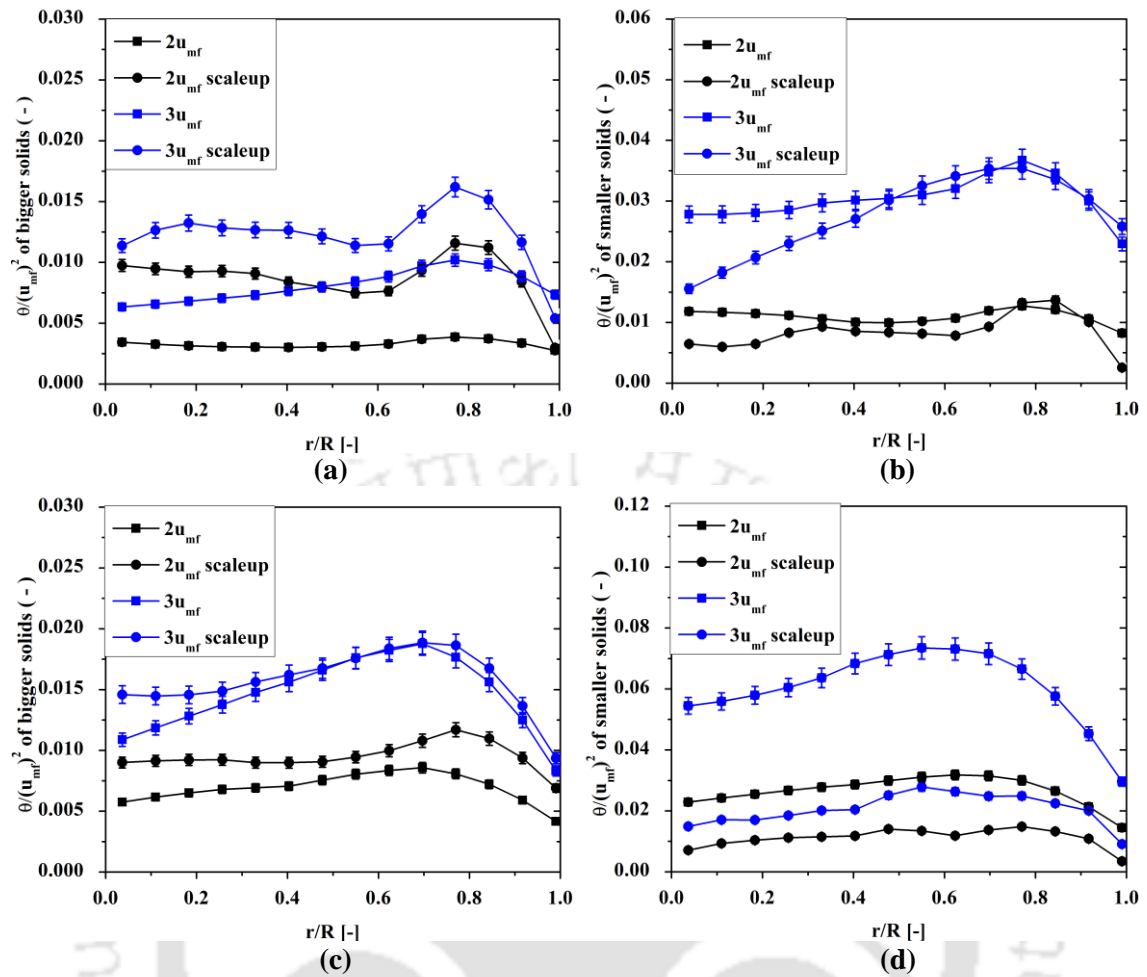


Figure 5.13 Variation of non-dimensionalized granular temperature of solid in 50b-50s bed, (a) top section bigger solid, (b) top section smaller solid, (c) bottom section bigger solid, and (d) bottom section smaller solid

5.6.4 Hurst exponent

Table 5.5 shows the Hurst exponent value for both solids and columns. The ‘ H ’ values for both columns are greater than 0.5 indicating persistence nature of the solid velocity. Further, the ‘ H ’ values are the same for both columns which indicate the dispersive nature of both columns is similar even in binary bed.

Table 5.5 Hurst exponents at different operating conditions for both the columns

u / u_{mf} gas velocity	Type of solid	Hurst exponent	
		Large column	Small column
2	Small	0.85	0.7
2	Big	0.64	0.68
3	Small	0.91	0.89
3	big	0.8	0.88

5.6.5 Autocorrelation

Figures 5.14a and 5.14b present axial autocorrelation of bigger solids at different velocities in the large column. Figures 5.14c and 5.14d represent the axial autocorrelation of bigger solids at low and high velocities in the small column. The axial autocorrelation of bigger solids in binary bed shows oscillation which is not observed in mono bed. However, the autocorrelation shows similar oscillating nature as the monodispersed bed. The oscillations also increase with velocity as the monodispersed bed.

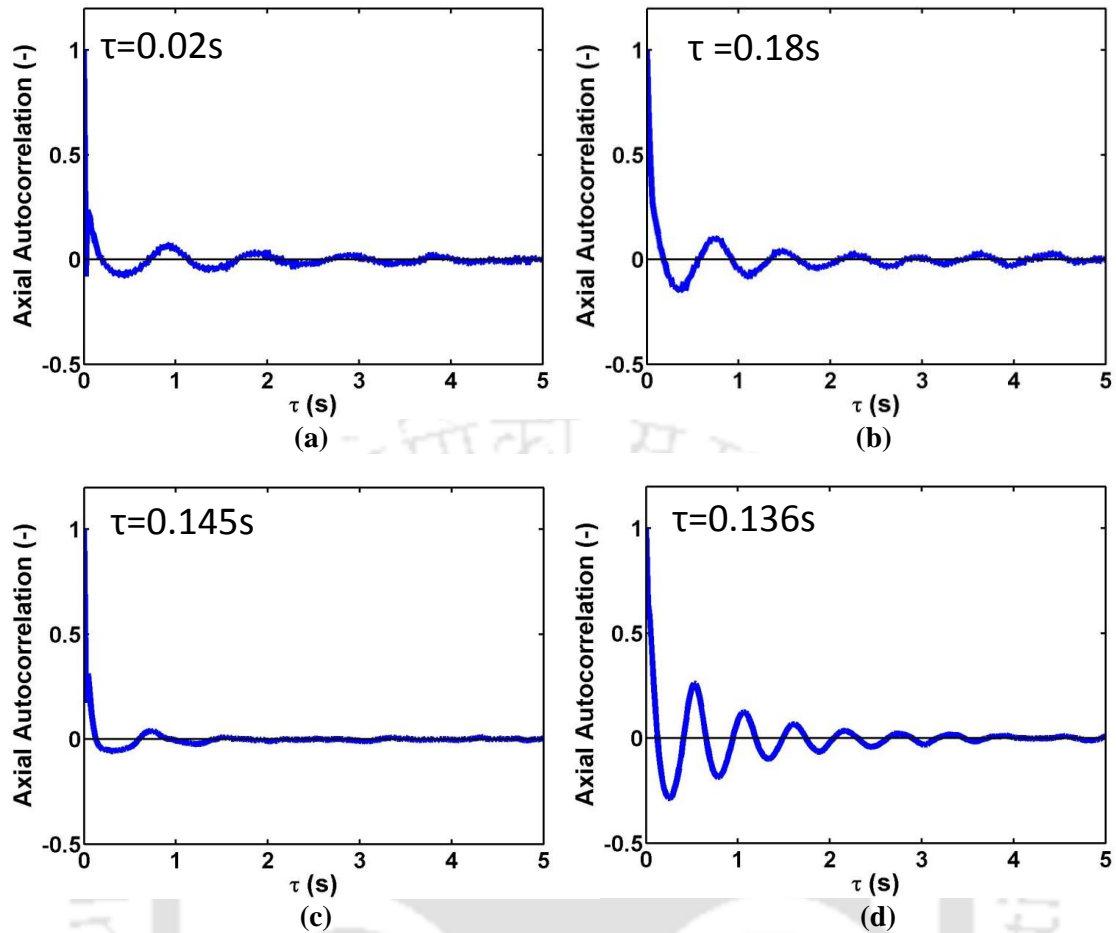


Figure 5.14 Variation of axial autocorrelation of solid in 50b-50s bed (a) 2 mm particle at 5.4 m/s in large column, (b) 2 mm particle at 8.1 m/s in large column, (c) 1 mm particle at 3.8 m/s in small column, and (d) 1 mm particle at 5.7 m/s in small column

Figures 5.15a and 5.15b present axial autocorrelation of smaller solids at low and high velocities in the large column. Figures 5.15c and 5.15d represent the axial autocorrelation of smaller solids at low and high velocities in the small column. In the case of smaller solids, the rate of fluctuation is less for large column compared to small columns. Thus, indicates different phenomena of bubble interaction in large column compared to the small column.

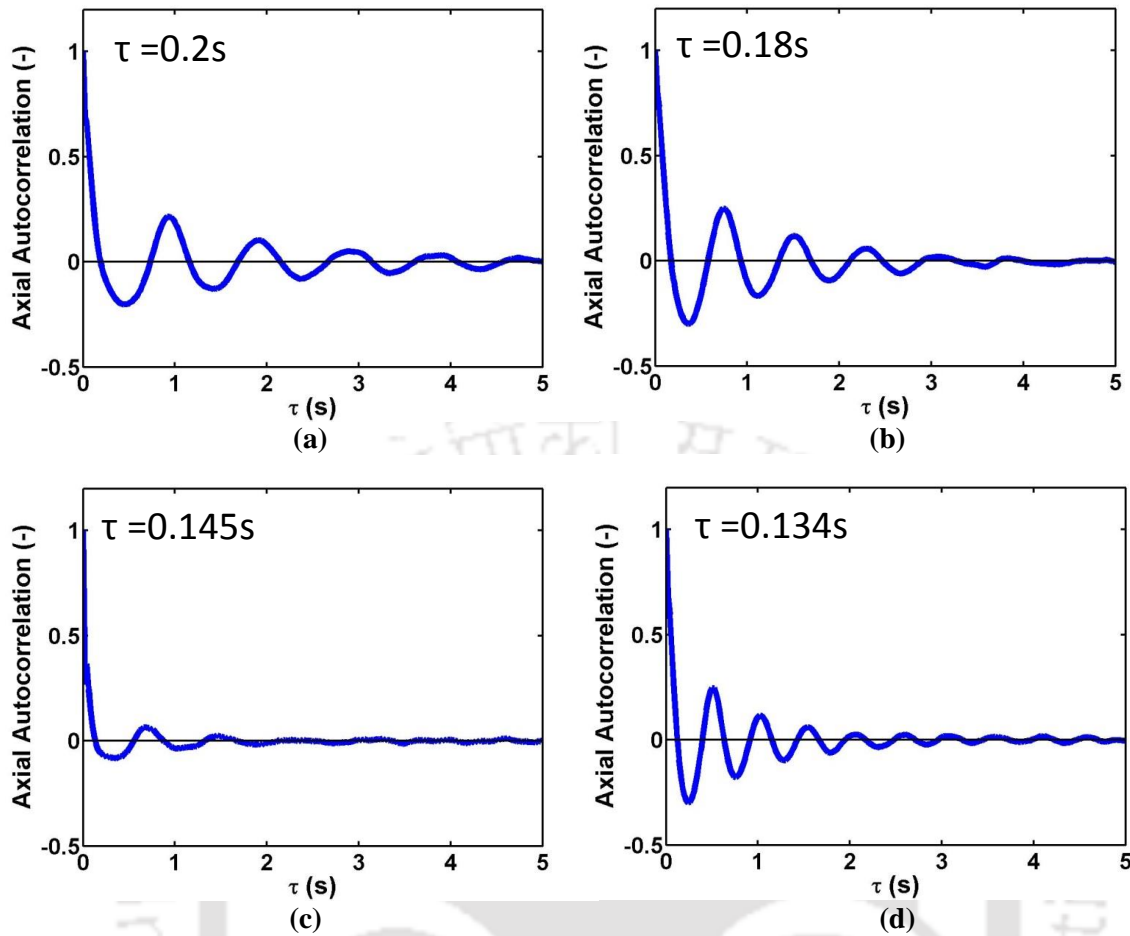


Figure 5.15 Variation of axial autocorrelation of solid in 50b-50s bed (a) 1 mm particle at 5.4 m/s in large column, (b) 1 mm particle at 8.1 m/s in large column, (c) 0.6 mm particle at 3.8 m/s in small column, and (d) 0.6 mm particle at 5.7 m/s in small column

Figures 5.16a and 5.16b present radial autocorrelation of bigger solids at low and high velocities in the large column. Figures 5.16c and 5.16d represent the radial autocorrelation of bigger solids at low and high velocities in the small column. Figure 5.16 shows that the radial autocorrelation decays very fast than axial autocorrelation. The radial autocorrelation takes the same time to decay for both columns for bigger solids.

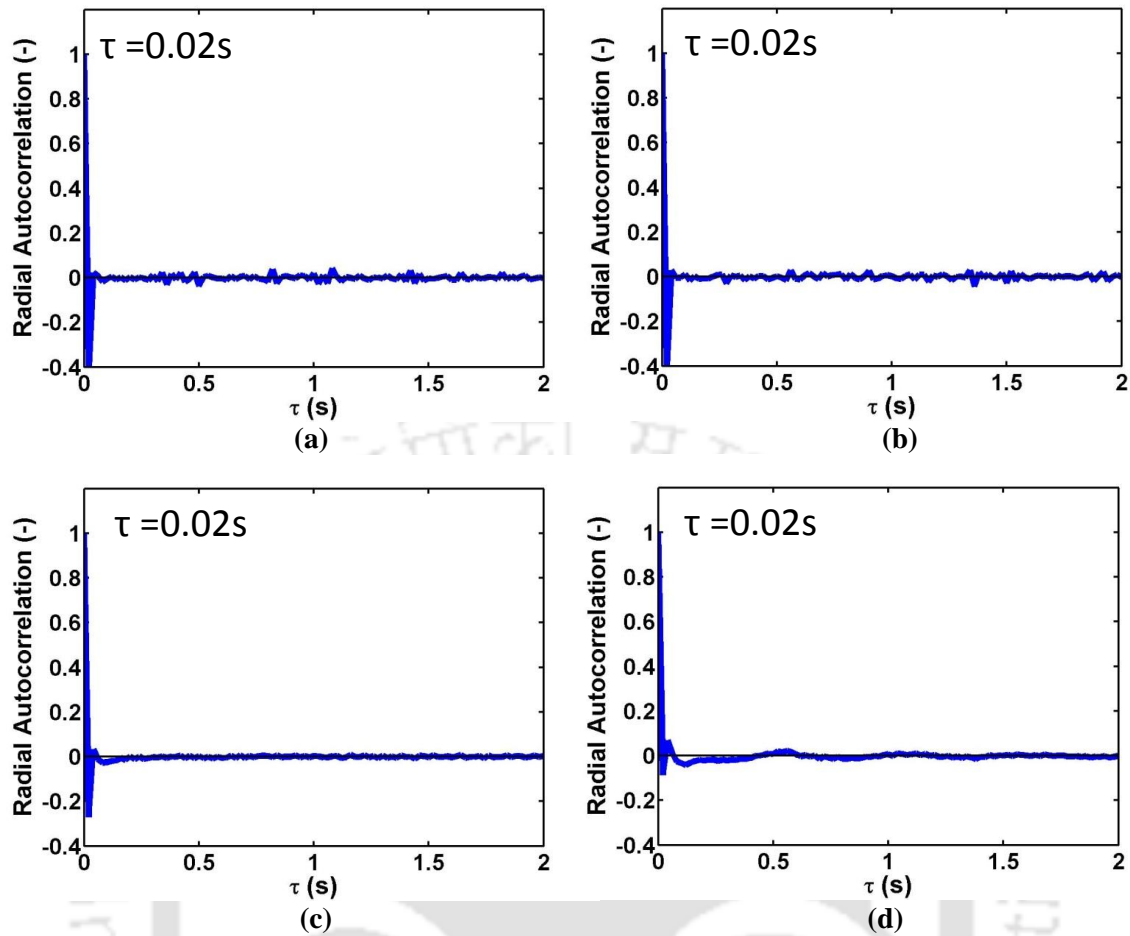


Figure 5.16 Variation of radial autocorrelation of solid in 50b-50s bed (a) 2 mm particle at 5.4 m/s in large column, (b) 2 mm particle at 8.1 m/s in large column, (c) 1 mm particle at 3.8 m/s in small column, and (d) 1 mm particle at 5.7 m/s in small column

Figures 5.17a and 5.17b present radial autocorrelation of smaller solids at low and high velocities in the large column. Figures 5.17c and 5.17d represent the radial autocorrelation of smaller solids at low and high velocities in the small column. In case of smaller solid, the radial autocorrelation of large column takes a longer time to decay than the small column.

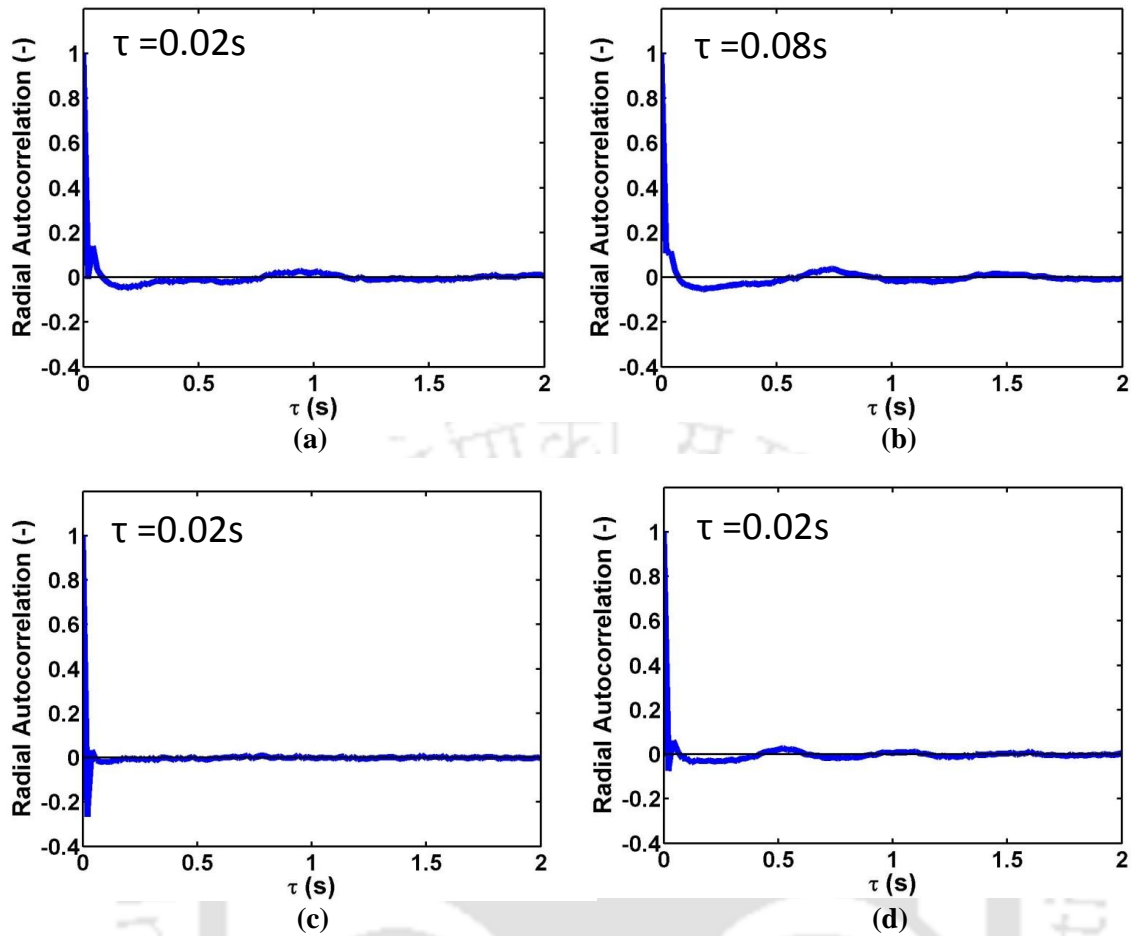


Figure 5.17 Variation of radial autocorrelation of solid in 50b-50s bed (a) 1 mm particle at 5.4 m/s in large column, (b) 1 mm particle at 8.1 m/s in large column, (c) 0.6 mm particle at 3.8 m/s in small column, and (d) 0.6 mm particle at 5.7 m/s in small column

5.6.6 Kolmogorov entropy

Table 5.6 shows the Kolmogorov entropy value for different conditions in both the columns. The Kolmogorov entropy of both the columns is not matching. Hence, the scaling law used is not suitable for scaling the conical fluidized bed.

Table 5.6 Kolmogorov entropy at different operating conditions for both the columns

u / u_{mf} gas velocity	Type of solid	Kolmogorov entropy	
		Large column	Small column
2	Small	1.25559	0.45713
2	Big	1.18258	0.38626
3	Small	2.5931	4.36523
3	big	2.80435	3.98531

5.6.7 Correlation dimension

Table 5.7 shows the Correlation dimension value for different conditions in both columns. The CD values are higher for the large column than the small one. It indicates that the number of parameters needed to explain the bed dynamic for the large column is more than the small column. Results further conclude that the gas-solid conical binary fluidized bed cannot be properly scaled by using inertia set of Glicksman.

Table 5.7 Correlation dimension at different operating conditions for both the columns

u / u_{mf} gas velocity	Type of solid	Correlation dimension	
		Large column	Small column
2	Small	7.00179	3.95083
2	Big	5.34476	4.0167
3	Small	6.98964	5.92096
3	big	5.80113	5.84643

5.7 Summary

In this work, we studied the scale-up of fluidized bed reactors based on matching dimensionless groups methodology proposed by Glicksman et al. (1984). Radioactive particle tracking technique was employed for both columns for obtaining the data. Mean solids velocities for monodispersed solids were similar in both columns qualitatively and quantitatively when non-dimensionalized. Hence, it can be concluded that the inertia set of Glicksman can match the mean axial velocity profile in monodispersed bed. However, the axial RMS velocities show high value in the bigger column compared to small column indicating different solid-solid and fluid-solid interaction. The granular temperature in the large column is significantly higher in magnitude than the small column. The autocorrelation indicates the rate of bubble formation and breakage and the solid circulation in the large column is different than the small column. The results of chaos analysis show the KE and CD value are not matching for both columns. The variation indicates the global parameters that used for

the scaling laws (Glicksman inertia set) are not sufficient for accurate scaling of the monodispersed gas-solid conical fluidized bed. The same set of laws was tested for scaling up the gas-solid conical binary fluidized bed. The Glicksman inertia set was not able to even match mean axial velocity in case of binary bed. Hence, it is not suitable for scaling up binary conical fluidized bed. A similar conclusion was drawn through time series and chaos analysis of binary conical bed data obtained at two different scales. Hence, a new scales up methodology is required for proper scaling of the conical fluidized bed.

Notations

D_c	Column diameter, m
d_p	Solid diameter, m
Fr_s	Froude number, -
h	Static bed height, m
H	Hurst exponent, -
u_g	Inlet velocity, m/s
u_{mf}	Minimum fluidization velocity at partially fluidized bed, m/s
u_{mff}	Minimum fluidization velocity at fully fluidized bed, m/s
$\langle v_z \rangle$	Mean axial solid velocity, m/s
$\langle v_r \rangle$	Mean radial solid velocity, m/s
ρ_g	Fluid density, kg/m ³
ρ_s	Particle density, kg/m ³
μ_g	Fluid viscosity, kg s/m ²
τ	Time, s

θ Granular temperature, m^2/s^2

References

- Al-Dahhan, M., Aradhya, S., Zaid, F., Ali, N., Aljuwaya, T., 2014. Scale-up and on-line monitoring of gas-solid systems using advanced and non-invasive measurement techniques. *Procedia Eng.* 83, 469–476.
- Bashiri, H. Mostoufi, N., Ramin, R., Rahmat, S., Chaouki, J., 2010. Effect of Bed Diameter on the Hydrodynamics of Gas-Solid Fluidized Beds. *Iran. J. Chem. Chem. Eng.* 29, 27–36.
- Di Maio, F.P., Di Renzo, A., 2013. Verification of scaling criteria for bubbling fluidized beds by DEM-CFD simulation. *Powder Technol.* 248, 161–171.
- Efhaima, A., Al-Dahhan, M.H., 2015. Local time-averaged gas holdup in fluidized bed reactor using gamma ray computed tomography technique (CT). *Int. J. Ind. Chem.* 6, 143–152.
- Efhaima, A., 2016. Scale-up Investigation and Hydrodynamics Study of Gas-Solid Fluidized Bed Reactor Using Advanced Non-invasive Measurement Techniques, Ph.D. Thesis, Missouri University of Science and Technology, USA.
- Efhaima, A., Al-Dahhan, M.H., 2017. Assessment of scale-up dimensionless groups methodology of gas-solid fluidized beds using advanced non-invasive measurement techniques (CT and RPT). *Can. J. Chem. Eng.* 95, 656–669.
- Fitzgerald, T., Bushnell, D., Crane, S., Shieh, Y.C., 1984. Testing of cold scaled bed modeling for fluidized-bed combustors. *Powder Technol.* 38, 107–120.
doi:10.1016/0032-5910(84)80040-6

- Glicksman L.R., 1984. Scaling relationships for fluidized beds, Chem. Eng. Sci. 39 (9), 1373–1379.
- Glicksman, L. R. 1988. Scaling Relationships for Fluidized Beds. Chem. Eng. Sci. 43 (6), 1419-1421.
- Glicksman, L.R., Hyre, M., Woloshun, K., 1993. Simplified scaling relationships for fluidized beds. Powder Technol. 77, 177–199.
- Horio, M., Nonaka, A., Sawa, Y., Muchi, I., 1986. A new similarity rule for fluidized bed scale-up. AIChE J. 32, 1466–1482.
- Knowlton, T.M., Karri, S.B.R., Issangya, A., 2005. Scale-up of fluidized-bed hydrodynamics. Powder Technol. 150, 72–77.
- Newby, R.A., Keairns, D.L. 1986. Test of the scaling relationships for fluidized bed dynamics, in fluidization, Engineering Foundation, New York, 31-38.
- Nicastro, M.T., Glicksman, L.R., 1984. Experimental verification of scaling relationships for fluidized bed. Chem. Eng. Sci. 39, 1381–1391.
- Rüdisüli, R., Tilman, J. Schildhauer, Serge M.A. Biollaz J. Ruud van Ommen. 2012. Scale-up of bubbling fluidized bed reactors - A review. Powder Technol. 217, 21-38.
- Sanderson, J., 2007. The 12th International Conference on Fluidization - New Horizons in Fluidization An Investigation of Fluidized Bed Scaling Laws by DEM Simulation.
- Schouten, J.C., Vander Stappen, M.L.M., Van Den Bleek, C.M., 1996. Scale-up of chaotic fluidized bed hydrodynamics. Chem. Eng. Sci. 51, 1991–2000.

- Stein, M., Ding, Y.L., Seville, J.P.K., 2002. Experimental verification of the scaling relationships for bubbling gas-fluidized beds using the PEPT technique. *Chem. Eng. Sci.* 57, 3649–3658.
- Tahmasebpour, M., Zarghami, R., Sotudeh-Gharebagh, R., van Ommen, J.R., Mostoufi, N., 2017. Dynamic analysis of the scale-up of fluidized beds. *Adv. Powder Technol.* 28, 2621–2629.
- Taofoeq, H., Al-Dahhan, M., 2018. Comparison between the new mechanistic and the chaos scale-up methods for gas-solid fluidized beds. *Chin. J. Chem. Eng.* 26, 1401–1411.
- Van den Bleek, C.M., Schouten, J.C., 1993. Can Deterministic Chaos Create Order in Fluidized-Bed Scale-up? *Chem. Eng. Sci.* 48, 2367–2373.
- van den Bleek, C.M., Schouten, J.C., 1993. Deterministic chaos: a new tool in fluidized bed design and operation. *Chem. Eng. J. and Biochem. Eng. J.* 53, 75–87.
- Van Den Bleek, C.M., Coppens, M.O., Schouten, J.C., 2002. Application of chaos analysis to multiphase reactors. *Chem. Eng. Sci.* 57, 4763–4778.
- Van der Stappen, M.L.M., 1996. Chaotic Hydrodynamics of Fluidized Beds, Phd Thesis, Delft University of Technology, Netherlands.
- van Ommen, J.R., Teuling, M., Nijenhuis, J., van Wachem, B.G.M., 2006. Computational validation of the scaling rules for fluidized beds. *Powder Technol.* 163, 32–40.
- Zaid, F., 2013. Gas-Solid Fluidized Bed Reactors: Scale-Up, Flow Regimes Identification and Hydrodynamics, Ph.D. Thesis, Missouri University of Science and Technology, USA.

Chapter 6

Summary and Recommendations

Scope

All the previous chapters gave summary and conclusions with respect to the research findings in respective chapters. In this chapter, broader conclusions from the thesis and potential future work are given.

6.1 Summary

The overall aim of the current thesis was to understand the flow behavior of conical fluidized bed. The work has three different aspects. The first aspect was to implement the radioactive particle tracking technique in a conical geometry. Only one literature shows the implementation of RPT in the conical fluidized bed. However, they were not able to measure the complete velocity field. So this is the first work in which detailed hydrodynamics of a conical bed is studied. The second aspect of the work was to investigate the hydrodynamics of gas-solid and liquid-solid conical fluidized beds. The scope of the work was extended to study the behavior of monodispersed and binary beds of different compositions. Being critically important from decades, the detailed characterization of conical fluidized bed was still not achieved and most of the literature on conical fluidized bed presents the data based on time-averaged quantities or develop correlations to predict minimum fluidization velocity or bed pressure drop. To the best of author knowledge, this is the first of its kind work where detailed flow behavior of conical fluidized bed was studied with state-of-the-art non-invasive measurement technique. Further, detailed post-processing of Lagrangian data was performed to infer the flow characteristics and

regime transition. The third aspect of the work was to study the scale-up of the conical fluidized bed. In literature, no dedicated scaling laws are available for the conical fluidized bed. Further, the scaling law available for cylindrical fluidized bed was never rigorously checked to match the fluctuation levels mainly due to the lack of data. The validity of scaling laws for binary or polydispersed bed was also not verified. In current work, first time scaling laws are tested in mono and binary dispersed conical fluidized beds. The comparison of two different scale reactor was performed for the time average and fluctuation quantities like RMS velocities and granular temperature. The specific conclusions of each chapter are individually given at the end of the chapter. This chapter is intended to summarize the overall conclusion of the key findings. The broader conclusions of the current thesis are as follows:

- It is found that the hydrodynamics of gas-solid conical bed is chaotic and that the degree of chaotic behavior depends on the gas velocity and bed composition.
- The axial mean velocity of both 1mm and 0.6 mm particles are found to be approximately same in 50b-50s wt. % binary bed at a higher velocity, which signifies the homogeneous distribution of solids. It indicates that the mixing and interaction of the gas-solids increases with an increase in velocity at the mean level. It was observed that in conical bed two different interaction phenomena dominate the behavior of the bed at the top and bottom section. At the bottom section, gas-solids interaction plays a dominating role while in the top section particle-particle interaction becomes crucial.
- In the gas-solid conical fluidized bed, the axial autocorrelation takes a longer time to decay compared to radial autocorrelation which signifies that motion is primarily in the axial direction.

- The segregation index calculated for binary bed indicates good mixing even at a lower gas inlet velocity which is contradictory to the cylindrical column. Hence, it can be stated that conical fluidized bed provides better mixing compared to the cylindrical fluidized bed.
- Correlation Dimension and Kolmogorov Entropy shows the chaotic nature of the mono and binary fluidized beds. Further, CD and KE values also indicate a change in flow regime (after 5.7 m/s gas velocity) for both mono and binary fluidized beds. Finally, it has been found that flow regime transition in conical bed mainly depends on gas inlet velocity and not on bed composition.
- The axial solid velocity of 1mm mono dispersed bed is lowest which increase with the fraction of 0.6 mm solid in the mixture on top section. This indicates that bigger particle gains momentum from the smaller particle and improves with the increase in smaller particle fraction in the bed. In contrast, the axial solid velocity of 0.6 mm mono dispersed bed is highest which keeps on decreasing with the addition of 1 mm solids into the mixture on top section. It indicates that in the case of binary dispersed bed particle-particle interaction plays a major role. However, the effect is not significant at the bottom section due to the high gas velocity that suppresses the particle-particle interaction effect.
- The figure indicates highest axial RMS velocity in case of 0.6 mm mono and lowest in case of 1 mm mono dispersed bed. This confirms the 0.6 mm solid have the highest RMS velocity due to highest u/u_{mf} ratio. The axial RMS velocity of 1mm binary bed is higher than 1 mm mono dispersed bed due to the addition of the smaller particle. This indicates momentum transfer from 0.6 mm particle to 1 mm particle after the collision.

- The segregation index indicates good mixing condition for all the bed composition. No regime transition was observed for binary bed operated at different bed composition for same gas inlet velocity.
- It is found that the hydrodynamics of liquid-solid conical bed is chaotic and that the degree of chaotic behavior depends on the liquid velocity and bed composition.
- The axial mean velocity of both 1mm and 0.6 mm particles are found to be approximately same in 50b-50s binary bed at a higher velocity, which signifies homogeneous distribution of solids. It indicates that the mixing and interaction of liquid-solids increases with increase in velocity at the mean level. It was observed that in conical bed two different interaction phenomena dominate the behavior of the bed at the top and bottom sections. At the bottom section, liquid-solids interaction plays a dominating role while in top section particle-particle interaction becomes crucial.
- In the liquid-solid conical fluidized bed, the axial autocorrelation takes a longer time to decay compared to radial autocorrelation which signifies that motion is primarily in the axial direction.
- The segregation index calculated for binary bed indicates good mixing even at a lower liquid inlet velocity which is contradictory to the cylindrical column. Hence, it can be stated that conical fluidized bed provides better mixing compared to the cylindrical fluidized bed.
- Correlation Dimension and Kolmogorov Entropy shows the chaotic nature of the mono and binary fluidized beds. Further, CD and KE values also indicate the change in flow regime (after 0.1 m/s gas velocity) for 1 mm mono and binary fluidized bed. Finally, it

has been found that flow regime transition in conical bed mainly depends on liquid inlet velocity and not on bed composition.

- The axial solid velocity of 1mm mono dispersed bed is lowest which increase with the fraction of 0.6 mm solid in the mixture on top section. This indicates that bigger particle gains momentum from the smaller particle and improves with the increase in smaller particle fraction in the bed. In contrast, the axial solid velocity of 0.6 mm mono dispersed bed is highest which keeps on decreasing with the addition of 1 mm solids into the mixture on top section. It indicates that in the case of binary dispersed bed particle-particle interaction plays a major role.
- The figure indicates highest axial RMS velocity in case of 0.6 mm mono and lowest in case of 1 mm mono dispersed bed. This confirms the 0.6 mm solid have the highest RMS velocity due to highest u/u_{mf} ratio. The axial RMS velocity of 1mm binary bed is higher than 1 mm mono dispersed bed due to the addition of the smaller particle. This indicates momentum transfer from 0.6 mm particle to 1 mm particle after the collision.
- The segregation index indicates good mixing condition for all the bed composition.
- Mean solids velocities for the monodispersed bed were similar in both the columns qualitatively and quantitatively when non-dimensionalized. Hence, it can be concluded that the inertia set of Glicksman can match the mean axial velocity profile in the monodispersed bed.
- Axial RMS velocities show high value in the bigger column compared to small column indicating different solid-solid and fluid-solid interaction.
- The results of chaos analysis show the KE and CD value are not matching for both columns.

- Glicksman inertia set is not sufficient for accurate scaling of the mono and binary dispersed gas-solid conical fluidized beds.

6.2 Recommendations and future directions

Future work recommendations are an integral part of any research work. Here given are few sets of recommendations:

- One needs to be careful with the type of solids used in conical fluidized bed. The study on even course particle with the poly-dispersed bed will be more useful for industrial applications.
- Detailed CFD simulation of conical bed can solve the scaling problem and the data generated in the current work can be used for the validation.
- The work can be performed to develop better scaling laws dedicated to the conical fluidized bed.
- Scale up studies can be performed for liquid-solid conical bed.
- A further effect of cone angle on scaling and flow behavior can be characterized for the different type of particles.
- CFD can be validated against the obtained benchmarking data for gas-solid and liquid-solid conical fluidized beds. Further, CFD approach can be used for design and scale-up of the system after validation.

Appendix A

Euler-Euler Simulations of Gas-Solid Conical Fluidized Bed

A.1 Introduction

Computational fluid dynamics (CFD) is the technique used to analyze systems involving fluid flow by solving mathematical equations using a numerical process. CFD is a tool for numerical analysis that can provide better insights into the flow, sometimes which is not achievable through the experiments. CFD is also an inexpensive technique which can be used for design as well as scale up. This approach is also good at laboratory, pilot plant and industrial scales.

Euler - Euler and Euler - Lagrangian are two different approaches used for modeling of the fluidized bed. In Euler – Lagrangian approach, Navier-Stokes equation is solved for continuous phase and Newton's second law of motion is solved to track the history of each particle (discrete phase) (Tsuji et al., 1987; Deen et al., 2007). Euler – Lagrangian approach is used for the system where the behavior of the discrete phase is much more important. Euler – Euler approach is used for the bigger system, where both the phases are treated as continuous phase interacting everywhere. In the Euler-Euler approach, separate mass and momentum equations are employed to treat corresponding phases. The interaction between both phases is solved using drag closer.

In modeling of the fluidized bed, the selection of suitable closer is more important. The closer selection depends on the system completely. In the current work, Euler – Euler approach is used for modeling gas-solid conical fluidized bed. In addition, the effect of inlet fluid velocity on fluidization behavior is studied. Finally, the obtained results are compared with experimental RPT results.

A.2 Euler – Euler modeling approach

In Euler-Euler (E-E) modeling of the fluidized bed, both fluid and solid phases are considered as interpenetrating continuum. This refers that both solid and fluid phases can co-exist at the same location inside the bed and their summation of volume fraction at that point is equal to one.

Two sets of mass and momentum conservation equations are used in E-E simulations. The interaction between the two phases is accounted by the momentum exchange coefficient (drag). Solid fluctuation is accounted by Kinetic theory of granular flow (KTGF). ANSYS® Fluent 14.5 commercial solver is used in this work.

Conservation equations

Governing conservation equations are

Continuity equation:

The continuity equation for phase q is represented by equation A.1

$$\frac{\partial}{\partial t}(\varepsilon_q \rho_q) + \nabla \cdot (\varepsilon_q \rho_q \vec{v}) = 0 \quad (\text{A.1})$$

where, $q = f, s$. Equation A.1, is solved for both fluid, f , and solid, s , phases

Momentum equation:

The momentum equation for fluid phase is represented by equation A.2

$$\frac{\partial}{\partial t}(\varepsilon_f \rho_f \vec{v}_f) + \nabla \cdot (\varepsilon_f \rho_f \vec{v}_f \vec{v}_f) = -\varepsilon_f \nabla p + \nabla \cdot \bar{\bar{\tau}}_f + \varepsilon_f \rho_f \vec{g} + K_{sf}(\vec{v}_s - \vec{v}_f) + \vec{F}_f \quad (\text{A.2})$$

The momentum equation for solid phase is represented by equation A.3

$$\frac{\partial}{\partial t}(\varepsilon_s \rho_s \vec{v}_s) + \nabla \cdot (\varepsilon_s \rho_s \vec{v}_s \vec{v}_s) = -\varepsilon_s \nabla p - \nabla p_s + \nabla \cdot \bar{\bar{\tau}}_s + \varepsilon_s \rho_s \vec{g} + K_{sf}(\vec{v}_f - \vec{v}_s) + \vec{F}_s \quad (\text{A.3})$$

$$\varepsilon_s + \varepsilon_f = 1 \quad (\text{A.4})$$

The continuity equation shown in equation A.1 represents the temporal and spatial gradients in the first and second terms on the left side. The right side term is zero as there is no mass generation and consumption due to any reaction or any mass exchange between the phases.

Equation A.2 and A.3 represent the momentum conservation equations for the fluid and solid phases, respectively. The local and convection acceleration are represented by the left side term and the source and sink terms are represented by the right side term. The right side also includes hydrodynamic pressure generated by both phases. However, in case of the solid phase, an extra pressure term is included known as solid pressure that occurs due to the collision between solids. Normal stress is due to solid pressure and shear stress of solid $\nabla \cdot \bar{\tau}_s$ is due to the collision of solid phase while shear stress of the fluid phase $\nabla \cdot \bar{\tau}_f$ is due to viscous forces.

The body forces of the solid and fluid phases are represented as $\varepsilon_s \rho_s \vec{g}$ and $\varepsilon_f \rho_f \vec{g}$, respectively. The momentum exchanges between the two phases are represented as interphase momentum exchange terms $K_{sf}(\vec{u}_s - \vec{u}_f)$ and $K_{sf}(\vec{u}_f - \vec{u}_s)$. The momentum exchange coefficient K_{sf} is a function of slip velocity and volume fraction. Other external forces like magnetic, electrical forces are represented with \vec{F}_f and \vec{F}_s , which are accounted as zero.

Solid phase fluctuations

The solid phase interactions in a fluidized bed are described based on the kinetic theory of granular flow (KTFG) (Chapman and Cowling, 1990; Ding and Gidaspow, 1990). In

KTGF the solid phase stresses are considered as a result of momentum transfer between the solid particles. The particles behave similarly to the molecules in a gas as it moves. Hence granular temperature is introduced to express the kinetic energy of the fluctuating motion of the particles.

The granular temperature is represented by equation A.5

$$\frac{3}{2} \left[\frac{\partial}{\partial t} (\varepsilon_s \rho_s \Theta_s) + \nabla \cdot (\varepsilon_s \rho_s \vec{u}_s \Theta_s) \right] = \left(-p_s \bar{I} + \bar{\tau}_s \right) : \nabla \vec{u}_s + \nabla \cdot (k_{\Theta_s} \nabla \Theta_s) - \gamma_{\Theta_s} + \phi_{fs} \quad (\text{A.5})$$

The four terms on the right side are the generation of energy by solid stress tensor, diffusion of energy, collisional dissipation of energy and interphase energy exchange, respectively. The solids pressure, p_s as given by Ding and Gidaspow (1990) is expressed by equation A.6

$$p_s = \rho_p \varepsilon_s \Theta_s + 2(1 + e_{ss}) \rho_s \Theta_s g_o \varepsilon_s^2 \quad (\text{A.6})$$

The terms on the right side are the kinetic and additional pressure terms due to the collisions. Both terms are the function of volume fraction. Θ_s is the granular temperature; e_{ss} is the coefficient of restitution of particle that represents the reduction of pressure depending on the nature of the collision. The value of e_{ss} indicates the nature of the collision. If $e_{ss} = 0$, the collision is inelastic and if $e_{ss} = 1$, the collision is elastic. g_o is the radial distribution function ρ_s that indicates the increase of collision probability at high volume fraction. The radial distribution function of the solid phase, g_o is expressed as given in Ding and Gidaspow (1990) is:

$$g_o = \frac{1}{1 - \left(\frac{\varepsilon_s}{\varepsilon_{\max}} \right)^{\frac{1}{3}}} \quad (\text{A.7})$$

Solid shear stresses

The solid stress tensor consists of shear and bulk viscosities. The shear viscosity contains collisional, kinetic and frictional parts as given in Ding and Gidaspow (1990), and expressed as

$$\mu_s = \frac{4}{3} \varepsilon_s^2 \rho_s d_p g_0 (1 + e_{ss}) \left(\frac{\Theta_s}{\pi} \right)^{\frac{1}{2}} + \frac{5 \rho_s d_p}{48 \varepsilon_s (1 + e_{ss}) g_0} \sqrt{\Theta_s \pi} \left[1 + \frac{4}{5} g_0 \varepsilon_s (1 + e_{ss}) \right]^2 \quad (\text{A.8})$$

The right side terms are collision and kinetic terms, respectively. The collision term is a function of volume fraction and granular temperature whereas the kinetic term is the function of only granular temperature.

The bulk viscosity represents the resistance of the solid particles for compression and expansion and expressed as given in Lun et al. (1984) as follows

$$\lambda_s = \frac{4}{3} \varepsilon_s \rho_s d_s g_{0,ss} (1 + e_{ss}) \left(\frac{\Theta_s}{\pi} \right)^{1/2} \quad (\text{A.9})$$

Solids conductivity/ Diffusion coefficient of granular energy

The solid conductivity or diffusion coefficient of granular energy is given by (Gidaspow et al., 1992) as follows

$$k_s = \frac{15 d_p \rho_s \varepsilon_s \sqrt{\Theta_s \pi}}{4(41 - 33\eta)} \left[1 + \frac{12}{5} \eta^2 (4\eta - 3) \varepsilon_s g_0 + \frac{16}{15\pi} (41 - 33\eta) \eta \varepsilon_s g_0 \right] \quad (\text{A.10})$$

The right side terms are collision and kinetic terms, respectively. The collision term dominates in case of high solid holdup whereas the kinetic term dominates for both high and low solid hold-ups.

Collisional dissipation of energy

The collisional dissipation of energy due to inelastic collision is given by Lun et al. (1984) as follows

$$\gamma_{\theta n} = \frac{12(1-e_{ss}^2)g_{0,ss}}{d_s \sqrt{\pi}} \rho_s \alpha_s^2 \Theta_s^{\frac{3}{2}} \quad (\text{A.11})$$

Drag closure

The drag between fluid and solid phases plays an important role in the momentum exchange. Different drag coefficients are represented as below

Table A.1 Drag models

Drag model	Model description
Gibilaro (1985) drag model	$K_{s,f} = \left(\frac{17.3}{\text{Re}_p} + 0.336 \right) \frac{\rho_f v_f - v_s }{d_p} (1 - \varepsilon_f) \varepsilon_f^{-2.80}$ <p>where $\text{Re}_p = \frac{\varepsilon_f \rho_f d_p v_f - v_s }{\mu_f}$</p>
Gidaspow (1994) drag model is the combination of	$k_{s,f} = \frac{3}{4} C_D \frac{\varepsilon_s \varepsilon_f \vec{v}_s - \vec{v}_f \rho_f \varepsilon_f^{-2.65}}{d_p} \quad \text{for } \varepsilon_f > 0.8$
Wen-Yu and Ergun model	$k_{s,f} = 150 \frac{\varepsilon_s^2 \mu_f}{\varepsilon_s d_p^2} + 1.75 \frac{\rho_f \varepsilon_s \vec{v}_s - \vec{v}_f }{\varepsilon_f d_p} \quad \text{for } \varepsilon_f \leq 0.8$
Huilin and Gidaspow (2003) drag model	$K_{s,f} = \psi \left(150 \frac{(1 - \varepsilon_f) \varepsilon_s \mu_{lam,f}}{\varepsilon_f^2 d_p^2} + 1.75 \frac{\rho_f \varepsilon_s \vec{v}_f - \vec{v}_s }{\varepsilon_f d_p} \right) + (1 - \psi) \left(\frac{3}{4} C_d \frac{\varepsilon_s \rho_f \vec{v}_f - \vec{v}_s }{d_p} \varepsilon_f^{-2.65} \right)$

$$\text{where } C_d = \begin{cases} \frac{24}{\text{Re}} (1 + 0.15 \text{Re}^{0.68}), & \text{Re} \leq 1000, \\ 0.44, & \text{Re} > 1000, \end{cases}$$

$$\psi = \arctan \left(\frac{150 \times 1.75 (0.2 - \varepsilon_s)}{\pi} \right) + 0.5$$

HKL (2001) drag

model

$$K_{s,f} = 18 \mu_f \varepsilon_f^2 \varepsilon_s \left(\frac{F}{d_p^2} \right)$$

where

$$F = \begin{cases} 1 + 3/8 \text{Re}_r, \varepsilon_s \leq 0.01; \text{Re}_r \leq \left(\frac{F_2 - 1}{3/8 - F_3} \right) \\ F_0 + F_1 \text{Re}_r, \varepsilon_s > 0.01; \text{Re}_r \leq \frac{F_3 + \sqrt{F_3^2 - 4F_1(F_0 - F_2)}}{2F_1} \\ F_2 + F_3 \text{Re}_r, \text{otherwise} \end{cases}$$

$$F_0 = \begin{cases} (1-\omega) \times \left[\frac{1 + 3\sqrt{\varepsilon_s/2} + (135/64)\varepsilon_s \ln(\varepsilon_s) + 17.14\varepsilon_s}{1 + 0.681\varepsilon_s - 8.4\varepsilon_s^2 + 8.16\varepsilon_s^3} \right] + \omega \left[\frac{10\varepsilon_s}{(1-\varepsilon_s)^3} \right], & 0.01 < \varepsilon_s < 0.4; \\ 10 \frac{\varepsilon_s}{(1-\varepsilon_s)^3}, & \varepsilon_s \geq 0.4; \end{cases}$$

$$F_1 = \begin{cases} \sqrt{2/\varepsilon_s} / 40, & 0.01 < \varepsilon_s < 0.1; \\ 0.11 + 0.00051 \times \exp(11.6\varepsilon_s), & \varepsilon_s > 0.1; \end{cases}$$

$$F_2 = \begin{cases} (1-\omega) \times \left[\frac{1 + 3\sqrt{\varepsilon_s/2} + (135/64)\varepsilon_s \ln(\varepsilon_s) + 17.89\varepsilon_s}{10.681\varepsilon_s - 8.4\varepsilon_s^2 + 8.16\varepsilon_s^3} \right] + \omega \left[\frac{10\varepsilon_s}{(1-\varepsilon_s)^3} \right], & \varepsilon_s < 0.4; \\ 10 \frac{\varepsilon_s}{(1-\varepsilon_s)^3}, & \varepsilon_s \geq 0.4; \end{cases}$$

$$F_3 = \begin{cases} 0.935\varepsilon_s + 0.03667, & \varepsilon_s < 0.0953; \\ 0.0673 + 0.212\varepsilon_s + 0.0232 / (1-\varepsilon_s)^5, & \varepsilon_s \geq 0.0953; \end{cases}$$

Where

$$\omega = \exp\left(\frac{-10(0.4 - \varepsilon_s)}{\varepsilon_s}\right)$$

A.3 Base case formulation (Gas-solid fluidized bed)

In this work, two-dimensional transient model is developed to simulate the conical gas-solid fluidized bed. The schematic of the geometry is shown in Figure A.1. ANSYS 14.5 commercial CFD software has been used for simulation. Simulations are performed and compared at the operating conditions used for RPT experiments presented in chapter 3.

For the base case model formulation, operating conditions of 7.6 m/s gas inlet velocity with 1 mm solids is used. Table A.1 shows the simulation conditions and parameters used. The drag closure, specular coefficient, and restitution coefficients are selected based on the comparison with the experimental results. The time averaging is started after 30 seconds of simulation time and each simulation is time averaged for 100 seconds.

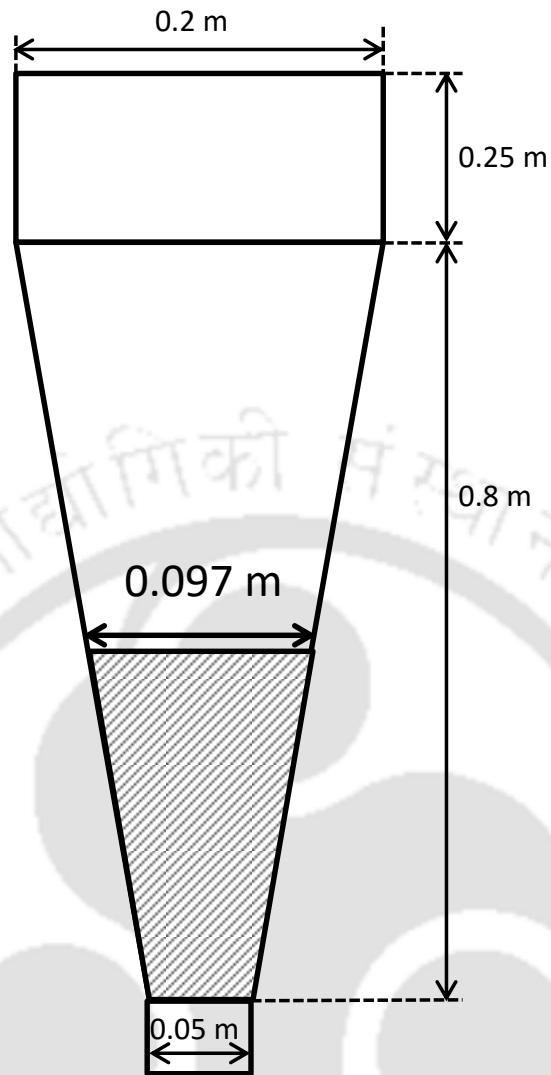


Figure A.1 Schematic of computational domain of conical fluidized bed

Table A.2 Simulation conditions and parameters in gas-solid (G-S) fluidized bed

Parameters	Model / Value
Particle diameter	600 μm , 1000 μm
Density	2500 kg/m^3
Superficial gas velocity	3.8, 5.7 , 7.6 m/s
Air inlet	Velocity inlet
Outlet	Pressure outlet
Wall (air)	No slip
Wall (solid)	Johnson and Jackson
Restitution coefficient (p-p)	0.96
Gas-solid drag	Wen and Yu (1966)
Shear viscosity	Gidaspow (1994)
Bulk viscosity	Lun et al. (1984)
Solid pressure	Lun et al. (1984)
Radial distribution	Lun et al. (1984)
Specularity coefficient	0.5
Pressure velocity coupling	SIMPLE
Momentum discretization	Second order UPWIND
Volume fraction discretization	QUICK
Grid	Uniform grid
Time step	0.001 sec

Grid convergence

Four grids of the radial and axial division of 50×262 , 25×262 , 12×262 and 8×174 were checked. Figure A.2 shows the mean axial velocity and volume fraction of solids for different grids. No significant difference is observed in the mean volume fraction plots of all the grid sizes. However, a small difference is observed for 8×174 in case of mean axial velocity plots. In the current work, the grid 25×262 is used as it gives similar values as of other grids.

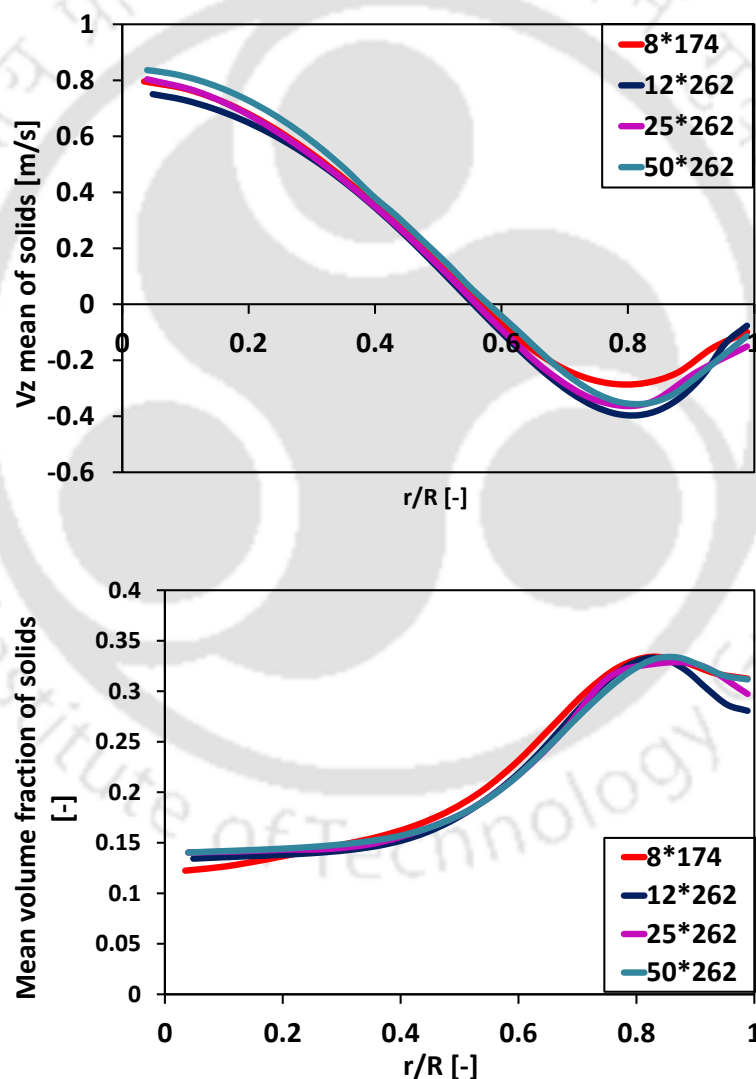


Figure A.2 Axial profiles of mean axial velocity and volume fraction for different grids in G-S conical fluidized bed ($U_g = 7.6$ m/s and 1 mm solid)

Drag closure

Figure A.3 shows the axial profiles of mean axial velocity and volume fraction for different drag model in G-S conical fluidized bed. For gas-solid fluidized bed Gibilaro et al. (1985), Gidaspow (1994), Huilin & Gidaspow (2003) and HKL (2001) drag models were used as shown in drag closer section above. Gidaspow, Huilin & Gidaspow drag model gives similar results. However, Gibilaro drag closure is not able to predict the inversion point perfectly and predicted higher downward velocity of the solids near the wall. HKL drag closure was predicting higher upward and downward velocity of the solids. Further, Gidaspow drag model has been used in the literature, for the conical fluidized bed. Hence, in this work Gidaspow drag model has been used.

Specularity and restitution coefficients

The specularity and restitution coefficients between wall and particle play an important role for simulation. Specularity coefficient indicates the fraction of exchange of momentum from particles to wall. It varies from zero (free-slip condition) to one (no-slip condition). In this work, specularity coefficient 0.5, 0.8 and 1 are used for simulation. Figure A.4 shows the axial profiles of mean axial velocity and granular temperature for different specularity coefficient in the conical fluidized bed. The specularity coefficient 0.5 gives result closer to experimental results of mean velocity. The simulation result shows both qualitative and quantitative agreement for mean axial solid velocity. However, the granular temperature shows only qualitative agreement. The experimental granular temperature will be always higher than simulation as in case of simulation particle-particle collisions are not well represented. Therefore, in current work, specularity coefficient of 0.5 is used for further simulations.

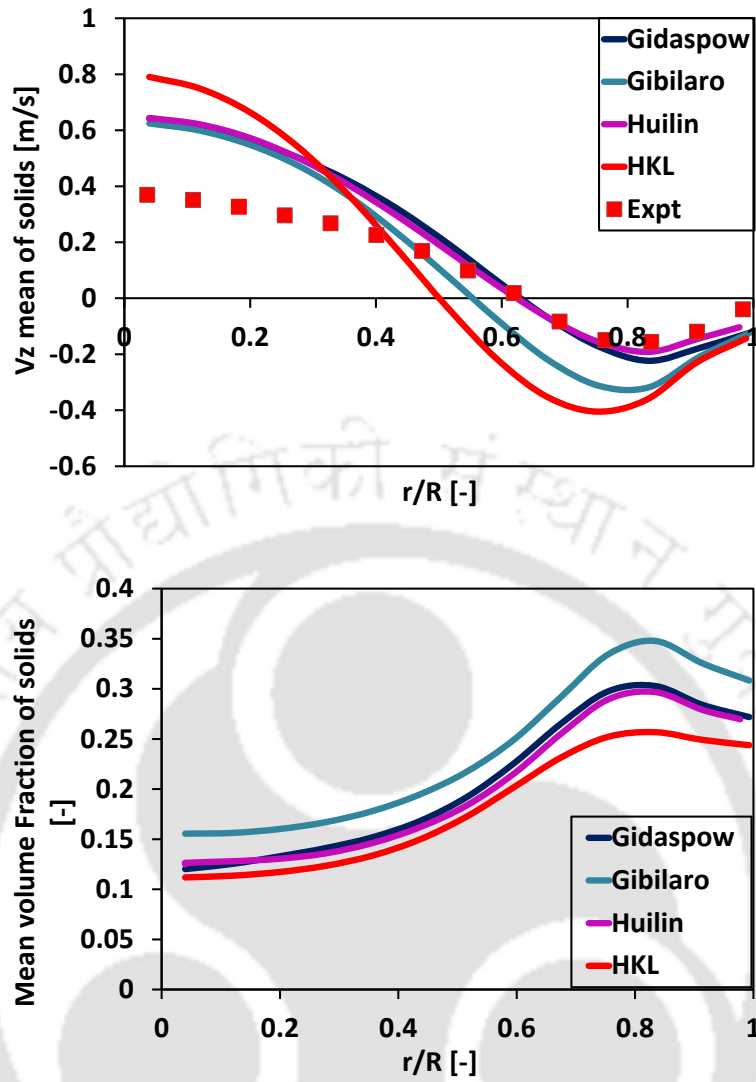


Figure A.3 Axial profile of mean axial velocity and volume fraction for different drag model in G-S conical fluidized bed ($U_g = 7.6$ m/s and 1 mm solid)

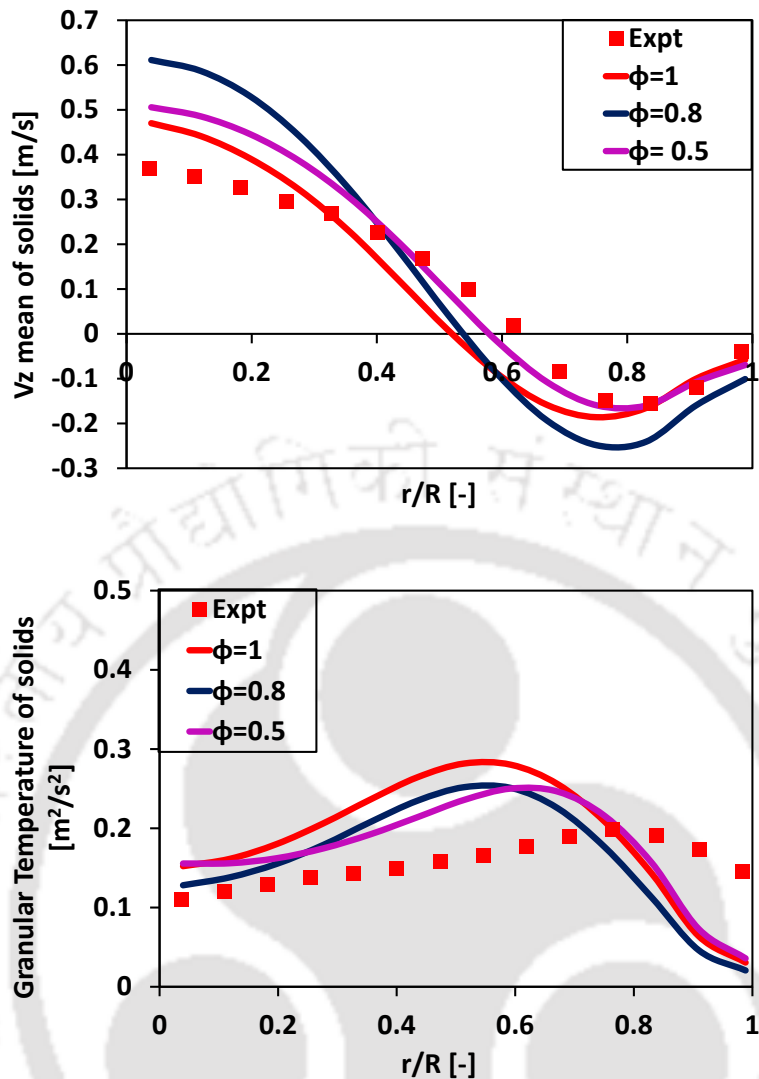


Figure A.4 Axial profiles of mean axial velocity and granular temperature for different specularity coefficient in G-S conical fluidized bed ($U_g = 7.6$ m/s and 1 mm solid)

The restitution coefficient predicts the elastic nature of the collision between the particle and the wall. In this work, the restitution coefficient of 0.95, 0.96 and 0.97 was investigated. Figure A.5 shows the axial profile of mean axial velocity and volume fraction for different restitution coefficient. The restitution coefficient 0.96 gives closer value to experimental results. Therefore, in current work, restitution coefficient of 0.96 is used for further simulations. Thus with this developed model parameters, the effect of gas inlet velocity and particle size were investigated.

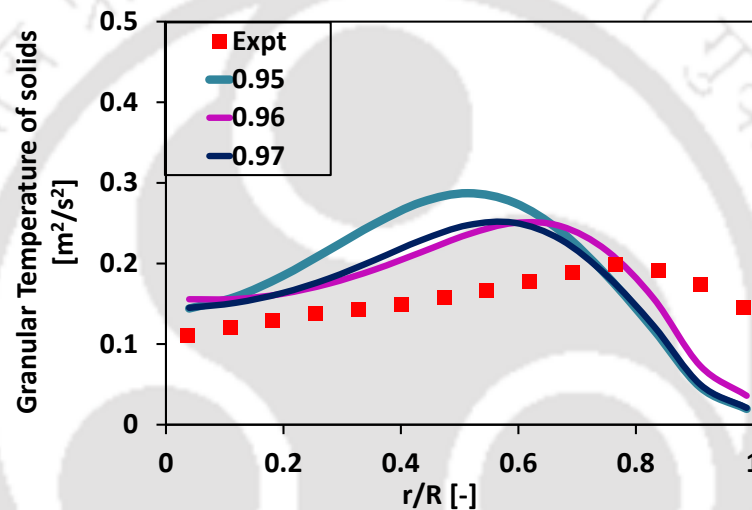
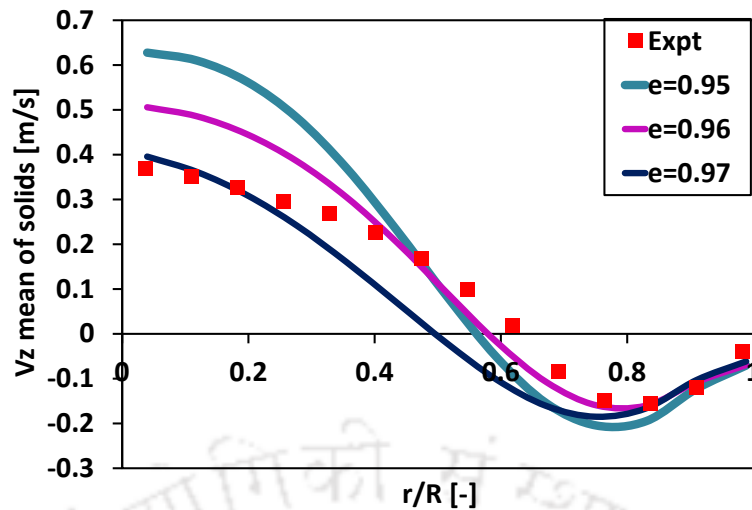


Figure A.5 Axial profiles of mean axial velocity and volume fraction for different restitution coefficient in G-S conical fluidized bed ($U_g = 7.6$ m/s and 1 mm solid)

A.4 Effect of gas inlet velocity

Figure A.6 shows the effect of gas inlet velocity on the mean axial velocity for 1 mm and 0.6 mm solids where values are compared with the experimental data. The blue points correspond to the solid axial velocity at a velocity of 3.8 m/s, red points correspond to the solid axial velocity at a velocity of 5.7 m/s and magenta points correspond to the solid axial velocity at a velocity of 7.6 m/s. The solid line of respective color represents the results those are numerically obtained. The simulation shows that the mean solid velocity

increases with an increase in gas inlet velocity. Simulation is able to predict the mean solid velocity qualitatively but not quantitatively. For higher velocities of 1 mm solids, the solid velocities are matching whereas for lower velocities of 1 mm solids the experimental values are underpredicted. However, for 0.6 mm solids, the solid velocities are underpredicted for all the velocities. The simulation results are higher than experimental results as the bed considered is two dimensional whereas in actual case the bed is three dimensional. Hence, the u/u_{mf} ratio for simulation is higher as compared to experimental results.

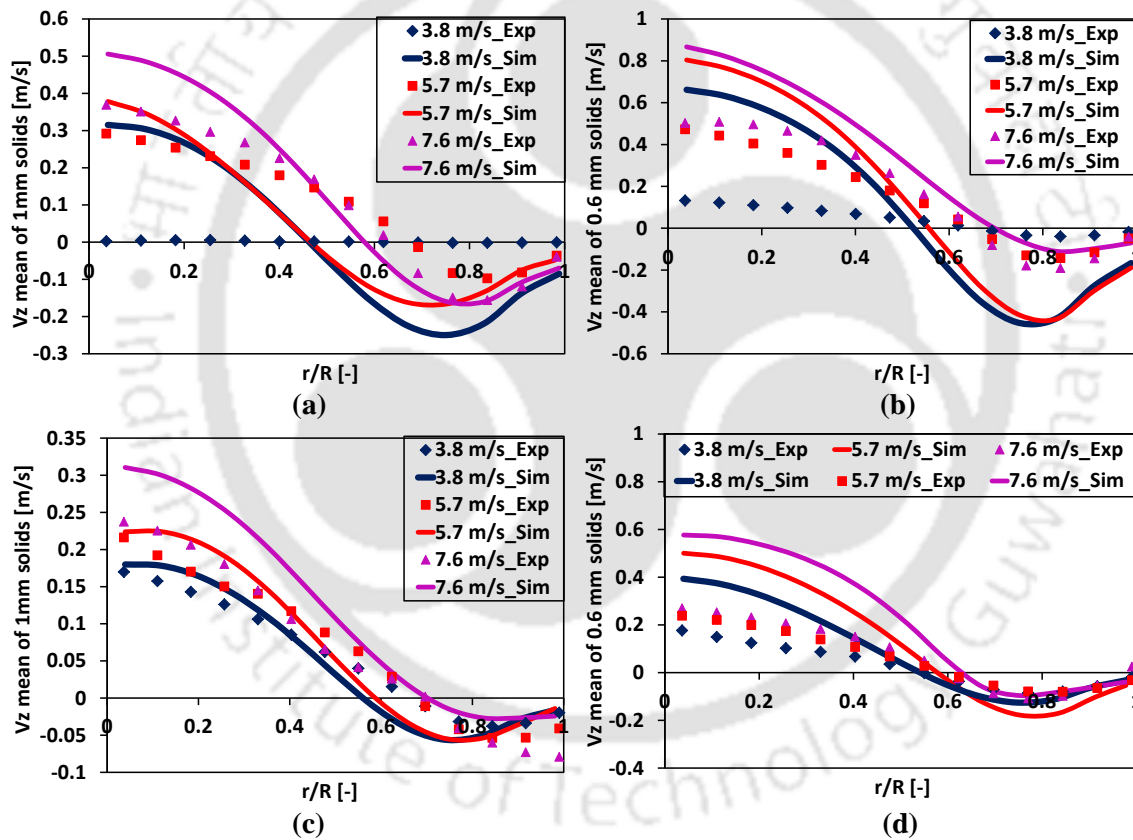


Figure A.6 Radial profile of mean axial velocity of solid at different velocities: (a) 1 mm particle on top section, (b) 0.6 mm particle on top section, (c) 1 mm particle at bottom section, and (d) 0.6 mm particle at bottom section

Figure A.7 shows the effect of gas inlet velocity on granular temperature prediction compared with the experimental values. Figure A.7 shows that the simulation is able to

predict the trend of granular temperature qualitatively. For both solids on the top section, the difference between simulation and experimental results are high compared to the bottom section. The granular temperature increases with an increase in gas inlet velocity for both simulation and experiment.

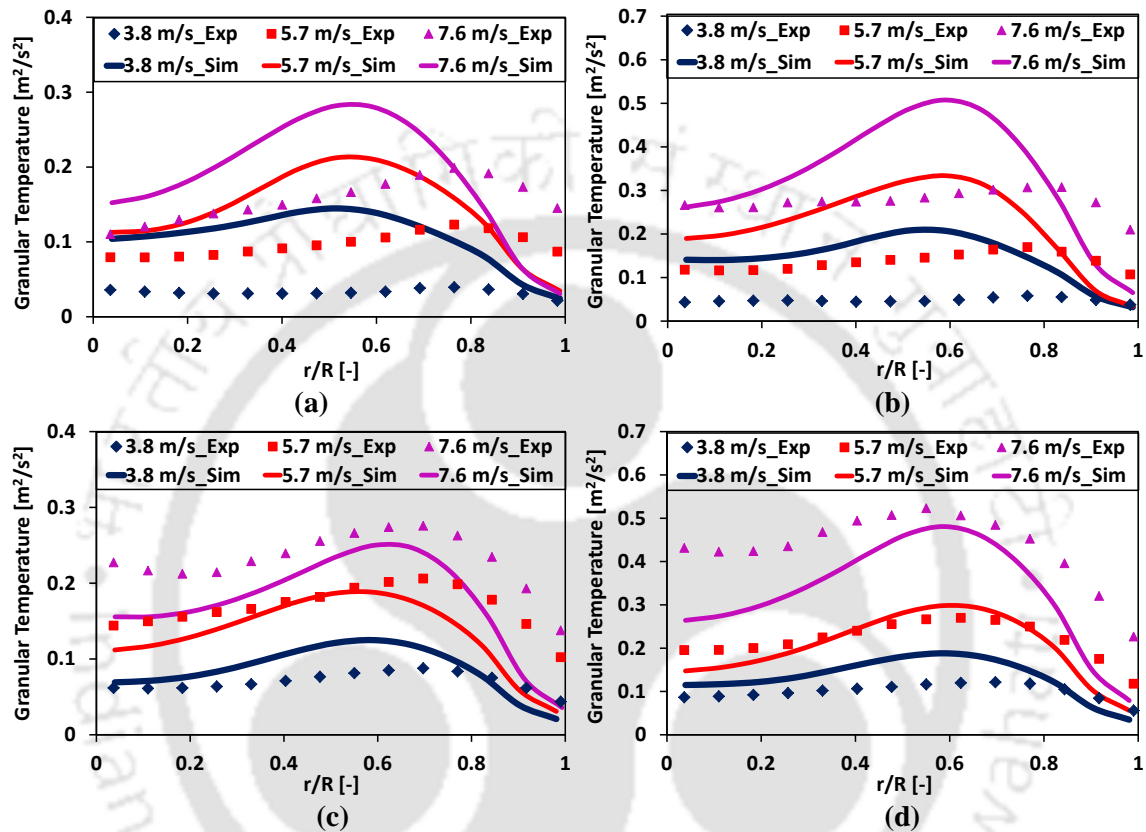


Figure A.7 Radial profile of mean granular temperature of solid at different velocities: (a) 1 mm particle on top section, (b) 0.6 mm particle on top section, (c) 1 mm particle at bottom section, and (d) 0.6 mm particle at bottom section

A.5 Summary

In this appendix, Euler – Euler simulations of the gas-solid conical fluidized bed are presented. The main objective of this Appendix is to study the performance of the Euler – Euler model as the design and scale-up tool. It is found that developed CFD simulations are able to predict the experimental data qualitatively. In addition to the first order moments, second-order moments are also validated. However, only a qualitative match is

obtained. More vigorous CFD simulations are required to improve the predictions by including particle-particle interactions. Euler-Lagrangian simulations can be a way forward for the same.

Notations

C_D	Drag coefficient, -
d_p	Particle diameter, μm
e_{ss}	Coefficient of restitution between solid particles, -
\vec{F}	Other forces, Kgm/s^2
\vec{g}	Acceleration due to gravity, m/s^2
g_0	Radial distribution function, -
$g_{0,ss}$	Solids radial distribution function, -
k_s	Kinetic energy per unit mass of solids, m^2/s^2
$K_{s,f}$	Momentum exchange coefficient, kgm^3/s
k_s	Solids conductivity/ Diffusion coefficient of granular energy, kg/ms
P	Pressure, N/m^2
Re	Reynolds number, -
U_g	Superficial gas velocity, m/s
\vec{v}	Velocity, m/s
\vec{u}_f	Ensemble averaged time smoothed velocity, m/s

Greek letters

ε	Volume fraction (holdup), -
ρ	Density, kg/m ³
$\bar{\bar{\tau}}$	Stress-strain tensor, N/m ²
$\bar{\tau}_f$	Total shear stress, N/m ²
Θ_s	Granular temperature, m ² /s ²
η	Index on realizations, -
φ_{fs}	Term modelling solids energy dissipation by correlations between solids and liquid velocity fluctuations, kg/ms ³
γ_{Θ_s}	Collisional dissipation of energy, kg/ms ³
μ_f^{turb}	Turbulent viscosity of fluid, kg/ms
μ	Viscosity, kg/ms
λ_s	Bulk viscosity, kg/ms

Subscript

f	Fluid
i	Projection subscript
p	Particle
q	Phase index
s	Solids

References

- Chapman, S. and Cowling, T.G., 1990. *The Mathematical Theory of Non-Uniform Gases*. 3rd Ed., Cambridge University Press.
- Deen, N.G., Annaland, M.V.S., van Der Hoef, M.A., Kuipers, J.A.M., 2007. Review of discrete particle modeling of fluidized beds. *Chem. Eng. Sci.* 62, 28–44.
- Ding, J. and Gidaspow, D., 1990. A Bubbling Fluidization Model Using Kinetic Theory of Granular Flow. *AIChE J.* 36, 523–538.
- Gibilaro, L.G., Di Felice, R., Waldram, S.P., Foscolo, P.U., 1985. Generalized friction factor and drag coefficient correlations for fluid-particle interactions. *Chem. Eng. Sci.* 40, 1817–1823.
- Gidaspow, D., Bezburuah, R., Ding, J., 1992. Hydrodynamics of circulating fluidized beds: Kinetic theory approach in *Fluidization VIII*, 75-82.
- Gidaspow, D., 1994 *Multiphase Flow and Fluidization: Continuum and Kinetic Theory Descriptions*, first ed. Academic Press, San Diego.
- Hill, R.J., Koch, D.L., Ladd, A.J.C., 2001. Moderate-Reynolds-number flows in ordered and random array of spheres, *J. Fluid Mech.* 448, 243-278.
- Huilin, L., Gidaspow, D., 2003. Hydrodynamic Simulations of Gas - Solid Flow in a Riser. *Ind. Eng. Chem. Res.* 42, 2390–2398.
- Lun, C.K.K., Savage, S.B., Jeffrey, D.J., Chepurny, N., 1984. Kinetic theories for granular flow: inelastic particles in couette flow and slightly inelastic particles in a general flow field. *J. Fluid Mech.* 140, 223-256.

Syamlal, M., O'Brien, T. J., 1989. Computer simulation of bubbles in a fluidized bed. AICHE Symp. Ser. 85, 22-31.

Tsuji, Y., Morikawa, Y., Tanaka, T., Nakatsukas, N., Nakatani, M., 1987. Numerical simulation of gas-solid two-phase flow in a two dimensional horizontal channel. Int. J. Multiph. Flow 13, 671-684.

Wen, C.Y., Yu, Y.H., 1966. Mechanics of fluidization. The Chemical Engineering Progress Symposium Series 162, 100-111





Appendix B

Pressure drop versus velocity plot

Figure B.1 and B.2 show the pressure drop versus velocity curve for 1 mm and 0.6 mm particles in gas-solid conical fluidized bed, respectively. The minimum fluidization velocity for partial and full fluidization for both 1 mm and 0.6 mm particles are matching with the calculated velocities from Peng and Fan (1997).

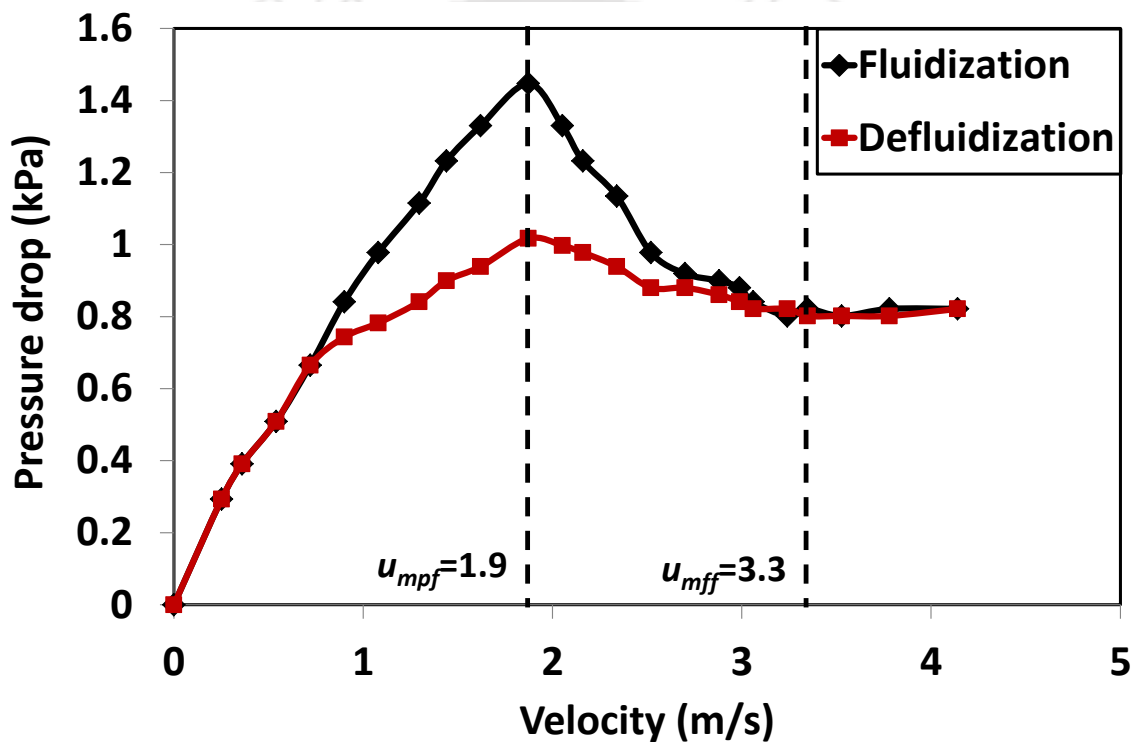


Figure B.1 Pressure drop versus velocity curve for 1 mm particle (G-S bed)

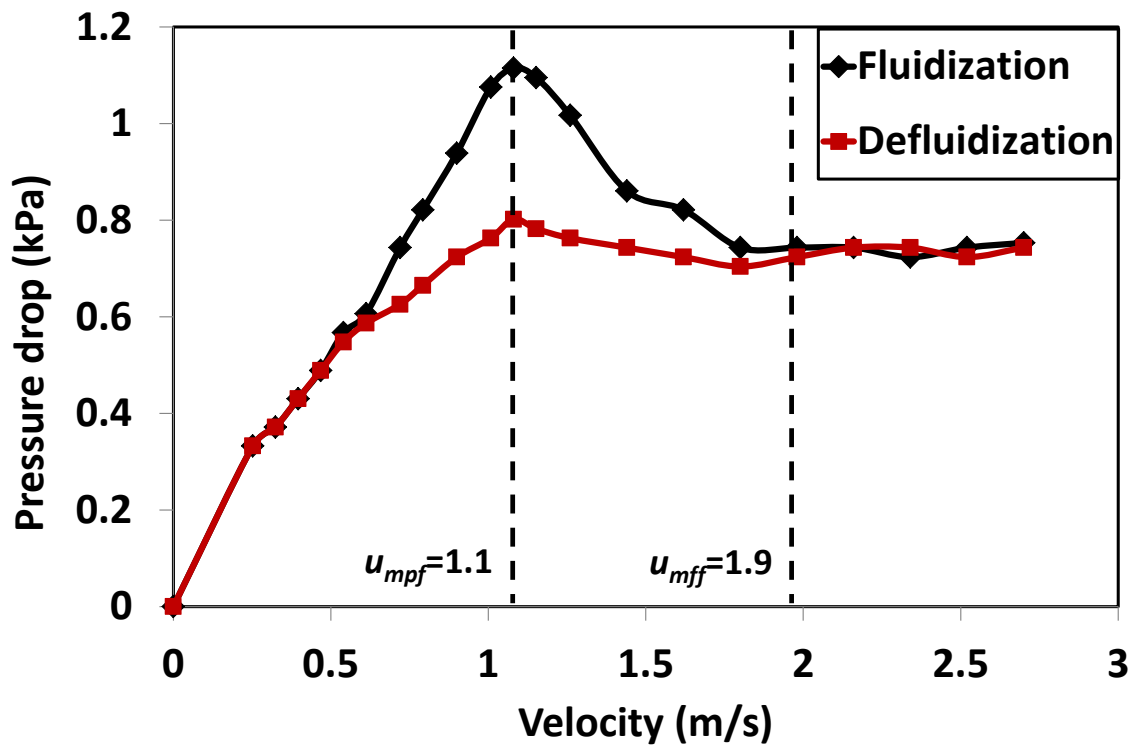


Figure B.2 Pressure drop versus velocity curve for 0.6 mm particle (G-S bed)

Table B.1 shows the calculated values of minimum fluidization velocity for partial and full fluidization for both 1 mm and 0.6 mm particles obtained from present experiment and Peng and Fan (1997) correlation.

Table B.1 Minimum fluidization velocity in gas-solid conical bed

Material	Size of solid (mm)	Peng and Fan correlation		Experimental data	
		u_{mpf} (m/s)	u_{mff} (m/s)	u_{mpf} (m/s)	u_{mff} (m/s)
Glass beads	1	1.97	3.34	1.97	3.34
Glass beads	0.6	1.1	1.94	1.1	1.94

Figure B.3 and B.4 show the pressure drop versus velocity curve for 1 mm and 0.6 mm particles in liquid-solid conical fluidized bed, respectively. The minimum fluidization velocity for partial and full fluidization for both 1 mm and 0.6 mm particles are matching with the calculated velocities from Peng and Fan (1997).

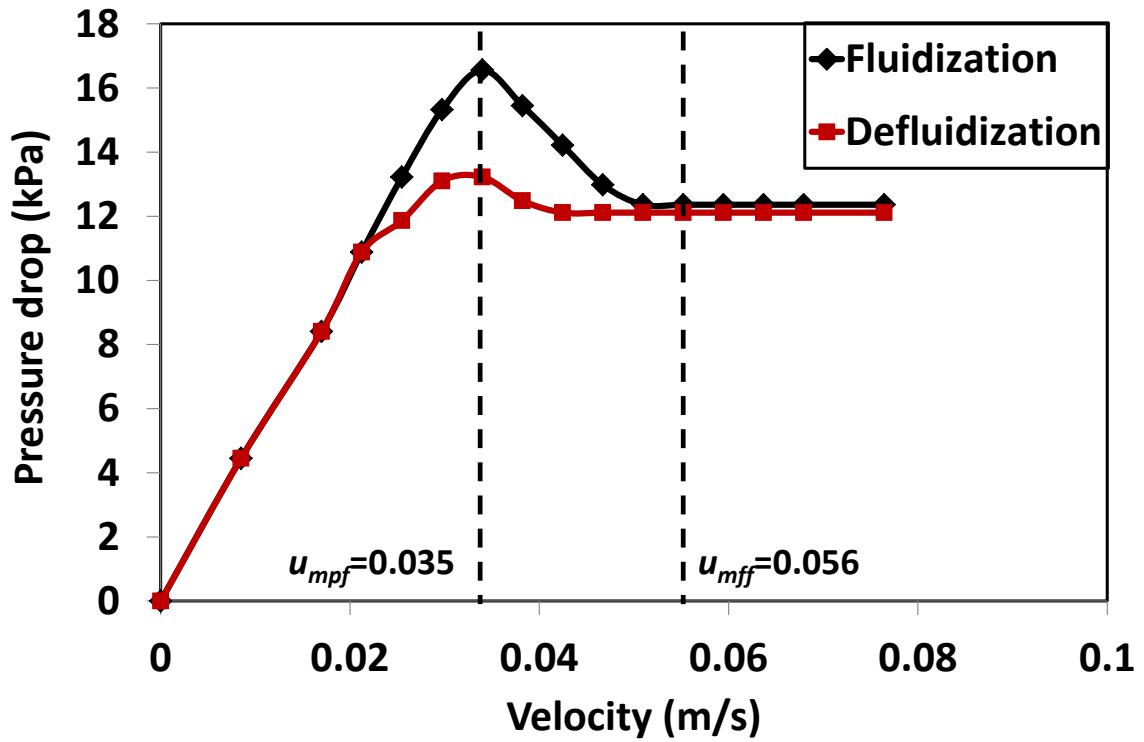


Figure B.3 Pressure drop versus velocity curve for 1 mm particle (L-S bed)

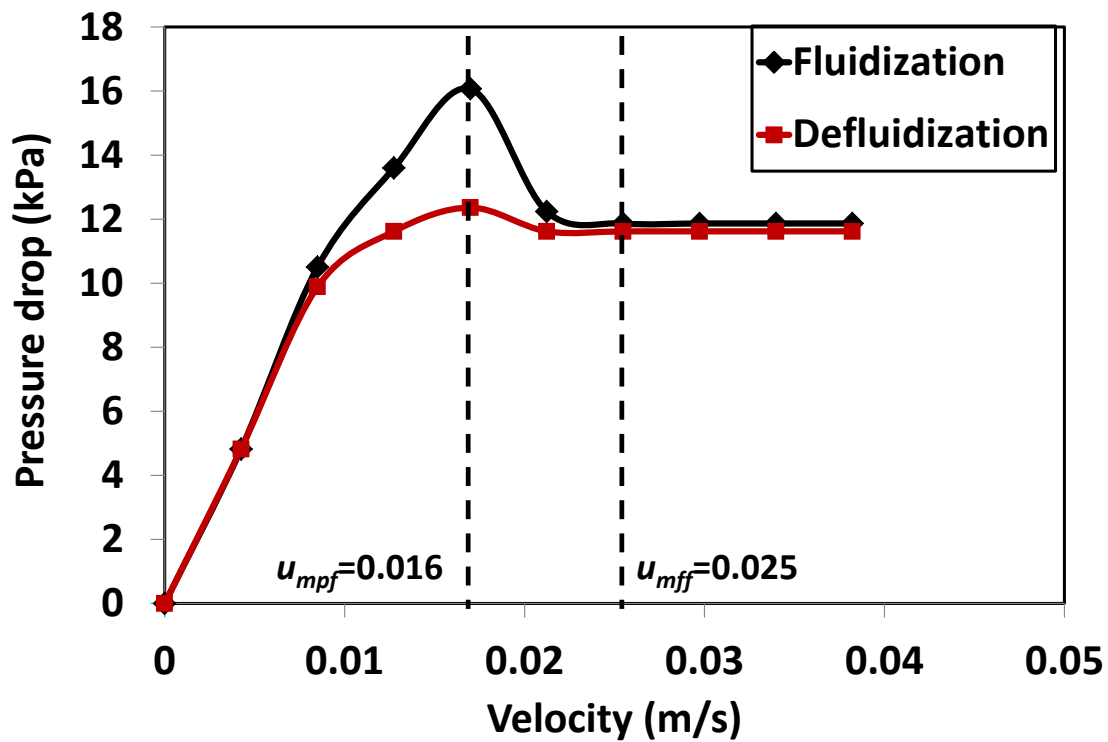


Figure B.4 Pressure drop versus velocity curve for 0.6 mm particle (L-S bed)

Table B.2 shows the calculated values of minimum fluidization velocity for partial and full fluidization for both 1 mm and 0.6 mm particles obtained from present experiment and Peng and Fan (1997) correlation.

Table B.2 Minimum fluidization velocity in liquid-solid conical bed

Material	Size of solid (mm)	Peng and Fan correlation		Experimental data	
		u_{mpf} (m/s)	u_{mff} (m/s)	u_{mpf} (m/s)	u_{mff} (m/s)
Glass beads	1	0.035	0.056	0.035	0.056
Glass beads	0.6	0.016	0.025	0.016	0.025

BIO-DATA

Lipika Kalo

Date of Birth 09.06.1989

Place of Birth Jharsuguda, India

Degrees B.Tech, Chemical Engineering, June 2010.

Indira Gandhi Institute of Technology,

Sarang, Odisha

M.tech, Chemical Engineering, June 2012.

National Institute of Technology,

Rourkela, Odisha

Ph. D, Chemical Engineering (Expected)

Indian Institute of Technology Guwahati, India.

Publications

In Referred Journals

Kalo, L., P. Kamalanathan, H. J. Pant, M. C. Cassanello and R. K. Upadhyay, "Mixing and regime transition analysis of liquid-solid conical fluidizedbed through RPT technique," Chemical Engineering Science 207 (2019) 702-712.

Kalo, L., H. J. Pant, M. C. Cassanello and R. K. Upadhyay, "Time Series Analysis of a Binary Gas-Solid Conical Fluidized Bed Using Radioactive Particle Tracking (RPT) Technique Data" Chemical Engineering Journal. <https://doi.org/10.1016/j.ccej.2018.08.193>

Jain, V., L. Kalo, D. Kumar, H. J. Pant and R. K. Upadhyay, "Experimental and numerical investigation of liquid-solids binary fluidized bed: radioactive particle tracking (RPT) technique and DDPM simulations," Particuology 33 (2017) 112–122.

Kamalanathan, P., L. Kalo, H. J. Pant and R. K. Upadhyay, "Effect of Dynamic Bias on Accuracy of Radioactive Particle Tracking (RPT) Technique at Different Data Acquisition Frequencies," Applied Radiation and Isotopes 128 (2017) 13–21.

Kalo, L., H. J. Pant and R. K. Upadhyay, "Scale-up of Gas-Solid Conical Fluidized Bed using Radioactive Particle Tracking (RPT) Technique," AIChE J. (Manuscript under preparation)

Conferences (International)

Kalo, L., R. K. Upadhyay, "Numerical and Experimental Investigation of Conical Gas-Solids Fluidized Bed with Head to Head Comparison," ISCREE 23, Bangkok, Thailand, 7-10 September 2014. [Oral Presentation]

Kalo L., D. Kumar, V. Jain, H.J. Pant and R. K. Upadhyay, "DEM-CFD Simulations for Liquid-Solids Binary Fluidized Bed with Experimental Validation by Using Radioactive Particle Tracking (RPT) Technique," ISCREE 23, Bangkok, Thailand, 7-10 September 2014. [Oral Presentation]

Kalo, L., R. K. Upadhyay, "Experimental and Numerical Investigation of Unary and Binary Gas-Solids Conical Fluidized Bed," CAMURE-9, Lyon, France, 7-10 December 2014. [Poster Presentation]

Kalo, L., R. K. Upadhyay, “Hydrodynamic Characteristics of Liquid Solids Binary Fluidized Bed through Radiotracer Techniques and Euler-Lagrangian Simulations,” GLS12, New York, USA, 28 June to 1 July 2015. [Oral Presentation]

Kalo, L., D. Kumar, R. K. Upadhyay, “Advanced CFD Modeling of Liquid-Solids Mono and Binary Conical Fluidized Bed with Experimental Validation Using Radiotracer Technique,” GLS12, New York, USA, 28 June to 1 July 2015. [Poster Presentation]

Kalo, L., H.J. Pant and R. K. Upadhyay, “Investigation of Conical Gas-Solid Fluidized Bed through Radiotracer Technique: Time Series Analysis,” CAMURE 10 & ISMR 9, Qingdao, China, 7 July to 10 July 2017. [Oral Presentation]

Tribedi, T., P. Kamalanathan, L. Kalo and R. K. Upadhyay, “Investigation of Gas-Solids Flow Behavior of Circulating Fluidized Bed Riser Using Pressure data and gamma Densitometry,” CAMURE 10 & ISMR 9, Qingdao, China, 7 July to 10 July 2017. [Poster Presentation]

Kalo, L., H.J. Pant and R. K. Upadhyay, “Experimental Investigation of Conical Liquid-solid Fluidized Bed using Radioactive Particle Tracking Technique,” NICSTAR 2018, Mumbai, India, 5th March to 7th March, 2018. [Poster Presentation]

Kalo, L., H.J. Pant and R. K. Upadhyay, “Experimental and Numerical Investigation of Conical Gas-solid Fluidized Bed,” NICSTAR 2018, Mumbai, India, 5th March to 7th March, 2018. [Poster Presentation]

Kalo, L., M. C. Cassanello and R. K. Upadhyay, “Time Series Analysis of a Binary Gas-Solid Conical Fluidized Bed Using Radioactive Particle Tracking (RPT) Technique Data,” ISCRE 25, Florence, Italy, 20th May-23rd May, 2018. [Oral Presentation]

Conferences (National)

Kalo, L., R. K. Upadhyay, “Conical Vs. Cylindrical Fluidized Bed: CFD Simulations and Experimental Validation,” CHEMCON, Mumbai, 27-30 December 2013. [Poster Presentation]

Kumar, D., L. Kalo, R. K. Upadhyay, “Study of Binary Liquid-Solid Fluidized Bed using DEM-CFD Simulation with Experimental Validation by using Radioactive Particle Tracking (RPT) Technique,” CHEMCON, Chandigarh, 27-30 December 2014. [Oral Presentation]

Kalo, L., P. Kamalanathan, H.J. Pant, R. K. Upadhyay, “Experimental Investigation of Liquid-Solids Conical Fluidized Bed,” CHEMCON, Guwahati, 27-30 December 2015. [Oral Presentation]

Pradeep, S., L. Kalo, R. K. Upadhyay, “Time Series Analysis of Radioactive Particle Tracking Technique Data in Liquid-Solid Fluidized Bed,” CHEMCON, Guwahati, 27-30 December 2015. [Poster Presentation]

Kalo, L., R.K. Upadhyay, “Study of a Mono-dispersed and Binary Gas-Solid Conical Fluidized Bed Using Radioactive Particle Tracking Technique”, COMPFLU-2018, Roorke, 6-9 December 2018. [Oral Presentation]